Ab initio Calculation of Parameters for Electron and Spin Transport in Organic Crystals

Subhayan Roychoudhury

School of Physics

Trinity College Dublin

A thesis submitted for the degree of

Doctor of Philosophy
September, 2017

Trinity College Dublin
Coláiste na Tríonóide, Baile Átha Cliath
The University of Dublin

Declaration

I, Subhayan Roychoudhury, hereby declare that this dissertation has not been submitted as an exercise for a degree at this or any other University.

It comprises work performed entirely by myself during the course of my Ph.D. studies at Trinity College Dublin. I was involved in a number of collaborations, and where it is appropriate my collaborators are acknowledged for their contributions.

A copy of this thesis may be lent or copied by the Trinity College Library upon request by a third party provided it spans single copies made for study purposes only, subject to normal conditions of acknowledgement.

Subhayan Roychoudhury

September, 2017

Abstract

Organic semiconductors offer several crucial advantages over their inorganic counterparts in electronic and spintronic applications. Besides offering structural advantages such as variety and flexibility, organic semiconductors can be manufactured with cheaper processes and at lower temperature. These promising potentials call for the development of a complete theoretical framework, without any need for experimental input, for description of charge and spin transport in these materials. A possible strategy can be to employ a multi-scale method where electronic structure is calculated with *ab-initio* methods and the information so obtained is used to construct a material specific model Hamiltonian. This Hamiltonian can then be solved with statistical techniques to extract transport-related quantities, like mobility, spin-diffusion length etc. Since, in a real device, the organic semiconductor will be attached to conducting electrodes, the interface between the two systems will play a crucial role in the device functionality. Keeping these in mind, in this thesis, we attempted to calculate several important properties and parameters of organic crystals related to electron and spin transport, both for the bulk material and at the interface.

A modification of the popular Density Functional Theory (DFT) method known as constrained DFT (cDFT) has been used to calculate the charge transfer energies between a graphene sheet and a benzene molecule absorbed on it. We have computed these energy values for several modifications of the system-configuration and have rationalized the results in terms of classical electrostatics. Next, we have developed a method,

within the framework of calculations employing localized basis orbitals, to determine the accurate forces when the energy of the system depends on a subspace population. Such method, in conjunction with cDFT, has been used to evaluate the reorganization energy of a pentacene molecule adsorbed on a flake of graphene. We have also developed the excitonic DFT method for calculating the optical gap of materials with cDFT, by confining certain number of electrons within a subspace of the Kohn-Sham eigenfunctions. We have shown that this method predicts the optical gaps of organic molecules with appreciable accuracy. We have also tried to extend this method to periodic solids.

As a step toward describing spin-related phenomena, we have extracted the spin-orbit coupling matrix elements, which can be responsible for spin-relaxation in organic crystals, with respect to a set of maximally localized Wannier functions. We have applied this on several materials and showed that the spin-orbit split band structures calculated from the Wannier functions match those obtained directly with first principles calculations. Since, in organic crystals, lattice vibrations play a major role at finite temperature, we have extended the aforementioned work to include the effects of phonons. To this end, we have calculated, with respect to the Wannier functions, the spin-phonon coupling, namely the effect of various phonon modes on modification of spin-orbit coupling. We have performed such calculation on a crystal of durene and showed that there is no apparent correlation between the electron-phonon and the spin-phonon coupling terms.

Acknowledgement

First and foremost, my sincere gratitude to **Prof. Stefano Sanvito**, my thesis supervisor and my role model. I have received guidance and freedom in a perfect blend from prof. Sanvito. Besides having numerous invaluable discussions on physics, he has taught me the art of solving problems by breaking up a big task into small manageable ones. Above all, he has taught me the value of ethics, compassion and humility. I could not have asked for a better advisor for my PhD.

I am greatly indebted to **Dr. David D. O'Regan** who showed incredible patience in giving thorough and detailed answers to millions of my questions. My interest in first principles calculations is largely a result of countless extensive discussions with Dr. O'Regan. The works presented in Chapter 5 and Chapter 6 resulted from discussions with him.

I want to thank **Dr. Carlo Motta** for introducing me with great care to DFT and to the software SIESTA. Throughout the duration of my PhD, he has frequently helped me with extremely valuable suggestions and discussions. Chapter 4 is a result of collaboration with Dr. Motta.

I want to thank the past and present members of the Computational Spintronics group at TCD for their friendship. In particular I would like to thank **Dr. Ivan Rungger** for frequent help with SMEAGOL and **Dr. Andrea Droghetti** for suggesting excellent books and other reading materials.

I am thankful to **Stefania Negro** for her efficient handling of all the administrative works. I would like to express gratitude to Trinity Center for High Performance Computing (**TCHPC**) and Irish Center for High End Computing (**ICHEC**) for letting me use their computational resources.

I am eternally grateful to **my parents** for their unconditional love, support and encouragement. I want to thank my uncle, **Dr. Saroj Maity** who greatly inspired me to study science. Very special thanks to **Debottama, Sayantan, Deborashmi and Kaushambi**, the best cousins in the world and to **Anais, Gaurav, Jorge, Sagnik** and to all other friends in Ireland and India.

Finally, no amount of thanks will be sufficient to express my gratitude to my best friends and family in Dublin, **Vikram-da** and **Bidisha-di**, who protected me from all perturbations and made sure I stayed under a time-independent Hamiltonian.

Abbreviations

BVK Born-Von-Karman

c.c Complex Conjugate

cDFT Constrained Density Functional Theory

CT Charge Transfer

FBZ First Brillouin Zone

DFT Density Functional Theory

GGA Generalized Gradients Approximation

HK Hohenberg-Kohn

HOID Hybrid Organic Inorganic Device

HOMO Highest Occupied Molecular Orbital

SO Spin-Orbit

KS Kohn-Sham

LDA Local Density Approximation

LED Light Emitting Diode

LUMO Lowest Unoccupied Molecular Orbital

MLWF Maximally Localized Wannier Function

NEGF Non-equilibrium Green's Function

NGWF Non-orthogonal Generalized Wannier Function

OLED Organic Light Emitting Diode

OSC Organic Semiconductor

PBE Perdew-Burke-Ernzerhof (exchange-correlation functional)

QP Quasi Particle

RKS Restricted Kohn Sham

TDDFT Time Dependent Density Functional Theory

UKS Unrestricted Kohn Sham

TB Tight Binding

XC Exchange-Correlation

Contents

Chapter 1

Introduction

The cornerstone of modern technology is the ability to process and store information with machines. It would be hard to think of any aspect of life where one does not use such technological advances. The most common format for processing and storing data by machines is the binary format in which all the data are represented as combination of two numbers (0 and 1) each occupying the storage space of one bit. In the basic electrical circuit used in such technology, these two numbers can be represented as currents of two different magnitudes, one high and one low. Devices, which can work with binary data in form of electrical responses, are broadly classified as electronic devices.

1.1 Electronics

The field of electronics concerns the control and manipulation of electrons in devices made of certain materials, which possess properties facilitating such actions. The science and technology of electronics form one of the most ubiquitous and indispensable backbones of modern life.

- Integrated circuits or ICs, made up of numerous transistors, are the primary components of the processing units responsible for the **logic operations** of almost all

devices related to computing such as computers, mobile phones, tablets, calculators etc.

- LED lights, used extensively for their versatility and low energy consumption, are electronic elements which, when activated, act as **light sources**.

- Traditional **solar cells**, which convert light into electric current, are essentially large area photodiodes, namely they are electronic components in which light can reach the sensitive part of the device resulting in the generation of an electrical response.

- **Sensors**, which are used to detect physical (light, temperature, magnetic field, gravity, vibration, motion, stretching, etc.) or chemical (toxins, glucose level, oxygen level, hormones, nutrients, etc.) properties depend on electronic components for their operations.

- Amplifiers, which increase the power of any electrical signal and find widespread application in **speakers**, are made with electronic components.

Among the applications listed above, the first one, namely logic is probably the most widely used. In this case, the basic principle of operation is that of detecting the change in electric current in the device as a function of an external electric stimulus. For instance, in a transistor the current between the source and the drain changes as the gate voltage is changed and the detection of the change of the former as a function of the latter forms the basis of logic operations. Fig. 1.1 shows the basic structure and working principle of the simplest electronic device, a p-n junction *diode* [1]. It consists of an n-type material, known as *donor*, which is rich in free electrons very weakly bound to the ions, and a p-type material, known as *acceptor*, which has many vacancies in its valence states, i.e. which, in other words is rich in free holes. When an initially charge-neutral donor is brought into contact with an initially charge-neutral acceptor, the free electrons from the former diffuse into the latter to fill the vacant positions, resulting in a negatively charged acceptor and a positively charged donor. The migrated charges accumulated near the interface of the two materials give rise to an electric field from the donor to the

acceptor and an associated potential called the barrier potential. This prevents further charge transfer, creating what is known as a depletion region. Thus, in this condition there is no current in the device. In the *reverse bias* condition a positive (negative) potential is applied to the donor (acceptor), thus enhancing the barrier potential even further and strengthening the condition of no charge flow. However, in the forward bias condition, when one applies a positive bias voltage to the acceptor and a negative bias voltage to the donor, one can create an electric field opposite to the one responsible for the creation of the depletion layer. Thus, the bias reduces the width of the depletion layer and the barrier potential. When the bias is strong enough, charge carriers overcome the barrier potential and current flows through the $p - n$ junction from the acceptor region to the donor region. From the description presented above, it is clear that such devices can be used as switch between two current states representing the two binary numbers.

Considering the requisite properties, we see that, in order to qualify as a donor or an acceptor, a material needs to have unique electronic properties which allow for the desired control of electrons in them. These materials form the *active component* of an electronic device. As such for the donor, one needs a material which is rich in free electrons but not in free hole and for the acceptor one needs a material possessing the exact opposite characteristics. This is done by choosing a crystal where the energy difference between the highest occupied and the lowest empty electronic bands does not vanish, as in metals nor is as large as in insulators. Such materials, which are ubiquitous in almost all electronic devices are known as *semiconductors* [2]. In order to create a donor material, a semiconductor is *doped* with impurities so that an additional filled level is created very close to the conduction band just below it. Thus, the Fermi level is now positioned between this additional level and the valence band, and at room temperature, electrons can move into the conduction band giving rise to conduction. For an acceptor material, the pristine semiconductor is doped to create an additional empty level just above the valence band facilitating hole conduction at room temperature.

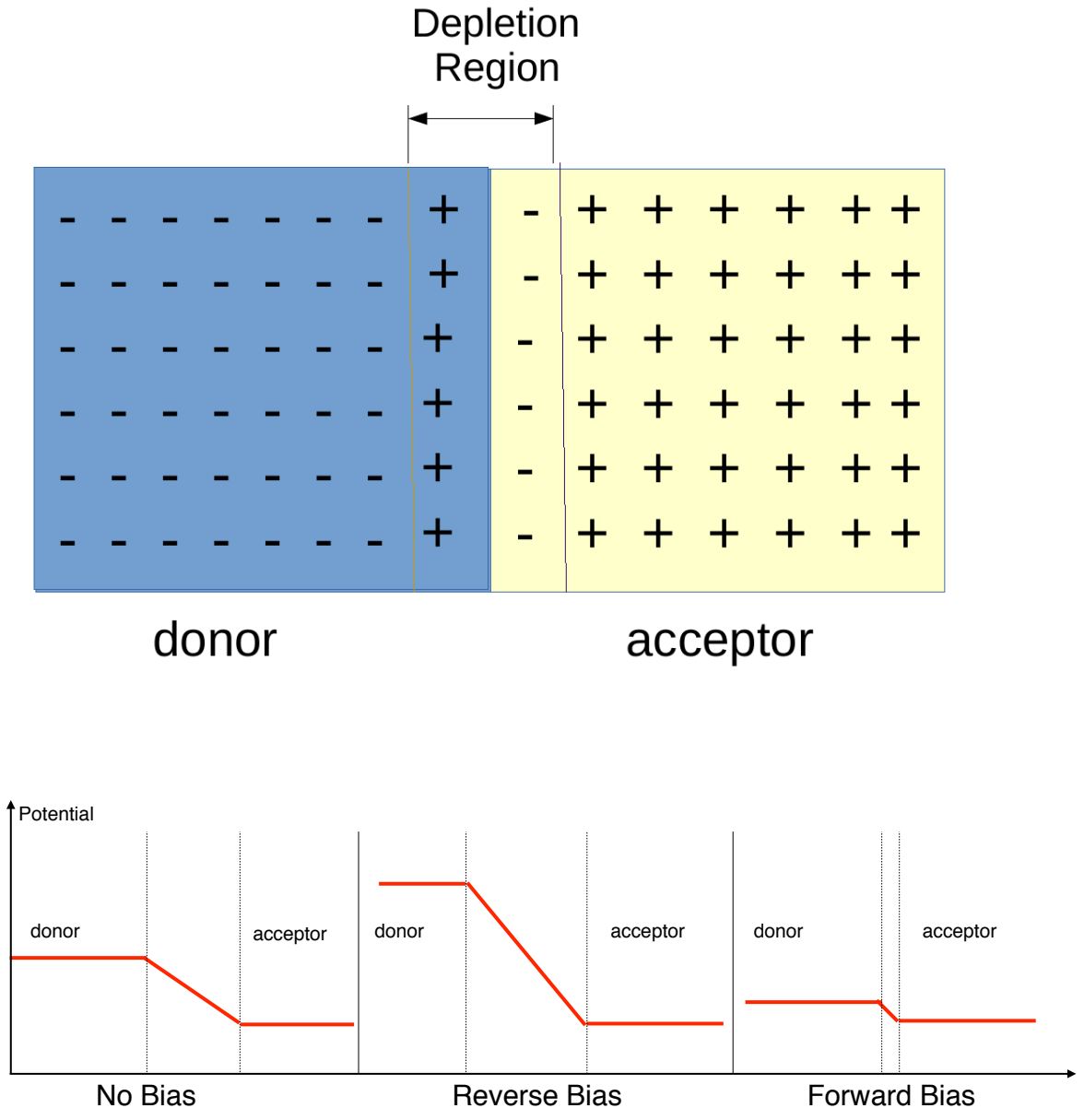

Figure 1.1: $p-n$ junction diode: Top panel shows an unbiased $p-n$ junction diode and its depletion region. Bottom panel shows potential profile of the $p-n$ junction under different conditions of bias; (From left to right) zero bias, reverse bias and forward bias, respectively.

1.2 Spintronics

In general, a magnetic field is less effective than an electric one in producing electronic motion. However, the magnetic properties of a material are associated with the spin of an electron and consequently in many cases an electric stimulus can be replaced by a magnetic one, provided that one exploits the spin degree of freedom, even if in an indirect fashion, in the detection process. The resistance faced by a charge carrier is independent of its spin in a non-magnetic material. However, if the material is magnetic, then the resistance typically depends on the relative orientation of the carrier spin and the local magnetization [3]. This inspires one to create the *spin valve* [4], which is a prototypical device for the interesting sub-field of electronics known as spin-electronics or *spintronics* [5]. The simplest spin valve consists of two layers of ferromagnetic materials sandwiching a non-magnetic spacer [6]. Usually, one of the ferromagnets have a fixed magnetization, while the magnetization of the other one is free to change. If both the ferromagnets have the same orientation of magnetization (say, up), then electrons with up (down) spin face very low (high) resistance in both of them. Here we invoke Mott's idea [3] that the current is carried by two parallel spin channels, one for up spin and one for down. Thus, in presence of a voltage difference, a current comprising predominantly up spin electrons will flow between the two layers. However, if the magnetizations of the two ferromagnets are opposite of each other, then an electron with any spin will face a high resistance in one layer and a low resistance in another layer. Now, if the resistance of the spacer is not too high, then the three layers can be thought of as resistors in series and for each spin channel, the net resistance will be the sum of the individual contributions of the three layers. In the parallel configuration there will be high current (because of the up spin electrons which face very low net resistance) but in the anti-parallel configuration there will be very low current (because all electrons face significant net resistance). Thus by knowing the magnetization direction of the fixed layer and by measuring the current flow, one can determine the magnetization of the free layer. This is smartly exploited in the read head of a hard disk drive, where one layer is held fixed and the other one, the free layer, has a magnetization that can

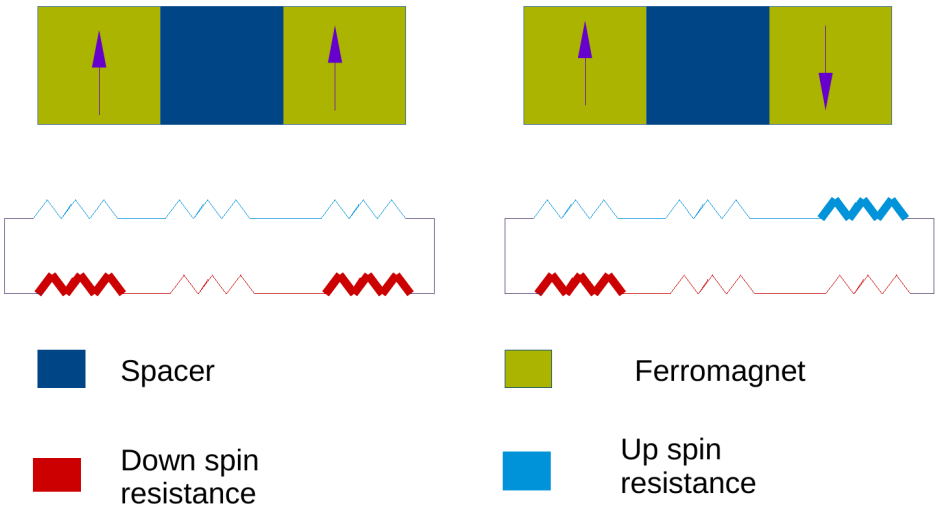

Figure 1.2: Schematic diagram showing a GMR based spin-valve where the spacer has low resistance. The arrows denote spin direction of the carrier. If, as shown in the left panel, both the ferromagnets have the same direction of magnetization (say up), then carriers with up (down) spin face very small (large) resistance in both ferromagnets. Therefore, a current comprising spin up carriers flows from one ferromagnet to the other. However, if, as shown in the right panel, the ferromagnets have opposite spins, then carriers of either spin will experience high resistance in one ferromagnet and low resistance in the other one, resulting in low current. In the schematic diagram for effective resistance, the top (bottom) series represents resistance faced by spin up (down) carriers while the thin and the thick lines denote low and high resistance, respectively. According to Mott's idea, the two parallel resistors for the two spin channels determine the effective resistance of the system.

be altered by the stray magnetic field of the hard disk. Today spintronics has found widespread application in the field of data storage as an integral component of the hard disk drives.

One of the crucial points related to spin-valves is the choice of material used as spacer. Historically, in giant magneto-resistance (GMR) [7, 8] devices, a metal was used as spacer so that no additional resistive effect was introduced on the spin-polarized charge carriers. In contrast, in the tunnelling magneto-resistance (TMR) case [9], an insulator is used as spacer so that instead of spin injection into the spacer, spins tunnel from one ferromagnet to the other. Yet another possibility is that of using semiconductors [10, 11] as spacers. However, since semiconductors have considerable resistance, which is equal for carriers of both spins, the net resistance of a spin-valve made with semiconductor spacers, depends very weakly on spin. This conductivity mismatch problem can be circumvented by adding layers of spin-selective large barriers on both sides of the semiconducting spacer [12]. The main motivation behind using semiconductors as spacers is the idea of having a common platform for logic operations (which use semiconductor based devices) and information storage. Besides, the electronic properties of semiconductors can be changed to a large extent as desired by tuning their electronic structure, which is a decided advantage.

1.3 Organic Electronics

Although inorganic semiconductor materials have traditionally been at the centre of focus for electronics and spintronics, a number of experimental and theoretical studies have propelled attention and interest in semiconductors made up of organic materials [13, 14, 15, 16]. Besides holding some key advantages related to properties and manufacturing, organic materials come in an infinite variety of shapes, forms and electronic structures which have endless possibilities for tuning and modification [17]. Organic semiconductors (OSCs) can be classified in two broad categories:

1. **Molecular crystals**, which are made up of organic molecules of well defined

structure and small molecular weight held together by Van der Waals interaction. Typical examples include crystals made of tris(8-hydroxyquinolinato)aluminium (abbreviated as Alq_3), copper phthalocyanine (abbreviated as CuPC), rubrene, durene, pentacene etc [18].

2. **Organic polymers**, which are mostly amorphous long chain-like molecules composed of repeated units known as monomers. Polymers like polyfluorene, polyphenylene vinylene (PPV), polythiophene etc. fall under this category.

There are vast differences among the general properties of organic and inorganic semiconductor materials. For example, the mobility of a conventional p-doped silicon is about 450 $cm^2V^{-1}s^{-1}$, whereas that of rubrene crystal, one of the best conductors among the OSCs, is approximately 10 $cm^2V^{-1}s^{-1}$ [19]. The differences in properties between OSCs and their inorganic counterparts suggests that the goal for application of organic electronics can not be that of displacing the existing inorganic counterparts but can be one of creating a separate niche area of its own [20].

1.3.1 Structural Properties of OSCs

A common structural property shared by most organic semiconductors is the presence of carbon σ and π bonds. The σ bonds are usually in the form of a planar sp^2 structures. The remaining p_z orbitals, which are perpendicular to the plane containing the bond, take part in forming π bonds between adjacent molecules (in crystal) or monomers (in polymer). These π-bonds play significant roles in the charge conduction in OSCs. The p_z orbitals from adjacent units form two delocalized levels- a π bonding level which contributes to the valence states and a π^* antibonding level contributing to the conduction states. Therefore, these π orbitals are usually responsible for charge transport in crystals or polymer.

Unlike typical inorganic semiconductors, which are held by covalent bonds whose strength as a function of distance (R) goes as $\frac{1}{R^2}$, the crystals or polymers in an OSC are held by the much weaker van der Waals force whose distance-dependence

goes as $\frac{1}{R^6}$. Therefore, OSCs are much softer and more fragile compared to the inorganic counterparts. Also, because of the weak bonding between individual units, charge carriers tend to be more localized on individual molecules. Therefore, charge transport in OSCs does not occur exclusively through delocalized band-like motion, but there is usually a significant contribution of localized hopping of carriers from one unit to another. This localization is also true for the neutral excitations, which are typically tightly bound Frenkel excitons confined to individual molecules.

1.3.2 Advantages of going Organic

The biggest advantages that OSCs offer over their inorganic counterparts are their mechanical flexibility, light weight and possibility of synthesis at low temperature [21]. Over the years, several low cost methods have been developed for fabricating OSC-based devices. An important advantage of organic electronic devices is that they can be manufactured at much lower temperature than that required for their inorganic counterparts. Thus, their production requires much less power and expenses and incurs less health-hazards. In particular, several possibilities for large area deposition and patterning for organic semiconductors have been demonstrated [20]. One huge advantage in organic electronics is the fact that organic thin films can be deposited on several inexpensive substrates like plastic, glass or metal foils- without having to worry about lattice matching conditions as with inorganic semiconductors.

1.3.3 Fabrication of Organic Electronic Devices

Thin films based on organic molecular crystals are formed usually with vapour-phase deposition techniques [22, 23]. In the Vacuum Thermal Evaporation (VTE) method, the source material is placed several centimeters below the substrate in a vacuum chamber. Heating of the source results in deposition of the film on the substrate. It is possible to deposit multiple layers with varied functionalities on the substrate and hence VTE is the most widely used method in commercial production of display devices based on organic

electronics. However, one of the biggest drawbacks of VTE is the difficulty experienced in maintaining a uniform rate of deposition. In a promising alternative technique called Organic Vapour Phase Deposition (OVPD) [24, 25], a hot walled vessel filled with an inert gas is used to place the source in. On heating the source, the gas saturates with the source material and deposits it on the cooled substrate. To manufacture an actual device, it is usually required to locally pattern the deposition on the substrate. This can be done at the time of deposition with Organic Vapour Jet Printing (OVJP) [26] where the evaporated organic molecules pass through a nozzle before being deposited on the substrate close to its tip. Several techniques [27, 28] are available for patterning the organic film after deposition.

Polymeric thin films are usually deposited with solution based techniques where the deposition takes place in the presence of a substrate (instead of being in vacuum or in an inert gas) which is fully evaporated after deposition. In this case patterning is possible with ink-jet printing [29, 30, 31] which promises unprecedented cost-effective efficiency. More recently, several complimentary methods for solution based processing have been proposed for molecular crystals as well [32, 33, 34].

1.3.4 Applications of Organic Electronics

Among the practical uses of organic electronic devices, **Organic Light Emitting Diode** (OLED) [15, 35] in display panels is by far the most widespread. OLED-based displays for phones, tablets and monitors are routinely manufactured in large scale - creating a huge commercially successful industry. Unlike liquid crystal displays, OLED displays function without a backlight and therefore have better power efficiency and can show deeper black levels. Since OLED pixels emit light directly, they have a greater contrast ratio and wider viewing angle compared to LCD screens. The response time for an OLED-based display device can be 1000 times faster than that of their LCD counterparts. Besides, OLEDs are thin, lightweight and flexible devices and therefore enjoy multiple advantages in technological applications. In a typical bilayer OLED an emissive layer and an absorptive layer of organic semiconductor are sandwiched between

two electrodes- all deposited on a substrate. The cathode and the anode injects electrons and holes into the semiconductor respectively. Since, in most cases the semiconductor has better mobility for holes, an electron and a hole combine close to the emissive layer to create a bound electron-hole pair, known as an exciton which eventually drops to a lower energy state with emission of electromagnetic wave with frequency in the visible spectrum.

Owing to the advantages of organic electronics, especially due to the cost effective fabrication technologies of large volume electronic devices, OSCs offer an alternative [36, 37] to their inorganic counterparts in photovoltaics. Even though there has been no large commercial production of **Organic Photovoltaic Cells** (OPV cells), due to two major drawbacks, (i) very low efficiency (10%) compared to silicon solar cells and (ii) the possibility of environmental degradation, these are subjects of active research in both the theoretical and experimental community. A typical OPV cell consists of an electron donor and an electron acceptor layer between two electrodes. One usually places additional blocking layers between the semiconductor and the electrodes. A photon from the sunlight excites an electron in the donor region. The resulting exciton is broken up into a free electron-hole pair by the effective field of the semiconductor heterojunction. The electron (hole) travels across the acceptor (donor) to be collected at the metal electrode and to feed into the circuit, thereby generating current flow.

Field Effect Transistors (FETs) made of OSCs are a common reality. Even though an **Organic Field Effect Transistor** (OFET) [38, 39, 40] is far from being usable in logic operations (due to low carrier mobility in organic crystals) it has promising features for other applications namely, as backpane of OLED displays, imagers, mechanical sensors, etc. An OFET follows the architecture of a Thin Film Transistor (TFT), where the source and the drain electrodes are deposited on the semiconductor channel, which is separated by an insulating layer from the gate electrode. As in any FET, a voltage between the gate and the source electrodes drives a current between the source and the drain.

Property	Organic Semiconductor	Inorganic Semiconductor
Mechanical Property	Higher mechanical flexibility, softer structure, lighter weight	Less flexibility and softness, heavier material
Production	Easy and low-cost production	Expensive and labour intensive production
Mobility	Low mobility	Much higher mobility
Variety	Large range of variety in structure and property	Less variety in structure and property
Temperature	Narrow window of optimum temperature for operation	Wider window of optimum temperature for operation
Spin relaxation time (T_2)	Lower spin relaxation time	Higher spin relaxation time

Table 1.1: Comparison of properties of organic semiconductors with the inorganic counterparts.

1.4 Organic Spintronics

As mentioned before, using inorganic semiconductors as spacer materials in spintronic devices offers the advantage of having a single platform for processing and storage of data. The ease of low-cost production of OSCs is a motivation enough to explore the possibility of incorporating them in spintronic devices. A desirable quality for a spacer material is that it should maintain the initial spin-polarization of the injected carrier as much as it can. In other words, the scattering of spins inside the spacer should be minimal. Since the main agents of spin scattering, namely spin-orbit coupling and hyperfine interaction are both low in OSCs [19], organic materials usually have very long spin-relaxation time, τ_s. This is a measure of the average time taken for spin relaxation.[1] This makes OSCs attractive candidates for research on spintronic applications. There are several questions related to such research and they prove to be challenging for experimentalists and theoreticians alike [41]. Since the mobility in OSCs is much lower than that of typical inorganic semiconductors, it is debated whether the transport of carriers from one ferromagnet to the other occurs by injection (as in GMR) or by tunnelling (as in TMR). Recent experiments have shown definitive evidence in support of spin-injection in CuPC [42] and Alq_3 [43] crystals. Experiments have also shown a negative magnetoresistance [44] in organic spin valves, i.e. the resistance diminishing with increment of an applied magnetic field. This apparently surprising experimental evidence has been explained [45] as the result of a renormalization of the widened molecular states at the metal-OSC contact. Such states hold the key to determining the spin-polarization of the injected current. This provides additional challenge to the modelling of these molecular levels and thereby predicting the current. Finally, a crucial question, which is yet to be answered is: which interaction, spin-orbit coupling or hyperfine interaction, is responsible for spin-relaxation in OSCs? As

[1] Here, it is worth mentioning that the spin-relaxation time can pertain to two very distinct phenomena. In the context of nuclear magnetic resonance, the longitudinal spin relaxation time, T_1 is the time needed for the spin to reach equilibrium with its surroundings. In contrast, the transverse relaxation time, T_2 is the time associated with relaxation of an injected spin from one configuration to the other. In this thesis, we are interested mostly in T_2.

conflicting experimental evidence is currently present in support of both [46, 47], it is conjectured that the relative dominance of one over the other depends on the specific OSC used.

1.5 Theoretical Description

The above discussion points to the need for a complete theoretical description of charge and spin transport in semiconductor devices made of organic materials. Since a typical organic electronic device consists of an OSC crystal sandwiched between metallic electrodes, an *ab initio* theory (i.e. one for which the only required inputs are the experimental conditions and the structure of the materials involved) for such a real Hybrid Organic/Inorganic Device (HOID) would be of great interest. Of particular importance will be a general transport theory for an HOID where the crystal ranges in length from 10-100 nm since this is the typical length-scale for exciton recombination [48] or spin relaxation [19]. The unique structural properties of OSCs, which in many cases serve as the advantages of organic electronics, make such theoretical description of transport extremely difficult and challenging. This can be attributed to mainly two reasons:

1. Since OSCs are composed of well-separated and weakly interacting molecules, charge carriers tend to be localized and the delocalized band-like transport seen in covalently bonded inorganic semiconductors is not observed. In organic crystals, charge transport likely occurs as a mixture of band-like transport and hopping of localized carriers. The relative contribution of the two mechanisms depend largely on the particular crystal and experimental conditions such as the temperature. This makes it very difficult to formulate a general, computationally viable framework valid across all regimes of transport in such materials [49].

2. The weak intermolecular attraction also results in the abundance of vibrational modes at finite temperature. These vibrational motions play a crucial role in defining the transport in such materials and renders popular *ab initio* methods like

DFT in conjunction with the Non-equilibrium Green's Function (NEGF) method inadequate in their treatment.

In addition, in a real HOID, the effect of injection of charge/spin carrier from the electrode into the OSC must be fully incorporated within the theoretical model. Such injection in general depends heavily on the electronic structure at the interfacial region between the metal and the crystal making the modelling of transport a multi-faceted problem. The most promising general framework in this regard is to calculate the accurate electronic structure of the system in question: including both the semi-conductor crystal and the metal-organic interface. Then one can construct a model Hamiltonian for the system, using parameters obtained from the electronic structure calculations. By solving this model Hamiltonian, one can obtain the observables associated with transport in the real HOID.

In the next chapter we will present a brief review of the existing models for describing charge transport in OSCs in various limits. This provides an idea of the state of the art in this area and also highlights the challenges present.

Chapter 2

Modelling Transport in Organics

Modelling charge transport in organic materials is as challenging as it is important. The density functional theory+ Non-equilibrium Green's Function (DFT+NEGF) scheme [50, 51], one of the most popular techniques for the theoretical description of transport, proves to be inadequate in treating real organic devices for several reasons. This fully quantum mechanical treatment is limited to devices comprising a few hundreds of atoms. A real Hybrid Organic Inorganic Device (HOID) of 10-100 nm length can contain about 10,000-10,000,000 atoms rendering it computationally intractable for the DFT+NEGF scheme. Secondly, this scheme is designed for phase-coherent transport. Although inelastic effects can be included perturbatively, any system where the transport is dominated by the vibrational degrees of freedom are off-limits for this method. Organic crystals are typically composed of molecules loosely bound to each other by weak Van der Waals' force. This is in contrast with common inorganic semiconductors in which the bond is typically a much stronger covalent bond. Since the molecules are weakly bound, at finite temperature they vibrate with large amplitude about their equilibrium position. This means that at finite temperature, organic semiconductors typically have a large number of phonons in them. The electrons and the phonons influence each other and their combined effect is described with a collective quasiparticle named *polaron*. The interplay between ionic and electronic motion makes the theoretical modelling of transport in organic semiconductors much more challenging and complicated than in

their inorganic counterparts. Thus, the DFT+NEGF scheme is not a wise choice for such systems. Furthermore, in organic crystals the nature and effects of impurities, which play a crucial role in charge transport, are usually very different [52]. All these differences suggest that the common methods used for describing transport in inorganic semiconductors can not be used in their unmodified forms for organic crystals.

We begin this chapter with a very brief discussion of experimental observations. This will help us to appreciate the merits and drawbacks of various state-of-the art theoretical transport models that follow. Here we shall focus our attention mainly on transport of charge because, once the mechanism of transport and a viable method for its treatment are established, such method can be largely transferred to the spin-dependent case with an appropriate change in the Hamiltonian. Finally we shall provide a short description of the aims of a project proposed by Prof. Stefano Sanvito titled QUantitative Electron and Spin Transport theory for organic crystals based devices (QUEST), of which this thesis forms an integral part.

2.1 Experimental Results

The experimental investigation of charge transport in OSC is challenging due to the difficulty in obtaining ultra-pure semiconductor crystals without defects. Early investigations involved mostly impure crystals and demonstrated activated transport [53], i.e. one where the mobility increases with temperature. However, more sophisticated measurements have attributed such behaviours mostly to the presence of defects. Experiments with highly purified pentacene [54], tetracene, rubrene and functionalized pentacene [55] have shown a temperature dependence of mobility that goes like $\mu \sim T^{-n}$. Since such relations are typical of delocalized band like transport, it is natural to think of such transport to be prevalent in organic semiconductors also. However, electron spin resonance experiment on a thin film of pentacene at room temperature have shown that the carriers are localized within approximately 10 molecules [56]. Furthermore, a recent experiment based on charge modulated spectroscopy (CMS) for pentacene showed sig-

natures of charge localization despite displaying a reduction of mobility with increasing temperature [57]. All these evidences seem to point, at least for highly purified and ordered organic crystals, to the apparently contradictory phenomenon of charge transport with localized carriers where mobility decreases with increasing the temperature.

2.2 Band Like Transport

In any ideal periodic crystal structure, the energy eigenstates are delocalized Bloch states, $\psi_{n\mathbf{k}}$, characterized by their crystal momentum, $\mathbf{k}$. A Bloch state can be expressed as a linear combination of plane waves with wave numbers differing by translations in the reciprocal lattice.

$$|\psi_{n\mathbf{k}}\rangle = \sum_{\mathbf{G}} C_n(\mathbf{k}+\mathbf{G})\,|\mathbf{k}+\mathbf{G}\rangle \tag{2.1}$$

where $\mathbf{G}$ denotes reciprocal lattice vectors and $|\mathbf{q}\rangle$ denotes a plane wave with wavenumber $\mathbf{q}$. This is discussed in detail in Section 3.1.

2.2.1 Inclusion of Phonons in the Model

As mentioned earlier, in organic crystals the vibrational degrees of freedom play an important role in charge transport. In quantum mechanics, the lattice vibrations are taken into account in terms of bosonic quasi-particles known as phonons (see Section 3.6 for a detailed account). Since the crystal in composed of weakly bonded molecular units, we intend to use a tight-binding (TB) Hamiltonian which is written with respect to localized basis orbitals (see observation 4 in section 3.1). The TB hamiltonian can be modified in the following way to include both electrons and phonons

$$\hat{H} = \sum_m \epsilon_m a_m^\dagger a_m + \sum_{m \neq n} \gamma_{mn} a_m^\dagger a_n + \sum_{mn\mathbf{Q}} \hbar\omega_{\mathbf{Q}} g_{\mathbf{Q}mn} (b_{\mathbf{Q}}^\dagger + b_{-\mathbf{Q}}) a_m^\dagger a_n + \sum_{\mathbf{Q}} \hbar\omega_{\mathbf{Q}} (b_{\mathbf{Q}}^\dagger b_{\mathbf{Q}} + \frac{1}{2}). \tag{2.2}$$

Here $\omega_{\mathbf{Q}}$ is the angular frequency of the phonon mode $\mathbf{Q}$ (here $\mathbf{Q}$ includes both the phonon wavevector $\mathbf{q}$ and the branch λ), $b_{\mathbf{Q}}^\dagger$ ($b_{\mathbf{Q}}$) is the creation (annihilation) operator for phonon mode $\mathbf{Q}$ and $g_{\mathbf{Q}mn}$ is the electron-phonon coupling. In the above equation, the first term corresponds to the on-site Hamiltonian, the second term is the hopping term, the third term denotes the electron-phonon coupling Hamiltonian, while the fourth one denotes the purely phononic part of the Hamiltonian. We can see that the terms in the above equation can be regrouped in the following manner:

$$\hat{H} = \sum_m \left(\epsilon_m + \sum_{\mathbf{Q}} \hbar\omega_{\mathbf{Q}} g_{\mathbf{Q}mm} (b_{\mathbf{Q}}^\dagger + b_{-\mathbf{Q}}) \right) a_m^\dagger a_m \tag{2.3}$$

$$+ \sum_{m \neq n} \left(\gamma_{mn} + \sum_{\mathbf{Q}} \hbar\omega_{\mathbf{Q}} g_{\mathbf{Q}mn} (b_{\mathbf{Q}}^\dagger + b_{-\mathbf{Q}}) \right) a_m^\dagger a_n \tag{2.4}$$

$$+ \sum_{\mathbf{Q}} \hbar\omega_{\mathbf{Q}} \left(b_{\mathbf{Q}}^\dagger b_{\mathbf{Q}} + \frac{1}{2} \right).$$

Except for the last term, which does not act on the electronic degrees of freedom, this looks like a TB hamiltonian with the onsite and hopping terms modified due to the presence of phonons. The phononic terms modifying the on-site energy and the hopping are known respectively as the **Hosltein term** and the **Peirls term**. In Eq. (2.3), the electronic and phononic degrees of freedom are coupled. Therefore, the goal here is to decoupled them to make further progress. By applying a canonical transformation [58]

$$H \rightarrow \tilde{H} = e^{S} H e^{S^{\dagger}}$$

where

$$S = \sum_{mn} C_{mn} a_m^{\dagger} a_n,$$

$$C_{mn} = \sum_{\mathbf{Q}} g_{\mathbf{Q}mn} (b_{\mathbf{Q}}^{\dagger} - b_{-\mathbf{Q}}) \tag{2.5}$$

one can obtain, for low electron density the transformed Hamiltonian, written with respect to the previous electronic creation and annihilation operators,

$$\tilde{H} = \sum_{mn} \tilde{E}_{mn} a_m^{\dagger} a_n + \sum_{\mathbf{Q}} \hbar\omega_{\mathbf{Q}} (b_{\mathbf{Q}}^{\dagger} b_{\mathbf{Q}} + \frac{1}{2})$$

where,

$$\tilde{E}_{mn} = (e^{C} E e^{-C})_{mn},$$

$$E_{mn} = \epsilon_{mn} - \sum_{\mathbf{Q}} \hbar\omega_{\mathbf{Q}} (g_{\mathbf{Q}} g_{-\mathbf{Q}})_{mn}. \tag{2.6}$$

It is important to note that unlike ϵ_{mn} or E_{mn} which are numbers, $\tilde{E}_{mn}$ is an operator since it contains the phonon creation and annihilation operators. It is difficult to proceed further with this exact Hamiltonian. However, one can approximate the operator terms $\tilde{E}_{mn}$ with their thermal averages $\langle \tilde{E}_{mn} \rangle$. This makes the electronic and the phononic operators completely decoupled in the Hamiltonian of Eq. (2.6). Clearly, the term proportional to $\langle \tilde{E}_{mn} \rangle$ for $(m \neq n)$ acts as the modified hopping parameter and gives a measure of the electronic bandwidth in presence of phonons. A calculation of these terms for a given finite temperature shows that the presence of the non-local electron-phonon coupling term results in a narrowing [58] of the polaronic bandwidth compared to the bare electronic one. A similar thermal averaging of the phononic operators can be performed in the context of transport calculation [59] and an expression of mobility can be obtained from the Kubo formula under such approximations. This

has been used successfully for modelling transport in ordered organic crystals at low temperature [60, 61].

2.2.2 Drawback of this model: Dynamic Disorder

The narrowing of the bands due to the presence of phonons implies an increment of the effective mass of charge carrier and consequently a reduction of the mobility. Therefore, at sufficiently high temperature, the mean free path of the carrier becomes comparable with intermolecular distances rendering the assumption of delocalized bandlike transport inapplicable.

Looking at it from a slightly different perspective, one can see that replacing the terms involving the phonon operators by their thermal averages is equivalent to assuming that the onsite energy and hopping (which are numbers) of the zero temperature TB Hamiltonian can be modified (replaced by other numbers) to take into account the effect of phonons. In other words, we assume that at all instants the crystal is still periodic and on average, it is sufficient to replace the tight binding Hamiltonian in absence of phonons with another one with different parameters in order to describe the temperature dependence of the mobility. However, at a high temperature the lattice sites oscillate about their equilibrium positions with large amplitudes. Due to the presence of a large number of phonon modes in the system, the thermal motion of the various sites are highly uncorrelated resulting in a loss of general periodicity of the system [62]- a phenomenon known as **dynamic disorder**. Thus, at each instant, the coupling between different lattice sites varies largely and the Hamiltonian becomes disordered. Such a disordered system can not be treated with a delocalized Bloch wave and thereby calls for new theoretical approaches to modelling transport.

2.3 Polaronic Hopping Transport

We have seen that dynamic disorder introduced by lattice vibrations makes a crystal non-periodic and treatment of the system with delocalized Bloch states becomes inadequate. Such disorder results in localization of the charge carrier over one or a few lattice sites. Although it doesn't take the dynamic disorder into account, a popular method for treating transport of localized charge at a finite temperature T is through the hopping of such localized charge carriers [63, 64] (small polaron) from one site m to another n. The rate k_{ET} of such a charge transfer is given by Marcus' theory [65]:

$$k_{ET} = \frac{|\gamma_{mn}|^2}{\hbar}\sqrt{\frac{\pi}{\lambda k_B T}}\exp\left[-\frac{(\lambda + \Delta G^0)^2}{4\lambda k_B T}\right] \tag{2.7}$$

where, k_B is the Boltzman constant, λ, known as the **re-organization energy** is the change in energy corresponding to the ionic re-arrangement following the charge transfer and ΔG^0 is the change in Gibbs' free energy corresponding to the same. Since the on-site energy in the TB picture (for the HOMO/LUMO) is a measure of charging energy of the site and since the local electron-phonon coupling provides a measure of the modification of this on-site energy due to the lattice vibrations, the re-organization energy can be thought of as an alternative way of charaterizing local electron-phonon coupling strength. This description ignores the non-local electron-phonon coupling (Peierls term) and the resulting dynamical disorder. It can be shown [49] that for a system without dynamic disorder, for $\gamma \geq \frac{\lambda}{2}$, there can not be any localized small polaron at any temperature and therefore the concepts of hopping and rate equation become moot. One of the most important limitations of this approach is its prediction of thermally activated transport- i.e. increment of mobility with temperature, which is in contrast with experimental results on highly purified and ordered organic crystals, in which the mobility is shown to decrease with temperature.

2.4 Model with Dynamic Localization

The preceding paragraphs suggest that though at very low temperature, the transport in a highly pure and ordered organic crystal can be considered to be band like, for a more general case, an effective model for charge transport in pure organic crystals at finite temperature should be able to predict a reduction in mobility with increment in temperature without assuming transport through delocalized Bloch states. An interesting procedure, developed by Troisi et al. [66, 67] solves this problem by using a semiclassical time-dependent Hamiltonian which treats the electronic and ionic degrees of freedom with quantum mechanical and classical approaches respectively. For the simplest case of a one-dimensional periodic system with nearest neighbour interaction and one localized orbital per site, the Hamiltonian takes the form:

$$H = \sum_j \left[-\gamma + g(u_{j+1} - u_j)\right] \left(|j\rangle \langle j+1| + |j+1\rangle \langle j|\right) + \sum_j \frac{1}{2}\left(m\dot{u}_j^2 + Ku_j^2\right), \quad (2.8)$$

where the time-dependent quantity u_j denotes the displacement of the j-th site from the equilibrium position at any instant, γ is the average hopping parameter between sites, g is the electron-phonon coupling and m and K are the mass and the force constant of the oscillator respectively. Clearly, here the first sum on the right hand side denotes the electronic Hamiltonian H^{el} (including electronic coupling with vibrations) and the second term denotes purely vibrational Hamiltonian. By treating the classical displacements $\{u_j\}$ as simple harmonic motion, their equation of motion can be expressed as

$$m\ddot{u}_j(t) = -Ku_j(t) - \frac{\partial}{\partial u_j} \langle \psi(t)|H^{el}|\psi(t)\rangle \quad (2.9)$$

where $|\psi(t)\rangle$ is the state of the quantum system evolving through the Schrödinger equation.

$$|\dot{\psi}(t)\rangle = -iH^{el}(t)\,|\psi(t)\rangle\,. \quad (2.10)$$

Temperature enters into the model in terms of the distribution of the initial lattice positions $\{u_j(0)\}$ and velocities $\{\dot{u}_j(0)\}$ and of the initial wave function $\psi(0)$. This model does not assume the transport to be delocalized band like although it predicts such transport at very low temperature. Studying the evolution of the wave function in such system, one can notice that the initially localized wave function spreads across the lattice due to the time-dependence of the effective transfer integrals. Most importantly, calculating a temperature averaged diffusion coefficient (D) and the corresponding mobility ($\mu = \frac{eD}{k_B T}$), one can see that the mobility decreases with increasing temperature- as is expected from experimental evidences. For a given temperature, in the limit of large γ and low g, the modulation of effective transfer integral due to the vibrations is much smaller than the average hopping and one reaches to the high mobility regime of delocalized band like transport.

2.5 Methodology for QUEST

We have discussed some model-based approaches for investigating charge transfer in organic crystals. The parameters required for such Hamiltonians are either obtained from experimental data or calculated with *ab initio* methods. With this background, we are now ready to briefly discuss the proposed methodology of the QUEST project. QUEST aims to construct a computationally viable semiclassical model Hamiltonian of a real Hybrid Organic Inorganic Device (HOID) with parameters obtained from first principles calculations and to solve the Hamiltonian using statistical techniques to obtain important properties related to charge and spin transport. Note that for a real device, the presence of inorganic electrodes near the organic crystal requires a theoretical description of the interface adding significant complexity to the modelling of transport. The description of the electrodes, which is not taken into account in any of the model-Hamiltonian-based approached discussed above, is incorporated naturally in the DFT+NEGF scheme. As such, QUEST aims to combine the best of both methods into a unified framework for complete *ab initio* description of charge and spin transport in real devices including the electrodes.

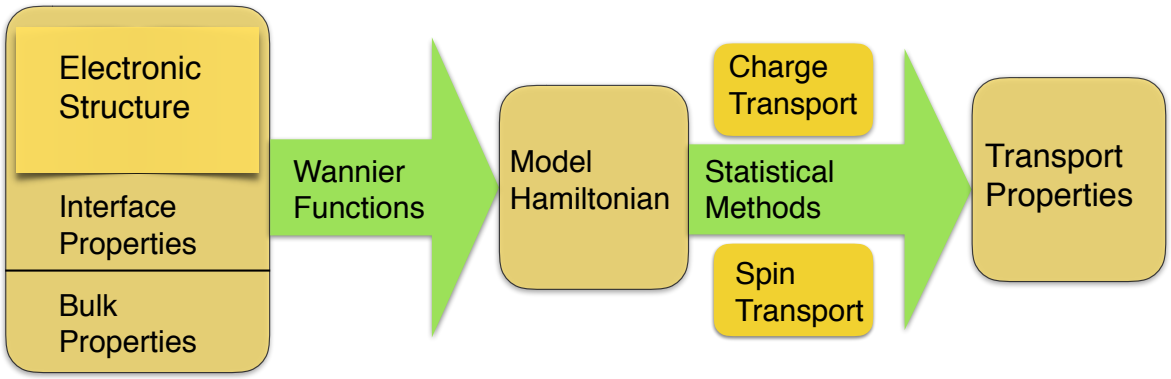

Figure 2.1: Flowchart showing methodology for QUEST.

The main parameters required for the Hamiltonian at the interface are the charge transfer energies and the transfer integrals. For a molecular crystal in the vicinity of an inorganic electrode, the electrode-molecule charge transfer energies can not be obtained from the frontier orbitals of the isolated molecule. Neither can they be calculated directly from DFT. However, these can be obtained with cDFT and the corresponding shift can be incorporated into the scheme of further calculations with the help of scissor operators [68]. For constructing the model Hamiltonian, one would also need the transfer integrals between the relevant states of the electrode and the molecule. These can be calculated [69] within the DFT+NEGF formalism by calculating the relevant level-broadening (this is essentially the imaginary part of the embedding self-energy of the electrode).

The Hamiltonian for transport inside the crystal must contain vibrational modes as well as description of the electronic degrees of freedom. In this approach, we adopt a classical description of the former and a quantum mechanical one for the latter. The local and non-local coupling between the electrons and the vibrational normal modes can be calculated through DFT based calculations with finite differences. An excellent basis set for such calculations is that formed by the Maximally Localized Wannier Functions (MLWFs) [70]. These take into account only the energetically relevant energy eigenstates, and thus allow one to limit the size of the calculation to a computationally tractable regime without losing crucial information. The various geometries corresponding to molecular vibrations can be sampled with a Monte Carlo method at a

given temperature (i.e. the weight function depends on the free energy, which, in turn would depend on the temperature). For each geometry, one would get a Hamiltonian similar to Eq. (2.8) (with parameters obtained from DFT calculations) and the net mobility can then be calculated as a statistical average over different configurations from Kubo formula. For the spin-transport, a similar approach can be adopted (one needs a spin-dependent Kubo formula for this) provided that we include spin-dependent terms like spin-orbit coupling, hyperfine interaction etc. in the Hamiltonian. Such model Hamiltonians should (at least in principle) be able to calculate interesting observables like spin-diffusion length or time in organic materials without any external input parameter. It is noteworthy that the existing calculations for spin-transport in organic materials rely exclusively on parameters obtained from experiments [71].

2.5.1 First-Principles Calculations

One important message emerging from the previous discussion is that the *ab initio* theoretical description of charge/spin transport in OSC-based devices must begin with a first principles calculation of electronic structure from which various parameters for further calculations are to be extracted. This is true not only for the QUEST workfow, but also for all the formalisms mentioned above, though the required parameters may vary. For charge/spin injection, this requires description of the electronic structure at the interface. Such descriptions include an accurate account of the energy levels relevant for electron transfer and energy associated with ionic relaxation following such transfer. For the transport in the bulk crystal this requires representation of the crystal Hamiltonian, including the spin dependent terms with respect to a suitable basis set- e.g. the Wannier functions [72, 73] (note that for the spin independent terms this approach has been recently employed successfully in ref. [61]). It is also necessary to calculate the ionic vibrational modes and their couplings with the electrons. This thesis reports calculations of such parameters through an *ab initio* approach based on DFT, which is the most widely used first-principles theoretical method for calculating ground state properties of materials [74, 75].

2.6 Thesis Outline

This thesis explore the key areas mentioned below:

1. In the next chapter (Chapter 3) we discuss some of the relevant theoretical concepts and methodologies used in this thesis. These create the platform for the research presented in subsequent chapters.

2. The energy change corresponding to the transfer of electron from a conductor to an adjacent organic molecule and vice-versa. Since a typical OSC contains many weakly bound organic molecules, we have also explored how the presence of nearby molecules affects such *charge transfer energies*. Chapter 4 contains a detailed report on this.

3. Since the charge transfer from an electrode to a molecule is followed by the relaxation of the ionic coordinates of the molecule, such events have an associated energy cost, known as *reorganization energy*. Such *reorganization energy*, which is a measure of local electron-phonon coupling has been calculated with advanced first-principles method taking the necessary forces into account. These are presented in Chapter 5.

4. The *optical gap*, which is a crucial quantity for applications related to OLEDs and photovoltaics, have been calculated with a technique which involves much less computational cost than the existing ones based on many body methods. This is discussed in detail in Chapter 6

5. For calculations related to spin transport, we have reported a method for the representation of the *spin-orbit matrix elements* of organic crystals with respect to MLWFs. We have presented this method and supporting calculations in Chapter 7.

6. Finally, since the spin-diffusion at finite temperature depends on the coupling between such spin-orbit terms with the ionic oscillations, we employ the aforementioned method in conjunction with calculations of lattice vibration to determine the *spin-phonon coupling*. This is discussed in Chapter 8.

Chapter 3

Theoretical Background

Since all the works presented in this thesis rely heavily on calculations of electronic structures, we dedicate this chapter to briefly outlining the underlying theories and techniques that form the basis of such calculations. The discussion begins with the framework for treating independent electrons in periodic crystals. This is followed by an outline of DFT, which is a widely used theory for treating the problem of interacting electrons by mapping it onto an equivalent problem of noninteracting ones and of cDFT, a slightly modified version of DFT which has been extensively employed in this thesis. Next we have discussed the basic working principle of computational software based on DFT and in particular of two softwares SIESTA and ONETEP with which all the electronic structure calculations have been performed. Finally we discuss the theory of lattice vibration and how these can be described from the results of a DFT calculation.

3.1 Energy Eigenstates of a Periodic Lattice

The Hamiltonians of a periodic lattice with lattice vectors $\mathbf{R_1}$, $\mathbf{R_2}$ and $\mathbf{R_3}$ obeys the condition

$$H(\mathbf{r}) = H(\mathbf{r} + \mathbf{R}), \tag{3.1}$$

where $\mathbf{R} = n_1\mathbf{R_1} + n_2\mathbf{R_2} + n_3\mathbf{R_3}$ and n_1, n_2, n_3 are any integers.

The Bloch theorem states that in such a system, the energy eigenfunctions have the form

$$\psi_{\mathbf{k}}(\mathbf{r}) = u_{\mathbf{k}}(\mathbf{r})e^{i\mathbf{k}.\mathbf{r}} \text{ where } \quad u_{\mathbf{k}}(\mathbf{r}) = u_{\mathbf{k}}(\mathbf{r}+\mathbf{R}), \tag{3.2}$$

which implies that

$$\psi_{\mathbf{k}}(\mathbf{r}+\mathbf{R}) = u_{\mathbf{k}}(\mathbf{r}+\mathbf{R})e^{i\mathbf{k}.\mathbf{r}}e^{i\mathbf{k}.\mathbf{R}} = \psi_{\mathbf{k}}(\mathbf{r})e^{i\mathbf{k}.\mathbf{R}}. \tag{3.3}$$

A proof of this theorem can be found in chapter 8 of reference [76]. A number of very important observations follow from Bloch's theorem.

1. **Observation 1:** The free electron stationary states are momentum eigenstates of the form

$$\langle \mathbf{r}|\mathbf{k}\rangle = \psi_{\text{free},\mathbf{k}}(\mathbf{r}) = e^{i\mathbf{k}.\mathbf{r}}. \tag{3.4}$$

Clearly, in a periodic crystal these are not energy eigenstates. However, the energy eigenstates of the crystal is expressible as a linear combination of the free particle waves, namely

$$|\psi\rangle = \sum_{\mathbf{k}} C_{\mathbf{k}} |\mathbf{k}\rangle . \tag{3.5}$$

Bloch's theorem offers us important insights about the coefficients $C_{\mathbf{k}}$. It says that any particular $|\psi\rangle$ is composed only of $|\mathbf{k}\rangle$ states differing by translations in the reciprocal lattice. That is to say that, only one $|\mathbf{k}\rangle$ state from each unit cell of the reciprocal lattice contributes toward a Bloch state. Consequently that Bloch state can be indexed by the corresponding $\mathbf{k}$-vector of the first Brillouin zone (FBZ).

$$|\psi_{m,\mathbf{k}}\rangle = \sum_{\mathbf{G}} C_m(\mathbf{k}+\mathbf{G}) |\mathbf{k}+\mathbf{G}\rangle , \tag{3.6}$$

where $\mathbf{G} = n_1\mathbf{K_1} + n_2\mathbf{K_2} + n_3\mathbf{K_3}$; $\mathbf{K_1}$, $\mathbf{K_2}$, $\mathbf{K_3}$ being the reciprocal lattice vectors. The subscript "m", which is known as the band index serves to remind that corresponding to each "k", there can be multiple Bloch states differing in energy.

2. **Observation 2:** in order to find out the allowed $\mathbf{k}$ values, one can apply the Born-Von-Karman (BVK) periodic boundary condition on the lattice such that the Bloch states have to obey the relation

$$\psi(\mathbf{r} + N_i\mathbf{R_i}) = \psi(\mathbf{r}), \tag{3.7}$$

where $i = 1, 2, 3$ and N_i is an integer denoting the BVK periodicity. It must be noted that this periodicity, which is a periodicity of the energy eigenstate is different from that of the Bloch theorem where the periodicity is in the Hamiltonian. The BVK condition restricts the k-values to

$$\mathbf{k} = \sum_{i=1}^{3} \frac{m_i}{N_i}\mathbf{K_i}. \tag{3.8}$$

Therefore, there are $N_1N_2N_3 = N$ possible values for the vector $\mathbf{k}$ and these form a continuum for a crystal with BVK periodicity at infinity.

3. **Observation 3:** Since the Bloch states are indexed with the $\mathbf{k}$ vectors, one can plot the energy eigenvalues against $\mathbf{k}$ and the resulting plot is known as the band-structure. For a given $\mathbf{k}$, one can have multiple energy eigenvalues corresponding to Bloch states with different "m"s. These are known as bands.

4. **Observation 4 (The Tight Binding Model):** Instead of expressing the Bloch states in terms of plane waves, we can write them out in terms of basis functions localized at lattice points as

$$|\psi_{n\mathbf{k}}\rangle = \sum_{\mu,\mathbf{R}} C'_{\mu n}(\mathbf{k}, \mathbf{R}) \, |\phi_{\mu,\mathbf{R}}\rangle \tag{3.9}$$

where $|\phi_{\mu,\mathbf{R}}\rangle$ is the μ-th orbital at the lattice site $\mathbf{R}$ and $C'_{\mu n}(\mathbf{k}, \mathbf{R})$ is a coefficient of linear combination. Focusing on one band for the moment (thus suppressing the band index 'n') we can write

$$\begin{aligned}\psi_{\mathbf{k}}(\mathbf{r}+\mathbf{R}) &= \langle \mathbf{r}+\mathbf{R}|\psi_{\mathbf{k}}\rangle\,, \\ &= \sum_{\mathbf{R}'}\sum_{\mu} C'_{\mu}(\mathbf{k},\mathbf{R}')\,\langle \mathbf{r}+\mathbf{R}|\phi_{\mu,\mathbf{R}'}\rangle\,, \\ &= \sum_{\mathbf{R}'}\sum_{\mu} C'_{\mu}(\mathbf{k},\mathbf{R}')\,\langle \mathbf{r}|\phi_{\mu,\mathbf{R}'-\mathbf{R}}\rangle\,, \\ &= \sum_{\mathbf{R}'}\sum_{\mu} C'_{\mu}(\mathbf{k},\mathbf{R}'+\mathbf{R})\,\langle \mathbf{r}|\phi_{\mu,\mathbf{R}'}\rangle\,.\end{aligned}$$

Bloch's theorem dictates that $\psi_{\mathbf{k}}(\mathbf{r}+\mathbf{R}) = e^{i\mathbf{k}.\mathbf{R}}\psi_{\mathbf{k}}(\mathbf{r})$ (see Eq. (3.3)). Therefore, one can write the equality

$$\sum_{\mathbf{R}'}\sum_{\mu} C'_{\mu}(\mathbf{k},\mathbf{R}'+\mathbf{R})\,\langle \mathbf{r}|\phi_{\mu,\mathbf{R}'}\rangle = e^{i\mathbf{k}.\mathbf{R}}\sum_{\mathbf{R}'}\sum_{\mu} C'_{\mu}(\mathbf{k},\mathbf{R}')\,\langle \mathbf{r}|\phi_{\mu,\mathbf{R}'}\rangle\,. \tag{3.10}$$

Hence,

$$C'_{\mu}(\mathbf{k},\mathbf{R}'+\mathbf{R}) = e^{i\mathbf{k}.\mathbf{R}}C'_{\mu}(\mathbf{k},\mathbf{R}'), \tag{3.11}$$

which is possible when $C'_{\mu}(\mathbf{k},\mathbf{R})$ is expressible in the following form:

$$C'_{\mu}(\mathbf{k},\mathbf{R}) = C_{\mu}(\mathbf{k})e^{i\mathbf{k}.\mathbf{R}}. \tag{3.12}$$

So, bringing the band-index back, the Bloch state is now:

$$\psi_{n\mathbf{k}} = \sum_{\mathbf{R}} e^{i\mathbf{k}.\mathbf{R}}\left(\sum_{\mu} C_{\mu n}(\mathbf{k})\,|\phi_{\mu,\mathbf{R}}\rangle\right), \tag{3.13}$$

where the Bloch state is normalized over the unit cell. Note that the term inside the parenthesis is a localized function. The Hamiltonian of this periodic system can be written as

$$\hat{H} = \sum_{\mu,\nu,\mathbf{R}_m,\mathbf{R}_n} V_{\mu,\nu}(\mathbf{R}_m-\mathbf{R}_n)\,|\phi_{\mu,\mathbf{R}_m}\rangle\,\langle\phi_{\nu,\mathbf{R}_n}|\,. \tag{3.14}$$

Since, $|\psi_{n\mathbf{k}}\rangle$ is the eigenket, it is related to the corresponding energy eigenvalue $E_n(\mathbf{k})$ with the following equation:

$$\hat{H}\left|\psi_{n\mathbf{k}}\right\rangle = E_n(\mathbf{k})\left|\psi_{n\mathbf{k}}\right\rangle$$

$$\sum_{\mathbf{R}'} e^{i\mathbf{k}.\mathbf{R}'} \sum_{\nu} C_{\nu n}(\mathbf{k}) \left\langle \phi_{\mu,\mathbf{R_1}} | \hat{H} | \phi_{\nu,\mathbf{R}'} \right\rangle = E_n(\mathbf{k}) \sum_{\mathbf{R}} e^{i\mathbf{k}.\mathbf{R}} \sum_{\gamma} C_{\gamma n}(\mathbf{k}) \left\langle \phi_{\mu,\mathbf{R_1}} | \phi_{\gamma,\mathbf{R}} \right\rangle$$

$$\sum_{\mathbf{R}',\nu} e^{i\mathbf{k}.(\mathbf{R}'-\mathbf{R_1})} C_{\nu n}(\mathbf{k}) \left\langle \phi_{\mu,\mathbf{R_1}} | \hat{H} | \phi_{\nu,\mathbf{R}'} \right\rangle = E_n(\mathbf{k}) \sum_{\mathbf{R},\gamma} e^{i\mathbf{k}.(\mathbf{R}-\mathbf{R_1})} C_{\gamma n}(\mathbf{k}) \left\langle \phi_{\mu,\mathbf{R_1}} | \phi_{\gamma,\mathbf{R}} \right\rangle$$

$$\sum_{\nu} C_{\nu n}(\mathbf{k}) H_{\mu\nu}(\mathbf{k}) = E_n(\mathbf{k}) \sum_{\gamma} C_{\gamma n}(\mathbf{k}) S_{\mu\gamma}(\mathbf{k}). \tag{3.15}$$

Here we have defined

$$H_{\mu\nu}(\mathbf{k}) = \sum_{\mathbf{R}} e^{i\mathbf{k}.(\mathbf{R}-\mathbf{R_1})} \left\langle \phi_{\mu,\mathbf{R_1}} | \hat{H} | \phi_{\nu,\mathbf{R}} \right\rangle, \tag{3.16}$$

$$S_{\mu\nu}(\mathbf{k}) = \sum_{\mathbf{R}} e^{i\mathbf{k}.(\mathbf{R}-\mathbf{R_1})} \left\langle \phi_{\mu,\mathbf{R_1}} | \phi_{\nu,\mathbf{R}} \right\rangle. \tag{3.17}$$

Note that due to the translational symmetry of the crystal, $H_{\mu\nu}(\mathbf{k})$ and $S_{\mu\nu}(\mathbf{k})$ are the same for all $\mathbf{R_1}$. If these matrices are known, then Eq. (3.15), which is a generalized eigenvalue problem representing the Schrödinger equation, can be solved to find $E_n(\mathbf{k})$ and $C_{\nu n}(\mathbf{k})$.

3.2 Density Functional Theory

The density corresponding to a normalized N-electron state $|\Psi\rangle$ is given by

$$n(\mathbf{r}) = N \int d^3\mathbf{r_2} \int d^3\mathbf{r_3} ... \int d^3\mathbf{r_N} \Psi^*(\mathbf{r}, \mathbf{r_2}, ..., \mathbf{r_N}) \Psi(\mathbf{r}, \mathbf{r_2}, ..., \mathbf{r_N}) \tag{3.18}$$

where $\Psi(\mathbf{r}, \mathbf{r_2}, ..., \mathbf{r_N})$ is the wave-function corresponding to the aforementioned state $|\Psi\rangle$. According to DFT, if $|\Psi\rangle$ is a ground state of the N-electron system then the above equation is in principle invertible- i.e. the ground state density uniquely determines the corresponding ground state(s).

Let us consider the standard method of finding the ground state energy (E_0) by minimizing the expectation value of the Hamiltonian ($\hat{H} = \hat{T} + \hat{V}_{ee} + \hat{V}_{ext}$) with respect to the quantum state through variational principle.

$$
\begin{aligned}
E_0 &= \min_{|\Psi\rangle} \langle\Psi|\hat{H}|\Psi\rangle \\
&= \min_{|\Psi\rangle} \langle\Psi|\hat{T} + \hat{V}_{ee} + \hat{V}_{ext}|\Psi\rangle \\
&= \min_{n} \left[\min_{|\Psi\rangle\to n} \left(\langle\Psi|\hat{T} + \hat{V}_{ee}|\Psi\rangle + \langle\Psi|\hat{V}_{ext}|\Psi\rangle \right) \right] \quad (3.19) \\
&= \min_{n} \left[\int d\mathbf{r} v_{ext}(\mathbf{r}) n(\mathbf{r}) + \min_{|\Psi\rangle\to n} \left(F_{LL}[n(\mathbf{r})] \right) \right] \\
&= \min_{n} E_{LL}[n(\mathbf{r}), v_{ext}(\mathbf{r})]
\end{aligned}
$$

Here, in the third line, the outer minimization is over all N-representable [1] densities and the inner minimization is over all N-particle states that produce the density $n(\mathbf{r})$. The term inside the large square bracket is a unique functional of density and external potential [77, 78]- we call this the Levy-Lieb energy functional $E_{LL}[n(\mathbf{r}), v_{ext}(\mathbf{r})]$. This is true even if many degenerate ground states produce the same density; since they all produce the same value for $\langle\Psi|\hat{H}|\Psi\rangle$. The fourth equality in Eq. (3.19) defines the Levy-Lieb universal functional $F_{LL}[n(\mathbf{r})]$ which is the same for all systems (i.e. independent of external potential). It must be noted that in the search over $n(\mathbf{r})$ (and $|\Psi\rangle$) it is okay to include even those densities (and quantum states) that can not result from the given (in fact any[2]) $v_{ext}(\mathbf{r})$ because such densities (and quantum states) can not minimize $E_{LL}[n(\mathbf{r}), v_{ext}(\mathbf{r})]$ (or $\langle\Psi|\hat{H}|\Psi\rangle$) anyway.

Thus we see that, given the ground state density $n_0(\mathbf{r})$ and the external potential $v_{ext}(\mathbf{r})$, the ground state energy E_0 is uniquely determined by $E_0 = E_{LL}[n_0(\mathbf{r}), v_{ext}(\mathbf{r})]$. Now let us go one step further. Let us assume, for a system of N electrons, that there are two external potentials $\hat{V}_{ext1}$ and $\hat{V}_{ext2}$, differing by more than just a constant, that

[1] An N-representable density is one which can be obtained from any anti-symmetric state.

[2] densities which can be associated with the antisymmetric ground state of a Hamiltonian are called v-representable

produce the same ground state density $n_0(\mathbf{r})$. Let $|\Psi_1^0\rangle$ and $|\Psi_2^0\rangle$ be the ground states, E_1^0 and E_2^0 be the associated energy eigenvalues of the Hamiltonians (say $\hat{H}_1$ and $\hat{H}_2$) for the two different external potentials. Since, by definition $|\Psi_1^0\rangle$ is the state producing the lowest eigenvalue of $\hat{H}_1$, we have

$$E_1^0 = \langle\Psi_1^0|\hat{H}_1|\Psi_1^0\rangle < \langle\Psi_2^0|\hat{H}_1|\Psi_2^0\rangle\,, \tag{3.20}$$

following which we may write

$$\begin{aligned} E_1^0 = \langle\Psi_1^0|\hat{H}_1|\Psi_1^0\rangle &< \langle\Psi_2^0|\hat{H}_1|\Psi_2^0\rangle \\ &= \langle\Psi_2^0|\hat{H}_2|\Psi_2^0\rangle + \langle\Psi_2^0|\hat{H}_1 - \hat{H}_2|\Psi_2^0\rangle \\ &= E_2^0 + \langle\Psi_2^0|\hat{V}_{ext1}|\Psi_2^0\rangle - \langle\Psi_2^0|\hat{V}_{ext2}|\Psi_2^0\rangle \\ &= E_2^0 + \int d\mathbf{r} n_0(\mathbf{r}) v_{ext1}(\mathbf{r}) - \int d\mathbf{r} n_0(\mathbf{r}) v_{ext2}(\mathbf{r}). \end{aligned} \tag{3.21}$$

The last line is valid for any multiplicative $\hat{V}_{ext}$ such that $\langle\mathbf{r}|\hat{V}_{ext}|\mathbf{r}'\rangle = v_{ext}(\mathbf{r})\delta(\mathbf{r}-\mathbf{r}')$. Starting with E_2^0 and following a similar method we could have arrived at

$$E_2^0 < E_1^0 + \int d\mathbf{r} n_0(\mathbf{r}) v_{ext2}(\mathbf{r}) - \int d\mathbf{r} n_0(\mathbf{r}) v_{ext1}(\mathbf{r}) \tag{3.22}$$

By adding these two inequalities we get

$$E_1^0 + E_2^0 < E_2^0 + E_1^0 \tag{3.23}$$

This contradiction proves that our initial assumption of two different external potentials producing the same density is wrong. Therefore, the ground state density of an N-electron system uniquely specifies the external potential, except for a trivial additive constant. This is the celebrated *first Hohenberg-Kohn (HK) theorem* [79]. Since the external potential for an N-electrons system completely specifies its Hamiltonian, which in turn specifies all properties of the system, one can say that in principle the ground state density uniquely determines all ground state and excited state properties

of the system. This means we can write the quantum ground state and the ground state energy as a functional of the ground state density alone:

$$|\Psi_0\rangle = |\Psi[n_0(\mathbf{r})]\rangle\,, \tag{3.24}$$

$$E_0 = E_{LL}[n_0(\mathbf{r}), v_{ext}(\mathbf{r})] = E[n_0(\mathbf{r})]. \tag{3.25}$$

This automatically implies that for any density $n'(\mathbf{r})$ which is not the ground state density of $v_{ext}(\mathbf{r})$

$$E_0 = E_{LL}[n_0(\mathbf{r}), v_{ext}(\mathbf{r})] < E_{LL}[n'(\mathbf{r}), v_{ext}(\mathbf{r})]. \tag{3.26}$$

This is the *second Hohenberg-Kohn (HK) theorem.* Since the ground-state density is the one that produces a total of N electrons and minimizes E_{LL} we can write a constrained equation of minimization as follows:

$$\frac{\partial}{\partial n(\mathbf{r})}\left[E_{LL}[n(\mathbf{r}), v_{ext}(\mathbf{r})] - \mu_L\left(\int d^3\mathbf{r} n(\mathbf{r}) - N\right)\right]_{n(\mathbf{r})=n_0(\mathbf{r})} = 0. \tag{3.27}$$

Here, μ_L is the Lagrange Multiplier used to incorporate the condition of a fixed number N of total electrons. It can be proved that all N-representable densities are dense enough for Eq. (3.27) to be valid. However, this implies that $E_{LL}[n(\mathbf{r}), v_{ext}(\mathbf{r})]$ must be defined for fractional particle numbers. So, the definition of E_{LL} (as in Eq. (3.19)) must be extended to include densities yielding fractional particle numbers and this is done as follows through F_{LL},

$$
\begin{aligned}
F_{LL}[n(\mathbf{r})] &= \min_{\{|\Psi_N\rangle,|\Psi_{N+1}\rangle\}\to n(\mathbf{r})} \left[(1-\eta)\,\langle\Psi_N|\hat{T}+\hat{V}_{ee}|\Psi_N\rangle + \eta\,\langle\Psi_{N+1}|\hat{T}+\hat{V}_{ee}|\Psi_{N+1}\rangle\right] \\
\text{where } n(\mathbf{r}) &= (1-\eta)\,\langle\Psi_N|\Psi_N\rangle + \eta\,\langle\Psi_{N+1}|\Psi_{N+1}\rangle \\
\langle\Psi_N|\Psi_N\rangle &= N, \\
\langle\Psi_{N+1}|\Psi_{N+1}\rangle &= N+1,
\end{aligned}
\tag{3.28}
$$

and the total number of particles is non-integer.

$$
\int d^3(\mathbf{r}) n(\mathbf{r}) = N + \eta \quad [0 < \eta < 1]. \tag{3.29}
$$

Let us now consider a non-interacting N-electron system with some external potential $v^s_{ext}(\mathbf{r})$. The formalism described so far is valid for this system with the Levy-Lieb functional

$$
E^s_{LL}[n(\mathbf{r}), v^s_{ext}(\mathbf{r})] = \min_{|\Psi\rangle\to n} \left(\langle\Psi|\hat{T}|\Psi\rangle + \int d\mathbf{r} v^s_{ext}(\mathbf{r}) n(\mathbf{r}) \right). \tag{3.30}
$$

As usual, the quantum ground-state $|\Psi^s[n_0(\mathbf{r})]\rangle$ is a functional of the ground state density. For the non-interacting system, the ground state wave function is known to be the Slater determinant of the single particle wave functions $\phi_i(\mathbf{r_i}\sigma_i)[n_0(\mathbf{r})]$ which are also uniquely determined by the electron density.

$$
\Psi^s(\mathbf{r}_1\sigma_1, ..., \mathbf{r}_N\sigma_N) = \frac{1}{\sqrt{N!}} \begin{pmatrix} \phi_1(\mathbf{r}_1\sigma_1) & \cdots & \phi_N(\mathbf{r}_1\sigma_1) \\ \vdots & \ddots & \vdots \\ \phi_1(\mathbf{r}_N\sigma_N) & \cdots & \phi_N(\mathbf{r}_N\sigma_N) \end{pmatrix} \tag{3.31}
$$

where σ denotes the spin index. Clearly, the single particle energies (ϵ_i) and the corresponding wave-functions, $\phi_i(\mathbf{r_i}\sigma_i)$, are obtained by solving the Schröedinger equation for the non-interacting Hamiltonian:

$$\left(-\frac{1}{2}\nabla^2 + v^s_{ext}(\mathbf{r})\right)\phi_i(\mathbf{r}\sigma) = \epsilon_i\phi_i(\mathbf{r}\sigma). \tag{3.32}$$

Then, denoting the occupation of the i-th single-particle state by Θ_i, the ground state density $n_0(\mathbf{r})$ gives the ground state energy as

$$\begin{aligned} E^s_0 &= E^s_{LL}[n_0(\mathbf{r}), v^s_{ext}(\mathbf{r})] \\ &= \langle\Psi^s[n_0(\mathbf{r})]|\hat{T}|\Psi^s[n_0(\mathbf{r})]\rangle + \int d\mathbf{r} v^s_{ext}(\mathbf{r})n_0(\mathbf{r}) \\ &= \sum_i \Theta_i \sum_\sigma \int d^3\mathbf{r}\phi^*_i(\mathbf{r}\sigma)\frac{(-i\hbar\nabla)^2}{2m}\phi_i(\mathbf{r}\sigma) + \int d^3\mathbf{r} v^s_{ext}(\mathbf{r})n_0(\mathbf{r}) \\ &= T^s[n_0(\mathbf{r})] + V^s[n_0(\mathbf{r})] \end{aligned} \tag{3.33}$$

Eq. (3.27) for the noninteracting system takes the form

$$\frac{\partial T^s[n_0(\mathbf{r})]}{\partial n(\mathbf{r})} + v^s_{ext}(\mathbf{r}) = \mu. \tag{3.34}$$

Then the KS scheme begins with the understanding that all N-representable densities (i.e, densities for which E_{LL} is valid) can be written as $n(\mathbf{r}) = \sum_i \sum_\sigma |\phi_i(\mathbf{r}\sigma)|^2$, namely that they all correspond to a Slater determinant for some set of single particle eigenstates. Thus, we can write the Levy-Lieb energy functional of the interacting electrons as

$$E_{LL}[n] = T^s[n] + E_H[n] + E_{ext}[n] + E_{xc}[n] \tag{3.35}$$

where the first term on the right hand side is the kinetic energy of non-interacting electrons of the same density n and is given by the first term on the right hand side of Eq. (3.33). The second and the third terms on the right hand side of Eq. (3.35) are the classical Coulomb energy ($\frac{1}{2}\int d\mathbf{r}\int d\mathbf{r}'\frac{n(\mathbf{r})n(\mathbf{r}')}{|\mathbf{r}-\mathbf{r}'|}$) and the energy due to the external potential ($\int d\mathbf{r} v_{ext}(\mathbf{r})n(\mathbf{r})$) respectively. The last term E_{xc} in the above equation denotes the energy that is not contained in the other three terms and is called the Exchange-Correlation (XC) energy. Note that $T^s[n]$ is not the full kinetic energy of the interacting

system and hence E_{xc} contains some contributions from the kinetic energy as well. For this system the variational equation would take the following form

$$\begin{aligned}\mu_L &= \frac{\partial E_{LL}[n_0(\mathbf{r})]}{\partial n(\mathbf{r})} \\ &= \frac{\partial T^s[n_0(\mathbf{r})]}{\partial n(\mathbf{r})} + \int d\mathbf{r}' \frac{n(\mathbf{r}')}{|\mathbf{r}-\mathbf{r}'|} + v_{ext}(\mathbf{r}') + \frac{\partial E_{xc}[n_0(\mathbf{r})]}{\partial n(\mathbf{r})} \\ &= \frac{\partial T^s[n_0(\mathbf{r})]}{\partial n(\mathbf{r})} + v_{KS}(\mathbf{r}),\end{aligned} \tag{3.36}$$

where the Kohn-Sham potential $v_{KS}(\mathbf{r})$ is defined as

$$v_{KS}(\mathbf{r}) = \int d\mathbf{r}' \frac{n(\mathbf{r}')}{|\mathbf{r}-\mathbf{r}'|} + v_{ext}(\mathbf{r}') + \frac{\partial E_{xc}[n]}{\partial n}. \tag{3.37}$$

Comparing Eq. (3.36) with Eq. (3.34) we see that they would look identical for $v^s_{ext}(\mathbf{r}) = v_{KS}(\mathbf{r})$. Thus the interacting system corresponding to Eq. (3.36) will have the same electron density as a non-interacting system in an external potential $v_{KS}(\mathbf{r})$. The latter is called the equivalent Kohn-Sham system of the former. Thus, if one knows the exact $v_{KS}(\mathbf{r})$ for the interacting system one knows the full quadratic Hamiltonian of the Kohn-Sham non-interacting system. From this Hamiltonian one can obtain the single particle eigenstates ($\phi_i(\mathbf{r}\sigma)$) plugging $v^s_{ext}(\mathbf{r}) = v_{KS}(\mathbf{r})$ in Eq. (3.32)

$$\left(-\frac{1}{2}\nabla^2 + v_{KS}(\mathbf{r})\right)\phi_i(\mathbf{r}\sigma) = \epsilon_i \phi_i(\mathbf{r}\sigma). \tag{3.38}$$

Eq. (3.38) is known as the Kohn-Sham equation [80] corresponding to the given interacting system and the electron density of the Kohn-Sham system is given by $\sum_\sigma \sum_i |\phi_i(\mathbf{r}\sigma)|^2$. Since this density is the same as that of the original interacting system, one can find the energy of the interacting system from Eq. (3.35). It must be noted that the last term on the right hand side of Eq. (3.35) must be a density functional since all other terms in Eq. (3.35) are functionals of $n(\mathbf{r})$. In many cases this term has a small contribution to the total energy.

It is interesting to note that since the ground state density of the Kohn-Sham system uniquely determines $v_{KS}(\mathbf{r})$ which, in turn, uniquely determines the Kohn-Sham orbitals $\phi_i(\mathbf{r_i}\sigma_i)$ and since the ground state density of the Kohn-Sham system is same as that $(n(\mathbf{r}))$ of the interacting system, not only the Kohn-Sham potential but also all the Kohn-Sham orbitals are unique functionals of $n(\mathbf{r})$. Exploiting this relation, one can minimize the energy directly as a functional of the Kohn-Sham orbitals (subject to the condition of orthonormality of the orbitals) and obtain the Kohn-Sham equation Eq. (3.38).

To conclude, the Kohn-Sham scheme can be roughly broken down as follows:

- Given the external potential $v_{ext}(\mathbf{r})$ of the interacting system, start with an initial guess for density $n(\mathbf{r})$ and construct $v_{KS}(\mathbf{r})$.
- Obtain the density of the Kohn-Sham system either by diagonalizing the quadratic Hamiltonian or by directly minimizing the energy functional of the Kohn-Sham system.
- With the density so obtained, construct a new $v_{KS}(\mathbf{r})$ and repeat the procedure until the density and the energy converge.

3.2.1 Band Gap Problem

One of the most important limitations of KS DFT is its inability to accurately predict the electronic gap of extended systems [81, 82]. Let us take a closer look at this problem here. We begin with the expression for a system with $(N+\eta)$ particles (where N is an integer and $0 \leq \eta < 1$). As mentioned in Eq. (3.28), this is expressed as superposition of two states- one ($|\Psi_N\rangle$) with N particles and one ($|\Psi_{N+1}\rangle$) with $N+1$ particles. In this case $E_{LL}[n(\mathbf{r}), v_{ext}(\mathbf{r})]$ is minimized such that $n(\mathbf{r}) = (1-\eta)\langle\Psi_N|\Psi_N\rangle + \eta\langle\Psi_{N+1}|\Psi_{N+1}\rangle$ corresponds to an $F_{LL}[n(\mathbf{r})]$ where $|\Psi_N\rangle$ and $|\Psi_{N+1}\rangle$ both are ground states (with the corresponding number of particles) for the same $v_{ext}(\mathbf{r})$ (see, for example, chapter 2.4 of ref. [83]). This means:

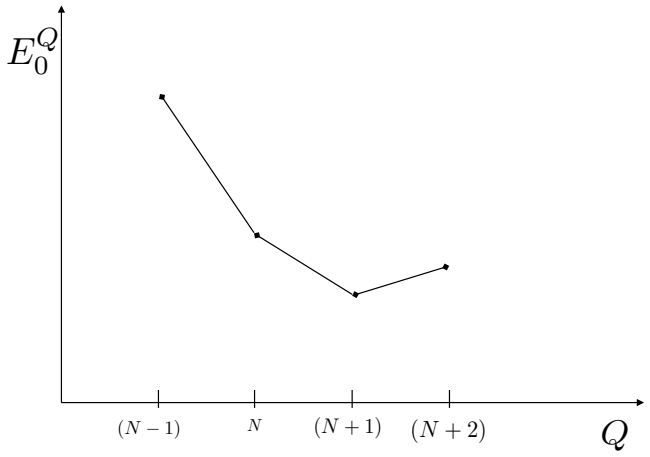

Figure 3.1: Representative plot of ground state energy vs number of electrons

$$E_0^{N+\eta} = (1-\eta)E_0^N + \eta E_0^{N+1}, \tag{3.39}$$

where E_0^Q is the ground state energy of the system containing Q electrons. This establishes E_0^Q as a function of Q, as plotted in Fig. 3.1 which shows linear behaviour between points with integral values of particle number where E_0^Q is not differentiable.

The fundamental gap of any N-particle system is defined as:

$$E_{FG} = (E_0^{N+1} - E_0^N) - (E_0^N - E_0^{N-1}). \tag{3.40}$$

Note that for a non-interacting system, this is equal to the difference between the $(N+1)$-th and the N-th eigenvalue. Since the KS system consists of non-interacting electrons, the above statement is true for it (with KS eigenvalues denoted by ε^{KS}). Here, E_{FG} is

$$\Delta_{KS} = \varepsilon_{N+1}^{KS} - \varepsilon_N^{KS}. \tag{3.41}$$

Going back to the general case of interacting particles, since the plot of E_0^Q against Q is linear between any two integer points, E_{FG} is equal to the derivative gap E_{DG}

$$E_{DG} = \left.\frac{\partial E_0^N}{\partial N}\right|_{N^+} - \left.\frac{\partial E_0^N}{\partial N}\right|_{N^-}, \tag{3.42}$$

where, N^+ and N^- correspond to approaching the limit from the positive and negative side respectively. Now we shall prove an important relation for the quantity $\frac{\partial E_0^N}{\partial N}$. If n_Q is the ground state density for the Q-particle system, then $E_{LL}[n_Q(\mathbf{r})] = E_0^Q$ where we have omitted the $v_{ext}(\mathbf{r})$ parameter in the Levy-Lieb energy functional for simplicity. We have [83]

$$\begin{aligned}
\frac{\partial E_0^N}{\partial N} &= \lim_{\eta\to 0}\frac{1}{\eta}[E_0^{N+\eta} - E_0^N] \\
&= \lim_{\eta\to 0}\frac{1}{\eta}[E_{LL}[n_{N+\eta}(\mathbf{r})]] - E_{LL}[n_N(\mathbf{r})] \\
&= \lim_{\eta\to 0}\frac{1}{\eta}\left[E_{LL}[n_N(\mathbf{r})] + \int d^3\mathbf{r}\left.\frac{\delta E_{LL}[n]}{\delta n}\right|_{n=n_N}[n_{N+\eta}(\mathbf{r}) - n_N(\mathbf{r})] - E_{LL}[n_N(\mathbf{r})]\right] \\
&= \mu_L\left[\lim_{\eta\to 0}\int\frac{1}{\eta}d^3\mathbf{r}[n_{N+\eta}(\mathbf{r}) - n_N(\mathbf{r})]\right] \\
&= \mu_L
\end{aligned}$$

Where $\mu_L = \left.\frac{\delta E_{LL}[n]}{\delta n}\right|_{n=n_N}$ has been previously encountered in Eq. (3.27). This equates E_{DG} to

$$\begin{aligned}
E_{DG} &= \left.\frac{\delta E_{LL}[n]}{\delta n}\right|_{n_{N^+}} - \left.\frac{\delta E_{LL}[n]}{\partial n}\right|_{n_{N^-}} \\
&= \left[\left.\frac{\delta T_S[n]}{\delta n}\right|_{n_{N^+}} - \left.\frac{\delta T_S[n]}{\delta n}\right|_{n_{N^-}}\right] + \left[\left.\frac{\delta E_{xc}[n]}{\delta n}\right|_{n_{N^+}} - \left.\frac{\delta E_{xc}[n]}{\delta n}\right|_{n_{N^-}}\right] \\
&= \Delta_{KS} + \Delta_{xc}
\end{aligned}$$

The second equality follows from the fact that the external potential and the Hartree potential have continuous density derivatives at all particle numbers. Δ_{KS} is the KS gap defined in Eq. (3.41) and Δ_{xc}, which is known as the derivative discontinuity [84, 85], is a many-body correction. Standard XC-functionals used in DFT (such as Local

Density Approximation or LDA, Generalized Gradient Approximation or GGA, etc.) have $\Delta_{xc} = 0$, which implies that for such functionals:

$$E_{DG} = \Delta_{KS}. \tag{3.43}$$

Unfortunately, this does not mean that E_{FG} can be calculated easily with these functionals. In fact, for these functionals, $\frac{\partial E_0^N}{\partial N}$ is not a straight line between integer points and as a consequence $E_{FG} \neq E_{DG}$.

The following discussion closely follows that presented in Ref. [81]. In Fig. 3.2 a we show a representative plot of $E^N - E^{N_0}$ vs N for a fixed number N_0 for the exact functional (showing perfectly linear behaviour between integer points) and for LDA (showing convex behaviour between integer points). This plot holds true for a small molecule. This convex behaviour of the curve for LDA precludes its E_{DG} from being the same as E_{FG}. However, since the energy description is good at integer points, one can expect reasonable results for ionization energy (I.E.) and electron affinity (E.A.) calculated as total energy differences:

$$I.E. = E_0^{N-1} - E_0^N$$
$$E.A. = E_0^N - E_0^{N+1}$$

Now, let us focus on a finite system containing two unit cells each having an $E(N) - E(N_0)$ vs N behaviour as in Fig. 3.2a Then, within the LDA framework, an extra electron added to the system would be distributed equally between the two cells because

$$(E_0^{N+\frac{1}{2}} + E_0^{N+\frac{1}{2}}) < (E_0^N + E_0^{N+1}) \tag{3.44}$$

Extending this to the case of a finite system with M unit cells, we see that the single added electron will be delocalized over all the M unit cells since

$$M.E_0^{N+\frac{1}{M}} < [(M-1)E_0^N + E_0^{N+1}] \tag{3.45}$$

Fig. 3.2b shows the plot of $E(N) - E(MN_0)$ vs N for such a system with M unit cells. Now, each cell has an excess of $1/M$ charge and for each cell, this corresponds to the point $N = (N_0 + \frac{1}{M})$ in Fig. 3.2a. Hence, in the plot for the whole system, even the integer points are not captured properly any more. Therefore, a calculation based on total energy difference will fail to produce the electron affinity (or ionization energy) for this system. This delocalization error will keep increasing with M. Moving to a bulk limit, Fig. 3.2c shows the same plot of $E(N) - E(MN_0)$ vs N for a system with M unit cells where $M \to \infty$. Obviously, for such a system the added electron delocalizes over all unit cells resulting in infinitesimally small fractional charge per unit cell. So, the equivalent point in Fig. 3.2a would be the point $N = N + \delta$ where $\delta \to 0$. Thus, in Fig. 3.2c the plot between the points $N = MN_0$ and $N = MN_0 + 1$ would be a straight line with the slope of $\frac{\partial E_0^N}{\partial N}$ of Fig. 3.2a Thus, even though this plot will have linear behaviour between integer points (a property of the exact functional), it will have wrong values at the integer points.

The take home message from the preceding discussion is that LDA tends to delocalize an added charge over all space available. Hence, if we run a bulk DFT calculation on a very large supercell, LDA will spread the charge unphysically over the entire supercell and the IE (EA) would converge to the Kohn-Sham HOMO (LUMO). Thus for calculating the band gap of a periodic solid in terms of total energy difference if we use too small a unit cell and add an excess unit charge to it, the extra charge is artificially confined in the small unit cell (it must be noted that for such a calculation, an unit extra charge is added to each unit cell of the periodic system)- leading to unphysical scenario and inaccurate result for any XC-functional, including the exact one. However, if we use too large a unit cell, LDA will delocalize the charge excess over the entire unit cell giving rise to unphysical condition again (this would not happen with the exact XC-functional). However, if one can somehow use a unit cell of just the right size- i.e. the size in which an extra charge would be confined in an actual experiment- then even with LDA one can get a good band gap in terms of total energy differences.

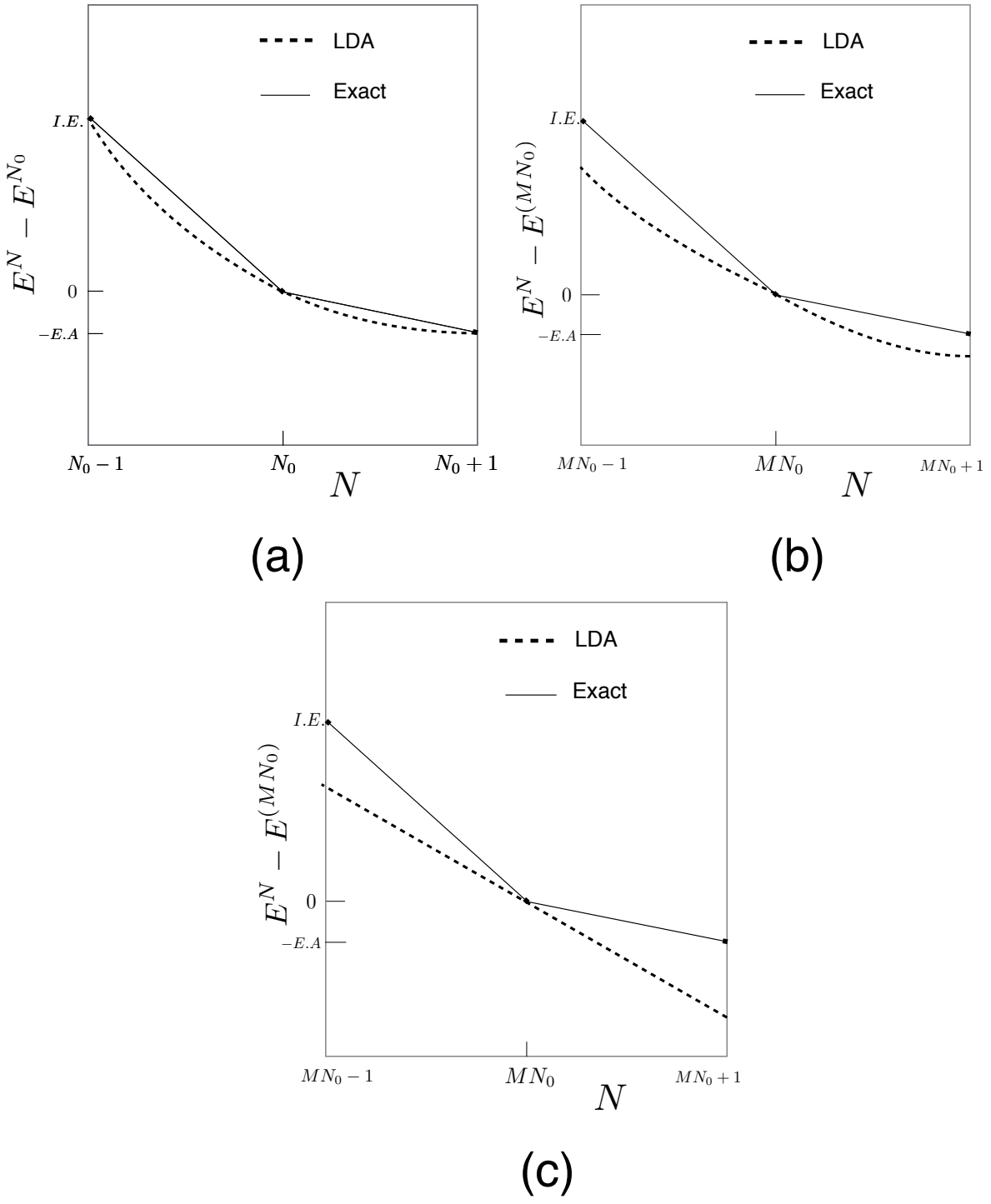

Figure 3.2: (a)Representative plot of energy of a finite system as a function of electron number for the exact XC functional and for LDA. (b) same plot as (a) but for a system containing a finite number M of identical units as in the previous plot. Plot (c) corresponding to the bulk limit, for $M \to \infty$.

3.3 Constrained Density Functional Theory

DFT is a ground state theory. One possible way to access excited states with this formalism is to perform the minimization of the energy functional subject to additional conditions, for example, by fixing the number (N_c) of electrons in a given subpsace, which is typically a spatial region, represented by a projection operator $\hat{\mathbb{P}}$. This can be expressed as

$$\mathrm{Tr}[\hat{\mathbb{P}}\hat{\rho}] = \mathrm{N_c} \tag{3.46}$$

where $\hat{\rho}$ is the density operator. Subject to this condition, the variational equation Eq. (3.27) takes the form

$$\frac{\partial}{\partial n(\mathbf{r})}\left[E_{LL}[n(\mathbf{r}), v_{ext}(\mathbf{r})] - \mu\left(\int d^3\mathbf{r} n(\mathbf{r}) - N\right) + V_c\left(\mathrm{Tr}[\hat{\mathbb{P}}\hat{\rho}] - \mathrm{N_c}\right)\right]_{n(\mathbf{r})=n_0(\mathbf{r})} = 0, \tag{3.47}$$

where V_c is the Lagrange multiplier corresponding to the condition of constraint Eq. (3.46).

Let us denote the term inside the square bracket of Eq. (3.47) as $W[n(\mathbf{r}), V_c]$. For each value of V_c, one gets a unique ground state density from Eq. (3.47). In this sense, W can be thought of as a function of V_c only: $W[n_0(\mathbf{r})[V_c], V_c] = W(V_c)$ (exceptions to this can be constructed though [86]). By differentiating this function, we get

$$\begin{aligned}\frac{dW}{dV_c} &= \frac{\partial W}{\partial n(\mathbf{r})}\frac{\partial n(\mathbf{r})}{\partial V_c}\bigg|_{n(\mathbf{r})=n_0(\mathbf{r})} + \frac{\partial W}{\partial V_c} \\ &= \frac{\partial W}{\partial V_c} \\ &= \mathrm{Tr}[\hat{\mathbb{P}}\hat{\rho}] - \mathrm{N_c},\end{aligned} \tag{3.48}$$

where, in the second equality one uses Eq. (3.47), i.e $\frac{\partial W}{\partial n(\mathbf{r})}\Big|_{n(\mathbf{r})=n_0(\mathbf{r})} = 0$. So, the extremum of $W(V_c)$ reproduces the condition of constraint Eq. (3.46). Taking screening

effects, i.e., the change in density due to change in V_c into account, it can be proved [86] that the maximum of $W(V_c)$ yields the stable ground state density of the system subject to the given constraint. Also, since $\mathrm{Tr}[\hat{\mathbb{P}}\hat{\rho}] - \mathrm{N_c}$ vanishes at this density, W gives the total energy of this stable ground state. The method of cDFT aims to find this maximum point [87, 88].

Note that for a given V_c, solving Eq. (3.47) amounts to finding the stationary density, conserving the number of electrons, for an interacting system whose Hamiltonian contains an additional term $V_c\hat{\mathbb{P}}$. Note that the HK theorem remains valid for such modified Hamiltonian, even if the additional term is non-local [89]. To find this stationary density, one invokes the KS formalism and, following a route similar to that for arriving at Eq. (3.37) from Eq. (3.27), can show that the equivalent non-interacting system having the same electron density is under a KS potential given by

$$v_{KS}(\mathbf{r}) = \int d\mathbf{r}' \frac{n(\mathbf{r}')}{|\mathbf{r} - \mathbf{r}'|} + v_{ext}(\mathbf{r}') + \frac{\partial E_{xc}[n]}{\partial n} + V_c\hat{\mathbb{P}}. \tag{3.49}$$

By solving the KS equations with this $v_{KS}(\mathbf{r})$, one can find the desired density for a given V_c. Thus, in cDFT, the Hamiltonians of the interacting system and of the equivalent KS system are modified by addition of a term $V_c\hat{\mathbb{P}}$ such that, for the value of V_c which maximizes $W(V_c)$, the ground state density of the modified Hamiltonian corresponds to the density of that stable lowest-energy state of the original interacting Hamiltonian which satisfies the constraint Eq. (3.46).

The iterative method for finding the maximum of $W(V_c)$, until the attainment of self-consistency for V_c is as follows:

1. Start with an initial guess for V_c.

2. With V_c in hand start with an initial density $n(\mathbf{r})$ and construct the KS potential $v_{KS}(\mathbf{r})$ according to Eq. (3.49).

3. Obtain a self-consistent density and $v_{KS}(\mathbf{r})$ like in regular DFT.

4. Update V_c with some optimization method (e.g. Newton's method, conjugate-gradient etc.) and repeat the entire procedure with the new V_c.

3.4 Calculations based on the Kohn-Sham Scheme

The Kohn-Sham procedure maps an interacting many-body problem onto a non-interacting single-particle problem. DFT-based computer programs are devoted to constructing and solving the KS Hamiltonian iteratively to extract the ground-state energy and from that other important quantities [90]. The two commonly used types of basis sets used for the construction and solution of the KS Hamiltonian in periodic systems are:

1. Plane waves, with respect to which the KS states are written as in Eq. (3.6).
2. Localized orbitals, with respect to which the KS states are written as in Eq. (3.13).

In this thesis, we have only used methods of the second type and in all of these codes, the system under investigation is always periodic (note that this is not a necessity for a DFT-based code). Hence, even when solving for a molecule, the system is artificially made periodic by repeating in space the unit cell. This is made large enough so that the neighbouring cells do not interact much with each other.

Most of the physical properties for the systems of interest are related to the valence electrons only; the core electrons do not contribute much. Hence, it is possible to account for the effects of the core electrons on the valence ones with great accuracy by replacing them with an effective screening potential added to the ionic potential. This resultant potential, which is much weaker than the original ionic one is known as the *pseudopotential* and can be thought to act on a set of pseudo valence wave functions. This formalism efficiently serves the purpose, since, in the spatial region of interest (i.e. outside the core region very close to the ion), the pseudopotential is essentially the same as the ionic potential and same is true for the true valence wavefunctions and the pseudo wavefunctions. In the core region, the true wave functions oscillate rapidly in space and

hence, the charge density in that region is also oscillatory. In contrast, the pseudo wave functions have no nodes in the core region and consequently the pseudo charge density is smooth there. The smoothness is associated to the fact that the valence wave-functions do not need to be orthogonal to the core ones. This is a desirable condition for practical calculations. Since the KS energy functional depends on the density, which in turn depends on the amplitude of the wave function at a point in space, it is usually desirable to match the pseudo wave functions with the true valence wave functions outside the core region. This match has to take place not only in spatial dependence but also in absolute amplitude. In norm-conserving pseudopotentials [91], this condition is satisfied by ensuring that inside the core region the spatially integrated square of the amplitude of the pseudo wave function is the same as that of the true valence wave function. In all DFT calculations reported in this thesis, such norm-conserving pseudopotentials have been employed.

3.4.1 Exchange-Correlation Functional

If the XC-functional, $E_{xc}[n(\mathbf{r})]$ is known exactly, then the density obtained from the KS equations is exactly equal to the ground state density of the interacting system and from it, one can determine the precise ground state energy of such system. However, this quantity, which must be a functional of density is only known within certain approximations. Below, we briefly discuss two such approximations, the Local Density Approximation (LDA) and the Generalized Gradient Approximation (GGA). These are the only XC-functionals used in this thesis.

Local Spin Density Approximation

In the LDA approximation, if, at a point $\mathbf{r}$ in space, the electron density is $n(\mathbf{r})$, then $E_{xc}[n(\mathbf{r})]$ is taken to be the XC energy of a fully interacting uniform electron gas with density $n(\mathbf{r})$. Thus, we may write

$$E_{xc}[n(\mathbf{r})] = \int d^3\mathbf{r} n\varepsilon(n),$$

where $\varepsilon(n)$ is the XC energy density of the uniform gas. This quantity is exactly known as a sum of the exchange and the correlation contribution. LDA offers an exact treatment for uniform density and is a good approximation for densities that vary slowly, as in metals. Thus, one can expect LDA to work well for metals, for which the electron density is close to homogeneous. On the other hand, for atoms, in which the density is highly inhomogeneous and is expected to drop to zero continuously as one moves away from the nucleus, the LDA is not expected to work so well [92]. The remarkable usefulness of the LDA functional is usually attributed to a systematic error cancellation, i.e., to the fact that it overestimates the correlation contribution and underestimates the exchange one [93].

Generalized Gradient Approximation

In LDA, the XC functional at point $\mathbf{r}$ has only one argument, the density at point $\mathbf{r}$. Improvement on this can be achieved by including more terms of importance. In the Generalized Gradient Approximation, besides $n(\mathbf{r})$, the XC-functional $E_{xc}[n(\mathbf{r})]$ depends on $\nabla n(\mathbf{r})$. Various flavours of GGA functional exist in the literature. In this thesis we shall use the approximation proposed by Perdew, Burke and Ernzerhoff [94]. It is also worth mentioning that several other approximations (e.g. meta GGA, hybrid functionals) that are typically (but not always) more accurate and more computationally expensive, have also been discovered.

DFT-based calculations are usually performed with software packages, developed over the years, that typically come with a large number of functionalities. In the following we present a brief description of the working mechanism of SIESTA [95] and ONETEP [96], the two DFT based softwares used in this thesis.

3.4.2 SIESTA

The SIESTA software [95] solves the KS equations [Eq. (3.38)] by diagonalizing the effective single particle KS Hamiltonian written in terms of localized atomic orbitals $\{|\phi_{\nu,\mathbf{R}}\rangle\}$ [see Eq. (3.9)] which are eigenfunctions of the atomic pseudopotential and are truncated to zero beyond a certain radius. The Hamiltonian operator consisting of the non-interacting kinetic energy, non-local pseudopotential, local pseudopotential, Hartree term and the exchange-correlation operator can be written in the aforementioned order as

$$\hat{H} = \hat{T} + \sum_I \hat{V}_I^{KB} + \sum_I \hat{V}_I^{NA} + \hat{V}^H + \hat{V}^{xc}. \tag{3.50}$$

All these operators, and also the overlap $\langle\phi_{\mu,\mathbf{R_1}}|\phi_{\nu,\mathbf{R_2}}\rangle$ have a general matrix form with respect to the basis orbitals. The matrix representation of a generic operator $\hat{X}$ reads

$$X_{\mu\nu}(\mathbf{R_1} - \mathbf{R_2}) = \langle\phi_{\mu,\mathbf{R_1}}|\hat{X}|\phi_{\nu,\mathbf{R_2}}\rangle \tag{3.51}$$

where, for the overlap matrix, $\hat{X} = \hat{S} = \hat{\mathbb{1}}$.

If the eigenstates of the Hamiltonian are $\{|\psi_i\rangle\}$ and the corresponding occupation numbers are n_i, then the density operator is defined as:

$$\hat{\rho} = \sum_i n_i \, |\psi_i\rangle \, \langle\psi_i| \tag{3.52}$$

and the density matrix is defined in terms of the vector duals ($|\tilde{\phi}_\mu\rangle$) of the basis vectors such that $\langle\tilde{\phi}_\mu|\phi_\nu\rangle = \delta_{\mu\nu}$, and

$$\rho_{\mu\nu}(\mathbf{R_1} - \mathbf{R_2}) = \langle\tilde{\phi}_{\mu,\mathbf{R_1}}|\hat{\rho}|\tilde{\phi}_{\nu,\mathbf{R_2}}\rangle \, . \tag{3.53}$$

Then the real space representation of the charge density is determined as

$$\rho(\mathbf{r}) = \sum_{\mu,\nu,\mathbf{R_1},\mathbf{R_2}} \langle \mathbf{r}|\phi_{\mu,\mathbf{R_1}}\rangle \langle \tilde{\phi}_{\mu,\mathbf{R_1}}|\hat{\rho}|\tilde{\phi}_{\nu,\mathbf{R_2}}\rangle \langle \phi_{\nu,\mathbf{R_2}}|\mathbf{r}\rangle$$
$$= \sum_{\mu,\nu,\mathbf{R_1},\mathbf{R_2}} \rho_{\mu\nu}(\mathbf{R_1}-\mathbf{R_2})\phi_{\mu,\mathbf{R_1}}(\mathbf{r})\phi^*_{\nu,\mathbf{R_2}}(\mathbf{r}). \quad (3.54)$$

The matrix elements of the first and the second terms (which are non-local operators) of Eq. (3.50) along with the overlap ($S_{\mu\nu}(\mathbf{R_1}-\mathbf{R_2})$) are calculated in the Fourier space. For example, the overlap matrix is determined as

$$S_{\mu\nu}(\mathbf{R}) = \int d\mathbf{k}\phi^*_\mu(\mathbf{k})\phi_\nu(\mathbf{k})e^{-i\mathbf{k}.\mathbf{R}} \quad (3.55)$$

where $\phi_\mu(\mathbf{k})$ is the Fourier transform of $\phi_\mu(\mathbf{R})$

$$\phi(\mathbf{k}) = \frac{1}{(2\pi)^{3/2}} \int d\mathbf{r}\phi(\mathbf{r})e^{-i\mathbf{k}.\mathbf{R}}. \quad (3.56)$$

The matrix elements of the local operators, namely the last three terms in Eq. (3.50), are calculated from the corresponding functions, $X(\mathbf{r})$ over a real space grid. The density $\rho(\mathbf{r})$ is used to calculate $V^H(\mathbf{r})$ [by solving Poisson equation; usually in Fourier space] and $V^{XC}(\mathbf{r})$. Once the local functions are known over the grid points, the matrix elements are

$$X_{\mu\nu}(\mathbf{R_1}-\mathbf{R_2}) = \langle \phi_{\mu,\mathbf{R_1}}|\hat{X}|\phi_{\nu,\mathbf{R_2}}\rangle \quad (3.57)$$
$$= \int_{\mathbf{r_1}}\int_{\mathbf{r_2}} d^3\mathbf{r_1}d^3\mathbf{r_2} \langle \phi_{\mu,\mathbf{R_1}}|\mathbf{r_1}\rangle \langle \mathbf{r_1}|\hat{X}|\mathbf{r_2}\rangle \langle \mathbf{r_2}|\phi_{\nu,\mathbf{R_2}}\rangle \quad (3.58)$$
$$= \int_{\mathbf{r}} d^3\mathbf{r}X(\mathbf{r})\phi_{\mu,\mathbf{R_1}}(\mathbf{r})\phi_{\nu,\mathbf{R_2}}(\mathbf{r}) \quad (3.59)$$

With the knowledge of the matrix elements $\langle \phi_{\mu,\mathbf{R_1}}|\hat{H}|\phi_{\nu,\mathbf{R_2}}\rangle$ and $\langle \phi_{\mu,\mathbf{R_1}}|\phi_{\nu,\mathbf{R_2}}\rangle$ one can solve Eq. (3.15) to find the eigenvalues and eigenstates. Of course, the entire process is repeated until the attainment of self-consistency.

3.4.3 ONETEP

An alternative of diagonalizing the KS Hamiltonians can be a minimization of the KS total energy as a function of the KS orbitals $\{\psi_i\}$:

$$E[\{\psi_i\}] = 2\sum_i \int d^3\mathbf{r}\left(-\frac{\hbar^2}{2m}\right)\psi_i\nabla^2\psi_i + \int V_{ion}(\mathbf{r})n(\mathbf{r})d^3(\mathbf{r}) + \frac{e^2}{2}\int \frac{n(\mathbf{r})n(\mathbf{r}')}{\mathbf{r}-\mathbf{r}'}d^3\mathbf{r}d^3\mathbf{r}' + E_{xc}[n(\mathbf{r})] + E_{ion}(\{\mathbf{R}_I\}) \tag{3.60}$$

In this regard, an equivalent of the KS orbitals is the KS single particle density matrix $\rho(\mathbf{r},\mathbf{r}')$

$$\rho(\mathbf{r},\mathbf{r}') = \sum_i \psi_i^*(\mathbf{r})\psi_i(\mathbf{r}) \tag{3.61}$$

Such KS density matrix can be written as

$$\begin{aligned}\rho(\mathbf{r},\mathbf{r}') &= \langle\mathbf{r}|\hat{\rho}|\mathbf{r}'\rangle \\ &= \sum_{\alpha,\beta}\langle\mathbf{r}|\phi_\alpha\rangle\langle\phi^\alpha|\hat{\rho}|\phi^\beta\rangle\langle\phi_\beta|\mathbf{r}'\rangle \\ &= \sum_{\alpha,\beta}\phi_\alpha(\mathbf{r})K^{\alpha\beta}\phi_\beta^*(\mathbf{r}')\end{aligned}$$

where $\{|\phi_\alpha\rangle\}$ is a set of localized non-orthogonal generalized Wannier functions (NGWFs) and $\{|\phi^\alpha\rangle\}$ is the set of corresponding duals such that $\langle\phi_\alpha|\phi^\beta\rangle = \delta_\alpha^\beta$. In ONETEP, in order to maintain an order-N approach, the KS energy functional is minimized directly with respect to the density kernel $K^{\alpha\beta}$. During such density kernel minimization three crucial conditions need to be satisfied [97]:

1. idempotency: $\rho^2(\mathbf{r},\mathbf{r}') = \rho(\mathbf{r},\mathbf{r}')$
2. Normalization: $2\int d^3\mathbf{r}\rho(\mathbf{r},\mathbf{r}') = N$, which is the number of electrons in the system

3. Compatibility: $[\rho, H] = 0$

In order to minimize the energy subject to these conditions, ONETEP follows the Li-Nunes-Vanderbilt (LNV) minimization procedure in conjunction with penalty functionals.

In DFT calculations using localized basis- the accuracy depends largely on the size of the basis set. In order to improve over the minimal basis set (which offers fast but inaccurate calculations) one needs to use larger basis- which increases computational cost. ONETEP uses an alternative approach in which the NGWF basis is always the minimal set but is iteratively optimized with a conjugate-gradient (CG) technique in a loop external to that of the $K^{\alpha\beta}$ minimization. This means that the NGWF basis set is not unique to the atoms but depends on the entire system. Each NGWF is centred on an atom and truncated to zero beyond a given localization radius (r_{loc}). An NGWF is expressed in terms of a set of spike-like highly localized psinc functions [98]: $D_k(\mathbf{r})$, centred at the k-th grid point of a dense spatial grid as

$$\phi_\alpha(\mathbf{r}) = \sum_k D_k(\mathbf{r}) C_{k,\alpha} \tag{3.62}$$

The grid spacing can be controlled with a single quantity: the maximum kinetic energy of the plane waves which constitute the psinc functions through Fourier transformation.

3.5 Löwdin Population Analysis

In many practical scenarios, it is important to determine the electronic population of a subspace of interest. Very often, this subspace is a spatial region spanned by some localized kets (these can be a subset of atomic orbitals used as the basis set) and is expressed as a projection operator over these kets. One particularly important and widely applied form of such population analysis is the Löwdin scheme [99] which we

shall discuss here briefly.

Population of a subspace is typically calculated as a trace of density matrix. However, matrix-trace of an operator does not have any physical meaning when the corresponding basis set is non-orthogonal. Here, the trace is not necessarily invariant under basis transformation). In the Löwdin scheme, this problem is circumvented by constructing an orthogonal set of basis kets from the non-orthogonal one. Let us assume we have a non-orthogonal set $\{|\phi_i\rangle\}$ of basis orbitals with overlap $S_{ij} = \langle\phi_i|\phi_j\rangle$. The overlap is a Hermitian and positive-definite matrix. This guarantees that it will have a Hermitian and positive-definite inverse square root $\mathbf{S}^{-\frac{1}{2}}$. Let us define a new set of orbitals $\{|\tilde{\phi}_i\rangle\}$ such that

$$(\tilde{\phi_1}(\mathbf{r})\tilde{\phi_2}(\mathbf{r})\cdots\tilde{\phi_N}(\mathbf{r})) = (\phi_1(\mathbf{r})\phi_2(\mathbf{r})\cdots\phi_N(\mathbf{r}))\begin{pmatrix}\mathbf{S}_{11}^{-\frac{1}{2}} & \cdots & \mathbf{S}_{1N}^{-\frac{1}{2}} \\ \vdots & \ddots & \vdots \\ \mathbf{S}_{N1}^{-\frac{1}{2}} & \cdots & \mathbf{S}_{NN}^{-\frac{1}{2}}\end{pmatrix} \tag{3.63}$$

Where the row matrices consist of wave functions corresponding to the aforementioned orbitals.

Taking the hermitian conjugate we get:

$$\begin{pmatrix}\tilde{\phi_1}^*(\mathbf{r}) \\ \tilde{\phi_2}^*(\mathbf{r}) \\ \vdots \\ \tilde{\phi_1}^*(\mathbf{r})\end{pmatrix} = \begin{pmatrix}(\mathbf{S}_{11}^{-\frac{1}{2}})^* & \cdots & (\mathbf{S}_{N1}^{-\frac{1}{2}})^* \\ \vdots & \ddots & \vdots \\ (\mathbf{S}_{1N}^{-\frac{1}{2}})^* & \cdots & (\mathbf{S}_{NN}^{-\frac{1}{2}})^*\end{pmatrix}\begin{pmatrix}\phi_1^*(\mathbf{r}) \\ \phi_2^*(\mathbf{r}) \\ \vdots \\ \phi_1^*(\mathbf{r})\end{pmatrix} \tag{3.64}$$

These give us the relations:

$$\tilde{\phi_i}(\mathbf{r}) = \sum_\mu \phi_\mu(\mathbf{r})\mathbf{S}_{\mu i}^{-\frac{1}{2}} \tag{3.65}$$

and

$$\tilde{\phi_i}(\mathbf{r})^* = \sum_{\mu} (\mathbf{S}_{\nu i}^{-\frac{1}{2}})^* \phi_\nu(\mathbf{r}) \tag{3.66}$$

Thus the inner product of the newly formed orbitals will be

$$\begin{aligned} \langle \tilde{\phi_i} | \tilde{\phi_j} \rangle &= \sum_{\mu\nu} (\mathbf{S}_{\nu i}^{-\frac{1}{2}})^* \mathbf{S}_{\mu j}^{-\frac{1}{2}} \langle \phi_\nu | \phi_\mu \rangle \\ &= \sum_{\mu\nu} \mathbf{S}_{i\nu}^{-\frac{1}{2}} \mathbf{S}_{\mu j}^{-\frac{1}{2}} \mathbf{S}_{\nu\mu} \\ &= \delta_{ij} \end{aligned} \tag{3.67}$$

In the second line we have used the hermiticity property of $\mathbf{S}^{-\frac{1}{2}}$. Thus the new set $\{|\tilde{\phi_i}\rangle\}$ is orthonormal.

Defining a subspace projector as

$$\hat{\mathbb{P}} = |\tilde{\phi_i}\rangle \langle \tilde{\phi_i}| \,, \tag{3.68}$$

the population of the desired subspace is:

$$\begin{aligned} \mathrm{Tr}[\hat{\rho}\hat{\mathbb{P}}] &= \sum_m \langle \tilde{\phi_m} | \hat{\rho}\hat{\mathbb{P}} | \tilde{\phi_m} \rangle \\ &= \sum_{i,m} \langle \tilde{\phi_m} | \hat{\rho} | \tilde{\phi_i} \rangle \langle \tilde{\phi_i} | \tilde{\phi_m} \rangle \\ &= \sum_{i,m} \langle \tilde{\phi_m} | \hat{\rho} | \tilde{\phi_i} \rangle \delta_{i,m} \\ &= \sum_i \langle \tilde{\phi_i} | \hat{\rho} | \tilde{\phi_i} \rangle \\ &= \sum_i \sum_{\mu,\nu} \mathbf{S}_{i\mu}^{-\frac{1}{2}} \mathbf{S}_{\nu i}^{-\frac{1}{2}} \langle \phi_\mu | \hat{\rho} | \phi_\nu \rangle \\ &= \sum_{\mu,\nu} \langle \phi_\mu | \hat{\rho} | \phi_\nu \rangle \sum_i \mathbf{S}_{\nu i}^{-\frac{1}{2}} \mathbf{S}_{i\mu}^{-\frac{1}{2}} \end{aligned} \tag{3.69}$$

Here all the sums are over all space except for the sum over i which is over the given subspace. Now, it must be kept in mind that the orbitals $\{|\tilde{\phi}_i\rangle\}$ can in principle be highly delocalized. Thus the operator defined in Eq. (3.68) is not guaranteed to be good representation of projection over a certain spatially confined subspace.

3.6 Lattice Vibrations

We know from the kinetic theory of gases that at any finite temperature the molecules of an ideal gas move with kinetic energy proportional to the temperature. It is not surprising that even for a solid, the ions should also execute some sort of movement, albeit with some constraint at finite temperature. At any finite temperature, the ions constituting a solid vibrate about their equilibrium position and in general the energy associated with such vibration increases with temperature. The theoretical description of classical lattice vibration presented in this thesis closely follows that found in Ref. [100]. Let us consider a monoatomic 3-D Bravais lattice where the time-dependent displacement of the atom of the $\mathbf{R}_j$ unit cell is given by $\mathbf{u}(\mathbf{R}_j) = \sum_{\alpha=x,y,z} u_\alpha(\mathbf{R}_j)\hat{\alpha}$, $\hat{\alpha}$ being the unit vector in the α-direction. The BVK boundary condition is applied on the lattice displacement at all time:

$$\mathbf{u}(\mathbf{R}_j + N_i\mathbf{R}_i) = \mathbf{u}(\mathbf{R}_j), i = 1, 2, 3 \tag{3.70}$$

The potential energy can be expanded as a Taylor series about the equilibrium point $U_0 = U[\mathbf{u}(\mathbf{R}_j) = \mathbf{0}], \forall j$ as

$$U \approx U_0 + \frac{1}{2}\sum_{\mathbf{R}_1,\mathbf{R}_2}\sum_{\alpha,\beta} u_\alpha(\mathbf{R}_1)\left[\frac{\partial^2 U}{\partial u_\alpha(\mathbf{R}_1)\partial u_\beta(\mathbf{R}_2)}\right]u_\beta(\mathbf{R}_2) \tag{3.71}$$

The quantity in the square bracket constitutes the strength matrix $\mathbf{D}(\mathbf{R}_1 - \mathbf{R}_2)$ which can be shown to follow the relation

$$-M\ddot{\mathbf{u}}(\mathbf{R}_i) = \sum_{\mathbf{R}_j} \mathbf{D}(\mathbf{R}_j - \mathbf{R}_i)\mathbf{u}(\mathbf{R}_j) \tag{3.72}$$

where M denotes mass. If we seek simple harmonic displacements of the lattice points (keeping in mind that these are normal modes and more general vibrations can be written out as linear combinations of them) then:

$$\mathbf{u}(\mathbf{R}_i) = \boldsymbol{\varepsilon} e^{i(\mathbf{k}.\mathbf{R}_i - \omega t)} \tag{3.73}$$

which gives

$$M\omega^2 \boldsymbol{\varepsilon} = \mathbf{D}(\mathbf{k})\boldsymbol{\varepsilon} \tag{3.74}$$

where $\mathbf{D}(\mathbf{k})$, known as the dynamical matrix, is the Fourier transform of the strength matrix such that

$$D_{\alpha\beta}(\mathbf{k}) = \sum_{\mathbf{R}_j} D_{\alpha\beta}(\mathbf{R}_j) e^{-i\mathbf{k}.\mathbf{R}_j} \tag{3.75}$$

Since $\mathbf{D}(\mathbf{k})$ is a (3×3) matrix for each of the $N = (N_1 N_2 N_3)$ values of $\mathbf{k} = \sum_{i=1}^{3} \frac{m_i}{N_i} \mathbf{K}_i$ (obtained from BVK boundary conditions), we know that it has three orthogonal eigenvectors $\boldsymbol{\varepsilon}_{\lambda\mathbf{k}}$ ($\lambda = 1, 2, 3$) and three corresponding eigenvalues $M\omega^2_{\lambda\mathbf{k}}$.

The displacement vector of the lattice point is then:

$$\mathbf{u}_{\lambda\mathbf{k}}(\mathbf{R}_i, t) = \boldsymbol{\varepsilon}_{\lambda\mathbf{k}} e^{i(\mathbf{k}.\mathbf{R}_i - \omega_{\lambda\mathbf{k}} t)} \tag{3.76}$$

Obviously, the phonon bandstructure, i.e. the plot of $\omega_{\mathbf{k}}$ vs $\mathbf{k}$ has three bands ($\lambda = 1, 2, 3$) each of which goes to zero at $\mathbf{k} = \mathbf{0}$. However, it is to be noted that so far we have been dealing with monoatomic basis- i.e. one ion per unit cell. For the general case of 'p' ions per unit cell λ runs from 1 to p and consequently [100]

- We have $3pN$ normal modes- $3p$ branches and N k-points per branch.

- For three of these branches, known as the acoustic branches, $\omega_{\mathbf{k}} \to 0$ as $\mathbf{k} \to 0$. If all the atoms are of the same mass, then in an acoustic branch, the atomic displacements of the atoms in any particular unit cell differ only slightly for $\mathbf{k} \neq \mathbf{0}$ and become identical for $\mathbf{k} = \mathbf{0}$. The remaining branches, which are known as the optical branches, do not follow such property.

- It must be noted that for 'p' atoms per unit cell Eq. (3.76) is modified into

$$\mathbf{u}_{\lambda m\mathbf{k}}(\mathbf{R}_i, t) = \boldsymbol{\varepsilon}_{\lambda m\mathbf{k}} e^{i(\mathbf{k}.\mathbf{R}_i - \omega_{\lambda\mathbf{k}} t)} \tag{3.77}$$

  where $m = 1, ..., p$ gives the index of the atom in the unit cell. Clearly at $\mathbf{k} = \mathbf{0}$

$$\mathbf{u}_{\lambda m\mathbf{k}}(\mathbf{R}_i, t) = \mathbf{u}_{\lambda m\mathbf{k}}(\mathbf{R}_j, t) \forall i, j \tag{3.78}$$

A quantum theory of lattice vibration proves helpful under many circumstances, especially in treating interaction of vibrations with other degrees of freedom like electrons, photons etc. Going back to the monoatomic lattice basis for notational simplicity, we write out the Hamiltonian in terms of the displacement $\hat{u}$ and the momentum $\hat{p}$ operators

$$\hat{H} = \sum_{\mathbf{R}_i} \frac{\hat{p}^2(\mathbf{R}_i)}{2m} + \frac{1}{2} \sum_{\mathbf{R}_i, \mathbf{R}_j} \sum_{\alpha\beta} D_{\alpha\beta}(\mathbf{R}_i, \mathbf{R}_j) u_\alpha(\mathbf{R}_i) u_\beta(\mathbf{R}_j) \tag{3.79}$$

Now, defining a new operator,

$$\hat{b}_{\lambda\mathbf{k}} = \frac{1}{\sqrt{2N}} \sum_{\mathbf{R}_i} e^{-i\mathbf{k}.\mathbf{R}} \left[\sqrt{\frac{m\omega_{\lambda\mathbf{k}}}{\hbar}} \hat{u}(\mathbf{R}_i) + i \sqrt{\frac{1}{\hbar m\omega_{\lambda\mathbf{k}}}} \hat{p}(\mathbf{R}_i) \right] \tag{3.80}$$

the Hamiltonian can be written in a very simple formula

$$\hat{H} = \sum_{\lambda\mathbf{k}} \hbar\omega_{\lambda\mathbf{k}} \left(\hat{b}^\dagger_{\lambda\mathbf{k}} \hat{b}_{\lambda\mathbf{k}} + \frac{1}{2} \right) \tag{3.81}$$

The operator $\hat{b}^\dagger_{\lambda\mathbf{k}}$ ($\hat{b}_{\lambda\mathbf{k}}$) creates (annihilates) a phonon of the mode $(\lambda, \mathbf{k})$, which is responsible for a crystal vibration in the normal mode $(\lambda, \mathbf{k})$. There is a phonon mode

associated with each normal mode oscillation of the lattice and the distribution of the phonons in the lattice determines the resultant lattice vibration as a linear combination of the normal modes. The number of phonons in a particular mode determines the amplitude of the corresponding normal mode harmonic oscillation.

Since the normal mode frequencies and eigenvectors can be obtained by diagonalizing the dynamical matrix, such calculations can be performed as post-processing of DFT based electronic structure calculations. The strength matrix $\mathbf{D}(\mathbf{R}_i - \mathbf{R}_j)$ [see Eq. (3.71)] is calculated from a successful DFT run (typically such functionality is built into the DFT based software). The strength matrix is then transformed into Fourier space to obtain the dynamical matrix $\mathbf{D}(\mathbf{k})$ [see Eq. (3.75)] which, in turn is diagonalized to get the phonon modes and corresponding eigenvectors.

Chapter 4

Charge Transfer Energy of Molecule on Substrate- Benzene Physisorbed on Graphene Sheet

For the theoretical description of charge transfer in a real HOID, one of the most important quantities related to the interface is the charge transfer (CT) energy between the inorganic electrode and the organic crystal. The calculation of CT energies is a challenging task especially in the single molecule limit. This is because the interface gives rise to physical effects that are hard to describe in a KS framework with common XC-functionals. In this chapter, we use the cDFT approach to study the CT energies of molecules adsorbed on a 2-dimensional (2D) metal in various configurations. It must be noted that, in contrast to a regular 3D metal, in a 2D one the image charge induced on the substrate is confined within a one-atom thick sheet. This means that in 2D, electron screening is expected to be less efficient than in a standard 3D metal and the features of the image charge formation in general more complex. In particular we consider here the case of graphene, whose technological relevance is largely established. Most importantly for our work, recently graphene has been used as template layer for the growth of organic crystals. It is then quite important to understand how such template layer affects the CT energies of the molecules with the metal. As a first step, we consider a simple

benzene molecule adsorbed on a sheet of graphene. Then, by investigating the effect of the presence of additional molecules, we study the approaching to the molecular crystal limit. Let us begin with the definition of the relevant energies for a molecule adsorbed on a substrate at a distance d.

- $E_0(d)$: ground state total energy of the entire system consisting of the molecule and the substrate.
- $E_+(d)$: energy of the system when the molecule contains one less electron and the substrate contains one additional one.
- $E_-(d)$: energy of the system when the molecule contains one extra electron and the substrate contains one extra hole.
- $E^+_{CT}(d) = E_+(d) - E_0(d)$: is the charge transfer energy for transferring an electron from the molecule to the substrate.
- $E^-_{CT}(d) = E_0(d) - E_-(d)$: is the charge transfer energy for transferring an electron from the substrate to the molecule.
- $\Delta E_{CT}(d) = E^+_{CT}(d) - E^-_{CT}(d)$: is the charge-transfer energy gap of the system.

Under certain conditions, the CT energies can be related to the well-known *quasiparticle energies* as we discuss below.

4.1 What Are the Quasiparticle Energies?

Let us begin with a discussion on the meaning of the quasiparticle (QP) energies. For non-interacting electrons, the energy of each electron is a well defined quantity and the energy eigenvalues of the system can be found simply by diagonalizing the quadratic Hamiltonian. However, things are not so straightforward for interacting electrons, since the very concept of individual electronic energies loses its strict validity. In this case, the creation or annihilation of any electron in the system is invariably followed by

a relaxation, which means that with the passage of time the particle will have finite probability of being found in other energy states as well. Hence, unlike non-interacting electrons, interacting electrons do not have energy eigenstates with infinite lifetime. This concept is best represented with the help of the greater (lesser) Green's function [101] $G^{>}$ ($G^{<}$). The quantity $G^{>}_{ii}(t,t')$ gives the inner product of two kets $|\alpha\rangle$ and $|\beta\rangle$ where

- $|\alpha\rangle$ is the final state of the system when we add an electron with quantum number i at time t' and evolve the system until time t.
- $|\beta\rangle$ is the final state of the system when we evolve the system until time t and then add an electron with quantum number i

For non-interacting systems, if $|i\rangle$ is an energy eigenket of a time-independent Hamiltonian, then $G^{>}_{ii}(t,t')$ is unity. This means that, if the Hamiltonian is time independent, then a particle added in an energy eigenstate will remain in that state forever. However, for interacting systems containing a large number of particles, when the quantum number $|i\rangle$ is coupled to infinitely many other quantum numbers by the Hamiltonian, the initial state of an electron $|i\rangle$ will spread with time and distribute itself over all such quantum numbers. In this case, $G^{>}_{ii}(t,t')$ is a decreasing function of $|t-t'|$ (going to zero in the limit $|t-t'| \to 0$), signifying the fact that as time progresses, the added particle has finite probability of being found in other states. In other words, the particle has a *finite lifetime* in this quantum state. For a time-independent Hamiltonian and stationary initial preparation, this is actually a function of $(t-t')$ and therefore can be Fourier transformed. The Fourier transform, $G^{>}_{ii}(\omega)$ is a measure (with a factor of imaginary i) of the **probability that a particle added in the quantum state i has an energy ω.** To be a little more pedantic, let us say

ΔE=Total energy of the system *after* adding an electron with quantum number i − Total energy of the system *before* adding an electron with quantum number i

Then $iG^{>}_{ii}(\omega)$ is the probability that $\Delta E = \omega$. Clearly, for a system of inter-

acting electrons, the phrase *energy of the electron* means change in the total energy of the system after the removal (or addition) of the electron from the system.

A similar interpretation can be made for the lesser counterparts of the Green's function ($G^<$), which act as a similar measure for quantities related to the removal of an electron rather than the addition of one. A quantity more widely used in literature for this purpose is a combination of the two Green's functions. The spectral function operator $\hat{A}(\omega)$ is defined as $i[\hat{G}^>(\omega) - \hat{G}^<(\omega)]$. The expectation value of this operator with respect to a quantum number (say i), $A_{ii}(\omega)$ gives the probability that a particle with quantum number i added to or removed from the system has energy ω. As expected, for a non-interacting system (or a system in which each particle is treated to be in a mean field produced by all other particles), this quantity is unity for the energy eigenvalue and zero for all other values. For a system of interacting electrons, these are usually smooth functions peaked at some energy ϵ_λ. To distinguish these energies from the infinitely long-lived particle energies of a non-interacting system (or a system treated at a mean field level), these 'ϵ_λ's are called Quasiparticle (QP) energies. So, essentially these are the most probable energies for added or removed particles in a many particle system. For a molecule (or any finite system), the highest occupied and the lowest unoccupied QP energies are known as HOMO (Highest Occupied Molecular Orbital) and LUMO (Lowest Unoccupied Molecular Orbital), respectively.

We claim that for the charge transfer between a molecule and an infinitely large substrate with zero band-gap, the charge transfer energy gap is a good approximation for the quasiparticle gap of the molecule. If the substrate is infinite and metallic (or semi-metallic) then we can say that an electron added to the substrate will have the same energy as one removed from it- both given by the Fermi energy E_F of the substrate. In this case,

$$\begin{aligned}\Delta E_{CT}(d) &= E_{+}(d) - E_0(d) - E_0(d) + E_{-}(d) \\ &= E_{+}(d) + E_{-}(d) - 2E_0(d) \\ &= E_0(d) - E_{HOMO}(d) + E_F + E_0(d) + E_{LUMO}(d) - E_F - 2E_0(d) \\ &= E_{\mathrm{LUMO}}(d) - E_{\mathrm{HOMO}}(d)\end{aligned}$$

This is actually the QP gap of the molecule physisorbed on the substrate at a height d. However, it must be noted that such equivalence is fully maintained only if the substrate is infinite and there is absolutely no coupling between the adsorbed molecule and the adsorber. This amounts to saying that the interaction between the excess charges in the molecule and in the substrate must be purely classical. In practice, the electronic coupling is usually not strictly zero, which gives rise to effects of exciton binding energy in the charge transfer energy calculated and therefore, the calculated gap is not exactly equal to the quasiparticle gap anymore. However, these effects are expected to be very small if the distance between the substrate and the molecule is not too short.

4.2 Energy Level Renormalization

The treatment presented in this section closely follows Ref. [102]. Let us try to answer the following question: **"What happens to the electronic quasiparticle levels of a molecule when it is brought close to a surface?"** In a nutshell, there are predominantly two effects:

1. The electronic levels, which, neglecting the electronic interactions within the molecule were delta-like in a plot of energy vs probability of finding electron, spread out in energy.

2. The peak of such function shifts in energy.

These two effects are now discussed in some detail. Our discussion closely follows that presented in Ref [102].

4.2.1 Level Broadening

The first effect can be easily shown without having to take any electronic interaction into account. Let us consider a molecule with a single localized energy orbital $|\epsilon_0\rangle$ with energy ϵ_0 coupled to a substrate with energy levels given by a set of $|k\rangle$ (having energies ϵ_k). We assume that these levels are discrete but closely spaced. Since the Hamiltonian is quadratic, we can write it in first quantization as a simple tight-binding model

$$\hat{h} = \sum_k \epsilon_k |k\rangle \langle k| + \epsilon_0 |\epsilon_0\rangle \langle \epsilon_0| + \sum_k (T_k |k\rangle \langle \epsilon_0| + T_k^* |\epsilon_0\rangle \langle k|), \tag{4.1}$$

where T_k is the coupling between the molecule and the substrate. Let $|\lambda\rangle$ be an eigenket of this Hamiltonian. Now, the atomic occupation n_0 can be defined as the sum (over all occupied eigenkets) of the probability of finding an electron in the state $|\epsilon_0\rangle$. Thus,

$$\begin{aligned} n_0 &= \sum_{\lambda:\epsilon\lambda\leq\epsilon_F} |\langle\epsilon|\lambda\rangle|^2 \\ &= \int_{-\infty}^{\epsilon_F} \frac{d\omega}{2\pi} \sum_\lambda 2\pi\delta(\omega-\epsilon_\lambda) |\langle\epsilon_0|\lambda\rangle|^2 \\ &= \int_{-\infty}^{\epsilon_F} \frac{d\omega}{2\pi} \langle\epsilon_0| 2\pi\delta(\omega-\hat{h}) |\epsilon_0\rangle . \end{aligned}$$

This can be shown to be equal to

$$n_0 = -2 \lim_{\eta\to 0^+} \int_{-\infty}^{\epsilon_F} \frac{d\omega}{2\pi} \mathrm{Im} \frac{1}{\omega - \epsilon_0 - \Sigma_{\mathrm{em}}(\omega) + \mathrm{i}\eta} = \int_{-\infty}^{\epsilon_\mathrm{F}} \frac{\mathrm{d}\omega}{2\pi} \mathrm{A}_{00}(\omega)$$

where the *embedding self-energy* $\Sigma_{em}(\omega)$ modifies the molecular occupation for the coupling between the substrate and the molecule. This term vanishes for $T_k = 0$. In this expression, one can notice the useful observable $A_{00}(\omega)$ called the *molecular spectral*

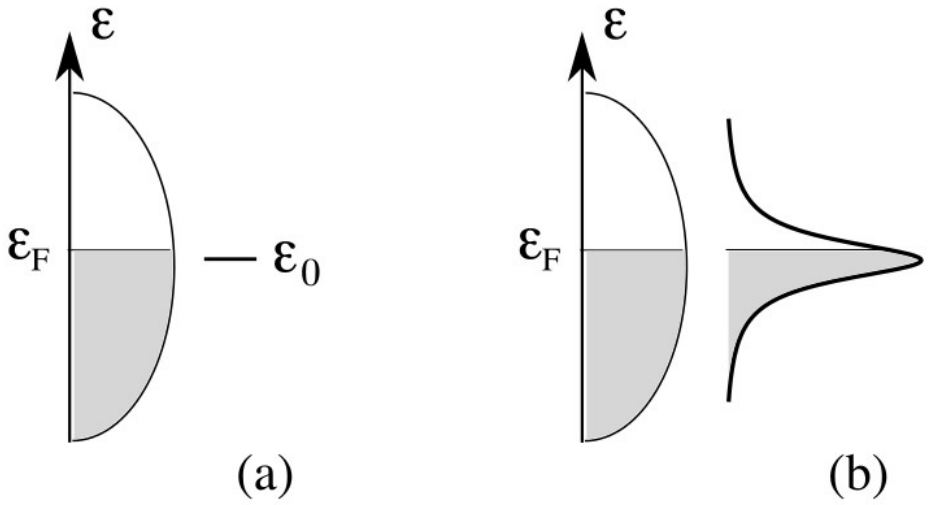

Figure 4.1: Diagram showing the distribution of the continuum of substrate states and molecular spectral function for (a) zero coupling ($T_k = 0$) and (b) finite coupling ($T_k \neq 0$) between the two entities. Figure adapter from [102]

function, which gives the probability that an electron in the molecular level has an energy ω. If we approximate $\Sigma_{em}(\omega)$ to be independent of ω, then this *wide-band limit approximation*(WBLA) leads to

$$n_0 = \int_{-\infty}^{\epsilon_F} \frac{d\omega}{2\pi} \frac{\Gamma}{(\omega - \epsilon_0)^2 + \Gamma^2/4}$$

where Γ is the imaginary part of Σ_{em}. In WBLA, the real part of Σ_{em} vanishes. In the case of isolated molecule, $\Gamma = 0$ and one recovers the expected result

$$A_{00_{isolated}}(\omega) = \delta(\omega - \epsilon_0)$$

Physically, this means that the sharp molecular level of an isolated molecule transforms into a probability distribution of finite width. There is no broadenning when $T_k = 0$. It is worth noting that this result is derived from the Hamiltonian Eq. (4.1), which is true for non-interacting electrons.

4.2.2 Shifting of the Energy Levels

Unlike the broadening, the shift of the molecular levels in the presence of a substrate has to do with the interaction between the electrons in the molecule and the substrate.

We shall first discuss an extremely simplified model that describes this phenomenon and then discuss what approximate terms are required to obtain these effects in calculation with an effective Hamiltonian.

Let us assume the model Hamiltonian $\hat{H}$ to be composed of three terms: one for the molecule, $\hat{H}_{mol}$, one for the substrate, $\hat{H}_{sub}$, and one term for interaction between the two, $\hat{H}_{int}$.

If we assume the substrate to be a one-dimensional chain comprising N sites with nearest-neighbour hopping and zero onsite energy then

$$\hat{H}_{sub} = T \sum_{j=1}^{N-1} (\hat{d}_j^\dagger \hat{d}_{j+1} + \hat{d}_{j+1}^\dagger \hat{d}_j).$$

We model the molecule as a two level (a and b) system with onsite energy ϵ_0 and hopping T_0. Hence

$$\hat{H}_{mol} = \epsilon_0 \sum_{i=a,b} \hat{d}_i^\dagger \hat{d}_i + T_0(\hat{d}_a^\dagger \hat{d}_b + \hat{d}_b^\dagger \hat{d}_a)$$

As for the interaction term, let us deal only with a physisorbtion situation and omit any overlap term between the orbitals of the molecule and the substrate. Let us also assume that for the substrate, the interaction is limited to its first 'r' sites. So, we write an interaction term of the form

$$\hat{H}_{int} = U \left(\sum_{i=a,b} \hat{n}_i - 1 \right) \left(\sum_{j \le r} \hat{n}_j - \overline{N}_r \right).$$

Here, 1 and $\overline{N}_r$ are the ground state values of the number of electrons in the molecule and the first r sites of the substrate respectively. Clearly, there is no chemical coupling between the substrate and the molecule and if the number of electrons in either the molecule or the first r sites of the substrate equals the ground state value, then there is no interaction between them.

Let $\hat{c}_{\lambda_i}$ be the set of operators that diagonalizes the quadratic Hamiltonian $\hat{H}_{sub}$; i.e. $\hat{H}_{sub} = \sum_\lambda \epsilon_\lambda \hat{c}_\lambda^\dagger \hat{c}_\lambda$. The eigenkets of $\hat{H}_{sub}$ can be given by $|\Psi_{sub}\rangle = \hat{c}_{\lambda_M}^\dagger ... \hat{c}_{\lambda_1}^\dagger |0\rangle = |\lambda_1 ... \lambda_M\rangle$, where $|0\rangle$ is the vacuum level. Similarly, let $\hat{c}_{H,L}$ be the operators that bring $\hat{H}_{\rm mol}$ into the quadratic form $(\epsilon_H \hat{c}_H^\dagger \hat{c}_H + \epsilon_L \hat{c}_L^\dagger \hat{c}_L)$. Since we have assumed that the

molecule contains one electron in the ground state, the energies ϵ_H and ϵ_L can be interpreted as the $HOMO$ and $LUMO$ energy respectively. Since the number operator for the molecule $\sum_{i=a,b} \hat{d}_i^\dagger \hat{d}_i$ commutes with the total Hamiltonian $\hat{H} = \hat{H}_{mol} + \hat{H}_{sub} + \hat{H}_{int}$, each many-body eigenket of $\hat{H}$ must have a definite number of electrons in the molecule. Evidently, the eigenkets of $\hat{H}$ containing M electrons in the substrate and a single electron in the molecular $HOMO$ is given by $|\Psi\rangle = \hat{c}_H^\dagger |\Psi_{sub}\rangle$. Note that there is no effect of $\hat{H}_{int}$ on this state since it contains one electron in the molecule. The ground state of $\hat{H}$ satisfying these conditions is $|\Psi_0\rangle = \hat{c}_H^\dagger |\Psi_{sub,0}\rangle$ where $|\psi_{sub,0}\rangle$ is the ground state of $\hat{H}_{sub}$ containing M electrons. It must also be mentioned that $|\Psi_{sub}\rangle$ is not an eigenket of $\hat{H}$ since this ket is obtained by removing the $HOMO$ electron from $|\Psi\rangle$ and not allowing any relaxation. Keeping in mind that for such a state $\sum_{i=a,b} \hat{n}_i = 0$, the net Hamiltonian acting on this state can be given by $\hat{H}_{sub}^- = \hat{H}_{sub} - U(\hat{N}_r - \overline{N}_r)$ since the part $(\hat{H} - \hat{H}_{sub}^-)$ has no effect on $|\Psi_{sub}\rangle$. Although $|\Psi_{sub}\rangle$ is an eigenket of $\hat{H}_{sub}$ it is not so for $\hat{N}_r$ an consequently is not one for $\hat{H}_{sub}^-$ or H either.

We can now calculate the lesser and greater components of the Green's function of the $HOMO$ level for the many-body state $|\Psi_0\rangle$ corresponding to energy E_0,

$$G_{HH}^<(t,t') = i \langle \Psi_0 | \hat{c}_H^\dagger e^{-i(\hat{H}-E_0)(t'-t)} \hat{c}_H |\Psi_0\rangle , \tag{4.2}$$

$$= i \langle \Psi_{sub,0} | e^{-i(\hat{H}_{sub}^- - E_0)(t'-t)} |\Psi_{sub,0}\rangle , \tag{4.3}$$

and

$$G_{HH}^>(t,t') = 0.$$

Thus the spectral function of the same level is given by

$$A_{HH}(\omega) = 2\pi \langle \Psi_{sub,0} | \delta(\omega - E_0 + \hat{H}_{sub}^-) |\Psi_{sub,0}\rangle .$$

In order to evaluate such expression we need to expand $|\Psi_{sub,0}\rangle$ over a complete set of M electron eigenkets $|\lambda_1^- ... \lambda_M^-\rangle$ of $\hat{H}_{sub}^-$

$$|\Psi_{sub,0}\rangle = \frac{1}{M!} \sum_{\lambda_1 ... \lambda_M} |\lambda_1^- ... \lambda_M^-\rangle \langle \lambda_1^- ... \lambda_M^- | \Psi_{sub,0}\rangle .$$

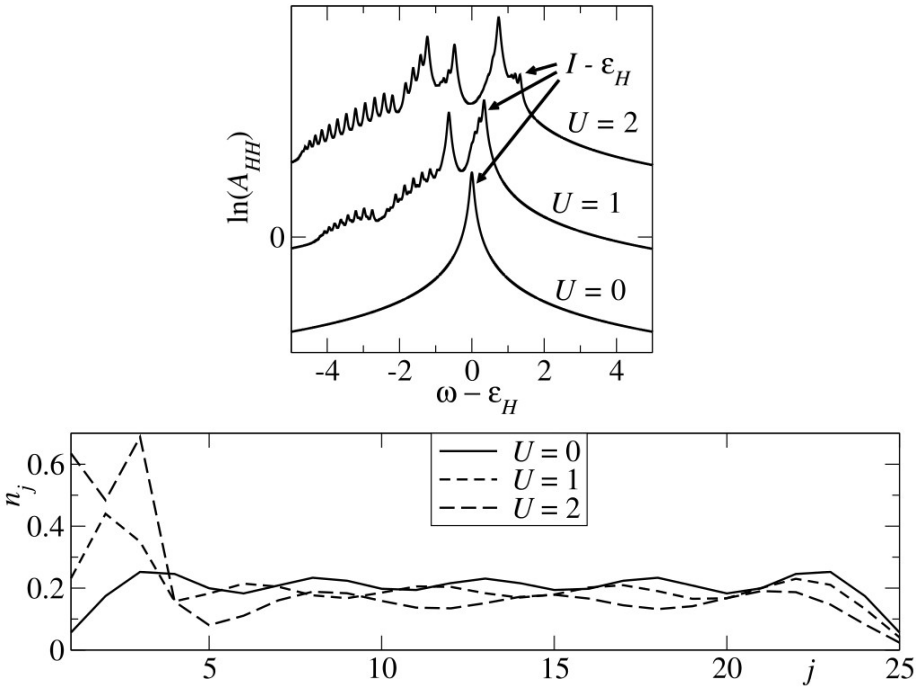

Figure 4.2: Diagram (a) shows molecular HOMO spectral function (in log scale) as a function of energy. Multiple peaks appear as the interaction parameter is increased. The sharp levels have been artificially broadened by using small finite η in Eq. (4.4)(b) Shows the charge density for different U at different sites of the substrate. Figure adapted from [102]

.

This gives us

$$A_{HH}(\omega) = -\frac{2}{M!}\sum_{\lambda_1 \ldots \lambda_M} \mathrm{Im}\frac{|\langle \lambda_1^- \ldots \lambda_M^- | \Psi_{\mathrm{sub},0}\rangle|^2}{\omega - E_0 + \epsilon_{\lambda_1}^- + \ldots + \epsilon_{\lambda_M}^- + U\overline{N}_r + i\eta} \tag{4.4}$$

Here ϵ_λ^- are the eigenvalues of $\hat{h}_{sub}^-$, which is the single-particle Hamiltonian counterpart of $\hat{H}_{sub}^- = \sum_{i,j} \langle i| \hat{h}_{sub}^- |j\rangle \hat{d}_i^\dagger \hat{d}_j + U\overline{N}_r$

Fig. 4.2(a) shows a plot of $\ln(A_{HH})$ vs energy with varying U for a large $N(=25)$ and for $r=3$ and $M=5$. Both the predicted effects can be seen from this figure. Since the *HOMO* electron can now scatter with electrons of the substrate, the plot of $\ln(A_{HH})$ is no longer a single sharply defined peak but it contains many peaks. Clearly,

these peaks originate from the fact that the state $|\Psi_{sub,0}\rangle$ is now coupled to the states $|\lambda_1^-...\lambda_M^-\rangle$. Each such coupling results in a peak of $A_{HH}(\omega)$ as can be seen from Eq. (4.4). If $|\Psi_{sub,0}\rangle$ is coupled to an infinite number of states, all such peaks will close in to form a continuum. We can also notice that the peak of $\ln(A_{HH})$ shifts rightward as U increases, indicating an upward energy shift of the $HOMO$ as the molecule approaches the surface. A similar treatment on $A_{LL}(\omega)$ reveals that, as a result of the proximity of the substrate, the single sharply peaked $LUMO$ level of the isolated molecule splits into many peaks and also shifts toward lower energy. Thus, the presence of the substrate essentially raises the energy of the $HOMO$ and and lowers that of the $LUMO$ levels respectively, resulting in a reduction of the quasiparticle gap.

The reason for such realignment of the $HOMO$ can be appreciated in Fig. 4.2(b) which shows a plot of the the ground-state density of $\hat{H}_{sub}^-$ on the substrate as a function of its sites. For $U = 0$, the state $|\Psi_{sub,0}\rangle$, which has the same density in the substrate sites as that of the state $|\Psi_0\rangle$ is an eigenket of $\hat{H}_{sub}^-$. The density of the metallic sites is what it would be in the presence of the $HOMO$ electron and any value of U (since, in the presence of the $HOMO$ electron, the interaction Hamiltonian is zero anyway). From the plot, one can see that this is more or less symmetric with respect to the sites. However, as U increases, asymmetry sets in and the electron density increases in the first few sites: i.e. in the sites which are coupled to the molecule. Thus, the charge density in the first few substrate sites is always greater in absence of the $HOMO$ electrons than what it would have been in the presence of the same. This image charge is actually the result of the electrostatic attraction between the positive charge in the molecule (due to the absence of the $HOMO$ electron) and the electrons of the substrate. Clearly, this attraction lowers the energy of the system in the absence of the molecular $HOMO$ electron, thereby resulting in an upward energy shift of the $HOMO$ level.

4.3 The Quasiparticle Equation

We have previously defined the QP energies as the peaks of the spectral function. However, the same energies can be obtained by diagonalizing a first quantization operator, which serves as an effective hamiltonian ($\hat{h}_{eff}$) in a single particle picture for the many electron system. In order to do this, one needs to introduce the *self-energy operator* $\hat{\Sigma}(t,t')$. This is a first quantization operator representing all the effects of electronic interactions. If the system Hamiltonian in Fock space is time-independent, then this operator becomes a function of the time difference only $\hat{\Sigma}(t,t') = \hat{\Sigma}(t-t')$ and as a consequence can be Fourier transformed into energy space, $\hat{\Sigma}(\omega)$ [102]. Then one can write the effective Hamiltonian as $\hat{h}_{eff} = \hat{h} + \hat{\Sigma}(\omega)$ where $\hat{h}$ is the non-interacting single-electron Hamiltonian. Then, the eigenvalues $\epsilon_{n\mathbf{k}}$ and eigenkets $|\psi_{n\mathbf{k}}\rangle$ of this operator will follow the equation

$$\begin{aligned}
\left(\hat{h} + \hat{\Sigma}(\epsilon_{n\mathbf{k}})\right)|\psi_{n\mathbf{k}}\rangle &= \epsilon_{n\mathbf{k}}\,|\psi_{n\mathbf{k}}\rangle \\
\int d\mathbf{r}'\,\langle r|\,\hat{h} + \hat{\Sigma}(\epsilon_{n\mathbf{k}})\,|r'\rangle\,\langle \mathbf{r}'|\psi_{n\mathbf{k}}\rangle &= \epsilon_{n\mathbf{k}}\,\langle \mathbf{r}|\psi_{n\mathbf{k}}\rangle\,, \\
h(\mathbf{r})\psi_{n\mathbf{k}}(\mathbf{r}) + \int d\mathbf{r}'\Sigma(\mathbf{r},\mathbf{r}';\epsilon_{n\mathbf{k}})\psi_{n\mathbf{k}}(\mathbf{r}') &= \epsilon_{n\mathbf{k}}\psi_{n\mathbf{k}}(\mathbf{r}),
\end{aligned} \tag{4.5}$$

where we have assumed $h(\mathbf{r})$ to be local in space. At variance with non-interacting systems, the energy eigenvalues $\epsilon_{n\mathbf{k}}$ are complex numbers with the real part representing the QP energy (i.e. position of peak of spectral function) and the imaginary part representing the width of the peak (the imaginary part, along with other quantities also acts as a measure of the rate of decay of a particle added to or removed from the corresponding state: in other words, the *lifetime* for that quantum state). A complex $\epsilon_{n\mathbf{k}}$ is thus a signature of the relaxation process mentioned earlier. Now, unlike $\hat{h}$, in practice $\hat{\Sigma}$ is not written out in any exact form. It can be written as a perturbation series with infinitely many terms, different terms signifying different processes in the interaction. It would be worth investigating which terms of such series are essential to obtain a proper approximation of the self-energy so as to get acceptable values for the

QP energies. Within a broad classification, the self energy can be written as sum of three different terms

$$\hat{\Sigma} = \hat{\Sigma}_H + \hat{\Sigma}_F + \hat{\Sigma}_C$$

$\hat{\Sigma}_H$ or the *Hartree* term describes the classical mean field (i.e. an approximation in which an electron interacts with the average classical field of all the other electrons in the system). The expectation value of this term with respect to position eigenket is local in space. In contrast, $\hat{\Sigma}_F$, the *Fock* term describes the mean-field exchange interaction, which is ignored in the Hartree approximation. Finally, $\hat{\Sigma}_C$, the *Correlation* term, comprises all the contributions beyond the mean field approximation, i.e. all the effects associated due to individual interactions. The first two terms are local in time and consequently, in Fourier space they are independent of energy. The only self energy term, that is nonlocal in time is the correlation term.

In order to get an idea about which of the infinite number of terms defining the perturbative expansion of the self-energy are required to appreciate the level-realignment of the molecule as a function of its distance from a surface, one can compare the QP energies calculated with different self-energy approximations with the exact ones obtained from Eq. (4.4). In Fig. 4.3 one can compare the exact value of the molecular spectral function against those calculated with the help of two different self-energy approximations: the Hartree-Fock (HF) and the second-Born [103] (SB) approximation. It is clear that with the HF approximation, which assumes the self-energy $\Sigma = \Sigma_H + \Sigma_F$ to be energy independent, the QP levels do not change with changing U. The spectral function calculated non-selfconsistently from the second-Born approximation for the self-energy, which includes a couple of terms beyond HF and therefore takes correlation explicitly into account, shows the trend of decreasing QP gap with increment of U. Clearly, in order to see the renormalization of the energy levels, one needs to include self-energy terms with correlation effects (i.e. terms which depend on energy).

One popular self-energy approximation for solving this QP equation is the GW-approximation. One typically approximates the self energy as $\Sigma(1,2) = iG(1,2)W(1^+,2)$[1]

[1]an index i in the parenthesis denotes the combined spatial and temporal coordinate $(\mathbf{r}_i, t_i)$. The

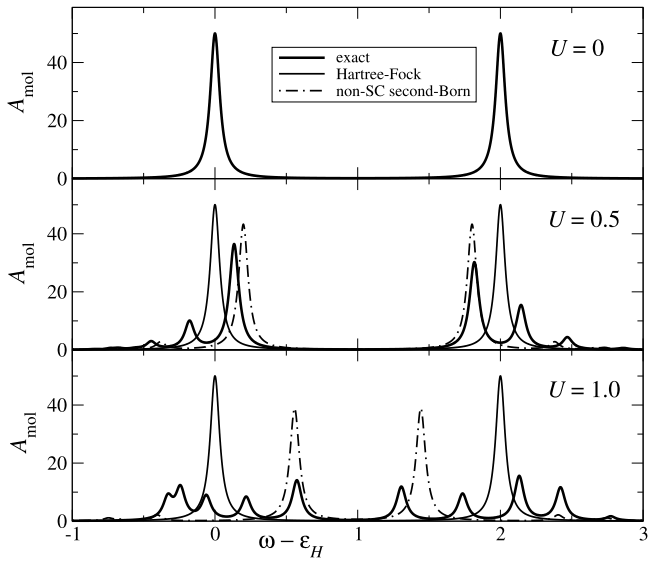

Figure 4.3: Diagram showing the molecular HOMO and molecular LUMO for different values of U calculated with three separate techniques.Figure adapted from [102]

where G is the single particle Green's function and W is the screened interaction (which physically signifies the interaction among two electrons taking into account the effects due to all other electrons in the system). Such self-energy can be evaluated by solving a set of five coupled equations, known as *Hedin equation* [104]. The self-energy so calculated is then used to compute the QP energies. It has been shown [105] that the QP energies obtained from the GW approximation match the exact ones excellently. However, this method for calculating the QP energies is extremely resource consuming and so it is usually limited to small systems.

4.3.1 DFT and quasiparticle energies

As mentioned before, there is no reason to believe that the single particle Kohn-Sham energy eigenvalues represent the precise single-particle quasiparticle energies of interacting-electron systems. For some metals and weakly correlated materials, the band structure obtained from the DFT KS eigenvalues agree remarkably well with the exact one. For

index i^+ denotes an infinitesimal positive shift δ in the time coordinate, i.e. $i^+ = (\mathbf{r}_i, t_i + \delta)$

example, Fig. 4.4 shows the bands structure and density of states of graphene calculated with DFT. These results are quite accurate due to the weak correlation in graphene. Also, the Fermi energy of graphene, which is obtained to be 4.45 eV with regular DFT agrees with experimental inverse work function.

However, from a theoretical point of view, with the exception of the KS HOMO, which for an exact XC functional equals the QP HOMO [106] (negative of the ionization energy), no other KS eigenvalue has any physical significance. This means that, strictly speaking, even for an isolated molecule, the QP gap can not be precisely determined directly from the KS eigenvalues obtained with an exact functional.

In our case, the situation is even more challenging since, a) we do not have access to the exact XC functional, and b) as discussed in the preceding section, for molecule adsorbed on a metal substrate one requires an excellent description of electronic correlation, which is absent in HF theory, to capture the effects of level renormalization in an effective single-particle theory. In the model described in section 4.2.2, the level renormalization of the molecule upon adsorbtion is seen to be caused solely by the non-local interaction $\hat{H}_{int}$. Commonly used XC-functionals, LDA and GGA, do not include any non-local correlation effect. Hence, the KS eigenvalues obtained with such functionals exhibit virtually no shift upon adsorption (much like the HF eigenvalues in Fig. 4.3) [105]. It is possible to use a Generalized Kohn-Sham (GKS) scheme (noting that the GKS HOMO and LUMO can be related to the QP counterparts) with non-local XC-functional to investigate this level renormalization [107].

When the molecule is charged, an opposite image charge forms on the substrate near the molecule and exerts Coulomb attraction. This attraction is the reason for the level renormalization, i.e. for the difference in the energy of the added charge in an isolated molecule and in an adsorbed molecule. Since this Coulomb attraction is not present until the molecule is charged, expecting an exact calculation of the energy levels of the adsorbed uncharged molecule amounts to expecting the theoretical tool to know about the response of the substrate to the addition/removal of an electron, which has not been added/removed yet! This is not impossible [108, 107]. But it requires an advanced

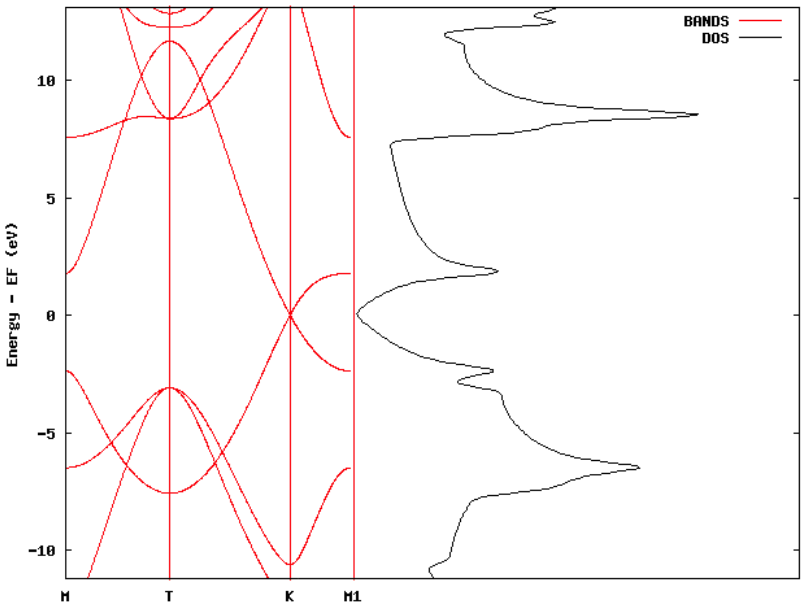

Figure 4.4: Diagram showing band structure of pristine graphene along high symmetry directions along with the density of states. From this figure it is evident that graphene has a zero band gap at the 'K' point.

level of theory since non-local correlation terms must be taken into account. As soon as the molecule is actually charged, a simple Coulomb interaction between the molecule and the image charge easily captures much of the effects encoded in the complicated correlation in the uncharged case. This motivates the possibility of a straightforward calculation, based on total energy differences for calculating the level-renormalization without having to worry about the correlation interactions.

4.4 Computational Details

In this work, by using cDFT implemented in the software SIESTA [95], we calculate the charge transfer energy between a graphene sheet and a benzene molecule physisorbed on it. In order to do this for a given distance d between the molecule and the substrate we need to run three different calculations:

1. a regular DFT calculation in order to determine the ground state total energy,

$E_0(d)$, and the charge distribution on each subsystem (*i.e.* on the molecule and on the graphene sheet)

2. a cDFT calculation with the constraint that the graphene sheet contains one extra electron and the molecule lacks an electron. This gives the energy $E_+(d)$.

3. a cDFT calculation with the graphene containing one less electron and the molecule containing an additional one. This gives the energy $E_-(d)$.

The charge transfer energy for removing an electron from the molecule and placing it on the graphene sheet is then $E^+_{\mathrm{CT}}(d) = E_+(d) - E_0(d)$. Similarly, that for a transfer of an electron from the graphene sheet to the molecule is $E^-_{\mathrm{CT}}(d) = E_0(d) - E_-(d)$. Since in each run the total charge of the system is zero, hence this approach does not require any monopole correction. However, we have to keep in mind that this method is best used when the two subsystems are well separated so that the amount of charge localized on each subsystem is a well-defined quantity. Thus, we shall concentrate on the case of weak physisorption, where the atomic orbitals of the two entities are sufficiently far apart. In other words, for the model Hamiltonian, we shall assume any hopping term between the molecule and substrate orbitals to vanish.

For our calculations, we use a CDFT implementation [109] on the popular DFT package SIESTA [95], which adopts a basis set formed by linear combinations of atomic orbitals (LCAO). Hence, instead of real space, the charge is actually constrained through a projection over a specified set of basis orbitals. Because of the use of localized basis orbitals, the amount of empty space between the molecule and the sheet (or above the molecule) does not does not require much additional computational time. While forming unit cells, we have kept sufficient space above the molecule to ensure negligible interaction between the periodic structures. We use the Löwdin projection scheme for all calculations. Throughout this work we adopt double-zeta polarized basis orbitals with an energy cutoff of 0.02 Ry. The calculations are performed with norm-conserving pseudopotentials and the local density approximation (LDA) has been used for the exchange-correlation functional. A mesh cutoff of 300 Ry has been used for the real-space grid. In all calculations we impose periodic boundary conditions with different

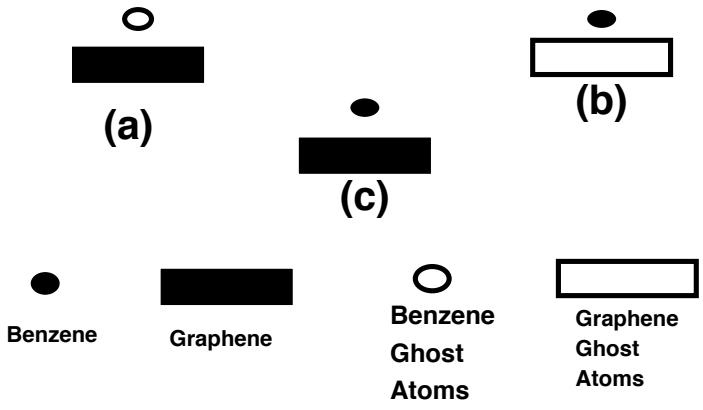

Figure 4.5: A schematic diagram showing the different energy calculations for counter-poise corrections

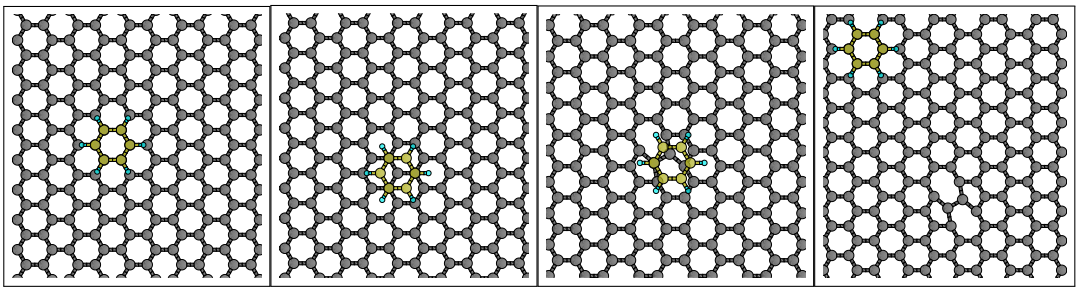

Figure 4.6: Top view of (a) Hollow, (b) Stack, (c) Top and (d) Away configurations. Yellow atoms are carbon atoms belonging to benzene ring while grey ones are those of the graphene sheet.

cell-sizes. The k-space grid is varied depending on the size of the unit cell. For instance, an in plane 5x5 k-grid has been used for a 13x13 unit cell in real space. Note that, the results presented in this chapter are obtained with non spin-polarized calculations.

4.5 Results

4.5.1 Equilibrium Heights

We begin this section with the discussion of the equilibrium height for benzene molecule adsorbed on graphene. We look for the height for which the interaction energy $\Delta E_{\rm int} = E_{\rm Benz+Gr} - (E_{\rm Benz} + E_{\rm Gr})$ is minimum.

These calculations are performed with regular DFT. However, in order to avoid basis set superposition error in the calculation of the interaction energy, we made use of ghost atoms [110], while calculating $E_{\rm Benz}$ and $E_{\rm Gr}$. In normal calculation using SIESTA, the total number of basis sets used in calculating $E_{\rm Benz+Gr}$ is greater than that used in calculating $E_{\rm Benz}$ or $E_{\rm Gr}$.

$$\Delta E_{\rm int} = E^{\rm B+G}_{\rm Benz+Gr} - (E^{\rm B}_{\rm Benz} + E^{\rm G}_{\rm Gr})$$

Where the superscript denotes the basis orbitals employed in the calculation. Clearly, this leads to artificial stabilization of the composite system compared to the isolated one. In order to eliminate such error, we need to use the same basis orbitals for each of the three calculations. Hence, for all the calculations we shall use the orbitals of the composite system (for that particular height). As shown in Fig. 4.5 this corrected interaction energy is obtained by subtracting the sum of (a) and (b) from (c),namely,

$$\Delta E^{\rm corrected}_{\rm int} = E^{\rm B+G}_{\rm Benz+Gr} - (E^{\rm B+G}_{\rm Benz} + E^{\rm B+G}_{\rm Gr}).$$

We perform this procedure for two different orientations of the benzene molecule with respect to the sheet: the *hollow* configuration, in which all the carbon atoms of the benzene ring are placed exactly above those of graphene, and the *stack* configuration, in which alternate carbon atoms of the benzene molecule are placed directly above carbons of the graphene sheet [c.f. Fig. 4.6(a,b)]. A plot of the interaction energy as a function of height is plotted in Fig. 4.7. For a hollow configuration, the above procedure gives an equilibrium height of 3.4 Å, while for a stack configuration the height is 3.25 Å. These results are in fair agreement with other studies [111].

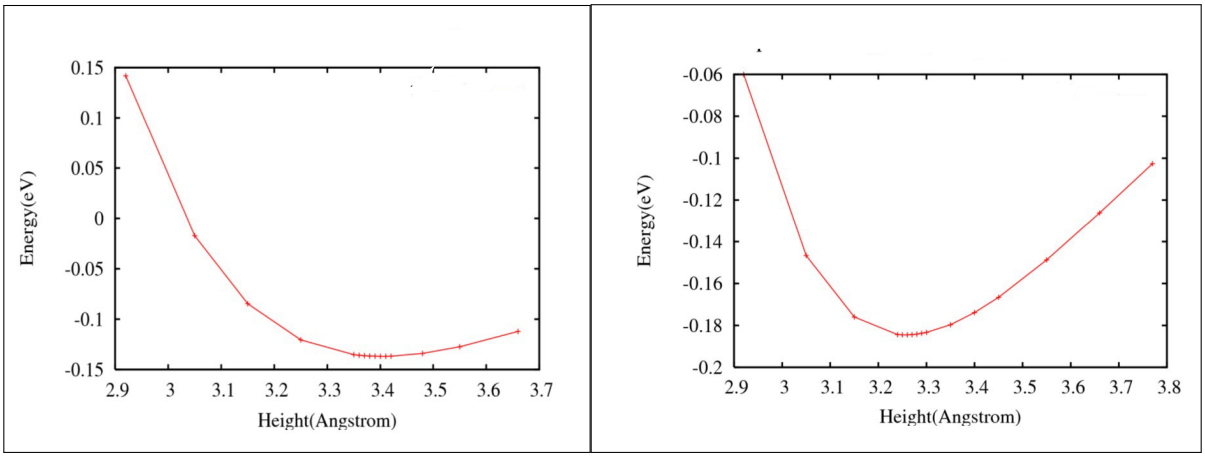

Figure 4.7: Plot of interaction energy as a function of distance between the graphene sheet and benzene molecule for (a) Hollow and (b) Stack configuration. The lowest energies are attained at 3.4 Åand 3.25 Årespectively.

4.5.2 Dependence of the CT Energies on the Cellsize

We then study the dependence of the charge transfer energies on the size of the graphene unit cell used for creating our periodic structure. This is done by analyzing the charge transfer gap, $E^{+}_{\mathrm{CT}}(d) - E^{-}_{\mathrm{CT}}(d)$, as a function of the unit cell size (see Fig. 4.8)

If the molecule is very close to the graphene sheet, after transferring an electron, the image charge on the sheet is strongly attracted by the oppositely charged molecule and thereby remains highly localized. However, as we move the molecule farther away from the graphene sheet, the attraction diminishes due to the distance resulting in a delocalization of the image charge, which spreads uniformly all over the sheet in the limit of infinite distance. For a small unit cell, the image charge on the graphene sheet is forcefully confined into a region smaller than required. This accounts for some extra energy in the charge-transfer states [i.e., for an overestimation of $E_{-}(d)$ and $E_{+}(d)$], which, in turn, results in higher charge transfer energies. Therefore, it is expected that for a smaller distance between the graphene and the molecule, the limit of infinite graphene sheet is obtained with a smaller unit cell. This effect can be clearly seen from Fig. 4.8 in which we show the variation of the CT energies with increasing cell size. Clearly, for the shorter distance 3.4 Å, a converged energy gap is obtained with a

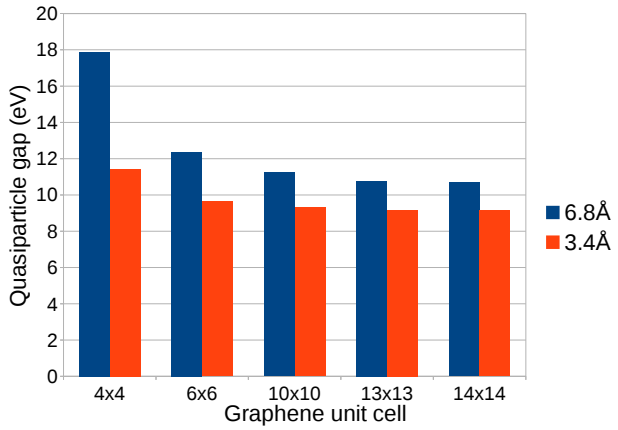

Figure 4.8: $E^{+}_{\mathrm{CT}} - E^{-}_{\mathrm{CT}}$ for different unit cell size of graphene sheet. The results are shown for two different heights: 3.4 Å and 6.8 Å.

smaller cell size. From the figure it is quite clear that for both heights, results with a 13×13 cell are sufficiently converged.

4.5.3 CT Energies as a Function of the Distance

Next we study the converged charge transfer energies as a function of the distance between the sheet and the molecule. In order to compare our results with the gap expected in the limit of infinite height, we need first to find the ionization energy, I_{MOL}, and the electron affinity (A_{MOL}) of isolated benzene. We found the quasiparticle energy gap to be 11.02 eV, in good agreement with other studies [112, 113]. In addition to this, we also determine the Fermi level of graphene, W_F, which is found to be 4.45 eV. In Fig. 4.9(a) we show the change in the charge transfer energy gap by varying the height of a benzene placed in a *hollow* configuration. As expected, when the molecule is very close to the surface, after the transfer of an electron there is considerably large attraction between the image charge on the plane and the opposite excess charge on the molecule. This results in an extra stabilization of the system and a reduction in magnitude of $E_{+}(d)$ and $E_{-}(d)$. Hence, in such cases the charge transfer energies have lower magnitude. However, as the molecule moves away from the sheet, the charge transfer energies keep increasing and the charge transfer energy gap ultimately saturates

at the HOMO-LUMO gap of the isolated molecule in the limit of infinite distance. For large separation, the electronic coupling can be expected to be low and consequently the contribution of exciton binding to the charge-transfer gap is small. In Fig. 4.9(b,c,d,e) we show the excess charge-density, $\Delta\rho$, in different parts of the system after transferring one electron. $\Delta\rho$ is defined as $\rho_{(\mathrm{CDFT})} - \rho_{(\mathrm{DFT})}$, where $\rho_{(\mathrm{DFT})}$ and $\rho_{(\mathrm{CDFT})}$ are the charge densities of the system before and after the charge transfer, respectively. Clearly, due to the stronger Coulomb attraction, the charge is more localized in the case of a shorter height, namely 3.4 Å, than for a larger one. In this context, it is worth mentioning that our result for the charge-transfer gap of benzene adsorbed in a *stack* configuration on graphene at equilibrium height of 3.25 Å is 8.91 eV. This is in good agreement (within about 4%) with the quasiparticle gap obtained by a G_0W_0 study on the same system [114], suggesting the excitonic effects probably plays a minor role here.

4.5.4 Effect Of Defects

It is known that, actual graphene samples always display lattice imperfections [115]. In order to determine the effect of such structural defects on the CT energies, we consider a reference system, where a Stone-Wales defect (in which a single C-C bond is rotated by a right angle) is present in the graphene sheet. We have calculated $E_{\mathrm{CT}}^{\pm}$ for two different positions of the molecule with respect to the defect on the sheet, namely the *top* position, in which the molecule is placed right above the defect and the *away* position, in which it is placed above the sheet far from the defect. Our findings are listed in Tab. 4.1. in which we enlist the charge transfer energies for the *top* and *away* configuration of benzene on a graphene sheet with Stone-Wales defect and also those for the hollow and stack configuration of benzene on a defectless sheet of graphene - all for the same height (3.4 Å) between graphene and benzene. The later two are presented for the purpose of comparison. From the results, it is evident that the small structural change in pristine graphene due to presence of such defect does not alter the CT energies of the molecule. One does not expect the image charge distribution on graphene to be hugely affected by presence of SW defect. Besides, the density of states (DOS) of graphene remains

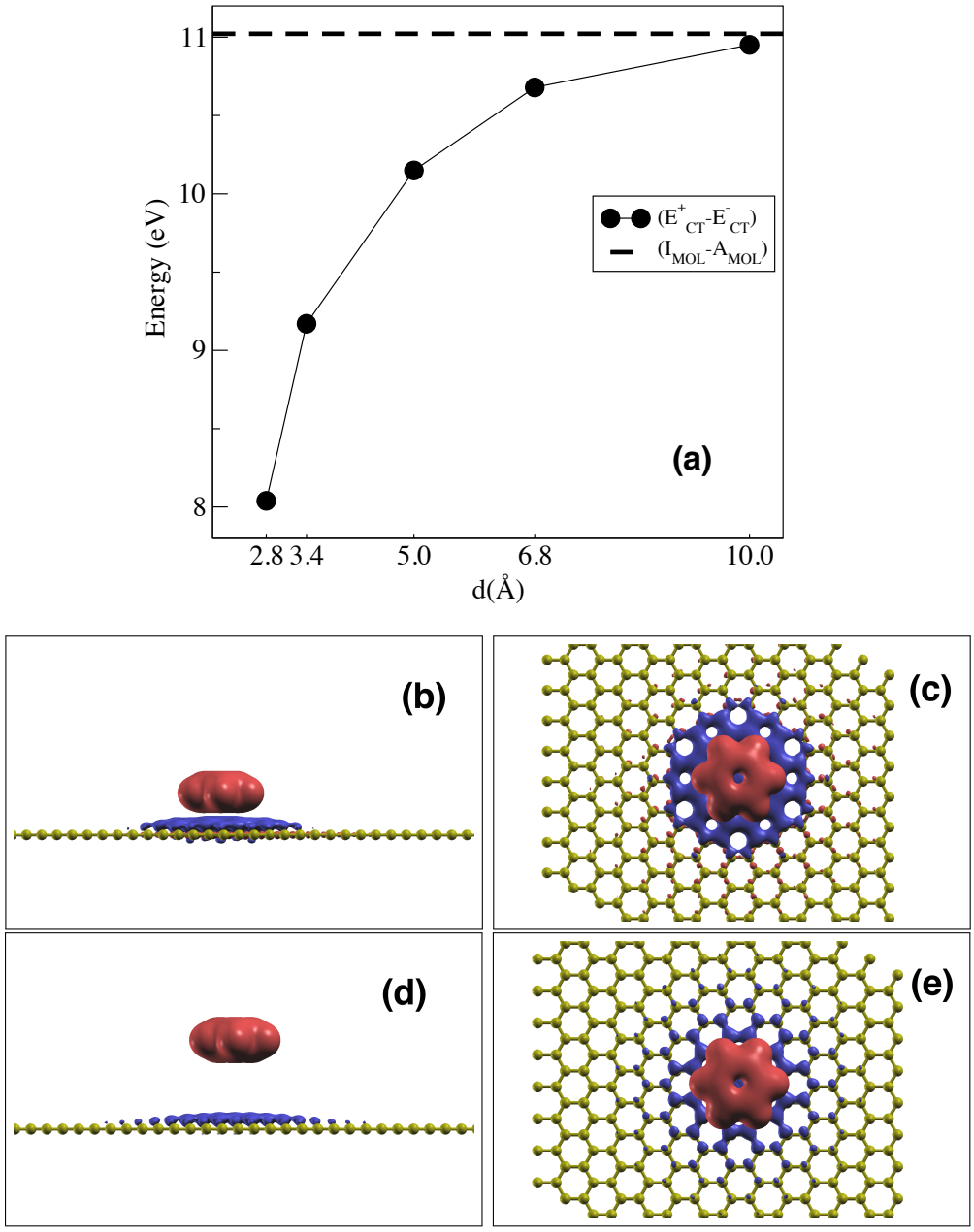

Figure 4.9: Panel (a) shows the charge transfer energy gap of a benzene molecule as a function of its height from the graphene sheet, plotted along with the QP gap of the isolated molecule. Panels (b) and (c) show the excess charge in different parts of the system after the transfer of an electron from the molecule to the sheet for $d = 3.4$ Å. Panels (d) and (e) show the same plot but for $d = 6.8$ Å. In both cases, red and blue denote isosurfaces of positive and negative net charge, respectively.

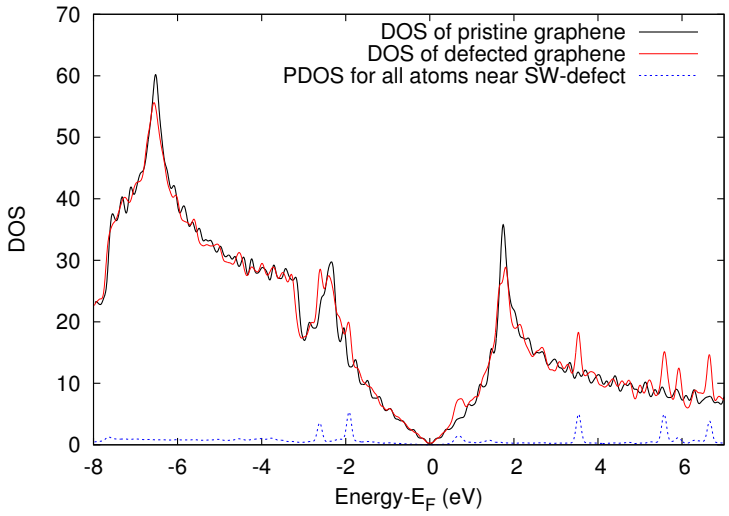

Figure 4.10: DOS of pristine graphene and of a graphene sheet with one SW defect. The PDOS for the atoms near the SW defect are plotted on the same graph. These calculations are performed with a supercell of 200 atoms.

Configuration	$E^{+}_{\mathrm{CT}}(d)(eV)$	$E^{+}_{\mathrm{CT}}(d)(eV)$
Top	4.30	-4.78
Away	4.34	-4.83
Hollow	4.32	-4.81
Stack	4.33	-4.81

Table 4.1: E^{+}_{CT} and E^{-}_{CT} for various aforementioned configurations of benzene physisorbed on graphene.

almost completely unchanged near its Fermi energy after the introduction of such defect as can be seen in Fig. 4.10, which shows that the partial density of states (PDOS) of the atoms affected by the SW defect have no significant presence near the Fermi level. Thus, after charge transfer, the electron added to (or removed from) the graphene sheet has the same energy that it would have in the absence of the defect. In this context, it is noteworthy that a G_0W_0 study [114] has concluded that altering the structure of pristine graphene by introducing dopant (which raises the Fermi level of graphene by 1 eV) also has minor effect on the QP gap of benzene, reducing it by less than 3%.

4.5.5 Effect of the Presence of Other Benzene Molecules

In real interfaces between organic crystals and substrates, the molecule is usually not isolated but found in proximity of other similar molecules. Hence, we investigate the effect of the presence of other benzene molecules near the one under consideration. To this end we selected three representative configurations. In the first one (DB1), the graphene sheet has two benzene molecules above it, one at 3.4 Å and another at 6.8 Å. We calculate the charge transfer energies of the middle benzene (3.4 Å from the sheet). The charge excess on different parts of the system, after transferring one electron to the sheet, is displayed in Fig. 4.11 (top panel). The second configuration (DB2) investigated is identical to the first one but we calculate the charge transfer energies of the molecule, which is farther from the graphene sheet, namely at a distance of 6.8 Å. For this configuration, the excess charge after a similar charge transfer is shown in Fig. 4.11(middle panel). In the third configuration (LB), we use multiple benzene molecules in the same plane. The molecules are in close proximity with each other although their atomic orbitals do not overlap. CT energies are calculated with respect to one benzene molecule keeping the others neutral and an isovalue plot for similar charge transfer is shown in Fig. 4.11 (bottom panel). The CT energies are shown in Tab. 4.2. In order to facilitate comparison, we also present the $E^{\pm}_{\mathrm{CT}}$ values for the cases of a single benzene adsorbed on graphene at 3.4 Å (SB1) and 6.8 Å (SB2) in the hollow configuration. We find that the presence of another molecule nearby does not bring about any significant change in the charge transfer energies. This is evident from the results presented in Tab. 4.2. However, in both cases one can see a slight reduction in the absolute value of the charge transfer energies and this can be explained in terms of simple classical effects. For the case of DB1, when one transfers an electron from the middle benzene to the graphene, the charge neutral and polarized topmost benzene can be thought of as a dipole with its moment pointing away from the other molecule. Hence, in principle, the presence of this dipole should lower the potential at the site of the other molecule and the sheet both. However, since the potential due to a dipole is inversely proportional to the square of the distance, this effect is more pronounced at the site of the middle benzene than at that of the graphene sheet. A similar effect can

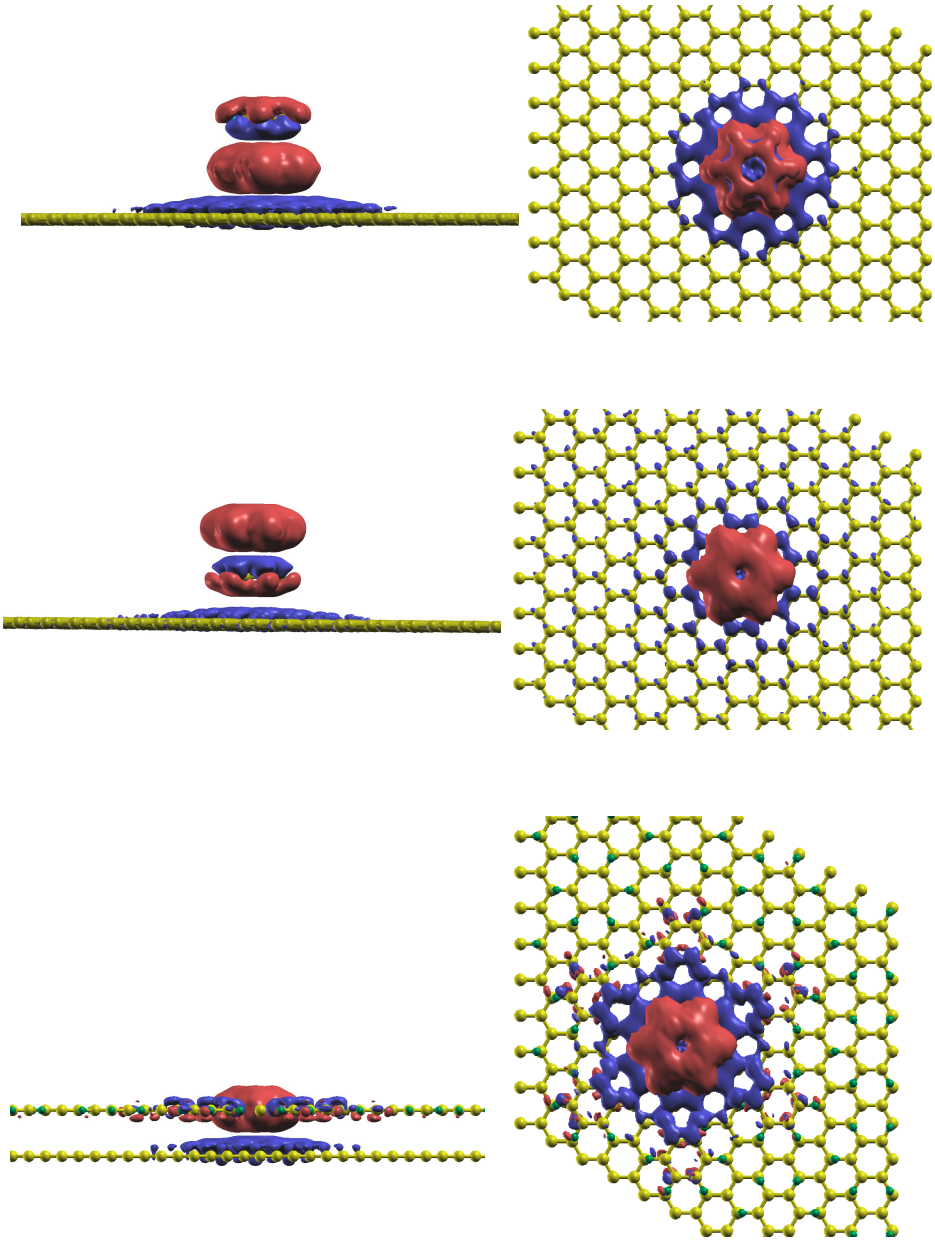

Figure 4.11: The left and right panels show respectively the side view and the top view of the isovalue of $\Delta\rho(\mathbf{r})$ after transferring one electron from the molecule to the sheet. The top, middle and bottom plots correspond to the H_{M1}, H_{M2} and H_L configurations respectively (see main text).

Configuration	$E^{+}_{\mathrm{CT}}(d)(eV)$	$E^{+}_{\mathrm{CT}}(d)(eV)$
DB1	4.12	-4.76
LB	4.27	-4.62
SB1	4.32	-4.81
DB2	4.73	-5.64
SB2	4.95	-5.72

Table 4.2: E^{+}_{CT} and E^{-}_{CT} for various configurations of the benzene molecule on pristine and defective graphene.

be observed for electron transfer from the graphene sheet to the middle benzene. Thus, the charge transfer energies of the molecule decrease due to the presence of another benzene on top of it. A similar effect is present in the case LB. For the case of DB2, the system consisting of the topmost benzene (from which we transfer charge) and the sheet can be thought of as a capacitor. The work, W, done to transfer Q charge from one plate to another of a capacitor is given by $\frac{Q^2}{2C}$, where C is the capacitance proportional to the dielectric constant of the medium between the capacitor plates. Hence, instead of vacuum (as in SB2), if we have another benzene molecule in the intermediate space, the molecule acts as a dielectric resulting in a reduction of W. Therefore, the charge transfer energies for DB2 are smaller than those for SB2.

4.5.6 Classical Image Charge Model

It is worth checking how our results for the renormalization of molecular levels with change of the height compares with classical electrostatics. Let us imagine an infinite substrate plane of relative permittivity ϵ in the x-y plane and a point charge q at a distance z above it. Due to presence of the point, some bound surface charge, $\sigma_b(\mathbf{r})$, will be induced on the substrate. Considering a linear dielectric, this must be given by

$$\sigma_b(\mathbf{r}) = \mathbf{P}(\mathbf{r}).\hat{\mathbf{n}} = \epsilon_0 \chi_e \mathbf{E}(\mathbf{r}).\hat{\mathbf{n}} = \epsilon_0 \chi_e E_z(\mathbf{r}),$$

where $\mathbf{P}(\mathbf{r})$ and $\mathbf{E}(\mathbf{r})$ denote the electrical polarization and the electric field respectively and χ_e is the electric susceptibility of the substrate. Here, $\hat{\mathbf{n}}$ denotes the unit normal

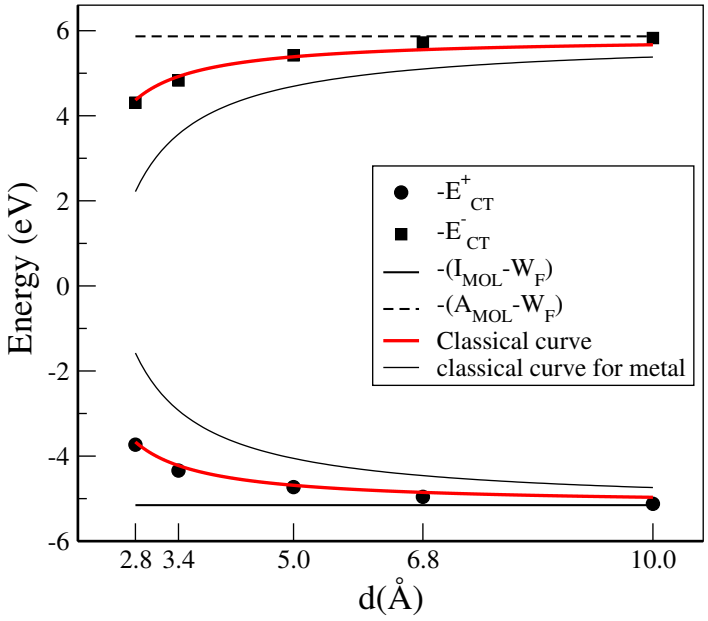

Figure 4.12: $-E^{+}_{\mathrm{CT}}$ (circles) and $-E^{-}_{\mathrm{CT}}$ (squares) for different heights of the molecule from the substrate. The CDFT results are seen to agree well with the classically calculated curve given in red. The horizontal lines mark the same quantities for an isolated molecule (gas-phase quantities). The continuous thin line shows the position of the classically calculated level curve for adsorption on a perfect metal $\epsilon = \infty$

pointing out of the surface. All quantities are referred to on the surface, with $\mathbf{r}$ the planar radial coordinate.

Now, there are two distinct charge distributions generating $E_z(\mathbf{r})$. The component due to the point charge is given by

$$E^1_z(\mathbf{r}) = -\frac{1}{4\pi\epsilon_0}\frac{qz}{(r^2+z^2)^{3/2}},$$

while that due to the bound charge distribution itself is given by

$$E^2_z(\mathbf{r}) = -\frac{\sigma_b(\mathbf{r})}{2\epsilon_0}.$$

By combining the three equations together we obtain

$$\sigma_b(\mathbf{r}) = \epsilon_0\chi_e[-\frac{1}{4\pi\epsilon_0}\frac{qz}{(r^2+z^2)^{3/2}}] - \frac{\sigma_b(\mathbf{r})}{2\epsilon_0}.$$

By solving for $\sigma_b(\mathbf{r})$ one has

$$\sigma_b(\mathbf{r}) = -\frac{1}{2\pi}\left(\frac{\chi_e}{\chi_e+2}\right)\frac{qz}{(r^2+z^2)^{3/2}}.$$

The field at point P=(r=0,ϕ=0,z) due to this surface charge distribution is in the z-direction. Its magnitude is given by:

$$F = \frac{1}{4\pi\epsilon_0}\int_0^\infty \frac{\sigma_b(\mathbf{r})2\pi r dr}{(r^2+z^2)^{3/2}}\cos\theta,$$

where θ is the angle between the two straight lines joining P with $(r=0,\phi=0,z=0)$ and P with $(r,\phi=0,z=0)$. The integration gives us

$$F = \frac{1}{4\pi\epsilon_0}\left(\frac{\chi_e}{\chi_e+2}\right).\frac{q^2}{4z^2}$$

Hence, the work done for bringing the point charge from an infinite distance to a height d above the surface is

$$W(d) = -\int_\infty^d F dz = -\frac{1}{4\pi\epsilon_0}\left(\frac{\chi_e}{\chi_e+2}\right).\frac{q^2}{4z}.$$

Clearly, this is the work done by the induced image charge to bring one electron from an infinite distance to the position of the molecule. However, in reality, the image charge will not confine itself strictly to a 2D plane and will form a lump on top of the surface instead. In order to account for such non-planar image-charge distribution, one can introduce a small modification to the above expression [116] and approximate $W(d)$ at a height d as

$$\begin{aligned} W(d) &= -\frac{1}{4\pi\epsilon_0}\left(\frac{\chi_e}{\chi_e+2}\right)\frac{q^2}{4(d-d_0)}, \\ &= -\frac{1}{4\pi\epsilon_0}\left(\frac{\epsilon-1}{\epsilon+1}\right)\frac{q^2}{4(d-d_0)}, \end{aligned}$$

where d_0 is the distance between the centre of mass of the image charge and the substrate plane. Now,

E_{CT}^{-} =-Energy for transferring one electron from substrate to molecule

=-(Energy for transferring one electron from infinity to molecule + E_F).

Hence, one can conclude that

$$E_{\mathrm{CT}}^{-} = \text{-}LUMO \text{ of the isolated molecule -}W(d) - E_F.$$

A similar argument for the HOMO level shows an elevation of same magnitude due to the presence of the substrate. In Fig. 4.12 we plot the CT energies and show that they compare quite well with the two curves calculated with the classical approximation with an effective dielectric constant of 2.4 [117] for graphene. For the latter calculation, we have used an approximate value $d_0 = 1.7$ Å, which is a good estimate for smaller distances. It is worth noting that for higher distances, though the actual value of d_0 should be much less, the overall effect of d_0 is very small and almost negligible.

Summary

We have used the method of cDFT implemented in SIESTA to calculate the CT energies of benzene molecule adsorbed on a sheet of graphene. We have shown that this energy depends on the distance between the molecule and the graphene sheet. If the molecule is very close to the graphene sheet, the Coulomb interaction between the two entities is large after the transfer of charge. This leads to a very localised image charge on the graphene sheet and a considerable reduction of the CT energy gap from the quasiparticle gap of the isolated molecule. However, as the distance increases, this gap keeps increasing and finally becomes equal to the isolated quasiparticle gap of benzene at infinite separation. We have also shown that the presence of simple structural defect, such as Stone-Wales defect on graphene does not significantly alter the CT energies. Also, the presence of another benzene molecule close to the one under consideration affects the CT energies only weakly.

Chapter 5

Constrained DFT with accurate ionic forces applied to the reorganization energy of graphene-adsorbed pentacene

5.1 Introduction

In many flavours of electronic structure theory calculations, such as cDFT [87, 88], DFT+U [118, 119], DFT+DMFT [120, 121], wave function-embedding methods [122, 123], various perturbative approaches in quantum chemistry [124] etc., the population of a particular subspace is important and the total energy depends explicitly on it. Thus, the ability to properly define and to calculate the population of a subspace is of great importance. This is exemplified by the sustained efforts in recent years toward the development of physically-motivated orbitals such as MLWF [125], nonorthogonal localized molecular orbital (NOLMO) [126], muffin-tin orbital (MTO) [127], natural bond orbitals (NBO) [124] etc., which are typically tuned for population analysis. Such population analysis through projection on subspaces has received a great deal of attention in recent years [128, 129] ranging from studies on tensorially correct scheme of projection [130] to effects of choice of projection for DFT+U [131] and DFT+DMFT [132] methods.

The trace of a matrix will not be invariant if the basis set is non-orthogonal. Therefore if an operator is written with respect to a non-orthogonal basis, the trace will not represent any physically meaningful quantity. Hence, for non-orthogonal orbitals, the population of a subspace cannot be calculated simply as the sum of the elements of density matrix over the orbitals spanning the subspace and one requires advanced tools for population analysis. When the energy of the system depends on such population, the problem presents additional challenges. If terms in the total energy are constructed from orbitals (e.g. atomic) that are tied to atomic centres then, when those orbitals move explicitly with ionic position, Pulay terms[1] arise in the Hellmann-Feynman forces. This is true regardless of whether the orbitals are orthonormal or not. What is less known, but which has been identified in the past with some progress [133], is that additional Pulay terms must be considered in cases where the degree of orbital nonorthogonality affects the total-energy. This occurs, whenever the energy depends on a nonorthogonality-respecting multi-centre projection of the density or Kohn-Sham density-matrix. It also occurs when using orthonormalised orbitals built from an underlying non-orthogonal set, since an ionic movement will typically break the orthornormality and render the orthonormalisation futile. Here we show that if we use the tensorially correct method of treating the population as a contraction of the density operator over kets and duals localized in the subspace [133], then we can have a simple and exact expression for the force without any need of constructing orthogonal orbitals.

An accurate population analysis treatment, with related forces, enables us to study reorganisation effects in large, constrained systems, such as those relevant to charge-transfer excitations in photovoltaic active layers, in heterogeneous photocatalysis, the reorganisation effect on the magnetic coupling of magnetic dimers, etc. In what follows we will focus on a particularly challenging example related to this thesis, namely that of calculating the reorganization energy of a molecule adsorbed on a surface.

[1] Terms containing derivatives of the orbitals themselves.

5.2 Physical Problem Investigated

The ionic coordinates of any system depends on its electronic occupation. If an electron is removed from a neutral system, such as in photoemission spectroscopy, its ionic coordinates readjust to the new geometry due to the local electron-phonon coupling [63, 64]. Figure 5.1 shows two parabolic curves corresponding to the energy of a neutral system and the same system after the removal of an electron, as a function of some generic atomic coordinate. For the neutral system, λ^0 is the difference in energy between the ground state geometry and the ground state geometry of the charged configuration [49]. In contrast, λ^+ is the same quantity but for the system with one less electron. Then, the re-organization energy, λ, of the system corresponding to removal of one electron is defined as:

$$\lambda = \lambda^0 + \lambda^+. \tag{5.1}$$

This quantity holds paramount importance in charge transport calculations. In the semi-classical Marcus' theory approach [65], in the high temperature regime, the probability per unit time of an electron hopping is computed according to Fermi's golden rule as [134, 135]

$$k_{ET} = \frac{|\langle i|\hat{H}|f\rangle|^2}{\hbar}\sqrt{\frac{\pi}{\lambda k_B T}}exp\left[-\frac{(\lambda+\Delta G^0)^2}{4\lambda k_B T}\right], \tag{5.2}$$

where $\hat{H}$ is the Hamiltonian, $|i\rangle$ and $|f\rangle$ are the initial and final electronic states respectively, ΔG^0 and λ are the change in Gibbs' free energy and the reorganization energy associated with the charge transfer, respectively. Thus we see that the re-organization energy is an important ingredient for the calculation of the hopping. In this work we calculate the re-organization energy of a pentacene molecule, that, in the crystal form, is a well known organic semiconductor. Due to its high HOMO level, pentacene is a p-type semiconductor [136] and has high hole-mobility [137]. Thus, the re-organization energy for ionization is of great interest.

This has been subject of several theoretical and experimental studies in the past [138, 139, 140]. In a recent experimental work [141], it has been shown that the reorganization energy of a molecule increases upon adsorption on a surface. The theoretical approach can be either that of directly calculating the energy difference from the adiabatic potential energy surface or one of indirectly calculating the various normal modes that constitute the reorganization energy [142]. In this work we adopt the former approach. For an isolated pentacene, an electron removal can be simulated with regular DFT and therefore does not require the aforementioned force corrections. However, when the molecule is adsorbed on a substrate whose Fermi level lies above the HOMO of the molecule, the application of cDFT becomes necessary. cDFT can simulate the photoemission event of removing an electron from the system and constraining the extra charge to the subspace of the orbitals of the molecule. cDFT has been widely applied to study charge transfer in organics [143, 144, 145, 146] and, in particular has been used to simulate removal or addition of electrons from adsorbed molecule in the context of calculating charge transfer energies [109, 147]. In this chapter we use cDFT in conjunction with self-consistent forces to calculate the re-organization energy of a pentacene molecule adsorbed on a flake of graphene. A very similar system, consisting of a film of weakly bound pentacene molecules adsorbed on highly oriented pyrolytic graphite (HOPG) has been the subject of several theoretical and experimental studies [141, 148, 149].

5.3 Method

5.3.1 Theory

As mentioned earlier, in cDFT one tries to find the ground state of the system subject to constraining a fixed number of electrons in a desired subspace C. This has the following mathematical form,

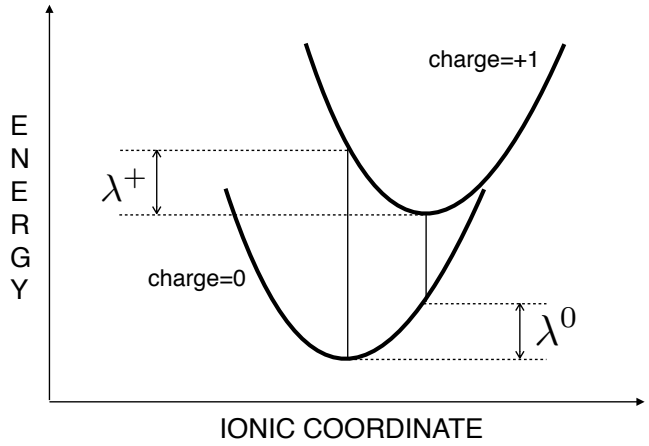

Figure 5.1: Schematic diagram of the energy as a function of the ionic coordinates for a charged and a neutral system. The re-organization energy is defined as $\lambda^0 + \lambda^+$.

$$\mathrm{Tr}[\hat{\rho}\hat{\mathbb{P}}] = N_c \tag{5.3}$$

where $\hat{\rho}$ is the density operator, $\hat{\mathbb{P}}$ is projection operator on the subspace and N_c is the number of electrons one wishes to constrain to the subspace. In order to find the density corresponding to this constrained ground state one finds the stationary point of $W[\rho, V_c]$ [87], where V_c is a Lagrange multiplier and

$$W[\rho, V_c] = E[\rho] + V_c \left(\mathrm{Tr}[\hat{\rho}\hat{\mathbb{P}}] - \mathrm{N_c}\right). \tag{5.4}$$

The stationary point of this function yields the ground state density of the system subject to the given constraint. At the stationary point, $W[\rho, V_c] = E[\rho]$, since the quantity in the brackets in Eq. (5.4) vanishes. Clearly, $E[\rho]$ is not stationary at this density and hence Hellmann-Feynman theorem cannot be applied to $E[\rho]$ at the cDFT ground state. However, it can be applied to $W[\rho, V_c]$ to find the force,

$$F_i = -\frac{dW}{dR_i} = -\frac{\partial W}{\partial R_i}, \tag{5.5}$$

where the index "i" incorporates the index of an ion and a spatial direction. At the stationary point, since $\left(\mathrm{Tr}[\hat{\rho}\hat{\mathbb{P}}] - \mathrm{N_c}\right) = 0$, the above equation reduces to:

$$F_i = -\frac{\partial E[\rho]}{\partial R_i} - V_c \frac{\partial}{\partial R_i} \mathrm{Tr}[\hat{\rho}\hat{\mathbb{P}}]. \tag{5.6}$$

The first term on the right hand side, $F_{i(DFT)}$, is the contribution from regular DFT [150], while the second term, $F_{i(cDFT)}$, represents the extra force due to the constraint. We devote the rest of the theory subsection to finding an exact expression for this term.

5.3.1.1 Population Analysis

In the widely used implementation of the Löwdin population analysis, a set of orthogonal functions $\{\tilde{\phi}_\mu(\mathbf{r})\}$, for the given subspace are generated for the non-orthogonal basis function $\phi_\mu(\mathbf{r})$ and the population is given by (see eq. (3.69))

$$\mathrm{Tr}[\hat{\rho}\hat{\mathbb{P}}] = \sum_{\mu,\nu} \langle\phi_\mu|\hat{\rho}|\phi_\nu\rangle \sum_{\mathrm{i}\in\mathrm{C}} \mathbf{S}^{-\frac{1}{2}}_{\nu\mathrm{i}} \mathbf{S}^{-\frac{1}{2}}_{\mathrm{i}\mu},$$

where $S_{\mu i}$ is an element of $\mathbf{S}$, the overlap matrix of the full system with μ being the basis vector index from all space and i being that from the given subspace, C. Note that for non-zero overlap between the non-orthogonal basis functions within the subspace and those outside it, the functions $\tilde{\phi}_i(\mathbf{r})$ are in principle delocalized over the entire system. Clearly, the above equation produces terms like $\frac{\partial}{\partial R_j}(S^{-1/2}_{\nu i})$ in the expression for the forces. Such terms are difficult to calculate. One possible exact expression for such terms requires diagonalizing the overlap matrix and therefore is incompatible with linear scaling concepts [151]. Also, this treatment can not be applied in case of complex valued projectors. Attempts have been made to approximate S by a diagonal matrix by using special linear combination of atomic orbitals as the projectors [133] although, as pointed out in the same paper, this is not possible in all situations.

For our population analysis, we define the subspace population as a tensor contraction over $\{|\varphi_m\rangle\}$, which is the set of non-orthogonal projectors spanning the subspace and $\{|\varphi^m\rangle\}$ which is the set of bi-orthogonal compliments. These are known as duals of the projectors such that $\langle\varphi^m|\varphi_{m'}\rangle = \delta^m_{m'}$ and $\hat{\mathbb{P}} = \sum_m |\varphi^m\rangle \langle\varphi_m|$ [130]. Then the projector and its dual are related by [152]

$$|\varphi^m\rangle = |\varphi_{m'}\rangle\, O^{m'm}, \tag{5.7}$$

where $O^{m'm}$ is the (m', m)-th element of the matrix $\mathbf{O}^{-1}$ and $\mathbf{O}$ is the square overlap matrix within the subspace with matrix elements $O_{mn} = \langle\varphi_m|\varphi_n\rangle$[2]. These duals are localized in the spatial region of interest. Then, the trace in Eq. (7.12), which essentially gives the number of electrons in the selected subspace can be written as,

$$\begin{aligned} \mathrm{Tr}[\hat{\rho}\hat{\mathbb{P}}] &= \langle\varphi_m|\,\hat{\rho}\,|\varphi^m\rangle\,, \\ &= \langle\varphi_m|\,\hat{\rho}\,|\varphi_{m'}\rangle\, O^{m'm}. \end{aligned} \tag{5.8}$$

This trace is obtained with a proper contraction of the contravariant and covariant indices and hence represents a tensorially invariant and physically meaningful occupancy [153].

5.3.1.2 Evaluation of Force

Inserting Eq. (5.8) in Eq. 5.6 we obtain

$$F_i = F_{i(DFT)} - V_c \left[\langle \frac{\partial\varphi_m}{\partial R_i}|\hat{\rho}|\varphi_{m'}\rangle\, O^{m'm} + \langle\varphi_m|\hat{\rho}|\frac{\partial\varphi_{m'}}{\partial R_i}\rangle\, O^{m'm} + \langle\varphi_m|\hat{\rho}|\varphi_{m'}\rangle\, \frac{\partial O^{m'm}}{\partial R_i} \right]. \tag{5.9}$$

The first and the second term in the square bracket on the right-hand side represent the force due to the change in the projectors as a result of the ionic displacements, while the third term represents that due to a change in the mutual overlap of the projectors. If the projectors are localized orbitals centred on the atoms, then the third term is exclusively due to the relative motion of the atoms corresponding to the

[2]note that unlike $\mathbf{S}$, which is the overlap of the basis orbitals over all space, $\mathbf{O}$ is overlap of projectors over the desired subspace.

subspace. For orthogonal basis functions, if orthonormality is preserved under ionic motion, this term will vanish. Now we evaluate the three terms in the square bracket. The first term gives,

$$\begin{aligned}
&\langle\frac{\partial\varphi_m}{\partial R_i}|\hat{\rho}|\varphi_{m'}\rangle\, O^{m'm} = \\
=&\langle\frac{\partial\varphi_m}{\partial R_i}|\hat{\rho}|\phi_\alpha\rangle\,\langle\phi^\alpha|\varphi_{m'}\rangle\, O^{m'm} = \\
=&\mathrm{Tr}[\hat{X}\hat{\rho}],
\end{aligned} \tag{5.10}$$

where the operator $\hat{X}$ is defined as $\hat{X} = |\varphi_{m'}\rangle\, O^{m'm}\,\langle\frac{\partial\varphi_m}{\partial R_i}|$. Similarly, the second term within the square bracket in Eq. (5.9) is $\mathrm{Tr}[\hat{X^\dagger}\hat{\rho}]$. For evaluating the third term we shall use the following matrix identity for a generic matrix $\mathbf{M}$,

$$\begin{aligned}
\mathbf{0} &= \frac{d}{dR}[\mathbf{M}\mathbf{M}^{-1}], \\
&= \frac{d\mathbf{M}}{dR}\mathbf{M}^{-1} + \mathbf{M}\frac{d(\mathbf{M}^{-1})}{dR}, \\
&= \mathbf{M}^{-1}\frac{d\mathbf{M}}{dR}\mathbf{M}^{-1} + \frac{d(\mathbf{M}^{-1})}{dR}, \\
\text{Then } \frac{d(\mathbf{M}^{-1})}{dR} &= -\mathbf{M}^{-1}\frac{d\mathbf{M}}{dR}\mathbf{M}^{-1}.
\end{aligned} \tag{5.11}$$

This, explicitly reads as $\frac{\partial}{\partial R_i}M^{m'm} = -M^{m'\mu}\frac{\partial M_{\mu\nu}}{\partial R_i}M^{\nu m}$. Using such an identity for the overlap matrix $\mathbf{O}$, the third term of Eq. (5.9) can be rewritten as

$$\begin{aligned}
&\langle\varphi_m|\hat{\rho}|\varphi_{m'}\rangle\,\frac{\partial O^{m'm}}{\partial R_i} = \\
=&-\langle\varphi_m|\hat{\rho}|\varphi_{m'}\rangle\, O^{m'\mu}\left[\langle\frac{\partial\varphi_\mu}{\partial R_i}|\varphi_\nu\rangle + \langle\varphi_\mu|\frac{\partial\varphi_\nu}{\partial R_i}\rangle\right] O^{\nu m} = \\
=&-\langle\varphi_\mu|\frac{\partial\varphi_\nu}{\partial R_i}\rangle\, O^{\nu m}\,\langle\varphi_m|\hat{\rho}|\varphi_{m'}\rangle\,\langle\varphi^{m'}|\varphi^\mu\rangle + c.c. = \\
=&-\mathrm{Tr}[\hat{X}^\dagger\hat{\rho}\hat{\mathbb{P}}] + c.c.
\end{aligned} \tag{5.12}$$

Now, by bringing all the terms together, the additional force due to the constraint is,

$$
\begin{aligned}
&F_{i(cDFT)} = \\
&= -V_c \left(\mathrm{Tr}[\hat{X}\hat{\rho}] + \mathrm{Tr}[\hat{X}^\dagger\hat{\rho}] - \mathrm{Tr}[\hat{X}^\dagger\hat{\rho}\hat{\mathbb{P}}] - \mathrm{Tr}[\hat{X}\hat{\rho}\hat{\mathbb{P}}] \right) \\
&= -2V_c \mathbb{R}\mathrm{Tr}\left[\hat{\rho}\hat{X}(\hat{\mathbb{1}} - \hat{\mathbb{P}}) \right].
\end{aligned} \tag{5.13}
$$

The additional force ($F_{i(cDFT)}$) in a cDFT calculation arises due to change in population ($\mathrm{Tr}[\hat{\rho}\hat{\mathbb{P}}]$) of the cDFT subspace due to movement of atoms. So, orbital movements which do not change the subspace population, should not contribute to F_i^c. This is the interpretation for the subtraction of the term $\hat{\rho}\hat{X}\hat{\mathbb{P}}$ from the term $\hat{\rho}\hat{X}$. Noting that $\hat{X}\hat{\mathbb{P}}$ contains a projection of the orbital derivative $\left(\frac{\partial\varphi_m}{\partial R_i}\right)$ over the cDFT subspace, we can say that only those Pulay terms, for which the orbital derivative goes beyond the cDFT subspace and results in variation of the population, should contribute. This is why the projection inside the cDFT subspace (the $\hat{\rho}\hat{X}\hat{\mathbb{P}}$ term) is subtracted from the total Pulay term (the $\hat{\rho}\hat{X}$ term).

This expression for the force under a charge constraint has been implemented in the linear-scaling code ONETEP [96]. For a DFT calculation, ONETEP optimizes the non-orthogonal generalized Wannier functions (NGWFs) with conjugate-gradients method and within each iteration of such optimization, it minimizes [98] the KS energy functional with respect to the density kernel $K^{\alpha\beta}$. This constructs the single-particle density matrix as $\rho(\mathbf{r},\mathbf{r}') = \phi_\alpha(\mathbf{r})K^{\alpha\beta}\phi^*_\beta(\mathbf{r}')$ [97](see section 3.4.3). Thus, for a geometry optimization in presence of a constraint of the form in Eq. 5.3, one needs to run the following optimization loops in the order shown in Fig. 5.2.

1. optimization of the system geometry
2. optimization of the NGWFs $\{\phi_\mu\}$
3. optimization of the cDFT Lagrange multiplier V_c
4. optimization of the density kernel $K^{\alpha\beta}$

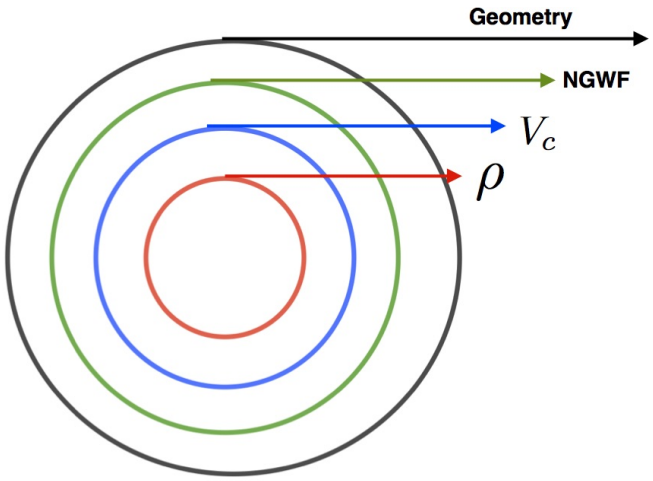

Figure 5.2: Relative position of the optimization loops in a ONETEP calculation involving atomic relaxation in presence of constrained charges.

5.3.2 Procedure for the Calculation

The scheme we follow for calculating the reorganization energy of a pentacene molecule adsorbed on a flake of graphene is highlighted bellow:

1. Optimize the geometry of the neutral system and calculate the GS energy with a DFT run. This gives the geometry G_1 and the energy $E1_{\mathrm{NEUT}}$.

2. Run cDFT for pentacene with a unit positive charge with geometry G_1 to obtain the energy $E1_{\mathrm{POS}}$.

3. Run a constrained geometry optimization to find the nuclear coordinates for the charged pentacene and the corresponding energy. This gives us a geometry G_2 and an energy $E2_{\mathrm{POS}}$.

4. Run DFT on neutral pentacene with geometry G_2 to find the energy $E2_{\mathrm{NEUT}}$ of the neutral system in the geometric configuration corresponding to the charged state.

The reorganization energy λ is then given by

$$\begin{aligned}\lambda &= \lambda^0 + \lambda^+, \\ &= (E2_{\mathrm{NEUT}} - E1_{\mathrm{NEUT}}) + (E1_{\mathrm{POS}} - E2_{\mathrm{POS}}).\end{aligned} \tag{5.14}$$

The calculations have been performed with the PBE [94] exchange-correlation functional and norm-conserving pseudopotentials with the ONETEP code. The switching from SIESTA to ONETEP package is primarily motivated by the fact that our desired population analysis (see Eq. 5.8) is already implemented in ONETEP. The NGWF radius is set to 9 Å. It was found that a very high plane-wave cutoff energy of 1500 eV is needed to avoid small changes in energy due to the eggbox effect. cDFT optimization is performed with a conjugate-gradient technique with the convergence threshold of 10^{-5} for the Lagrange multiplier gradient. This translates to an error of $< 4\text{x}10^{-4}\%$ in the population of the pentacene molecule. Geometry relaxation is performed with a quasi-Newton method [154] using a Broyden-Fletcher-Goldfarb-Shanno algorithm [155] with Pulay corrected forces and an energy convergence threshold of 2.5×10^{-6} eV per atom. Some additional features employed in our calculations are as follows.

Ensemble DFT. For a system with a large number of eigenstates in the vicinity of the Fermi level, the occupation numbers of these states are ill-conditioned. In other words, significant fluctuations in these occupation numbers and in the electron density can occur with a tiny change in energy and therefore the number of self-consistent steps necessary for locating the converged ground state can be large. In order to circumvent this problem, we employ the finite temperature ensemble DFT (EDFT) formalism [156, 157] which, instead of minimizing the energy of the system aims of minimizing the Helmholtz free energy

$$\begin{aligned}A[T, \{\epsilon_i\}, \{|\psi_i\rangle\}] &= \sum_i f_i \langle\psi_i| - \frac{1}{2}\nabla^2 |\psi_i\rangle \\ &+ \int d\mathbf{r} v_n(\mathbf{r})\rho(\mathbf{r}) + J[\rho] + E_{xc}[\rho^\alpha, \rho^\beta] - TS[\{f_i(\epsilon_i)\}].\end{aligned} \tag{5.15}$$

Here $S[\{f_i\}]$ is the entropy of the system given by

$$S[\{f_i\}] = -k_B \sum_i [f_i \ln f_i + (1 - f_i)\ln(1 - f_i)] \tag{5.16}$$

and the occupation number $f_i(\epsilon_i)$ is that of the i^{th} KS state and follows the Fermi-Dirac distribution

$$f_i(\epsilon_i) = \left(1 - \exp\left[\frac{\epsilon_i - \mu}{k_B T}\right]\right)^{-1}. \tag{5.17}$$

We use a temperature of 300K for our calculations.

Correction for periodic boundary conditions. Since ONETEP uses fast Fourier transform to solve the Poisson's equation, it always uses periodic boundary condition. For isolated systems it does so by constructing artificial periodic replicas of the simulation cell. This gives rise to undesired interactions between the unit cells. In order to correct this, we use the Martyna-Tuckerman scheme [158] of replacing the Coulomb interaction from the periodic images of the simulation cell with a minimum image convention technique. This essentially adds a screening potential term to cancel the Coulomb interactions from neighbouring cells [159]. We use a Martyna-Tuckerman convergence parameter [158] of 7.0 in our calculations.

Dispersion correction. Dispersion interactions, which are poorly accounted for in the popular XC-functionals, are expected to be present between the pentacene molecule and the graphene flake. Hence use an empirical correction $E_{disp}(r_{ij})$ on the total energy in the form of a damped London term summed over all pairs of atoms (i,j) with interatomic distance of r_{ij}

$$E_{disp}(r_{ij}) = -\sum_{ij, i>j} f_{damp}(r_{ij}) \frac{C_{6,ij}}{r_{ij}^6}, \tag{5.18}$$

where the damping term is given by [160]

$$f_{damp}(r_{ij}) = (1 - \exp(-c_{\text{damp}}(r_{ij}/R_{0.ij})^7))^4 \tag{5.19}$$

The parameters we use have been obtained and implemented previously by fitting a set of 60 complexes with significant dispersion [161].

5.4 Results

5.4.1 Test of the Forces on Isolated Pentacene

In order to show the role and necessity of the term due to the change in the overlap of the projectors spanning the subspace, $(-V_C \langle\varphi_m|\hat{\rho}|\varphi_{m'}\rangle \partial O^{m'm}/\partial R_i)$, in the expression for the forces [see Eq. (5.9)], we first present some tests on a very simple system consisting of a single isolated pentacene molecule. Starting from some commong initial geometry, we run three independent relaxations:

1. A **No constraint (DFT)** run, i.e. a regular relaxation where the force is $F_i = F_{i(DFT)}$.

2. Adding a constant constraining potential V_c to the entire space and relaxing **without force correction** for the change in overlap. This means that, in the expression for force, the last term in Eq. (5.9) is ignored.

3. Adding a constant constraining potential V_c to the entire space and relaxing **with force correction**, i.e. with force given by Eq. (5.9).

A constant constraining potential on the full Kohn-Sham space should in principle have no other effect than giving rise to a rigid shift of all the energy levels, and therefore should not affect the geometry optimization in any way. In this case, a full set of atomic pseudo orbitals for the initial geometry of the neutral pentacene molecule were used as projector orbitals. As a result, we may expect some deviation from perfect potential uniformity to arise in the constraining potential in the Kohn-Sham space of the molecule, and even more so as its geometry evolves. Therefore, at convergence we expect the behaviour of the third run to be similar to that of the first run since they are

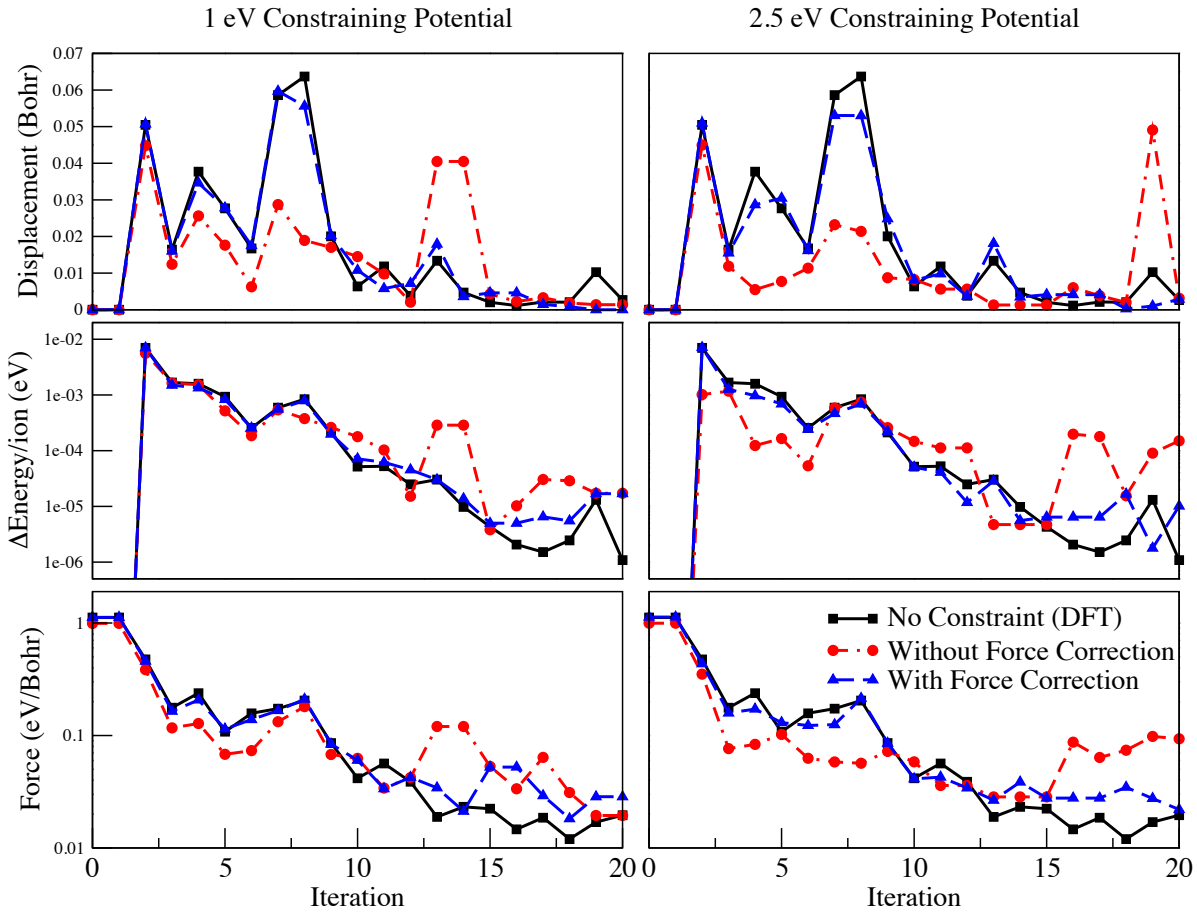

Figure 5.3: Maximum displacement, change in energy per atom and maximum force plotted against the iteration number in a geometry relaxation calculation. The black, blue and red curves show the plots for a regular DFT run, a constrained run with properly corrected forces and one without the proper correction for forces respectively. The constrained calculations are performed with a constant potential of 1 eV (left column) and 2.5eV (right column), respectively. Please see main text for details on the force terms.

Projector	Analysis	Population
Atomic orbitals	Summed	171.56
Atomic orbitals	Unified	100.74
Optimized NGWFs	Summed	172.72
Optimized NGWFs	Unified	102.11

Table 5.1: Number of electrons on the pentacene molecule for different choice of projectors and for different methods of population analysis. An isolated pentacene molecule has 102 valence electrons. Please see text in section 5.4.2.1 for definition 'Summed' and 'Unified'.

both subjected to the correct forces, and a similar (but not identical) potential modulo a constant shift. However, we can expect the behaviour of the second run, which does not have the correct force, to differ more substantially from those of the other two. In Fig. 5.3 we plot the maximum displacement, the change in energy per ion and the maximum force as a function of the iteration for the aforementioned calculations performed with two different V_c (1eV and 2.5 eV). We are particularly interested in the behaviour of the maximum force since this is a property of the current iteration and does not depend explicitly on the results of the previous iteration. For the 1eV constraining potential, the three calculations differ only slightly since the correction term in the expression for the force is small. However, for $V_c = 2.5eV$, especially for the maximum force, we see that the behaviour of the calculation with the incorrect force (red line) differs significantly from the other two, which are more similar.

5.4.2 Reorganization Energy of Graphene Adsorbed Pentacene

In this section we present and discuss our results concerning the reorganization energy of pentacene molecules adsorbed on a flake of graphene. The pentacene is positioned above the graphene flake at its centre and is oriented parallel to it. We have performed our calculations with two different shapes and sizes of hydrogen-passivated graphene flake, one with 358 atoms (hereafter referred to as the smaller flake) another with 474

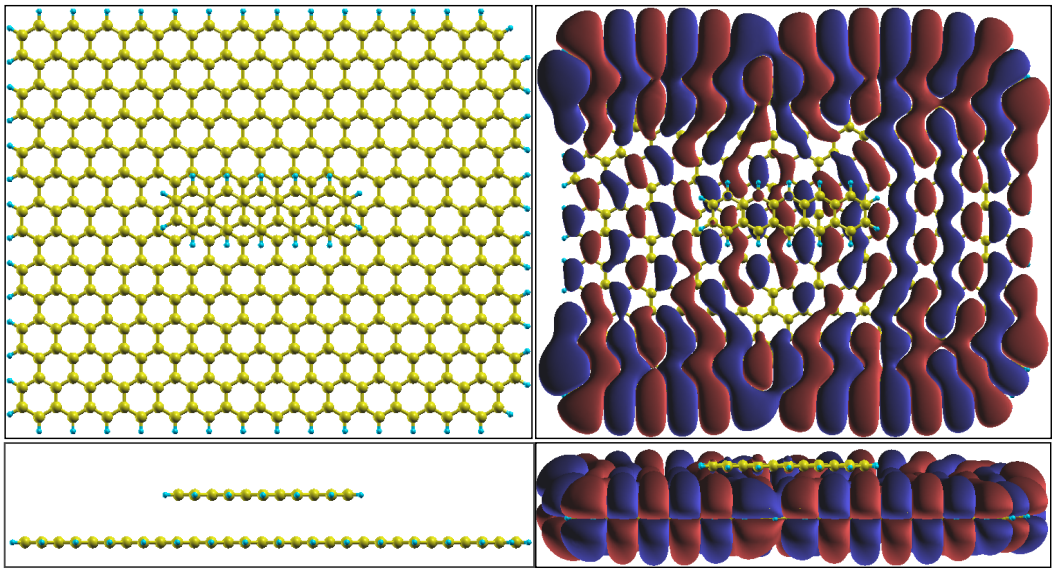

Figure 5.4: The left panel shows the system of interest- pentacene molecule adsorbed on a graphene flake. The right panel shows an isovalue plot of the HOMO of the neutral system. As is evident from the figure, the HOMO is mostly confined to the graphene flake.

atoms (hereafter referred to as the larger flake). The geometry of the smaller flake has been relaxed in isolation. However, for the larger flake we use the geometry of an infinite graphene sheet so that the positions of the carbon atoms are symmetric with each other. The system is shown in the left hand side panel of Fig. 5.4, while the right hand side panel shows a plot of the highest occupied molecular orbital (HOMO) of the entire system. Since this energy level is mostly confined to the graphene flake, simply running a DFT calculation with one less electron is not an option here as that would remove an electron from the graphene flake. Thus we use cDFT to constrain a unit positive charge on the pentacene.

5.4.2.1 Population Analysis

In the cDFT calculations, we intend to remove one electron from the pentacene molecule. It is therefore necessary to carry out a population analysis for the uncharged ground state to find the number of electrons in the molecule and to define the constraining

potential. This population depends on the choice of projectors used to represent the subspace assigned to the molecule. In ONETEP it is possible to use as projectors the atomic pseudo orbitals generated from a self-consistent pseudo-atomic solver or the optimized NGWFs from a previous successful run (in our case, a DFT run for the same system since that does not require specification of any projector). In both cases only the NGWFs associated with the relevant atoms, which, in our case are all the atoms of pentacene, are considered. Once the choice of projectors is made, ONETEP allows predominantly two kinds of population analysis on the set of target atoms. The first technique (the 'Summed' analysis) essentially calculates the populations on each individual atom and then sums them up. Namely this population is defined as

$$N = \sum_{I} \sum_{m_I, m_I'} \langle \varphi_{m_I} | \, \hat{\rho} \, | \varphi_{m_I'} \rangle \, O^{m_I' m_I}, \tag{5.20}$$

where "I" is an atom in the desired set and $O^{m_I' m_I}$ are the elements of the inverse of the overlap matrix of projectors $|\varphi_{m_I}\rangle$ and $|\varphi_{m_I'}\rangle$ belonging only to atom I. The second one (the 'Unified' technique) calculates the population of the entire subspace directly as $N = \sum_{m,m'} \langle \varphi_m | \, \hat{\rho} \, | \varphi_{m'} \rangle \, O^{m' m}$, where the sum is over all the orbitals of the given subspace and the inverse overlap matrix is constructed accordingly [153]. the 'Unified' technique is expected to be much more reliable since the other one double-counts the population shared by the projectors belonging to different atoms. This is clearly seen in Fig. 5.5, which shows a plot of $\langle r|\hat{\mathbb{P}}|r\rangle$ for the neutral pentacene molecule adsorbed on graphene flake. For the 'Summed' scheme (top panel) we see significant positive value of $\langle r|\hat{\mathbb{P}}|r\rangle$ in the interstitial region between the atoms indicating the aforementioned double-counting. As expected, this is not present in the plot for the Unified scheme (bottom panel).

5.4.2.2 Calculation of the Reorganization Energy

In Tab. 5.1 we tabulate the populations calculated with the different techniques and projectors on the pentacene molecule, which is adsorbed on a flake of graphene. Noting that an isolated pentacene molecule has 102 valence electrons we see that the combination of optimized NGWFs with the Unified scheme is the most accurate and we use this for further calculations. Once the population, N, of the molecule is determined, we

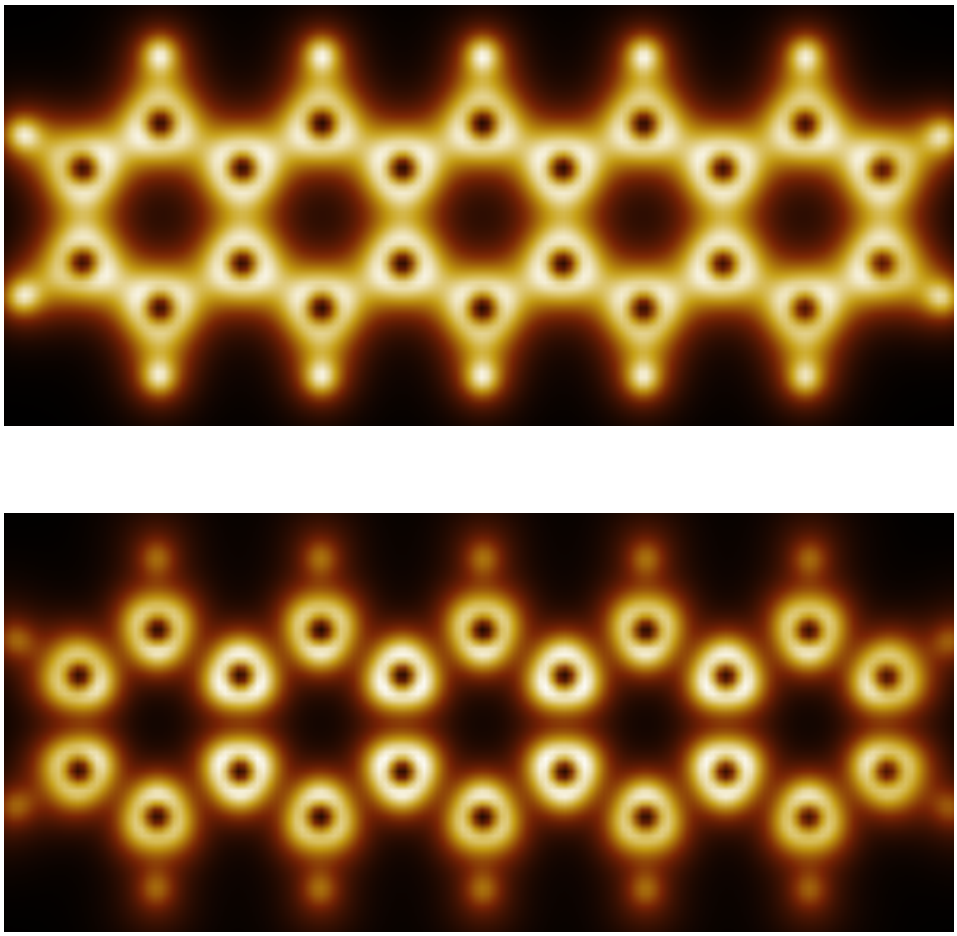

Figure 5.5: Plot of $\langle r|\hat{\mathbb{P}}|r\rangle$ for the pentacene molecule adsorbed on graphene in the neutral state. The top and the bottom panels correspond respectively to the 'Summed' analysis, which calculates population on individual atoms separately before adding them up, and the 'Unified' analysis, which calculates population of the entire subspace as a whole, respectively. In the case of the Summed method, significant brightness in the interstitial space between atoms indicates double-counting in the region of orbital overlap. Clearly, this is not the case with the Unified method.

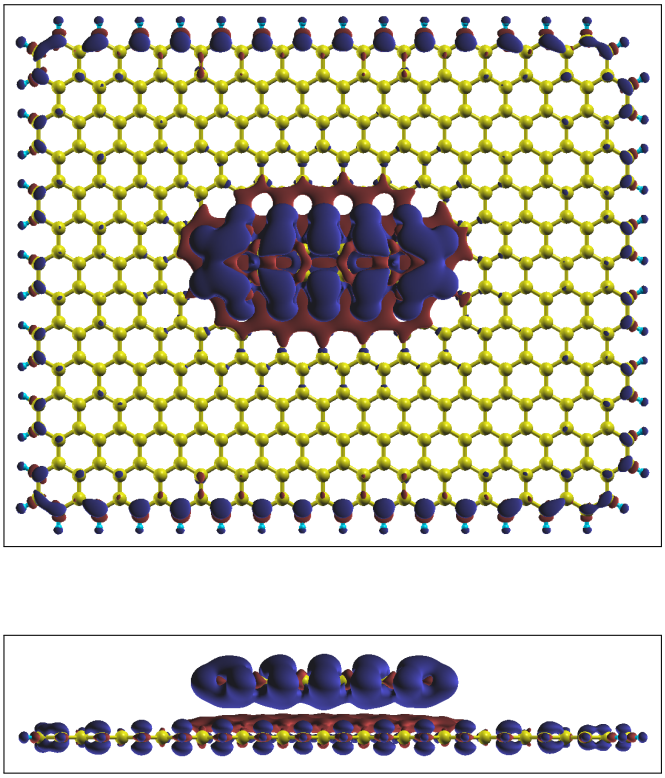

Figure 5.6: Plot of isovalues of the charge density after removal of an electron from the molecule with cDFT. Blue and red colors denote positive and negative charge densities respectively.

calculate the target population for the cDFT calculation as $\left(N * \frac{101}{102}\right)$. Fig 5.6 shows the plot of charge density on the system after removal of an electron from the molecule. As seen in the picture, a molecule with a net positive charge induces a negative charge in the region of the graphene flake immediately beneath the molecule. This is the image charge.

The main problem with such calculation is the existence of multiple local minima, differing only slightly in energy, in the landscape of energy vs geometry. The local minimum to which a structural relaxation converges depends largely on the initial geometry. Therefore we find the re-organization energy corresponding to the two local minima (one for the uncharged system and another for the charged system). As the opposite image charge formed on the flake results in a Coulomb attraction between the molecule and the flake, in the charged state geometry G_2, the molecule is closer

Cutoff energy	flake	λ^0	λ^+	λ	ΔV_c
900 eV	none	28.91	26.67	55.58	N.A.
900 eV	smaller	22.53	20.08	42.61	52.24
900 eV	larger	18.75	19.62	38.37	50.13
1500 eV	none	29.41	26.42	55.83	N.A.
1500 eV	smaller	21.09	20.25	41.34	35.22
1500 eV	larger	19.65	23.20	42.85	35.48

Table 5.2: Re-organization energies (corresponding to local minima in the geometry) of a pentacene molecule as a function of cutoff-energy and size of graphene flake. ΔV_c denotes the difference in the cDFT Lagrange multipliers corresponding to the two different geometries. All energies are in meV. The smaller and the larger flakes contain 358 and 474 atoms, respectively.

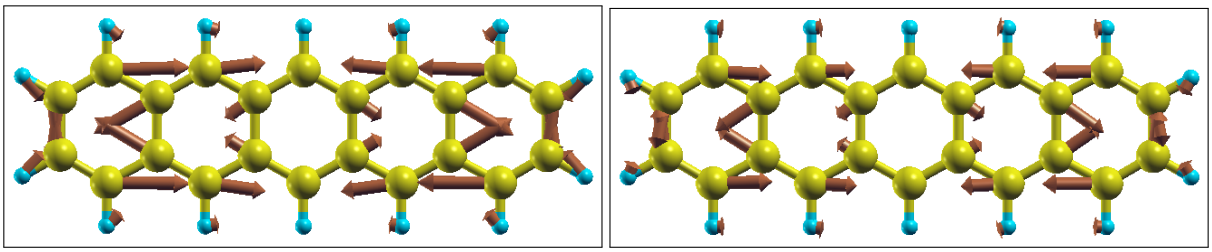

Figure 5.7: Pentacene molecule with arrows showing directions of in-plane displacement of the atoms. The arrow lengths denote magnitudes of displacement in arbitrary unit. The left and the right figures correspond to an isolated pentacene and one on a graphene flake respectively.

to the flake than in the uncharged geometry G_1. We also notice that the directions of the in-plane displacements of the atoms of the pentacene molecule upon charging are very similar for the isolated molecule and the molecule adsorbed on the graphene flake as can be seen from Fig. 5.7. Also, the average bond-length of the relaxed pentacene molecule is smaller for the charged molecule, for both the isolated and the adsorbed molecule indicating a shrinking of the molecule on electron emission. This change in average bond-length is larger for the isolated pentacene compared to the adsorbed one as indicated by the arrow lengths of Fig. 5.7. This can be attributed to the steric effects due to the presence of graphene. However, as mentioned earlier, one must keep in mind that these properties can, in principle, be specific to the pair of local geometry minima pertaining to the calculation. For a different pair of minima, these values could be different in principle. We also note that since the Lagrange multiplier, V_c, gives a measure of the elevation of the molecular level, the difference between the lagrange multipliers corresponding to the two geometries can serve as an approximation for the reorganization energy. Also, since this an object that is local to the molecule, it is free from the errors that may accrue due to small inaccuracies across the large graphene flake.

In Tab. 5.2 we summarize our results for the reorganization energy for two different cutoff-energies and different sizes of the graphene flake. We have also included the re-organization energy of an isolated pentacene molecule (flake=none) for comparison. Note that our results for isolated pentacene matches with that obtained with MP2 method in a earlier theoretical study [138]. As mentioned in Eq. (5.1) here, λ^0, λ^+ and λ refer to the reorganization energy of the uncharged molecule, the positively charged molecule and the total reorganization energy, respectively. We see that the re-organization energy of an isolated molecule is generally greater than that of the same on graphene. This can be attributed to steric effects for the latter case- i.e. the fact that an adsorbed molecule has less freedom for ionic relaxation. It is worth noting that we have tried to analyse the different contributions due to Hartree, exchange and correlation, pseudpotentials, and kinetic energy to the reorganization energy, but that the relatively small reorganisation energy turns out to be the remnant of the substantial cancellation of large variations in these individual terms. It is noteworthy that experimental stud-

ies [141, 148] on a rather different system of graphene-adsorbed pentacene, namely a thin film of pentacene deposited on HOPG, conversely exhibits an increase in reorganization energy with respect to the isolated pentacene molecule. This points to the possibility that intermolecular relaxation in the film contributes to the reorganization energy and more than compensates for the effects of steric hindrance.

5.5 Conclusion

In this chapter we have presented an accurate method for calculating self-consistent forces in conjunction with constrained DFT in first principles calculations employing non-orthogonal localized basis orbitals. We have shown that using a tensorially invariant population analysis for the desired subspace of cDFT automatically leads to an exact expression for force on the atoms. We have implemented this expression for force in the DFT based code ONETEP and have shown that the contribution to the force arising from the change in mutual overlap of the non-orthogonal projector orbitals of the subspace exerts significant influence on geometry relaxation. In order show a novel practical application of such forces, we calculate the re-organization energy of a pentacene molecule adsorbed on a flake of graphene. Since the geometry of such system has a huge number of local minima closely related in energy, the re-organization energy can only be calculated over such local minima, which depend largely on the initial geometry of the calculation. However, we show that for the local minima obtained in our calculations, the reorganization energy of the molecule adsorbed on a graphene flake is typically smaller than that of the isolated molecule, a fact that is consistent with the steric effect associated with an adsorbed molecule.

Chapter 6

Excitonic DFT: A Constrained DFT Based Approach For Simulation of Neutral Excitations

In materials used for optoelectronic applications, the optical gap is a crucial quantity. This is essentially the lowest energy required for a neutral excitation such that the system, without any exchange of electrons, exists in an excited state of the Hamiltonian. Typically, such excitation is associated with the promotion of one or more electrons from their valence energy levels to higher energy states. This results in the creation of a bound electron-hole pair, known as an exciton. The optical gap corresponds to the minimum energy needed for creating such exciton.

6.1 Background

Here we review some of the basic concepts and theoretical tools related to description of neutral excitations in quantum systems. Most of the treatments presented in this section closely follow those of two lectures given by Prof. Neepa Maitra at a summer school on "Teaching the Theory in Density Functional Theory" at the headquarters of

CECAM at Lausanne in June, 2017.

6.1.1 The Concept of Exciton

Let the time-dependent Hamiltonian of a system be given by

$$\hat{H}(t) = \hat{H}_0 + \delta\hat{V}(t), \tag{6.1}$$

where $\hat{H}_0$ is the time-independent part and $\delta\hat{V}(t)$ is a small time-dependent perturbation. The response function is defined as the rate of change in density for a change in the potential.

$$\chi(\mathbf{r}t, \mathbf{r}'t') = \frac{\delta n(\mathbf{r}, t)}{\delta V(\mathbf{r}', t')}, \tag{6.2}$$

which is a measure of the change in density at point $(\mathbf{r}, t)$ for a change in the potential, $V(\mathbf{r}', t')$, at point $(\mathbf{r}', t')$. The change in the density is given by

$$\delta n(\mathbf{r}, t) = \int_0^\infty dt' \int d^3\mathbf{r}' \chi(\mathbf{r}t, \mathbf{r}'t')\delta V(\mathbf{r}', t'). \tag{6.3}$$

Let the system be initially in its ground state

$$|\Psi(t = 0)\rangle = |\Psi_0\rangle\,. \tag{6.4}$$

We now move to the interaction picture in which the ket state and the operator are given respectively by

$$|\Psi^I(t)\rangle = e^{i\hat{H}_0 t}\,|\Psi(t)\rangle\,, \tag{6.5}$$

and

$$\hat{O}^I(t) = e^{i\hat{H}_0 t}\hat{O}e^{-i\hat{H}_0 t}. \tag{6.6}$$

Within this formalism the Schrödinger equation is written as

$$i\frac{\partial}{\partial t}\,|\Psi^I(t)\rangle = \delta\hat{V}^I(t)\,|\Psi^I(t)\rangle\,. \tag{6.7}$$

By solving this equation to approximation in first order, we obtain

$$|\Psi^I(t)\rangle = |\Psi_0\rangle - i\int_0^t dt'\delta\hat{V}^I(t')\,|\Psi_0\rangle\,. \tag{6.8}$$

Then, the expectation value of some arbitrary Hermitian operator $\hat{O}(t)$ is given by

$$\begin{aligned}\langle\hat{O}(t)\rangle &= \langle\Psi^I(t)|\hat{O}^I(t)|\Psi^I(t)\rangle\,,\\ &\approx \langle\Psi_0|\hat{O}^I(t)|\Psi_0\rangle - i\int_0^t dt'\,\langle\Psi_0|\left[\hat{O}^I(t),\delta\hat{V}^I(t')\right]|\Psi_0\rangle\,,\end{aligned} \tag{6.9}$$

where the first term in Eq. (6.9) is just $\langle\hat{O}(t=0)\rangle$ and the second term gives the change in $\langle\hat{O}\rangle$ to the first order in $\delta\hat{V}^I$. Here we enter the *linear response* regime by assuming that the change of an observable due to a change in the external potential follows a linear relation.

We are interested in calculating such second term for the density operator $\hat{n}(\mathbf{r})$. This is given by

$$n(\mathbf{r},t) - n(\mathbf{r},0) = \delta n(\mathbf{r},t) = -i\int_0^t dt'\,\langle\Psi_0|\left[\hat{n}^I(\mathbf{r},t),\delta\hat{V}^I(t')\right]|\Psi_0\rangle\,, \tag{6.10}$$

$$= -i\int_0^t dt'\int d^3\mathbf{r}'\delta V(\mathbf{r}',t')\,\langle\Psi_0|\left[\hat{n}^I(\mathbf{r},t),\hat{n}^I(\mathbf{r}',t')\right]|\Psi_0\rangle \tag{6.11}$$

The last equality follows from the definition

$$\delta\hat{V}(t') = \int \delta V(\mathbf{r}', t')\hat{n}(\mathbf{r}')d^3\mathbf{r}' \tag{6.12}$$

Thus we can finally obtain an expression for our response function, namely

$$\chi(\mathbf{r}t, \mathbf{r}'t') = -i\Theta(t-t') \langle\Psi_0| \left[\hat{n}^I(\mathbf{r}, t), \hat{n}^I(\mathbf{r}', t')\right] |\Psi_0\rangle . \tag{6.13}$$

Let us now denote the full set of the many-body state kets of $\hat{H}_0$ as $\{|\Psi_J\rangle\}$ and the set of eigenvalues as $\{E_J\}$. Then, the first term in the commutator on the right hand side of Eq. (6.13) gives

$$\begin{aligned}\langle\Psi_0|e^{i\hat{H}_0 t}\hat{n}(\mathbf{r})e^{-i\hat{H}_0 t}e^{i\hat{H}_0 t'}\hat{n}(\mathbf{r}')e^{-i\hat{H}_0 t'}|\Psi_0\rangle &= \sum_J \langle\Psi_0|e^{i\hat{H}_0 t}\hat{n}(\mathbf{r})e^{-i\hat{H}_0 t}|\Psi_J\rangle \langle\Psi_J|e^{i\hat{H}_0 t'}\hat{n}(\mathbf{r}')e^{-i\hat{H}_0 t'}|\Psi_0\rangle \\ &= \sum_J e^{i(E_0-E_J)(t-t')} \langle\Psi_0|\hat{n}(\mathbf{r})|\Psi_J\rangle \langle\Psi_J|\hat{n}(\mathbf{r}')|\Psi_0\rangle .\end{aligned} \tag{6.14}$$

The second term of the commutator can be evaluated likewise. This shows that $\chi(\mathbf{r}t, \mathbf{r}'t')$ is actually a function of $(t-t')$, i.e. $\chi(\mathbf{r}t, \mathbf{r}'t') = \chi(\mathbf{r}, \mathbf{r}', t-t')$. As such, χ can be Fourier transformed into energy space as

$$\begin{aligned}\chi(\mathbf{r}, \mathbf{r}', \omega) &= \int d(t-t')\chi(\mathbf{r}, \mathbf{r}', t-t')e^{i\omega(t-t')} \\ &= \sum_{J=1}^{\infty} \frac{\langle\Psi_0|\hat{n}(\mathbf{r})|\Psi_J\rangle \langle\Psi_J|\hat{n}(\mathbf{r}')|\Psi_0\rangle}{\omega - (E_J - E_0) + i0^+} + c.c.\end{aligned} \tag{6.15}$$

Note that $\chi(\mathbf{r}, \mathbf{r}', t-t')$ and consequently $\chi(\mathbf{r}, \mathbf{r}', \omega)$ are properties of the unperturbed Hamiltonian and do not depend on $\delta\hat{V}(t)$[1]. The poles of Eq. (6.15) are located

[1]This suggests that if the unperturbed Hamiltonian is translation invariant, then $\chi(\mathbf{r}, \mathbf{r}', \omega) = \chi(\mathbf{r} -$

at the energies $(E_J - E_0)$ that, by definition, are the excitation energies of the system. A Fourier space equivalent of Eq. (6.3) indicates that the poles of $\chi(\mathbf{r}, \mathbf{r}', \omega)$ correspond to significant changes in density brought about by the perturbation. In other words, if $\chi(\mathbf{r}, \mathbf{r}', \omega)$ has a pole at ω_α, then the ground-state system can be excited by supplying it with an energy of ω_α, resulting in significant change in density.

Within the QP framework, the excited states of the system typically correspond to states in which one or more electrons have been promoted from their valence levels to some excited state. The lowest excitation would be that of exciting an electron from the highest occupied level to the lowest available empty level. Such promotion of an electron leaves behind a hole in the valence space. Thus, the excitation can be thought of as the creation of an interacting electron-hole pair [see Appendix C], known as *exciton*. The coupling between the hole and the promoted electron results in energy gain and, as a consequence, the lowest excitation energy, known as the optical gap, is typically lower than the QP gap. The latter is the difference in addition and removal energies, both referring to systems with net charge and therefore lacking the aforementioned electron-hole coupling. The state of the art for finding the energies associated with such neutral excitations typically follows the route of finding the poles of $\chi(\mathbf{r}, \mathbf{r}', \omega)$.

6.1.2 State-of-the art

The most popularly used method for finding the poles of Eq. (6.15), at least for finite systems, is to use time-dependent density functional theory (TDDFT). To this end, one considers an equivalent KS system whose density $n_s(\mathbf{r}, t)$ is the same as that $(n(\mathbf{r}, t))$ of the interacting system at all time. The response function of such a non-interacting

$\mathbf{r}', \omega)$, i.e. the density response function is a function of difference in coordinates and can undergo Fourier transform into momentum space $\chi(\mathbf{r} - \mathbf{r}', \omega) \rightarrow \chi(\mathbf{q}, \omega)$. See section 15.5.1 of Ref. [102]. Then, with the help of the convolution theorem, the complicated Eq. (6.3) reduces, in momentum space, to $\delta n(\mathbf{q}, \omega) = \chi(\mathbf{q}, \omega)\delta V(\mathbf{q}, \omega)$.

system is given by

$$\chi_s(\mathbf{r},\mathbf{r}',\omega)=\sum_{j,k}(f_j-f_k)\delta_{\sigma_j,\sigma_k}\frac{\phi_k^*(\mathbf{r})\phi_j(\mathbf{r})\phi_j^*(\mathbf{r}')\phi_k(\mathbf{r}')}{\omega-(\varepsilon_k-\varepsilon_j)+i0^+}+c.c \tag{6.16}$$

where $|\phi_i\rangle$,f_i and ε_i are respectively the state-ket, occupation and energy eigenvalue of the i-th level. The poles of this function are at the excitation energies of the KS non-interacting system. However, the response functions for the two different systems are related (see, for example, appendix D of Ref. [92]) by

$$\chi(\mathbf{r},\mathbf{r}',\omega)=\chi_s(\mathbf{r},\mathbf{r}',\omega)+\int d^3\mathbf{r_1}d^3\mathbf{r_2}\chi_s(\mathbf{r},\mathbf{r_1},\omega)\left[\frac{1}{|\mathbf{r_1}-\mathbf{r_2}|}+f_{xc}(\mathbf{r_1},\mathbf{r_2},\omega)\right]\chi(\mathbf{r_2},\mathbf{r}',\omega) \tag{6.17}$$

where $f_{xc}(\mathbf{r_1},\mathbf{r_2},\omega)$ is the Fourier transform of

$$f_{xc}(\mathbf{r_1}t_1,\mathbf{r_2}t_2)=\frac{\delta V_{xc}(\mathbf{r_1}t_1)}{\delta n(\mathbf{r_2}t_2)} \tag{6.18}$$

Now, in general,$V_{xc}(\mathbf{r_1}t_1)$ is a functional of the density $n(t')$ at all times $t'<t_1$ and also of the initial many body state $[\Psi_0=\Psi(t=0)]$ and of the initial KS state $[\Phi_0=\Phi(t=0)]$. Thus,

$$V_{xc}(\mathbf{r_1}t_1)=V_{xc}[n(t'<t_1),\Psi_0,\Phi_0](\mathbf{r_1}t_1) \tag{6.19}$$

However, if the initial many-body state is the ground state, then the initial state dependence is redundant as ground state density uniquely specifies the ground state. Also, because of the one-to-one correspondence between the external potential $V_{ext}(t)$ and $n(t)$, one can write, if $\Psi_0=\Psi_{\text{Ground State}}$, then

$$V_{xc}(\mathbf{r}t)=V_{xc}[n(t)](\mathbf{r}t) \tag{6.20}$$

To uncomplicate matters, even in the general case, in most calculations one uses the adiabatic approximation which amounts to neglecting all memory and using the V_{xc} that we would have had if the system was in a ground state.

$$V_{xc}^{\text{Adiabatic}}[n,\Psi_0,\Phi_0](\mathbf{r}t)=V_{xc}^{\text{Ground State}}[n(t)](\mathbf{r}t) \tag{6.21}$$

In terms of computational resources, TDDFT is a relatively expensive method. Unlike regular DFT, which scales as $\mathcal{O}(N^3)$ with size of system, TDDFT, in the standard form, shows a scaling of $\mathcal{O}(N^4)$ [162]. This limits the system size treatable with TDDFT to a significant level. Additionally, TDDFT usually comes with significant memory overhead. Also, within the adiabatic approximation Eq. (6.21), beyond which the computational expenses and complications are even higher, TDDFT can only describe single excitations [163, 164, 165]. This is one major drawback of the adiabatic approximation.

The many-body based approach of solving the Bethe-Salpeter equations within the GW approximation [166, 167] yields accurate values for the neutral excitation energies. However, this method, which scales as $\mathcal{O}(N^6)$ [168] with system size, is significantly expensive. Besides, within the adiabatic approximation, i.e. approximating the kernel to be frequency-independent, this method is also unable to treat double excitations [169, 170].

Here, we note that, just like any other property of an interacting system, the excited state energies are uniquely specified by the ground state density, which has a one to one mapping with the Hamiltonian. One can prove the existence of a variational DFT, with a minimum principle and an equivalent non-interacting Kohn-Sham (KS) excited state, for an individual excited state of the interacting system [171]. Additionally, it is noted that [172, 173] every extremum of the Levy-Lieb energy functional $E_{LL}[n(\mathbf{r})]$ corresponds to a stationary state density and one can find equivalent non-interacting systems corresponding to them [174]. Motivated by the aforementioned observations, over the years, several first-principles methods based on regular (time-independent) DFT have been proposed and developed for calculating these energies. For example, in the **ΔSCF-DFT** formalism [174, 175], instead of filling up the lowest KS orbitals according to the aufbau principle, a self-consistent procedure is executed keeping on or more of the lowest KS orbitals empty and filling up equal number of higher energy KS orbitals. The **ensemble DFT** [176, 177, 178] approach finds the energy of an ensemble state where the individual electronic levels are filled in accordance with some weight function. The excitation energy is then found as a linear combination of two

different ensemble energies. In the **constricted variational DFT** [179, 180] method, which comes in several different flavours, the occupied and the virtual (unoccupied) KS ground state orbitals undergo a variational unitary transformation to form a new set of occupied and virtual orbitals corresponding to the excited state, which gives the excited state energy of the system. In the **maximum overlap method** [181, 182], the initial "guess" KS orbitals must lie within the basin of attraction of the desired excited state. Then, the occupied orbitals in each successive iteration of the SCF cycle are chosen such that their overlap with the old occupied set of orbitals is maximum. All these methods have their own strengths and weaknesses in terms of computational expenses and ease of implementation and convergence. One must note that, particularly in quantum-chemistry, a commonly used computational method for treatment of excited states is the **coupled cluster** formalism [183].

6.2 The Excitonic DFT Method

Here we introduce our *excitonic DFT* method, which is a computationally inexpensive, generally applicable, easy to converge *ab initio*, cDFT-based formalism for calculating excitation energies. This has been implemented within the ONETEP software for calculation of the energies presented in this chapter. Previously (see section 3.3), we have introduced cDFT as a method for determining the ground-state energy of a system subject to confining a given number of electrons, N_c, in a desired subspace. The condition for the constraint can be given by [see Eq. (5.3)]

$$\mathrm{Tr}[\hat{\rho}\hat{P}] = N_c,$$

where $\hat{P}$ is a projection operator onto the desired subspace, whose population is given by the left-hand side of the above equation. Then, the ground state of the system subject to the above constraint is given by the stationary point of [see Eq. (5.4)]

$$W[\rho, V_c] = E[\rho] + V_c \left(\mathrm{Tr}[\hat{\rho}\hat{\mathbb{P}}] - \mathrm{N_c} \right).$$

In cDFT, typically the subspace given by $\hat{\mathbb{P}}$ is a user-defined spatial region, creating distinct and spatially separated source and drain regions within the system for simulating charge transfer excitations [184]. In this work, in order to access excitations not limited to such charge separated states, we go beyond the condition of spatial confinement of charge and define the subspace in terms of KS eigenstates. Thus, our method promotes cDFT to a fully *ab initio* method without the need for user-specification of subspace. In this work, for a neutral system with N electrons, we propose to obtain the energy of the lowest excited state by confining $(N-1)$ electrons within the subspace spanned by the valence KS orbitals of the ground state calculation. We define the projector over this subspace as

$$\begin{aligned} \hat{P} &= \hat{\rho}_0, \\ &= \sum_i f_i \left|\varphi_i\right\rangle \left\langle\varphi_i\right|, \end{aligned}$$

where $\hat{\rho}_0$ is the ground state density operator, $|\varphi_i\rangle$ is the i-th KS orbital and f_i, which denotes the occupation number of the KS orbital, equals 0 for unoccupied states and 1 for occupied states[2].

It is interesting to note that the KS many-body excited state, obtained from the cDFT treatment, is orthogonal to the ground state. This is because the excited state is a Slater determinant composed of single-particle KS orbitals, the highest one of which is, by construction, orthogonal to each KS single-particle orbital composing the many-body KS ground state.

If the lowest unoccupied state is degenerate, then the occupation numbers will be ill-conditioned (see, for example, section (5.3.2)) for these single-particle states. Also, if there are a large number of unoccupied states in the vicinity of the lowest one, the

[2]We use materials which are insulator in the ground state

convergence will be unstable for the cDFT calculation, in which the promoted electron needs to occupy such state. Under these circumstances one needs to employ ensemble DFT for the cDFT run at a finite temperature.

The above formalism has been implemented within the ONETEP code and it is used to calculate the optical gaps for both singlet and triplet excitations. These excitations correspond to states with $S = 0$ and $S = 1$ respectively and they require the use of spin-polarized cDFT. Consequently, the condition for constraint is modified as

$$\mathrm{Tr}[\hat{\rho}^{\sigma}\hat{P}] = N_c^{\sigma}, \tag{6.22}$$

where σ denotes the desired spin of electron.

In many-body theory methods for determining QP gap (e.g. the GW scheme), we have remarked that the gap is calculated by a clever manipulation of the properties related to the inter-particle interaction in the charge neutral state, without actually adding/removing one electron. In contrast, in the cDFT formalism, one actually simulates the charge transfer in order to find the approximate QP gap in terms of energy difference. A similar difference can be appreciated, in the context of calculation of optical gaps, between the many-body based method (i.e, the solution of Bethe-Salpeter equation (see Appendix C)), TDDFT and our cDFT treatment. In the first two, without technically creating any excitation, one tries to find the excitation energies from the poles of certain quantities. Whereas, in the latter, one simulates the promotion of an electron in the KS system in order to evaluate the approximate energy change in the equivalent interacting system. This ensures the computational efficiency of such method compared to TDDFT and the many-body procedure. Also, since cDFT does not rely on adiabatic approximation, one can, in principle, access states corresponding to double excitations by promoting two electrons from the ground state KS system.

6.3 Results

6.3.1 Optical gap of Molecules

Here we present the triplet (i.e. corresponding to an excited state with spin quantum number $S = 1$) and singlet (i.e. corresponding to an excited state with spin quantum number $S = 0$) optical gaps of several molecules calculated with the excitonic DFT formalism. However, before presenting the results, we want to specify some terminology. The KS Slater determinant, which is the state including all the electrons, is referred to as the KS many-body state in order to distinguish from the single-particle KS orbitals. The KS many-body quantum state is a non-interacting state different from the quantum state of the interacting many-body system.

The requirement that the singlet excited state has to be an eigenstate of $\hat{S}^2$ with spin-quantum number zero prompts one to make certain approximations in its treatment. In the following, we discuss such approximations in detail.

The Sum Method

The non-interacting KS many-body state must be expressible as a single Slater determinant. For example, considering a simple two-orbital two-electron model (TOTEM) [185] in a singlet ground state, i.e. one with a spinor like $\frac{1}{\sqrt{2}}\left(|1\uparrow\rangle|2\downarrow\rangle - |1\downarrow\rangle|2\uparrow\rangle\right)$, the RKS many-body wave-function is given by

$$^{S=0}\Psi_{\mathrm{GS}} = \frac{1}{\sqrt{2}}\varphi_a\left[|1\uparrow\rangle|2\downarrow\rangle - |1\downarrow\rangle|2\uparrow\rangle\right], \tag{6.23}$$

where φ_a denotes the KS spatial level. Let us see how an equivalent expression will look for an excited state, where one electron has been promoted to a higher level. In the restricted KS (RKS) scheme, where the spatial orbital is independent of the spin, the energy eigenstate for the singlet excitation with one electron in the lower spatial level a

and another electron in the higher spatial level b can be written as[3]

$$
\begin{aligned}
{}^{S=0}\Psi^{(\mathrm{RKS})}_{m_s=0}(1,2) &= \frac{1}{\sqrt{2}}[\varphi_a(1)\varphi_b(2)+\varphi_b(1)\varphi_a(2)]\otimes[\uparrow(1)\downarrow(2)-\downarrow(1)\uparrow(2)]. \\
&= \frac{1}{\sqrt{2}}\left[\begin{vmatrix}\varphi_{a\uparrow}(1) & \varphi_{a\uparrow}(2)\\ \varphi_{b\downarrow}(1) & \varphi_{b\downarrow}(2)\end{vmatrix}+\begin{vmatrix}\varphi_{b\uparrow}(1) & \varphi_{b\uparrow}(2)\\ \varphi_{a\downarrow}(1) & \varphi_{a\downarrow}(2)\end{vmatrix}\right]. \qquad (6.24)
\end{aligned}
$$

${}^{S=0}\Psi^{(\mathrm{RKS})}_{m_s=0}(1,2)$ is an eigenstate of $\hat{S}^2$ and $\hat{S}_z$ with $S=0$ and $m_s=0$. As shown in Eq. (6.24), this can be written as a normalized sum of two SDs. These two SDs, which are energy degenerate with an energy of,say ${}^{\mathrm{SD}}E^{(\mathrm{RKS})}_{m_s=0}$, are eigenstates of $\hat{S}_z$ with an eigenvalue of 0, but they are not eigenstates of $\hat{S}^2$. Let us denote the first (say) SD as ${}^{\mathrm{SD}}\Psi^{(\mathrm{RKS})}_{m_s=0}$.

The RKS triplet state, in contrast, is three-fold degenerate. The three triplet ($S=1$) states, with $\hat{S}_z$ eigenvalues of $-1, 0$ and 1 are given by

$$
{}^{S=1}\Psi^{(\mathrm{RKS})}_{m_s=-1}(1,2) = \begin{vmatrix}\varphi_{a\downarrow}(1) & \varphi_{a\downarrow}(2)\\ \varphi_{b\downarrow}(1) & \varphi_{b\downarrow}(2)\end{vmatrix}, \qquad (6.25)
$$

$$
{}^{S=1}\Psi^{(\mathrm{RKS})}_{m_s=0}(1,2) = \frac{1}{\sqrt{2}}\left[\begin{vmatrix}\varphi_{a\uparrow}(1) & \varphi_{a\uparrow}(2)\\ \varphi_{b\downarrow}(1) & \varphi_{b\downarrow}(2)\end{vmatrix}-\begin{vmatrix}\varphi_{b\uparrow}(1) & \varphi_{b\uparrow}(2)\\ \varphi_{a\downarrow}(1) & \varphi_{a\downarrow}(2)\end{vmatrix}\right] \text{ and} \qquad (6.26)
$$

$$
{}^{S=1}\Psi^{(\mathrm{RKS})}_{m_s=1}(1,2) = \begin{vmatrix}\varphi_{a\uparrow}(1) & \varphi_{a\uparrow}(2)\\ \varphi_{b\uparrow}(1) & \varphi_{b\uparrow}(2)\end{vmatrix}. \qquad (6.27)
$$

Note that ${}^{S=1}\Psi^{(\mathrm{RKS})}_{m_s=-1}(1,2)$ and ${}^{S=1}\Psi^{(\mathrm{RKS})}_{m_s=1}(1,2)$ are single SD wave-functions and hence can, in principle, be accessed within the KS framework. In fact, one can expect a cDFT excited state calculation with *spin=-1* (*spin=1*) to converge to ${}^{S=1}\Psi^{(\mathrm{RKS})}_{m_s=-1}(1,2)$ (${}^{S=1}\Psi^{(\mathrm{RKS})}_{m_s=1}(1,2)$). However, one can not expect a single KS cDFT calculation to converge

[3]The number in the bracket is the particle index. So, $|\varphi_{as_1}(i)\rangle$ is the state ket of the i-th particle with spin s_1 in the spatial orbital φ_a.

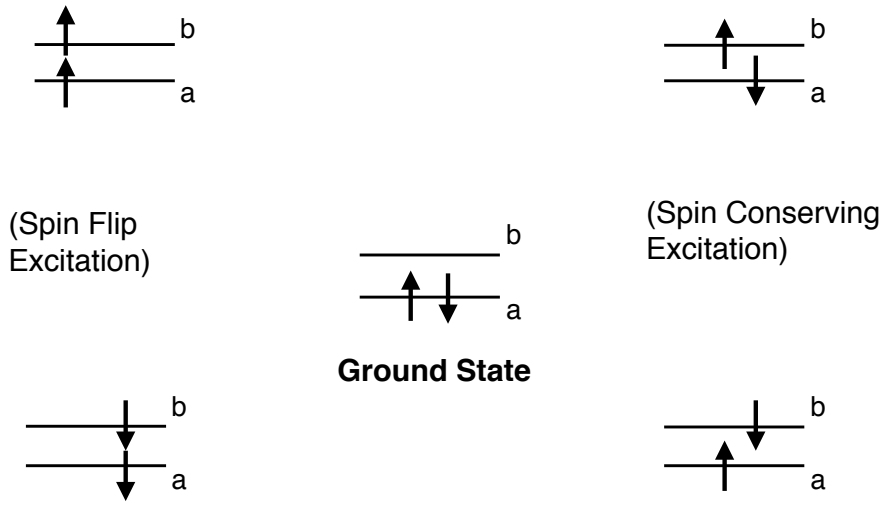

Figure 6.1: A schematic diagram of the different Slater determinant states presented within a restricted treatment. The state in the centre is the ground state singlet from Eq. (6.23). The other states, clockwise from top left, are the triplet state of Eq. (6.27), the second Slater determinant of Eq. (6.26), the first Slater determinant of Eq. (6.26) and the triplet state of Eq. (6.25), respectively.

to any of the states ${}^{S=0}\Psi^{(\mathrm{RKS})}_{m_s=0}(1,2)$ and ${}^{S=1}\Psi^{(\mathrm{RKS})}_{m_s=0}(1,2)$. An excited state cDFT calculation with *spin=0* can actually be expected to converge to one of their constituent degenerate SDs. Now, by expanding the respective Slater determinants, the energy eigenvalue ${}^{S=0}E^{(\mathrm{RKS})}_{m_s=0}$ of the RKS open-shell singlet can be expressed as [186]

$$\begin{aligned}
&\langle {}^{S=0}\Psi^{(\mathrm{RKS})}_{m_s=0}(1,2)|\hat{H}|{}^{S=0}\Psi^{(\mathrm{RKS})}_{m_s=0}(1,2)\rangle \\
&= 2\times\langle {}^{\mathrm{SD}}\Psi^{(\mathrm{RKS})}_{m_s=0}|\hat{H}|{}^{\mathrm{SD}}\Psi^{(\mathrm{RKS})}_{m_s=0}\rangle - \langle {}^{S=1}\Psi^{(\mathrm{RKS})}_{m_s=0}(1,2)|\hat{H}|{}^{S=1}\Psi^{(\mathrm{RKS})}_{m_s=0}(1,2)\rangle \\
&= 2\times\langle {}^{\mathrm{SD}}\Psi^{(\mathrm{RKS})}_{m_s=0}|\hat{H}|{}^{\mathrm{SD}}\Psi^{(\mathrm{RKS})}_{m_s=0}\rangle - \langle {}^{S=1}\Psi^{(\mathrm{RKS})}_{m_s=1}(1,2)|\hat{H}|{}^{S=1}\Psi^{(\mathrm{RKS})}_{m_s=1}(1,2)\rangle\,, \qquad (6.28)
\end{aligned}$$

where the last relation follows from the degeneracy of the RKS triplet states. In explicit energy notations

$$ {}^{S=0}E^{(\mathrm{RKS})}_{m_s=0} = 2\times^{\mathrm{SD}} E^{(\mathrm{RKS})}_{m_s=0} - {}^{S=1}E^{(\mathrm{RKS})}_{m_s=1}\,. \qquad (6.29)$$

Note that these energies pertain to non-interacting systems. At this point, we

make a simplifying assumption. We use Eq. (6.29), which is derived for a restricted non-interacting KS system, to evaluate the singlet excited state energy of an interacting many-body system

$$^{S=0}E^{\mathcal{I}}_{m_s=0} = 2 \times^{\mathrm{SD}} E^{\mathcal{I}}_{m_s=0} - ^{S=1} E^{\mathcal{I}}_{m_s=1}. \tag{6.30}$$

Here, as denoted by the superscript $\mathcal{I}$, each energy term corresponds to an interacting system, obtained from an equivalent unrestricted KS system whose density and spin density equal those of the interacting system. Then, the task of determining the triplet and singlet optical gaps boils down to running the three following first principles calculations.

1. An unconstrained DFT calculation to determine the ground state energy E_0,
2. a cDFT calculation with (spin=1), confining $(N-1)$ electrons to the valence subspace of the previous calculation to obtain the energy $^{S=1}E^{\mathcal{I}}_{m_s=1}$ corresponding to the triplet interacting state, and
3. a cDFT calculation with (spin=0), again confining $(N-1)$ electrons to the valence subspace of the DFT run to find the energy $^{\mathrm{SD}}E^{\mathcal{I}}_{m_s=0}$.

Then we use Eq. (6.30) to find the energy $^{S=0}E^{\mathcal{I}}_{m_s=0}$ corresponding to the excited singlet state. The triplet and the singlet optical gaps are then calculated as

$$^{S=1}E_{\mathrm{OG}} = ^{S=1} E^{\mathcal{I}}_{m_s=1} - E_0 \tag{6.31}$$

and

$$^{S=0}E_{\mathrm{OG}} = ^{S=0} E^{\mathcal{I}}_{m_s=1} - E_0, \tag{6.32}$$

respectively. For our excitonic DFT calculations, the constraining potential is always applied on one spin channel (we use up).

It is interesting to note that the (spin=1) cDFT calculation (see step 2 above) gives the exact same energy as an unconstrained DFT calculation with (spin=1). This is not too surprising since the KS single-particle orbitals are mutually orthogonal. Therefore, unless there is much relaxation among the low-lying states, in an unconstrained DFT calculation, we can expect that to accommodate two unpaired electrons with up-spin, one of them will be promoted out of the subspace spanned by the KS orbitals of all other electrons. In other words, we expect the excited state, obtained by promoting one up-spin electron out of the valence subspace (i.e., the KS state accessed by the cDFT calculation with spin=1), to be the lowest excited state where the two most energetic electrons have the same spin (i.e., the KS state accessed by the unconstrained DFT calculation with spin=1). This equality also suggests that in the unconstrained excited state, there is little relaxation among the lowest $N/2$ KS states (compared to their ground-state positions) and consequently, the lowest $(N-1)$ electrons in the excited state stay within the valence subspace of the ground state. Thus, this equality offers a validation of our cDFT approach.

The implementation of the excitonic DFT method in code ONETEP [96] has been used, with PBE exchange-correlation functional [94] to calculate the optical gaps for the 28 closed-shell organic molecules, which constitute the well known Thiel's set [187]. The structure of the molecules can be found in Fig. (6.2), (6.3) and (6.4). The calculations are performed using norm-conserving pseudopotentials with a plane-wave cutoff energy of 1500 eV and a radius of 14.0 Å for the NGWF basis functions. In Fig. 6.5, we show a scatter plot of the singlet and triplet optical gaps calculated with our cDFT-based method against those obtained with TDDFT and PBE functional in Ref. [188] (for singlet transition) and in Ref. [189] (for triplet transition). The TDDFT results are generally in agreement with experimental values [see the supporting information in Ref. [190]]. The green straight line in Fig. 6.5 represents $x = y$, namely the perfect match between cDFT and TDDFT results. Note that, as expected, the triplet optical gaps show much better match between the cDFT and the TDDFT results. This is because, being SDs (for $m_s \neq 0$), the KS triplet excited states are directly accessed by the cDFT procedure. However, Fig. 6.5 also shows that, in spite of the approximate

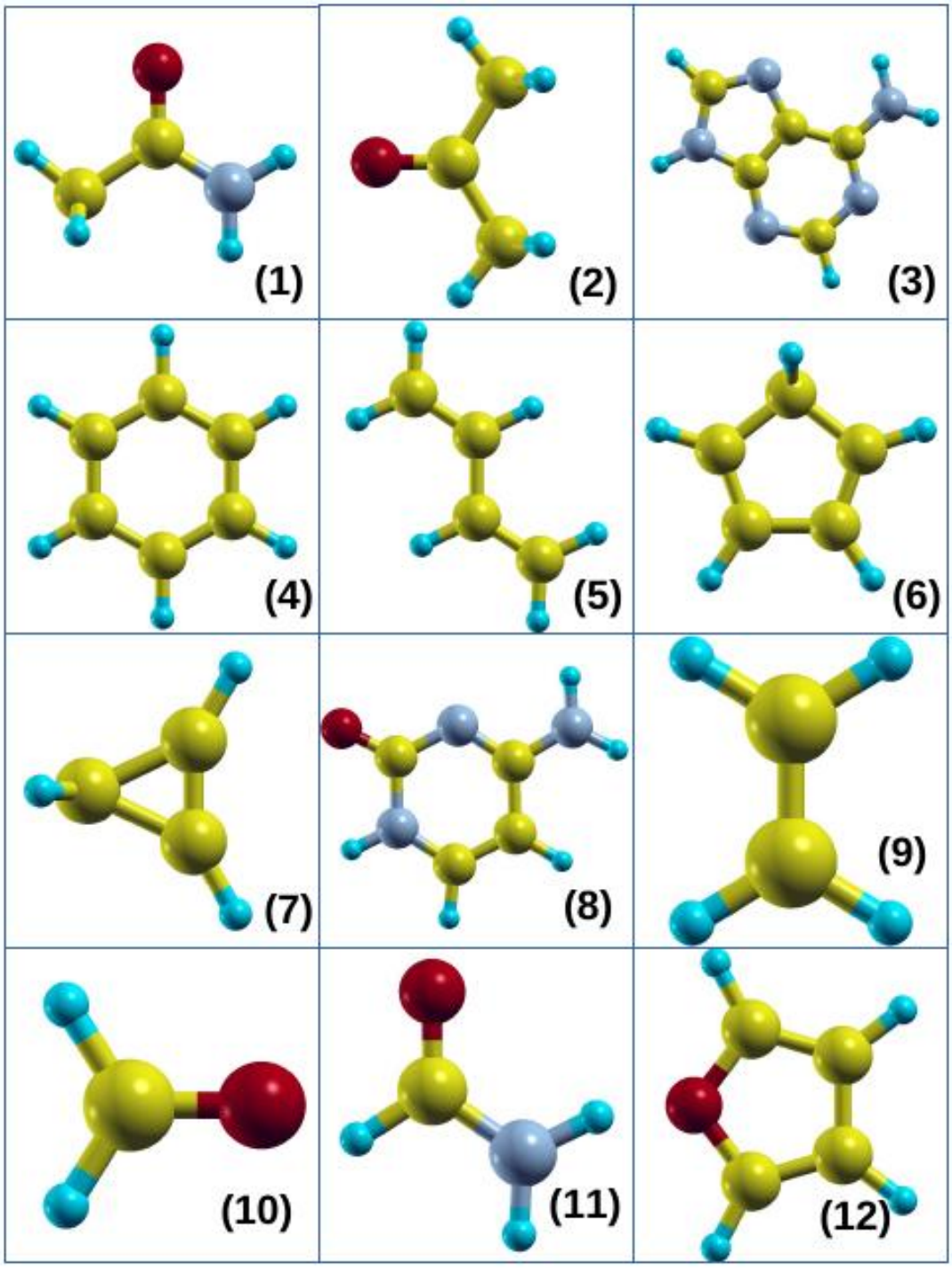

Figure 6.2: Structure of the molecules investigated in this chapter: (1)Acetamide, (2)Acetone, (3)Adenine, (4)Benzene, (5)Butadiene, (6)Cyclopentadiene, (7)Cyclopropene, (8)Cytosine, (9)Ethene, (10)Formaldehyde, (11)Formamide, (12)Furan. Colour code: Yellow-Carbon, Red-Oxygen, Turquoise-Hydrogen, Blue-Nitrogen.

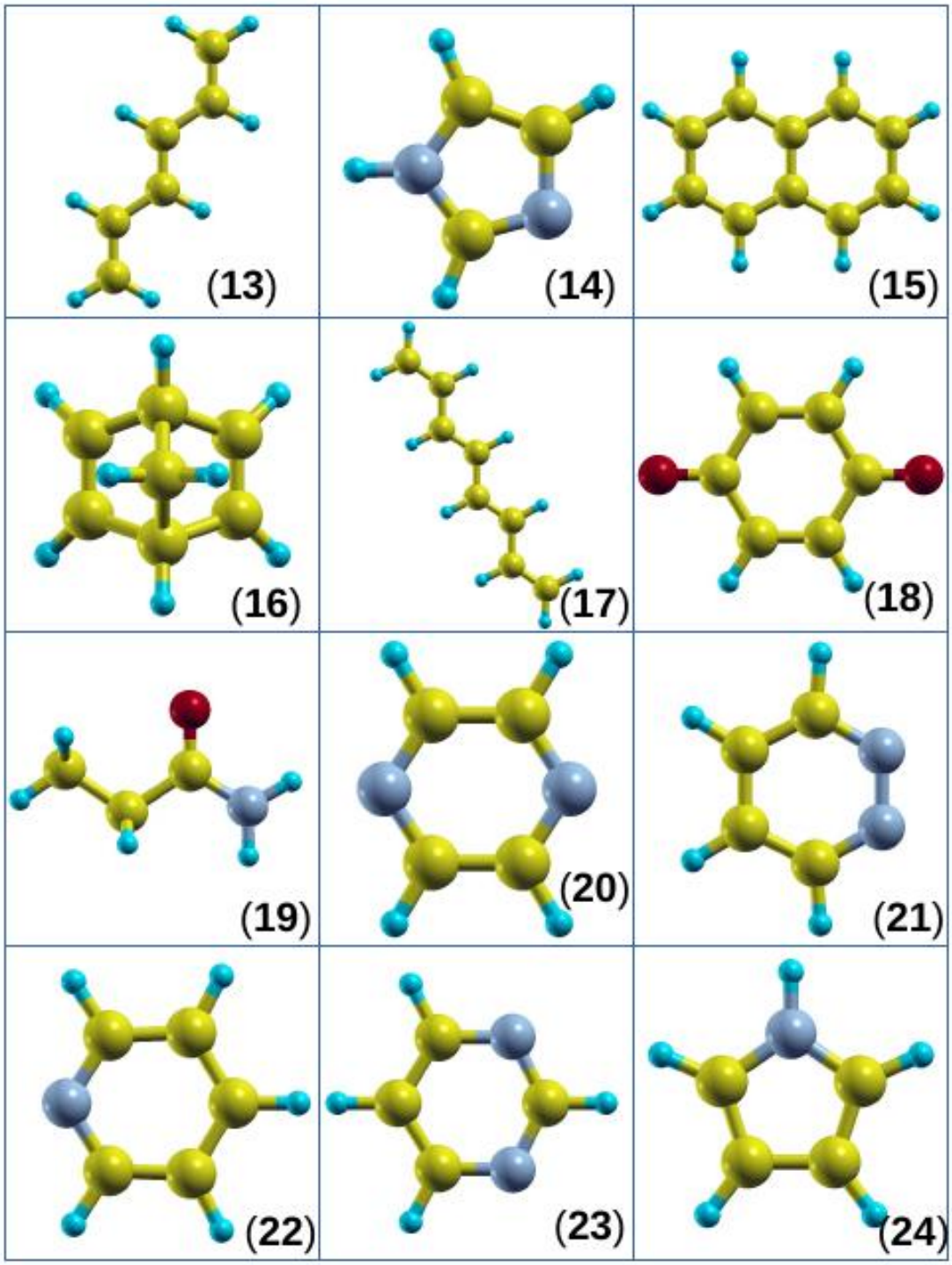

Figure 6.3: Structure of the molecules investigated in this chapter: (13)Hexatriene, (14)Imidazole, (15)Naphthalene, (16)Norbornadiene, (17)Octatetracene, (18)p-Benzoquinone, (19)Propanamide, (20)Pyrazine, (21)Pyridazine, (22)Pyridine, (23)Pyrimidine, (24)Pyrrole. Colour code: Yellow-Carbon, Red-Oxygen, Turquoise-Hydrogen, Blue-Nitrogen.

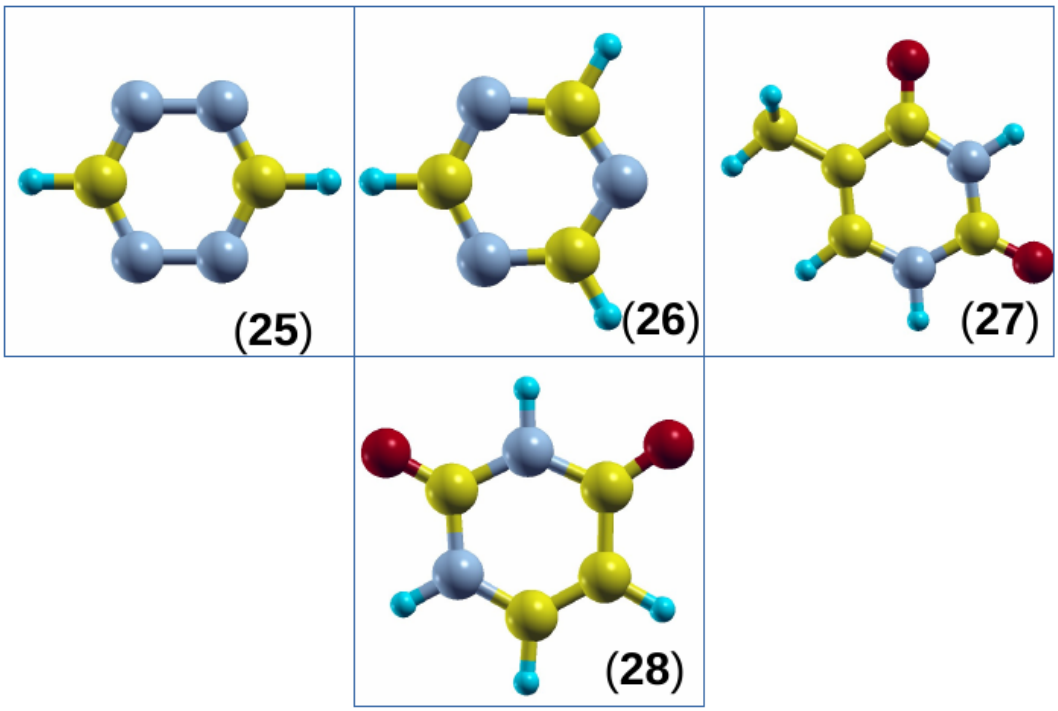

Figure 6.4: Structure of the molecules investigated in this chapter: (25)s-Tetrazine, (26)s-Triazine, (27)Thymine, (28)Uracil. Colour code: Yellow-Carbon, Red-Oxygen, Turquoise-Hydrogen, Blue-Nitrogen.

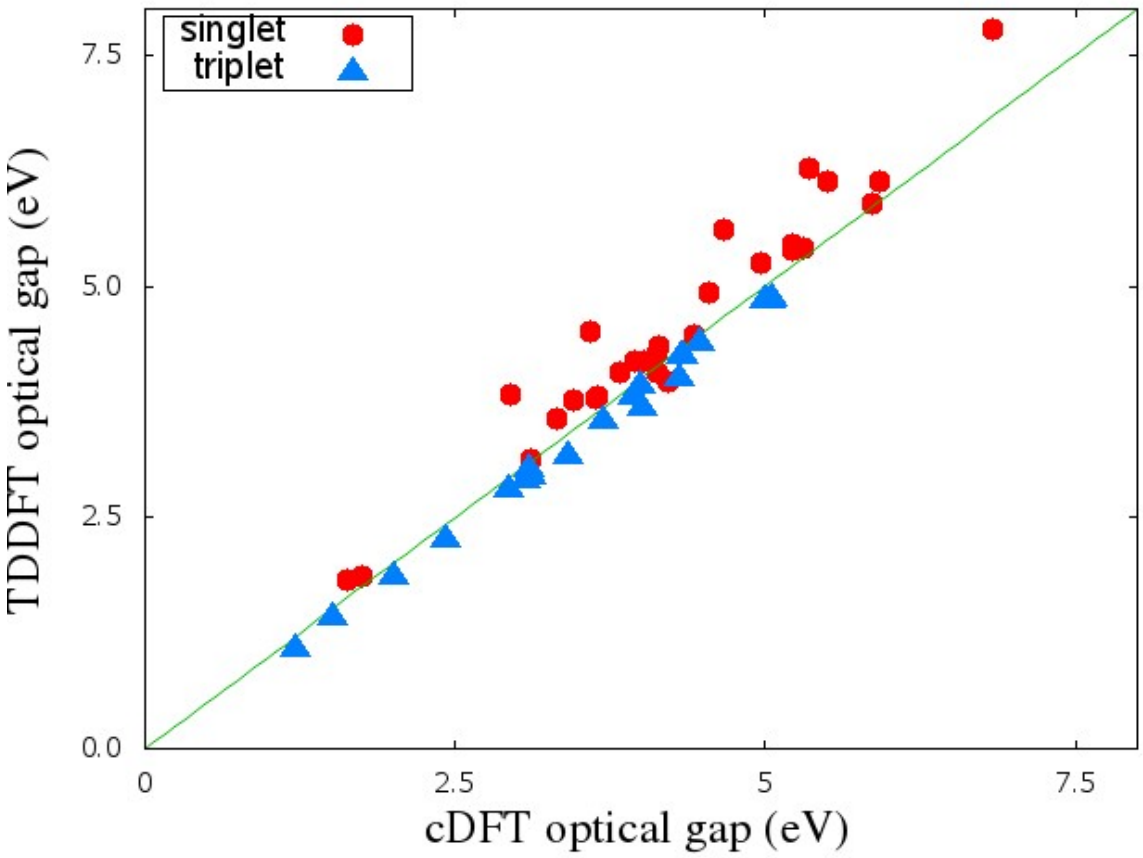

Figure 6.5: A scatter plot of the optical gap of molecules obtained with the excitonic DFT method and with linear response TDDFT. The blue dots and the red triangles denote singlet and triplet gaps, respectively. The green straight line stands for $(x = y)$

formula, the singlet optical gaps are also calculated by cDFT with appreciable accuracy.

A plot of the difference in charge density between the excited state and the ground state provides a good approximation for the exciton charge density. In Fig. 6.6 we show such plots for a representative molecule propanamide. A difference in charge density between the LUMO and the HOMO orbital would be a crude approximation for the exciton density in the KS system if the promotion of electron is not followed by a relaxation of the energy levels. We see that such plot, as shown in the panel (a) of Fig. 6.6 is in good agreement with the exciton density plots of the singlet and the triplet state obtained with our calculations, as shown in panel (b) and (c), respectively. However, the singlet exciton charge density is less pronounced than the LUMO-HOMO

density difference, as expected due to exciton binding. The singlet exciton density is also less pronounced than the triplet counterpart, as expected from Pauli exclusion principle.

The Spin Projection Correction Method

Eq. (6.30), which is used for calculating the singlet excitation energies, is an interacting many-body approximation of Eq. (6.29), which is true for an RKS system. However, we are operating under an UKS framework here. For the actual interacting many-body system, the three operators $\hat{H}$, $\hat{S}^2$ and $\hat{S}_z$ commute with each other. Therefore, the energy eigenstates can always be chosen as eigenstates of $\hat{S}^2$ and $\hat{S}_z$. For each eigenvalue of $\hat{S}^2$, there are always $(2S+1)$ degenerate eigenstates differing in their $\hat{S}_z$ eigenvalues. In UKS DFT, in addition to the total electron density, the spin-density is also identical for the KS system and the interacting system. However, even though for the UKS system, $\hat{S}_z$ and $\hat{H}$ still commute, the operator $\hat{S}^2$ does not commute with the KS Hamiltonian. Thus, the KS energy eigenstate does not have to be an eigenstate of $\hat{S}^2$. This is known as *spin contamination* [191], meaning that the KS eigenstates are a linear combination of eigenstates of $\hat{S}^2$ (note that this statement is true for the KS state, not for the true interacting state). Within the KS formalism, it is impossible to have $\hat{S}^2$ commuting with the Hamiltonian, if one enforces the spin-density of the KS system to match that of the interacting one [192]. Therefore, in a ground state UKS calculation employing the hypothetical exact XC-functional, the self-consistent field (SCF) cycle will converge to a non-interacting state with the same electron density and spin-density as those of the interacting many-body system but can have a different value for $\langle \hat{S}^2 \rangle$.

At this stage, it is important to note that, even though for the actual interacting system, $\hat{S}^2$ commutes with $\hat{H}$, this is not necessarily true for the interacting system accessible by the approximate density functional. Thus, we essentially have three different systems: 1) the non-interacting KS system, 2) the interacting system described by the approximate XC-functional such that its ground state density and spin-density match those of the UKS system (for these two systems, the energy eigenstate is not necessarily an eigenstate of $\hat{S}^2$), and 3) the actual many-body system that we want

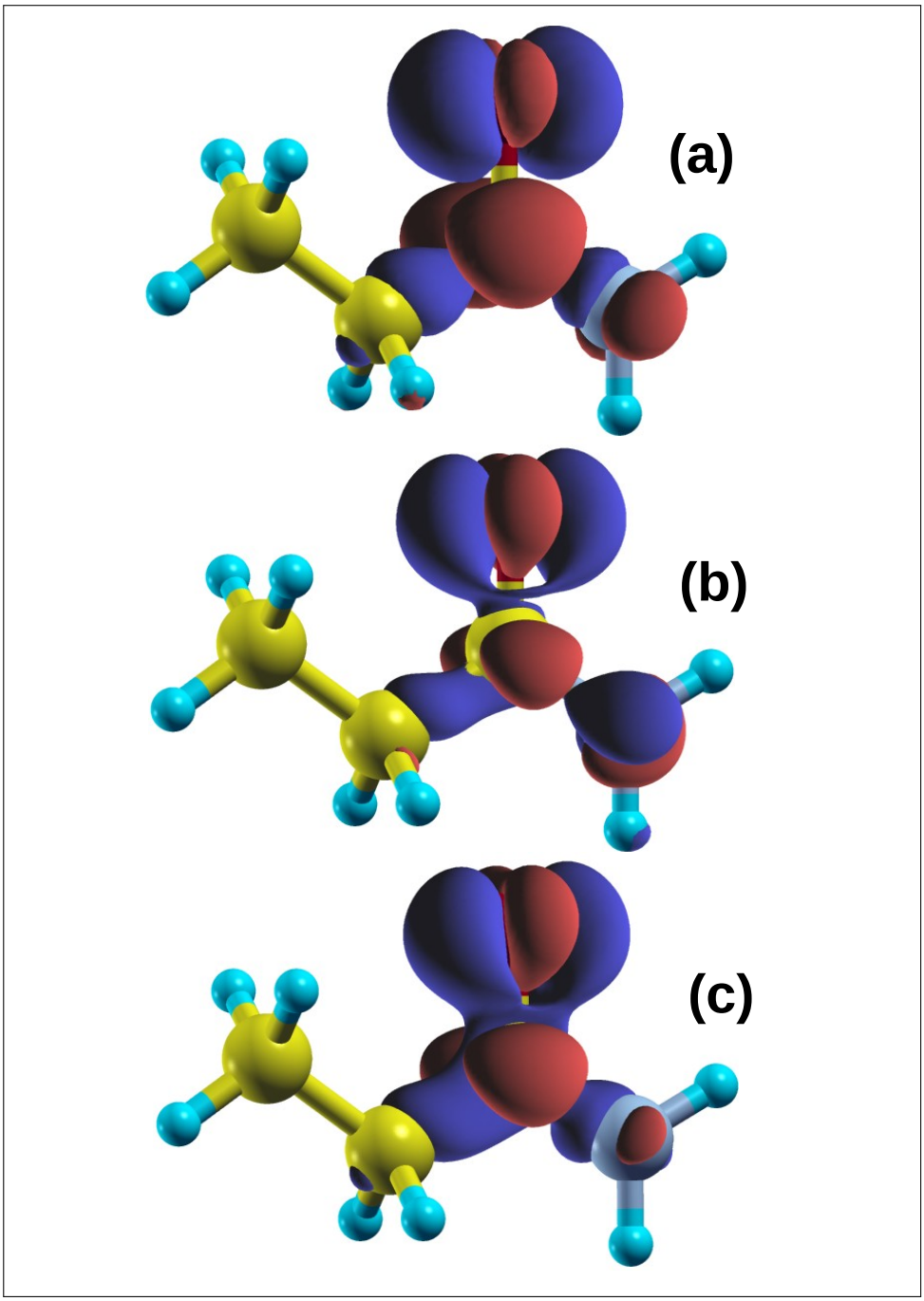

Figure 6.6: Plot of exciton charge density for the propanamide molecule. (a) shows the difference in charge density between the KS LUMO and HOMO orbital of the ground state. (b) and (c) show respectively the singlet and triplet exciton density obtained with the excitonic DFT method.

to be describe but whose properties are not accessible with the approximate density functionals.

Within the UKS formalism, where the single particle orbitals are spin-dependent, the equivalent of Eq. (6.24) would be

$$ {}^{S=0}\Psi^{(\mathrm{RKS})}_{m_s=0}(1,2) = \frac{1}{\sqrt{2}} \left[\begin{vmatrix} \varphi_{a\uparrow}(1) & \varphi_{a\uparrow}(2) \\ \varphi_{b'\downarrow}(1) & \varphi_{b'\downarrow}(2) \end{vmatrix} + \begin{vmatrix} \varphi_{b\uparrow}(1) & \varphi_{b\uparrow}(2) \\ \varphi_{a'\downarrow}(1) & \varphi_{a'\downarrow}(2) \end{vmatrix} \right] . \tag{6.33} $$

where a and b are single particle orbitals occupied by electrons with spin up, while a' and b' are those occupied by electrons with spin down. Not only do the two constituent SDs correspond to different energies, the state ${}^{S=0}\Psi^{(\mathrm{UKS})}_{m_s=0}(1,2)$ is not even an eigenstate of $\hat{S}^2$. So, strictly speaking, Eq. (6.30) is not valid for an UKS system.

Strictly speaking, the energy of the excited interacting state with $(S = 0, m_s = 0)$ is not accessible with the pristine UKS DFT formalism even with the exact XC-functional. This is because the KS orbitals have no physical meaning. They merely form a non-interacting many-body state, which, when determined with the hypothetical exact XC-functional, has the same density as that of the ground state of the real interacting system. A spin-contaminated UKS wave function does not necessarily mean that the corresponding interacting wave-function is spin contaminated. So, even if we manage to cure for the spin-contamination in the UKS wave-function by finding the desired eigenfunction of $\hat{S}^2$ as a linear combination of energy eigenfunctions, there is no formal reason to expect that the same linear combination will cure any spin-contamination present in the interacting wave function.

Here we would like to present calculations, performed with an alternative approximation for accessing the singlet many-body excited state.

We know that the many-body energy eigenstate described by the approximate XC-functional is not necessarily an eigenstate of $\hat{S}^2$. However, within the LDA, the value of this $\langle \hat{S}^2 \rangle$ can be calculated [193, 194] from the two-particle density matrix. In the *spin-projection correction scheme*, this information can be used to estimate the

spin-contamination $\langle S^2 \rangle_c$ of the many-body state [195, 196]. Let the contaminated many-body state $|\Psi_c\rangle$ be a linear combination of two states, $|^S\Psi\rangle$ and $|^{S+1}\Psi\rangle$. Then, we have

$$|\Psi_c\rangle = (1-a)\,|^S\Psi\rangle + a\,|^{S+1}\Psi\rangle\,, \tag{6.34}$$

and therefore

$$\begin{aligned} E_c &= (1-a)E_S + aE_{S+1} \\ \Rightarrow E_S &= \frac{E_c - aE_{S+1}}{1-a}, \end{aligned} \tag{6.35}$$

where the subscript c refers to the contaminated state. Eq. (6.34) gives us,

$$\begin{aligned} \langle S^2 \rangle_c &= (1-a)S(S+1) + a(S+1)(S+2), \\ a &= \frac{\langle S^2 \rangle_c - S(S+1)}{2(S+1)}. \end{aligned} \tag{6.36}$$

For our probelm, $S = 0$, so that the contaminated state is expressed as a linear combination of a triplet and a singlet. From an UKS calculation with (spin=0), we calculate $\langle S^2 \rangle$ in terms of two-particle density matrix in accordance with ref. [193] and find a from Eq. (6.36). This, with the knowledge of E_c and E_{S+1}, evaluated with cDFT calculations with (spin=0) and (spin=1), respectively, is then used to calculate the energy E_S of the singlet interacting state within the approximate XC-functional from Eq. (6.35). The cDFT singlet optical gap corresponding to this treatment is plotted against the results obtained with TDDFT in the scatter plot of Fig. (6.7). For the sake of comparison, in the same graph, we plot the singlet gaps obtained from the *sum method* as well. Interestingly, the results obtained with the *sum method* are in better agreement with the TDDFT results, than those obtained with the correction through spin-projection. We attribute this to possible errors in finding $\langle S^2 \rangle$ through the approximate formalism.

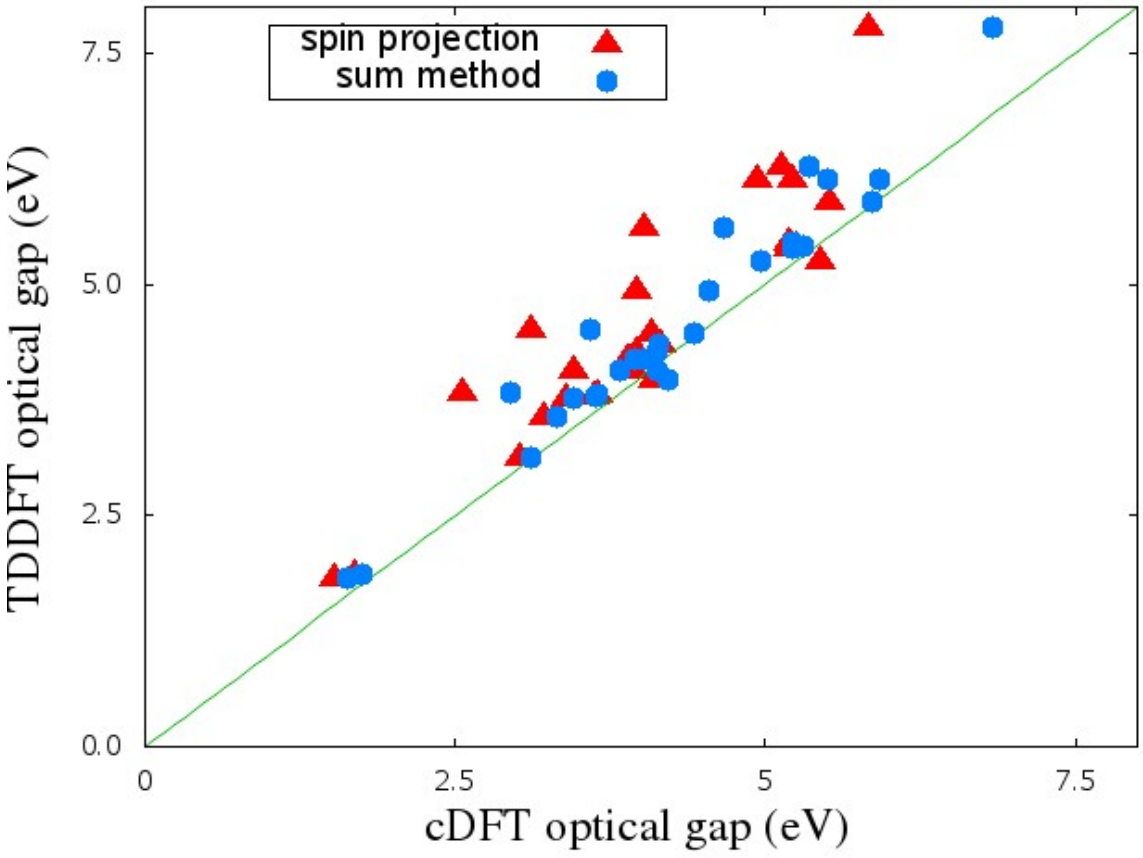

Figure 6.7: A scatter plot of the optical gap of molecules obtained with the excitonic DFT method and with linear response TDDFT. The blue dot and the red triangle represent singlet gaps obtained with the sum method and with spin-projection correction, respectively. The green straight line stands for $x = y$

Correction to the XC-Energy

Before concluding this section, we would like to briefly touch upon an additional scheme of further correction that we have tried. In Eq. (6.30), we find the energy of a singlet state from a linear combination of energies. Since this singlet state should be non spin-polarized, we attempt to remove contributions of spin-polarization from the linear combination. As post-processings on the cDFT ($m_s = 0$) and ($m_s = 1$) excited state runs, we estimate the non spin-polarized XC energy contribution to these systems, from the density matrices obtained with spin-polarized calculations, by setting a local copy of the spin-polarization to zero at all points. This gives us the non-spin polarized XC contribution due to the density matrix obtained with spin-polarization. Then, the spin-polarization corrected energy is estimated as

$$\begin{aligned} {}^{S=0}E_{corrected} = &\left[2 \times^{\mathrm{SD}} E^{\mathcal{I}}_{m_s=0}(\text{Total}) - {}^{S=1} E^{\mathcal{I}}_{m_s=1}(\text{Total})\right] \\ &- \left[2 \times^{\mathrm{SD}} E^{\mathcal{I}}_{m_s=0}(\text{XC Pol}) - {}^{S=1} E^{\mathcal{I}}_{m_s=1}(\text{XC Pol})\right] \\ &+ \left[2 \times^{\mathrm{SD}} E^{\mathcal{I}}_{m_s=0}(\text{XC Non-Pol}) - {}^{S=1} E^{\mathcal{I}}_{m_s=1}(\text{XC Non-Pol})\right] \end{aligned} \tag{6.37}$$

where the terms "Total", "XC Pol" and "XC Non-Pol" refer to the total energy, the XC contribution with polarization and the XC contribution without polarization respectively, the latter being obtained from the post-processing procedure mentioned above. The singlet gaps so calculated are plotted in the scatter plot Fig. 6.8.

6.3.2 Optical gap of Periodic System

Finally, as a more ambitious attempt of extending this method, we try to mention our ongoing work on the calculation of the optical gap of periodic solids. However, for this, one must address the problems arising due to unphysical charge delocalization caused by commonly used approximate XC-functionals. Earlier, we have discussed this in the context of error in band-gap (see section 3.2.1). In a large system (for a periodic system, when the unit cell is large) an added charge is unphysically delocalized due to the nature

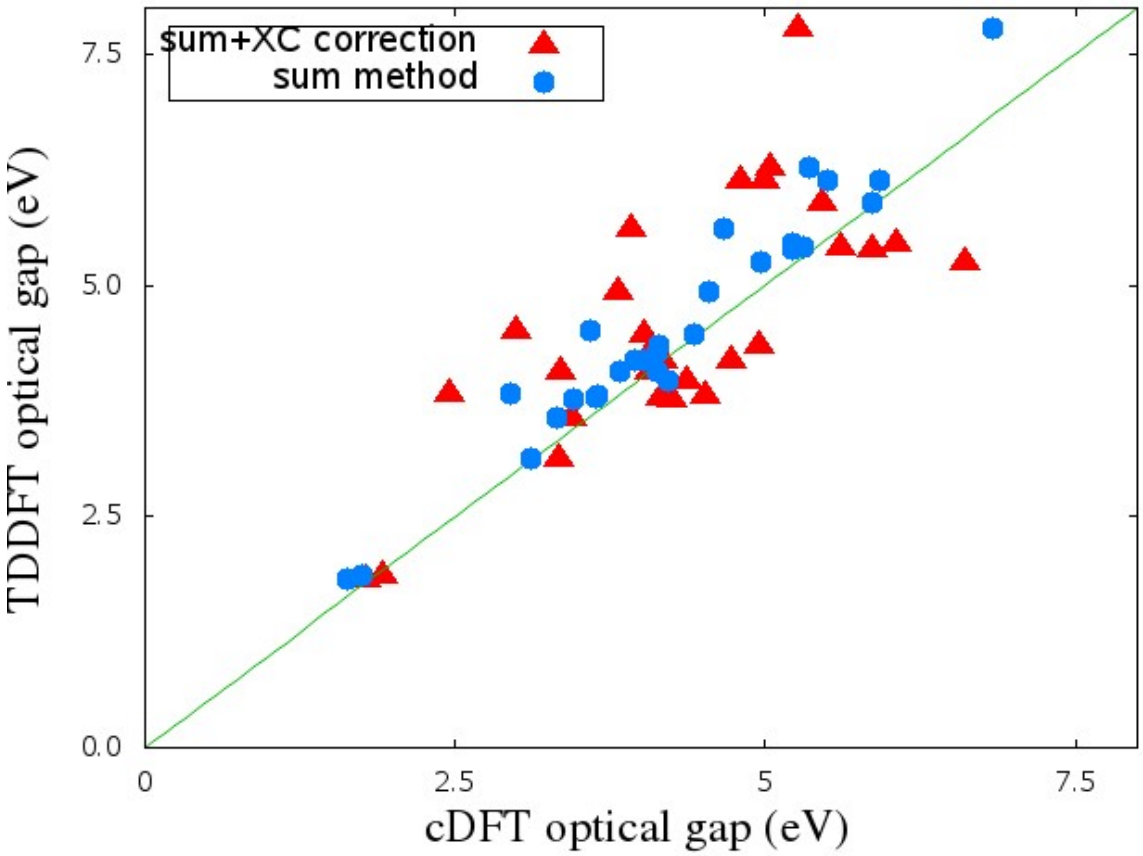

Figure 6.8: A scatter plot of the optical gap of molecules obtained with the excitonic DFT method and with linear response TDDFT. The cDFT gaps are obtained with the sum method. The the red triangle and the blue dot represent singlet gaps obtained with and without the correction with XC-functional, respectively. The green straight line stands for $x = y$

of the approximate XC-functional. This is responsible for lowering the energy of the charged system and consequently to reducing the energy gap. In contrast, if, for the periodic system, we use a unit cell that is too small, then the added charge will be artificially confined, resulting in an unphysically large gap. If the size of the unit cell is "just right" for containing the added charge, then we can expect reliable results. In a work from 2010, Chan and Ceder [197] used this idea and estimated the size of such a cell in order to calculate the band gap by introducing the Δ-sol method. In the Δ-SCF technique, which is widely used for the case of molecules, an electron is added to/removed from an N-electron system and the fundamental gap is calculated as in Eq. (3.40), namely as,

$$E_{FG} = (E_0^{N+1} - E_0^N) - (E_0^N - E_0^{N-1}). \tag{6.38}$$

The argument of the aforementioned paper is the following. If the value of N, from (to) which an electron is removed (added) is chosen to be the number of electrons present within the size of the exchange-correlation hole, then that unit-cell volume of is comparable to the screening length of the added charge and the cell size is "just right" for containing it. Thus, with this desired value of $N = N^*$, the band gap can be evaluated with the standard Δ-SCF method. XC-functionals, like LDA or GGA, give quite accurate results for the size of the exchange-correlation hole and in most cases, this is not very sensitive to the pair distribution function, which is a material specific property. Therefore, the same N^* can be used to calculate the band-gap of a wide range of solids. Based on computational tests on a variety of solids, the authors of Ref. [197] have found this value of N^*.

Since a similar delocalization error is present in the case of the creation of an exciton within LDA/GGA approximations, we intend to test the applicability of the aforementioned method for the calculation of optical gaps of solids. Here, one must note that the screening length and consequently the value of N^* is, in principle, different for an added charge and an exciton. However, in materials with low exciton-binding energy, i.e. in materials for which the optical gap is very close to the electronic gap,

Compound	Singlet gap (eV)	Triplet gap (eV)	Δ-sol gap (eV)
GaAs	1.53	1.44	1.5
ZnS	3.77	3.61	3.6
AlN	5.37	5.26	5.3

Table 6.1: Singlet and triplet optical gaps calculated at 300 K with the excitonic DFT method. For comparison, we also show electronic band-gaps calculated with the Δ-sol procedure in ref. [197]. For our calculation we use the values of $N*$ reported in the same paper.

one can expect the two 'N^*'s to be similar. Thus, one can use the value of N^* reported in Ref. [197] and calculate the optical gap of solids known to have low exciton binding energy.

Since ONETEP performs a $\Gamma-$ point calculation, all the energy eigenvalues can essentially be thought of as molecular levels and therefore only the lowest transitions are accessible. Here, we limit ourselves to solids with direct band-gap (in order to obtain the lowest band-gap of materials with indirect band gap, one must ensure that the levels pertaining to the valence band maximum and conduction band minimum are both accurately sampled). So far, we have obtained the optical gaps of GaAs, ZnS and AlN with our method at a temperature of 300 K with the LDA functional and the results are shown in Tab. (6.1) along with the band gaps calculated with the Δ-sol method of Chan and Ceder [197]. Note that the finite temperature calculations are performed with the ensemble DFT formalism [156]. Note that for these materials, the exciton binding energy is known to be very small [198, 199, 200] and consequently, their optical gaps should be very similar to the electronic band gaps.

Before concluding our discussion on single particle excitations, we note that, so far our proposed method simulates only the lowest energy excitations of a given spin state. However, in principle, excitations of higher energy can be simulated by employing multiple constraints, each containing one Lagrange multiplier V_c. For example, if $\hat{\mathbb{P}}_0$ and $\hat{\mathbb{P}}_1$ denote the projectors for the valence subspaces of the ground state, obtained with regular DFT and the first excited state, obtained with excitonic DFT, respectively, then

the energy of the second excited state can be found by confining $N-1$ electrons within the subspace of $\hat{\mathbb{P}}_0$ using a Lagrange multiplier V_c^1 and, separately, confining $N-1$ electrons within the subspace of $\hat{\mathbb{P}}_1$ using a multiplier V_c^2. In general, the total-energy of the I^{th} excited state system of a given spin symmetry will be found at the stationary point of

$$W = E\left[\hat{\rho}\right] + \sum_{i}^{I} V_c^i \left(\text{Tr}\left[\hat{\rho}\hat{\mathbb{P}}_{i-1}\right] - (N-1) \right) . \tag{6.39}$$

6.3.3 Double Excitation of Beryllium

Finally, we explore the ability of the excitonic DFT method to calculate energies related to double excitations, something that is not accessible by TDDFT within the adiabatic approximation. To this end, we choose the Beryllium (Be) atom for which, within a quasiparticle picture, a double excitation amounts to excitation of two electrons from the $2s$ level to the $2p$ level [207]. To calculate this within the excitonic DFT framework, we run three calculations (noting that, for Be, the $1s^2$ electrons are core electrons within the pseudopotential approximation):

1. A regular DFT calculation to calculate the ground state energy E_0.
2. A charge neutral cDFT calculation with spin=0 confining 0 electrons in the valence subspace of the DFT run to obtain the doubly excited singlet state energy $E_{s=0}^{\text{DE}}$.
3. A charge neutral cDFT calculation with spin=1 confining 0 electrons in the valence subspace of the DFT run to obtain the double excited triplet state energy $E_{s=1}^{\text{DE}}$.

Then the singlet and triplet double excitation energies are calculated simply as $(E_{s=0}^{\text{DE}} - E_0)$ and $(E_{s=1}^{\text{DE}} - E_0)$, respectively. Note that since our method is rooted in promoting an integer number of electrons out of the ground state valence KS subspace, at least in its current form, we can only access states which are pure (i.e. purely single excitonic, purely double excitonic etc.) in character. In Fig. 6.9 we plot the single and double excitation energies of Be atom calculated with different XC-functionals. The

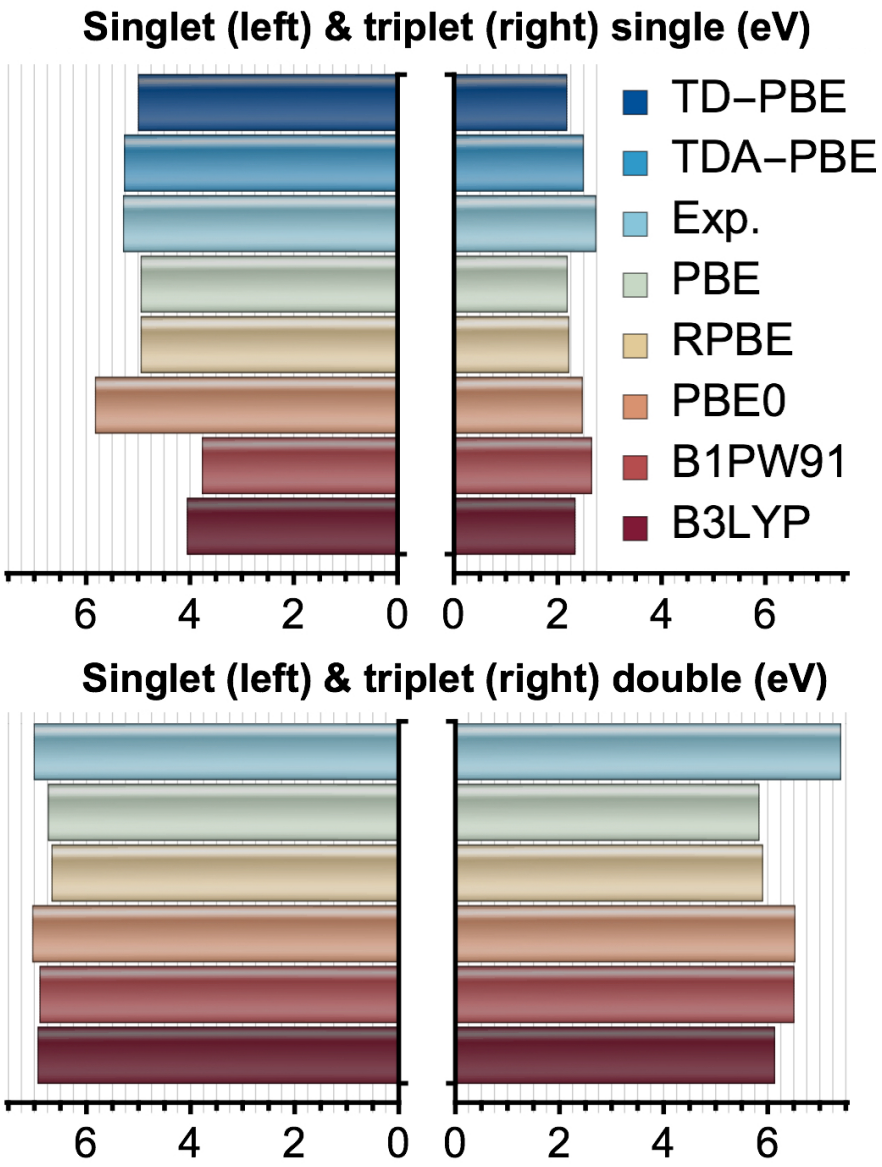

Figure 6.9: Plot of excitation energies for Beryllium. The top left, top right, bottom left and bottom right panels correspond to singlet single excitation, triplet singlet excitation, singlet double excitation and triplet double excitation respectively. The plots contain results obtained with the excitonic DFT method employing GGA-based XC-functionals like PBE [94], RPBE [201] and hybrid functionals like PBE0 [202], B3LYP [203] and B1PW91 [204]. For the single excitation, we also include results obtained with PBE functional from TDDFT calculations. Here TD-PBE and TDA-PBE refer to TDDFT calculations with linear response and Tam-Dancoff approximation [205], respectively. The plots also contain experimental values [206] of the excitation energy.

excitation energies so obtained agree well with those calculated with ensemble DFT in ref. [177], for all four excitations. However, note that although, for the singlet double excitation, our results agree well with experimental values, such agreement is not present in the case of triplet double excitation. For the triplet case, the $2s^2 \rightarrow 2p^2$ excitation energy is higher than the singlet one, contrary to what is expected from Hund's rule. We suspect that this is because the experimental triplet is not a pure double excitation but contains contribution from one or more single excitations.

6.4 Conclusion

In this chapter, we have presented *excitonic DFT*, an approximate method for obtaining the optical gap of materials in a computationally inexpensive way. As an approximation to the many-body excited state, we promote an electron of the KS system outside the valence subspace of the ground state. Then the optical gap is simply determined as the difference in energy between the aforesaid excited state and the ground state. In order to access the excited singlet state energy, we use the 'sum method' where the excited state is expressed as a linear combination of Slater determinants. By applying this method on 28 organic molecules, for which TDDFT results are available, we see that despite major approximations, this method produces remarkably good results. We propose the possibility of extension of this method to include periodic systems. This can be accomplished by creating an exciton within a unit cell commensurate with the size of the exciton. To demonstrate this, we show results for calculation of optical gaps on 3 direct band gap solids. Finally, we note that unlike TDDFT or BSE with kernels independent of frequency, the excitonic DFT technique can be used to access double excitations, as shown with calculations on an isolated Beryllium atom. As such, this method appears to be a promising technique, offering several advantages over the other existing methods, for calculation of optical gaps and it would be useful and interesting to extend it to the treatment of more exotic systems.

Chapter 7

Calculation of the Spin-Orbit Coupling Terms from Maximally Localized Wannier Functions

As mentioned earlier, the goal of the QUEST project is to construct and solve a tight-binding Hamiltonian, including spin degrees of freedom, for a molecular crystal. For the prospect of using OSCs in spintronic applications it would be important to study spin-relaxation in such crystals.

In an organic semiconductor (OSC) the unwanted spin-relaxation can be caused by the presence of paramagnetic impurities, by SO coupling and by hyperfine interaction. In general paramagnetic impurities can be controlled to a very high degree of precision and they can be almost completely eliminated from an OSC during the chemical synthesis [208]. The hyperfine interaction instead is usually considered small. This is because there are only a few elements typically present in organic molecules with abundant isotopes barring nuclear spins. The most obvious exception is hydrogen. However, most of the OSC crystals are π-conjugated and the π-states, responsible for the extremal energy levels, and hence for the electron transport, are usually delocalized. This means that the overlap of the wave function over the H nuclei has to be considered small. Fi-

nally, also the SO coupling is weak owing to the fact that most of the atoms composing organic compounds are light.

As such, since all the non-spin-conserving interactions are weak in OSCs, it is not surprising that there is contradictory evidence concerning the interaction mostly responsible for spin-diffusion in organic crystals. Conflicting experimental evidence exists supporting either the SO coupling [209, 210] or the hyperfine interaction [211, 212], indicating that the dominant mechanism may depend on the specific material under investigation. For this reason it is important to develop methods for determining the strength of both the SO and the hyperfine coupling in real materials. These can eventually be the basis for constructing effective Hamiltonians to be used for the evaluation of the relevant thermodynamics quantities (e.g. the spin diffusion length). Here we present one of such methods for the case of the SO interaction.

The SO interaction is a relativistic effect arising from the electronic motion in the nuclear potential. In the reference frame of the electron, the nucleus moves and creates a magnetic field, which in turn interacts with the electronic spin. This is the spin-orbit coupling [213]. Since the SO interaction allows the spin of an electron to change direction during the electron motion, it is an interaction responsible for spin relaxation. The SO coupling operator is given by [214]

$$\hat{V}_{\mathrm{SO}} = \sum_{k} \bar{V}_{l}^{\mathrm{SO}}(k)\hat{\mathbf{L}}(k) \cdot \hat{\mathbf{S}}, \tag{7.1}$$

where $\hat{\mathbf{S}}$ is the spin operator, $\hat{\mathbf{L}}(k)$ is the angular momentum operator corresponding to the k-th atom and $\bar{V}_{l}^{\mathrm{SO}}(k)$ is a scalar term depending on the orbital angular momentum quantum number l. Thus $\bar{V}_{l}^{\mathrm{SO}}(k)\hat{\mathbf{L}}(k).\hat{\mathbf{S}}$ is the term responsible for SO coupling due to the relative motion of the k-th ion about the electron. The SO matrix elements evaluated in the SIESTA code are,

$$V^{\mathrm{SO}}_{ij,s_1,s_2} = \langle \phi^{s_1}_i | \sum_k \bar{V}^{\mathrm{SO}}_l(k) \hat{\mathbf{L}}(k) \cdot \hat{\mathbf{S}} | \phi^{s_2}_j \rangle \,, \tag{7.2}$$

where $|\phi^s_i\rangle$, the i-th spin-polarized SIESTA atomic orbital with spin s, is given by,

$$|\phi^s_i\rangle = |\phi^s_{n_i,l_i,M_i}\rangle = |R_{n_i,l_i}\rangle \otimes |l_i, M_i\rangle \otimes |s\rangle \,. \tag{7.3}$$

Note that here, each orbital is denoted with a unique i, i.e. i contains both the index of the unit cell and the index of the orbital within the unit cell. Then, n_i, l_i, M_i and s denote the principal, azimuthal, magnetic and spin quantum number of the real orbital[1], respectively. The three terms on the right-hand side of Eq. (7.3) denote respectively the radial part, the real spherical harmonic and the spinor for the atomic orbital. The term $\bar{V}^{\mathrm{SO}}_l(k)$ is very short ranged. Hence, for computational simplicity, in the SIESTA implementation of the SO coupling [215], all the terms for which $|\phi^{s_1}_i\rangle$, $\bar{V}^{\mathrm{SO}}_l(k)$ and $|\phi^{s_2}_j\rangle$ are not on the same atom are taken to be zero (on-site approximation).

7.1 Maximally-Localized Wannier Functions

The computational applicability and success of the TB model depends largely on the basis set employed. So far, we have two possible complete basis sets at our disposal.

- The Bloch states, which are typically delocalized over the entire crystal and therefore are not suitable for a tight-binding method, which requires a localized basis set.
- The localized atomic orbital basis set of SIESTA. However, choosing this basis set amounts to working with a TB model with large dimensions and high computational demand. In many practical scenarios, the number of energy eigenstates that

[1] in SIESTA the complex spherical harmonics are linearly combined to form real spherical harmonics.

contribute toward interesting phenomena (typically the valence bands at the top and conduction bands at the bottom) are much smaller than the total number of states available from first principles calculations. Thus, if one can work with only the states of interest (disregarding all others), one can reduce the dimensionality of the problem and greatly save computational resources. Unfortunately, this is not a viable option with atomic basis functions.

Let us look at the example of a 100 nm long 1 dimensional crystal of triarylamine molecules, which is a known organic semiconductor. The relaxed distance between two molecules is 4.8 Å. Thus, the crystal will contain 208 molecules. In a SIESTA calculation with the standard double-zeta polarized basis set each molecule contains $3,164$ orbitals producing $658,112$ basis functions for the entire crystal.

We can see that neither the Bloch states nor the atomic orbitals are ideal for the construction of an effective TB model and one has to look for some alternate option. This alternate ideal basis set should be made of localized functions spanning the subspace of the desired Bloch states only. In order to satisfy this criterion, one uses the Wannier functions [73]. For a set of N' isolated Bloch states, $|\psi_{m\mathbf{k}}\rangle$ (these for instance can be the KS eigenstates of a crystal), one can obtain the associated N' Wannier functions from the definition,

$$|w_{n\mathbf{R}}\rangle = \frac{V}{(2\pi)^3}\int_{\mathrm{BZ}}\left[\sum_{m=1}^{N'} U_{mn}^{\mathbf{k}}\,|\psi_{m\mathbf{k}}\rangle\right] e^{-i\mathbf{k}\cdot\mathbf{R}} d\mathbf{k}\,, \tag{7.4}$$

where $|w_{n\mathbf{R}}\rangle$ is the n-th Wannier vector centred at the lattice site $\mathbf{R}$, V is the volume of the primitive cell and the integration is performed over the first Brillouin zone (BZ). In Eq. (7.4) $U^{\mathbf{k}}$ is a unitary operator that mixes the Bloch states and hence defines the specific set of Wannier functions. Clearly, to uniquely specify the set of Wannier functions, one needs a unique defintion for the unitary operator. A particularly convenient gauge choice for $U^{\mathbf{k}}$ is made by minimizing the Wannier functions spread, which is given by

$$\Omega = \sum_n \left[\langle w_{n\mathbf{0}}|\, r^2\, |w_{n\mathbf{0}}\rangle - |\,\langle w_{n\mathbf{0}}|\,\mathbf{r}\,|w_{n\mathbf{0}}\rangle\,|^2\right]\,. \tag{7.5}$$

The resulting Wannier functions are known as Maximally-Localized Wannier Functions (MLWFs) [125, 70] and a procedure for the construction of MLWFs is implemented in the package WANNIER90 [216]. WANNIER90 takes as input the Bloch states ans constructs the MLWFs by minimizing Ω. In the following, we describe a method for obtaining the SO coupling matrix elements with respect to these MLWFs.

7.2 Method

7.2.1 General idea

Here we describe the idea behind our method, which is general and does not depend on the specific implementation used for calculating the band structure. In the absence of SO coupling a Wannier function of spin s_1 is composed exclusively of Bloch states with the same spin, s_1. By moving from a continuos to a discrete k-point representation the spin-polarized version of Eq. (7.4) becomes [70]

$$|w^{s_1}_{n\mathbf{R}}\rangle = \frac{1}{N}\sum_{\mathbf{k}}\sum_{m} U^{s_1}_{mn}(\mathbf{k})\,|\psi^{s_1}_{m\mathbf{k}}\rangle\, e^{-i\mathbf{k}\cdot\mathbf{R}}\,. \tag{7.6}$$

Note that this represents either a finite periodic lattice comprising N unit cells or a sampling of N uniformly distributed k-points in the Brillouin zone of an infinite lattice. Here the Bloch states, which are normalized within each unit cell according to the relation $\langle\psi^{s_1}_{m\mathbf{k}}|\psi^{s_2}_{n\mathbf{k}'}\rangle = N\delta_{m,n}\delta_{\mathbf{k},\mathbf{k}'}\delta_{s_1,s_2}$, obey to the condition $\psi_{p\mathbf{k}}(\mathbf{r}_1) = \psi_{p\mathbf{k}}(\mathbf{r}_{N+1})$, where $\psi_{p\mathbf{k}}(\mathbf{r}_m)$ denotes the Bloch function for the p-th band at the wavevector $\mathbf{k}$ and position $\mathbf{r}_m$.

The projection of a generic Bloch state onto a MLWF in the absence of SO

coupling can be written as

$$\begin{aligned}
&\langle \psi^{s_1}_{q\mathbf{k}'} | w^{s_2}_{n\mathbf{R}_2} \rangle = \\
&= \frac{1}{N} \sum_{\mathbf{k}} \sum_{m} U^{s_2}_{mn}(\mathbf{k}) \, \langle \psi^{s_1}_{q\mathbf{k}'} | \psi^{s_2}_{m\mathbf{k}} \rangle \, e^{-i\mathbf{k}\cdot\mathbf{R}} = \\
&= \frac{1}{N} \sum_{\mathbf{k}} \sum_{m} U^{s_2}_{mn}(\mathbf{k}) e^{-i\mathbf{k}.\mathbf{R}} N \delta_{q,m} \delta_{\mathbf{k},\mathbf{k}'} \delta_{s_1,s_2} = \\
&= U^{s_2}_{qn}(\mathbf{k}') e^{-i\mathbf{k}'\cdot\mathbf{R}} \delta_{s_1,s_2} \, .
\end{aligned} \tag{7.7}$$

Hence a generic SO matrix element can be expanded over the MLWF basis set as

$$\begin{aligned}
&\langle w^{s_1}_{m\mathbf{R}_1} | \, \mathbf{V}_{\mathrm{SO}} \, | w^{s_2}_{n\mathbf{R}_2} \rangle \\
&= \frac{1}{N^2} \sum_{p,q} \sum_{\mathbf{k}_1,\mathbf{k}_2} \langle w^{s_1}_{m\mathbf{R}_1} | \psi^{s_1}_{p\mathbf{k}_1} \rangle \, (\mathbf{V}_{\mathrm{SO}})^{s_1,s_2}_{p\mathbf{k}_1,q\mathbf{k}_2} \, \langle \psi^{s_2}_{q\mathbf{k}_2} | w^{s_2}_{n\mathbf{R}_2} \rangle \\
&= \frac{1}{N^2} \sum_{p,q} \sum_{\mathbf{k}_1,\mathbf{k}_2} U^{*(s_1)}_{pm}(\mathbf{k}_1) e^{i\mathbf{k}_1\cdot\mathbf{R}_1} (\mathbf{V}_{\mathrm{SO}})^{s_1,s_2}_{p\mathbf{k}_1,q\mathbf{k}_2} \cdot U^{s_2}_{qn}(\mathbf{k}_2) e^{-i\mathbf{k}_2\cdot\mathbf{R}_2} \, ,
\end{aligned} \tag{7.8}$$

where

$$(\mathbf{V}_{\mathrm{SO}})^{s_1,s_2}_{p\mathbf{k}_1,q\mathbf{k}_2} = \langle \psi^{s_1}_{p\mathbf{k}_1} | \, \mathbf{V}_{\mathrm{SO}} \, | \psi^{s_2}_{q\mathbf{k}_2} \rangle \, . \tag{7.9}$$

It must be noted that in the absence of SO coupling, the Bloch states are spin-degenerate, i.e. there are two states corresponding to each spatial wave-function, one with spin up, $|\psi^{\uparrow}(\mathbf{r})\rangle = |\psi(\mathbf{r})\rangle \otimes |\uparrow\rangle$, and one with spin down, $|\psi^{\downarrow}(\mathbf{r})\rangle = |\psi(\mathbf{r})\rangle \otimes |\downarrow\rangle$. The same is true for the Wannier functions, i.e. one has always the pair $|w^{\uparrow}(\mathbf{r})\rangle = |w(\mathbf{r})\rangle \otimes |\uparrow\rangle$, $|w^{\downarrow}(\mathbf{r})\rangle = |w(\mathbf{r})\rangle \otimes |\downarrow\rangle$. In the presence of SO coupling, spin mixing occurs and each Bloch and Wannier state is, in general, a linear combination of both spin vectors. Since the Bloch states (or the Wannier ones) obtained in the absence of SO coupling form a complete basis set in the Hilbert space, the SO coupling operator can be written over such basis provided that one takes both spins into account. Therefore we use such spin-degenerate states as our basis for all calculations.

7.2.2 Numerical Implementation

The derivation leading to Eq. (7.8) is general and the final result is simply a matrix transformation of the SO operator from the basis of the Bloch states to that of the

Wannier ones. Note that both basis sets are those calculated in the absence of SO coupling, i.e. we have assumed that the spatial part of the basis function is not modified by the introduction of the SO interaction. For practical purposes we now we wish to re-write Eq. (7.8) in terms of a localized atomic-orbital basis set, i.e. we wish to make our method applicable to first-principles DFT calculations implemented over local orbitals. In particular all the calculations that will follow use the SIESTA package, which expands the wave-function and all the operators over a numerical atomic-orbital basis sets, $\{|\phi^s_{\mu,\mathbf{R}_j}\rangle\}$, where $|\phi^s_{\mu,\mathbf{R}_j}\rangle$ denotes the μ-th atomic orbital (μ is a collective label for the principal and angular momentum quantum numbers) with spin s belonging to the cell at the position $\mathbf{R}_j$. SIESTA uses scalar relativistic pseudopotentials to generate the spin-orbit matrix elements with respect to the basis vectors and truncates the range of the SO interaction to the on-site terms [215]. For a finite periodic lattice comprising N unit cells, a Bloch state is written with respect to atomic orbitals as

$$|\psi_{p\mathbf{k}}\rangle = \sum_{j=1}^{N} e^{i\mathbf{k}\cdot\mathbf{R}_j} \left(\sum_{\mu} C_{\mu p}(\mathbf{k}) \, |\phi_{\mu,\mathbf{R}_j}\rangle \right) , \tag{7.10}$$

where the coefficients $C_{\mu p}(\mathbf{k})$ are in general C-numbers. This state is normalized over a unit cell with the allowed $\mathbf{k}$-values being $\frac{m}{N}\mathbf{K}$, where $\mathbf{K}$ is the reciprocal lattice vector and m is an integer.

Hence, the SO matrix elements written with respect to the spin-degenerate Bloch states calculated in absence of SO interaction are

$$\begin{aligned} &\langle \psi^{s_1}_{p\mathbf{k}_1} | \, \mathbf{V}_{\mathrm{SO}} \, |\psi^{s_2}_{q\mathbf{k}_2}\rangle = \\ &= \sum_{j,l} e^{i(\mathbf{k}_2\cdot\mathbf{R}_l - \mathbf{k}_1\cdot\mathbf{R}_j)} \cdot \sum_{\mu,\nu} C^{*s_1}_{\mu p}(\mathbf{k}_1) C^{s_2}_{\nu q}(\mathbf{k}_2) \, \langle \phi^{s_1}_{\mu,\mathbf{R}_j} | \, \mathbf{V}_{\mathrm{SO}} \, |\phi^{s_2}_{\nu,\mathbf{R}_l}\rangle \ . \end{aligned} \tag{7.11}$$

As mentioned above SIESTA neglects all the SO matrix elements between atomic orbitals located at different atoms. This leads to the approximation

$$\langle \phi^{s_1}_{\mu,\mathbf{R}_j} | \, \mathbf{V}_{\mathrm{SO}} \, |\phi^{s_2}_{\nu,\mathbf{R}_l}\rangle = \langle \phi^{s_1}_{\mu} | \, \mathbf{V}_{\mathrm{SO}} \, |\phi^{s_2}_{\nu}\rangle \, \delta_{\mathbf{R}_j,\mathbf{R}_l} \ , \tag{7.12}$$

so that Eq. (7.11) becomes

$$\begin{aligned} &\langle \psi^{s_1}_{p\mathbf{k}_1} | \, \mathbf{V}_{\mathrm{SO}} \, |\psi^{s_2}_{q\mathbf{k}_2}\rangle = \\ &= \sum_{j} e^{i(\mathbf{k}_2 - \mathbf{k}_1)\cdot\mathbf{R}_j} \cdot \sum_{\mu,\nu} C^{*(s_1)}_{\mu p}(\mathbf{k}_1) C^{(s_2)}_{\nu q}(\mathbf{k}_2) \, \langle \phi^{s_1}_{\mu} | \, \mathbf{V}_{\mathrm{SO}} \, |\phi^{s_2}_{\nu}\rangle \ . \end{aligned} \tag{7.13}$$

This can be further simplified by taking into account the relation

$$\sum_{j=1}^{N} e^{i(\mathbf{k}_1-\mathbf{k}_2)\cdot\mathbf{R}_j} = N\delta_{\mathbf{k}_1,\mathbf{k}_2} \,, \tag{7.14}$$

which leads to the final expression for the SO matrix elements

$$\begin{aligned}&\langle\psi^{s_1}_{p\mathbf{k}_1}|\,\mathbf{V}_{\rm SO}\,|\psi^{s_2}_{q\mathbf{k}_2}\rangle \\ &= N\sum_{\mu,\nu} C^{*(s_1)}_{\mu p}(\mathbf{k}_1)C^{(s_2)}_{\nu q}(\mathbf{k}_1)\,\langle\phi^{s_1}_{\mu}|\,\mathbf{V}_{\rm SO}\,|\phi^{s_2}_{\nu}\rangle\,\delta_{\mathbf{k}_1,\mathbf{k}_2}\,.\end{aligned} \tag{7.15}$$

With the result of Eq. (7.15) at hand we can now come back to the expression for the SO matrix elements written over the MLWFs computed in absence of spin-orbit [see Eq. (7.8)]. In the case of the SIESTA basis set this now reads

$$\begin{aligned}&\langle w^{s_1}_{m\mathbf{R}_1}|\,\mathbf{V}_{\rm SO}\,|w^{s_2}_{n\mathbf{R}_2}\rangle \\ =&\frac{1}{N}\sum_{p,q,\mu,\nu}\sum_{\mathbf{k}} C^{*s_1}_{\mu p}(\mathbf{k})C^{s_2}_{\nu q}(\mathbf{k})U^{*(s_1)}_{pm}(\mathbf{k})U^{s_2}_{qn}(\mathbf{k})\cdot e^{i\mathbf{k}\cdot(\mathbf{R}_1-\mathbf{R}_2)}\,\langle\phi^{s_1}_{\mu}|\,\mathbf{V}_{\rm SO}\,|\phi^{s_2}_{\nu}\rangle\,.\end{aligned} \tag{7.16}$$

Finally, we go back to the continuous representation ($N\to\infty$), where the sum over $\mathbf{k}$ is replaced by an integral over the first Brillouin zone

$$\begin{aligned}&\langle w^{s_1}_{m\mathbf{R}_1}|\,\mathbf{V}_{\rm SO}\,|w^{s_2}_{n\mathbf{R}_2}\rangle \\ &= \frac{V}{(2\pi)^3}\sum_{p,q,\mu,\nu}\int_{\rm BZ} C^{*s_1}_{\mu p}(\mathbf{k})C^{s_2}_{\nu q}(\mathbf{k})U^{*s_1}_{pm}(\mathbf{k})U^{s_2}_{qn}(\mathbf{k})\cdot e^{i\mathbf{k}\cdot(\mathbf{R}_1-\mathbf{R}_2)}\,\langle\phi^{s_1}_{\mu}|\,\mathbf{V}_{\rm SO}\,|\phi^{s_2}_{\nu}\rangle\,d\mathbf{k}\,.\end{aligned} \tag{7.17}$$

To summarize, our strategy consists in simply evaluating the SO matrix elements over the basis set of the MLWFs constructed in the absence of SO interaction. These are by definition spin-degenerate and they are in general easy to compute since associated to well-separated bands. Our procedure thus avoids to run the minimization algorithm necessary to fix the Wannier's gauge over the SO-split bands, which in the case of OSCs have tiny splits. Our method is exact in the case the MLWFs form a complete set describing a particular bands manifold. In other circumstances they constitute a good approximation, as long as the SO interaction is weak, namely when it does not change significantly the spatial shape of the Wannier functions.

7.2.3 Workflow

The following procedure is adopted when calculating the SO-split band structures from the MLWFs Hamiltonian. The results are then compared to the band structure obtained directly from SIESTA including SO interaction.

1. We first run a self-consistent non-collinear spin-DFT SIESTA calculation and obtain the band structure.

2. From the density matrix obtained at step (1), we run a non self-consistent single-step SIESTA calculation including SO coupling. This gives us the matrix elements $\langle \phi_\mu^{s_1} | \, \mathbf{V}_{\mathrm{SO}} \, | \phi_\nu^{s_2} \rangle$. The band structure obtained in this calculation (from now on this is called the SO-DFT band structure) will be then compared with that obtained over the MLWFs. Note that we do not perform the SIESTA DFT calculation including spin-orbit interaction in a self-consistent way. This is because the SO interaction changes little the density matrix so that such calculation is often not necessary. Furthermore, as we cannot run the MLWF calculation in a self-consistent way over the SO interaction, considering non-self-consistent SO band structure at the SIESTA level allows us to compare electronic structures arising from identical charge densities.

3. Since the current version of WANNIER90 implemented for SIESTA works only with collinear spins, we run a regular self-consistent spin-polarized SIESTA calculation. This gives us the coefficients $C_{\mu n}^{s}(\mathbf{k})$, which are spin-degenerate for a non-magnetic material, $C_{\mu n}^{\uparrow}(\mathbf{k}) = C_{\mu n}^{\downarrow}(\mathbf{k})$.

4. We run a WANNIER90 calculation to construct the MLWFs associated to the band structure computed at point (3). This returns us the unitary matrix, $U_{pm}^{s}(\mathbf{k})$, the Hamiltonian matrix elements $\langle w_{m\mathbf{R}_1}^{s_1} | \, \mathbf{H}_0 \, | w_{n\mathbf{R}_2}^{s_2} \rangle$ ($\mathbf{H}_0$ is the Kohn-Sham Hamiltonian in absence of SO interaction) and the phase factors [2] $e^{i\mathbf{k}\cdot\mathbf{R}}$. For a non-magnetic material the matrix elements of $\mathbf{H}_0$ satisfy the relation $\langle w_{m\mathbf{R_1}}^{s_1} | \, \mathbf{H}_0 \, | w_{n\mathbf{R_2}}^{s_2} \rangle = \langle w_{m\mathbf{R_1}} | \, \mathbf{H}_0 \, | w_{n\mathbf{R_2}} \rangle \, \delta_{s_1,s_2}$.

[2] The correctness of the elements $U_{pm}^{s}(\mathbf{k})$ and $e^{i\mathbf{k}\cdot\mathbf{R}}$ is easily verified by ensuring that the following

5. From $\langle \phi^{s_1}_{\mu} | \, \mathbf{V}_{\mathrm{SO}} \, | \phi^{s_2}_{\nu} \rangle$ and the $C^{s}_{\mu n}(\mathbf{k})$'s we calculate the matrix elements $\langle \psi^{s_1}_{p\mathbf{k}} | \, \mathbf{V}_{\mathrm{SO}} \, | \psi^{s_2}_{q\mathbf{k}} \rangle$ by using Eq. (7.15).

6. Next we transform the SO matrix elements constructed over the Bloch functions, $\langle \psi^{s_1}_{p\mathbf{k}} | \, \mathbf{V}_{\mathrm{SO}} \, | \psi^{s_2}_{q\mathbf{k}} \rangle$, into their Wannier counterparts, $\langle w^{s_1}_{m\mathbf{R}_1} | \, \mathbf{V}_{\mathrm{SO}} \, | w^{s_2}_{n\mathbf{R}_2} \rangle$, by using Eq. (7.17).

7. The final complete Wannier Hamiltonian now reads

$$\langle w^{s_1}_{m\mathbf{R}_1} | \, \mathbf{H} \, | w^{s_2}_{n\mathbf{R}_2} \rangle = \langle w^{s_1}_{m\mathbf{R}_1} | \, \mathbf{H}_0 + \mathbf{V}_{\mathrm{SO}} \, | w^{s_2}_{n\mathbf{R}_2} \rangle \ , \qquad (7.19)$$

and the associated band structure can be directly compared with that computed at point (2) directly from SIESTA.

7.3 Results and Discussion

We now present our results, which are discussed in the light of the theory just described.

7.3.1 Plumbane Molecule

We start our analysis by calculating the SO matrix elements and then the energy eigenvalues of a plumbane, PbH_4, molecule [see figure 7.1(a)]. Due to the presence of lead, the molecular eigenstates change significantly when the SO interaction is switched on. For this non-periodic system the key relations in Eq. (7.15) and Eq. (7.8) reduce to

$$\langle \psi^{s_1}_{p} | \, \mathbf{V}_{\mathrm{SO}} \, | \psi^{s_2}_{q} \rangle = \sum_{\mu,\nu} C^{*s_1}_{\mu p} C^{s_2}_{\nu q} \, \langle \phi^{s_1}_{\mu} | \, \mathbf{V}_{\mathrm{SO}} \, | \phi^{s_2}_{\nu} \rangle \qquad (7.20)$$

---

relation is satisfied

$$\begin{aligned} \langle w_{m\mathbf{R}_1} | w_{n\mathbf{R}_2} \rangle &= \sum_{p} \int_{\mathrm{FBZ}} d\mathbf{k} \, \langle w_{m\mathbf{R}_1} | \psi_{p\mathbf{k}} \rangle \, \langle \psi_{p\mathbf{k}} | w_{n\mathbf{R}_2} \rangle \\ &= \sum_{p} \int_{\mathrm{FBZ}} d\mathbf{k} U^{*}_{pm}(\mathbf{k}) U_{pn}(\mathbf{k}) e^{i\mathbf{k}\cdot(\mathbf{R}_1 - \mathbf{R}_2)} \qquad (7.18) \\ &= \delta_{m,n} \delta_{\mathbf{R}_1,\mathbf{R}_2} \ . \end{aligned}$$

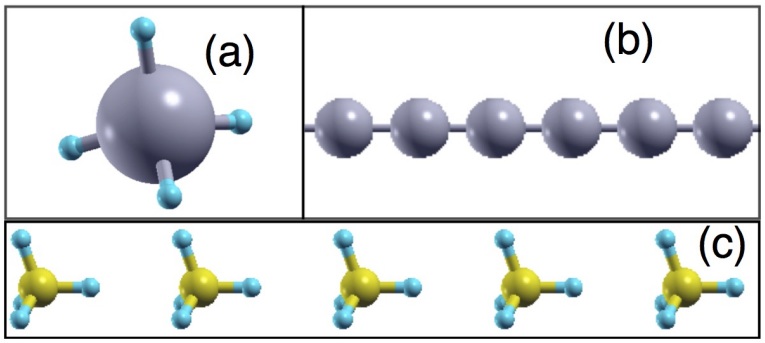

Figure 7.1: Atomic structure of (a) a plumbane molecule, (b) a chain of lead atoms and (c) a chain of methane molecules. We have also calculated the electronic structure of a chain of C atoms, which is essentially identical to that presented in (b). Color code: Pb = grey, H = light blue, C = yellow.

and

$$\langle w_m^{s_1} | \, \mathbf{V}_{\mathrm{SO}} \, | w_n^{s_2} \rangle = \sum_{p,q} U_{pm}^{*s_1} U_{qn}^{s_2} \, \langle \psi_p^{s_1} | \, \mathbf{V}_{\mathrm{SO}} \, | \psi_q^{s_2} \rangle \ , \qquad (7.21)$$

respectively, where now the vectors ψ_n^s are simply the eigenvectors with quantum number n and spin s.

In Table 7.1 we report the first 10 energy eigenvalues of plumbane, calculated either with or without SO coupling. These have been computed within the LDA (local density approximation) and a double-zeta polarized basis set. The table compares results obtained with our MLWFs procedure to those computed with SO-DFT by SIESTA. Clearly in this case of a heavy ion the SO coupling changes the eigenvalues appreciably, in particular in the spectral region around -13 eV. Such change is well captured by our Wannier calculation, which returns energy levels in close proximity to those computed with SO-DFT by SIESTA. In order to estimate the error introduced by our method, we calculate the *Mean Relative Absolute Difference (MRAD)*, which we define as $\frac{1}{N} \sum \frac{|\epsilon_i^s - \epsilon_i^w|}{|\epsilon_i^s|}$ for a set of N eigenvalues ($i = 1, ..., N$), where ϵ_i^s and ϵ_i^w are the i-th eigenvalues calculated from SIESTA and the MLWFs, respectively. Notably the *MRAD* is rather small both in the SO-free case and when the SO interaction is included. Most importantly, we can report that our procedure to evaluate the SO matrix elements over the MLWFs basis clearly does not introduce any additional error.

NonSO		SO	
SIESTA	MLWF	SIESTA	MLWF
-33.93534	-33.93521	-33.93532	-33.93521
-33.93530	-33.93521	-33.93528	-33.93521
-13.02511	-13.02507	-14.69573	-14.69568
-13.02511	-13.02507	-14.69573	-14.69568
-13.02510	-13.02506	-12.64301	-12.64298
-13.02509	-13.02506	-12.64301	-12.64298
-13.02320	-13.02315	-12.64166	-12.64162
-13.02318	-13.02315	-12.64165	-12.64162
-5.75256	-5.75251	-5.75255	-5.75251
-5.75245	-5.75251	-5.75245	-5.75251
$MRAD$=4.320 $\times$ 10^{-6}		$MRAD$=3.998 $\times$ 10^{-6}	

Table 7.1: The 10 lowest energy eigenvalues of a plumbane molecule calculated with (SO) and without (NonSO) spin-orbit interaction. The first and third columns correspond to the SO-DFT SIESTA calculation, while the second and the fourth to the MLWFs one. The *MRAD* for both cases is reported in the last row.

Before discussing some of the properties of the SO matrix elements associated to this particular case of a finite molecule, we wish to make a quick remark on the Wannier procedure adopted here. The eigenvalues reported in Table 7.1 are the ten with the lowest energies. However, in order to construct the MLWFs we have considered all the states of the calculated Kohn-Sham spectrum. This means that, if our SIESTA basis set describes PbH_4 with N distinct atomic orbitals, then the MLWFs constructed are $2N$ (the factor 2 accounts for the spin degeneracy). In this case the original local orbital basis set and the constructed MLWFs span the same Hilbert space and the mapping is exact, whether or not the SO interaction is considered.

In most cases, however, one wants to construct the MLWFs by using only a subset of the spectrum, for instance the first N' eigenstates. Since in general the SO interaction mixes all states, there will be SO matrix elements between the selected N' states and the remaining $N - N'$. This means that a MLWF basis constructed only from the first N' eigenstates will not be able to provide an accurate description of the SO-split spectrum. In the case of light elements, i.e. for a weak SO potential, one may completely neglect the off-diagonal SO matrix elements. This means that the SO spectrum constructed with the MLWFs associated to the first N' eigenstates will be approximately equal to the first N' eigenvalues of the MLWFs Hamiltonian constructed over the entire N-dimensional spectrum. Such property is particularly relevant for OSCs, for which the SO interaction is weak.

We now move to discuss a general property of the MLWF SO matrix elements, namely the relations $\langle w_m^s | \mathbf{V}_{\mathrm{SO}} | w_m^s \rangle = 0$ and $\mathbb{R}[\langle w_m^s | \mathbf{V}_{\mathrm{SO}} | w_n^s \rangle] = 0$. This means that the SO matrix elements for the same spin and the same Wannier function vanish, while those for the same spin and different Wannier functions are purely imaginary. This property can be understood from the following argument. The SO coupling operator is $\mathbf{V}_{\mathrm{SO}} = \sum_{\mathbf{R}_j} V_{\mathbf{R}_j} \mathbf{L}_{\mathbf{R}_j} \cdot \mathbf{S}$, where $V_{\mathbf{R}_j}$ is a scalar potential independent of spin, and $\mathbf{L}_{\mathbf{R}_j}$ is the angular momentum operator corresponding to the central potential of the atom at position $\mathbf{R}_j$. Here $\mathbf{S}$ is the spin operator and the sum runs over all the atoms. By now expanding $\mathbf{S}$ in terms of the Pauli spin matrices one can see that for any vector $|\gamma_i^s\rangle = |\gamma_i\rangle \otimes |s\rangle$, which can be written as a tensor product of a spin-independent part,

$|\gamma_i\rangle$, and a spinor $|s\rangle$, the following equality holds

$$\langle \gamma_m^{s_1}| \mathbf{L}\cdot\mathbf{S} |\gamma_n^{s_2}\rangle = \frac{1}{2}\Big[\langle\gamma_m| \hat{L}_z |\gamma_n\rangle \delta_{s_1\uparrow}\delta_{s_2\uparrow} + \langle\gamma_m| \hat{L}_- |\gamma_n\rangle \delta_{s_1\uparrow}\delta_{s_2\downarrow} + \langle\gamma_m| \hat{L}_+ |\gamma_n\rangle \delta_{s_1\downarrow}\delta_{s_2\uparrow} + \langle\gamma_m| -\hat{L}_z |\gamma_n\rangle \delta_{s_1\downarrow}\delta_{s_2\downarrow}\Big] . \quad (7.22)$$

Eq. (7.22) can then be applied to both the Kohn-Sham eigenstates and the MLWFs, since they are both written as $|\gamma_i^s\rangle = |\gamma_i\rangle \otimes |s\rangle$.

Now, the atomic orbitals used by SIESTA have the following form

$$|\phi_i\rangle = |R_{n_i,l_i}\rangle \otimes |l_i, M_i\rangle \ , \quad (7.23)$$

where $|R_{n,l}\rangle$ is a radial numerical function, while the angular dependence is described by the real spherial harmonic, [3] $|l, M\rangle$. It can be proved that the real spherical harmonics follow the relation

$$\langle l, M_i| \hat{L}_z |l, M_j\rangle = -iM_i\delta_{M_i,M_j} . \quad (7.24)$$

Since any Kohn-Sham eigenstate, $|\psi_p^{s_1}\rangle$, can be written as $|\phi_i\rangle \otimes |s_1\rangle$, Eq. (7.22) implies that only the terms in $\hat{L}_z$ (or $-\hat{L}_z$) contribute to the matrix element between same spins, $\langle\psi_p^{s_1}| \mathbf{L}\cdot\mathbf{S} |\psi_p^{s_1}\rangle$. Equation (7.24) together with the fact that the Kohn-Sham eigenstates are real for a finite molecule further establishes that $\mathbb{R}[\langle\psi_p| \hat{L}_z |\psi_q\rangle] = 0$. As a consequence $\langle\psi_m| \hat{L}_z |\psi_m\rangle = 0$. Finally, by keeping in mind that the unitary matrix elements transforming the Kohn-Sham eigenstates into MLWFs are real for a molecule, we have also

$$\langle w_m^{s_1}| \mathbf{L}\cdot\mathbf{S} |w_n^{s_1}\rangle = \pm \langle w_m| \hat{L}_z |w_n\rangle = \\ = \sum_{p\neq q} U_{pm}U_{qn} \langle\psi_p| \hat{L}_z |\psi_q\rangle \ , \quad (7.25)$$

which has to be imaginary. Thus we have $\mathbb{R}\langle w_m^{s_1}| \mathbf{V}_{\mathrm{SO}} |w_n^{s_1}\rangle = 0$ and $\langle w_m^{s_1}| \mathbf{V}_{\mathrm{SO}} |w_m^{s_1}\rangle = 0$ since $\mathbf{V}_{\mathrm{SO}}$ must have real expectation values.

[3] The real spherical harmonics are constructed from the complex ones, $|l, m\rangle$, as $|l, M\rangle = \frac{1}{\sqrt{2}}[|l, m\rangle + (-1)^m |l, -m\rangle]$ and $|l, -M\rangle = \frac{1}{i\sqrt{2}}[|l, m\rangle - (-1)^m |l, -m\rangle]$. For $M = 0$ the real and complex spherical harmonics coincide.

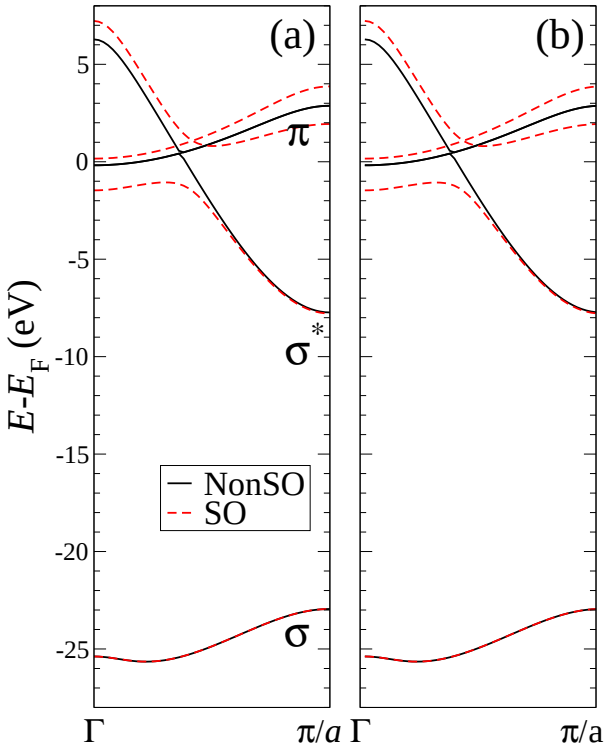

Figure 7.2: Bandstructure of a 1D Pb chain calculated (a) with SIESTA and (b) by diagonalizing the Hamiltonian matrix constructed over the MLWFs. Black and red lines are for the bands obtained with and without SO coupling, respectively. The σ, σ^* and π bands are identified in the picture.

7.3.2 Lead Chain

Next we move to calculating the SO matrix elements for a periodic structure. In particular we look at a 1D chain of Pb atoms with a unit cell length of 2.55 Å, which is the DFT equilibrium lattice constant obtained with the LDA. Note that free-standing mono-dimensional Pb chains have never been reported in literature, although there are studies of low-dimensional Pb structures encapsulated into zeolites [217]. Here, however, we do not seek at describing a real compound, but we rather take the 1D Pb mono-atomic chain as a test-bench structure to apply our method to a periodic structure with a large SO coupling. Also in this case we have constructed the MLWFs by taking the entire bands manifold and not a subset of it. For the DFT calculations we

have considered a simple s and p single-zeta basis set, which in absence of SO interaction yields three bands with one of them being doubly degenerate [see Fig. 7.2(a)]. The doubly-degenerate relatively-flat band just cuts across the Fermi energy, $E_{\rm F}$, and it is composed of the p_y and p_z orbitals orthogonal to the chain axis (π band). The other two bands are sp hybrid (σ bands). The lowest one at about 25 eV below $E_{\rm F}$ has mainly s character (σ band), while the other one mainly p_x (σ^* band).

Spin-orbit coupling lifts the degeneracy of the p-type band manifold, which is now composed of three distinct bands. In particular the degeneracy is lifted only in the π band at the edge of the 1D Brillouin zone, while it also involves the σ one close to the Γ point (after the band crossing). When the same band structure is calculated from the MLWFs we obtain the plot of Fig. 7.2(b). This is almost identical to that calculated with SO-DFT demonstrating the accuracy of our method also for a periodic system.

It must be noted that for a periodic structure the Bloch state expansion coefficients, $C_{\mu p}(\mathbf{k})$, and the elements of the unitary matrix U are complex and consequently the diagonal elements of $\mathbf{V}_{\rm SO}$ with respect to Wannier functions are not zero in general. However, as expected $\langle w^{s_1}_{m\mathbf{R}}| \mathbf{V}_{\rm SO} |w^{s_2}_{n\mathbf{R}'}\rangle$ tends to vanish as the separation $|\mathbf{R}-\mathbf{R}'|$ increases. Furthermore, it is clear from Eq. (7.22) that the SO matrix elements for the Wannier functions should obey the spin-box anti-hermitian relation

$$\langle w^{s_1}_{m\mathbf{R}}| \mathbf{V}_{SO} |w^{s_2}_{n\mathbf{R}'}\rangle = -\langle w^{s_2}_{m\mathbf{R}}| \mathbf{V}_{\rm SO} |w^{s_1}_{n\mathbf{R}'}\rangle^* \ . \quad (7.26)$$

These two properties can be appreciated in Fig. 7.3, where we plot the real [panel (a)] and imaginary [panel (b)] part of $\langle w^{s_1}_{m\mathbf{0}}| \mathbf{V}_{SO} |w^{s_2}_{n\mathbf{R}}\rangle$ for some representative band combinations, m and n, as a function of $\mathbf{R}$.

7.3.3 Carbon Chain

Next we look at the case of a 1D mono-atomic carbon chain with a LDA-relaxed interatomic distance of ~ 1.3 Å. This has the same structure and electron count of the Pb chain, and the only difference concerns the fact that the SO coupling in C is much smaller then that in Pb. In this situation we expect that an accurate SO-split band

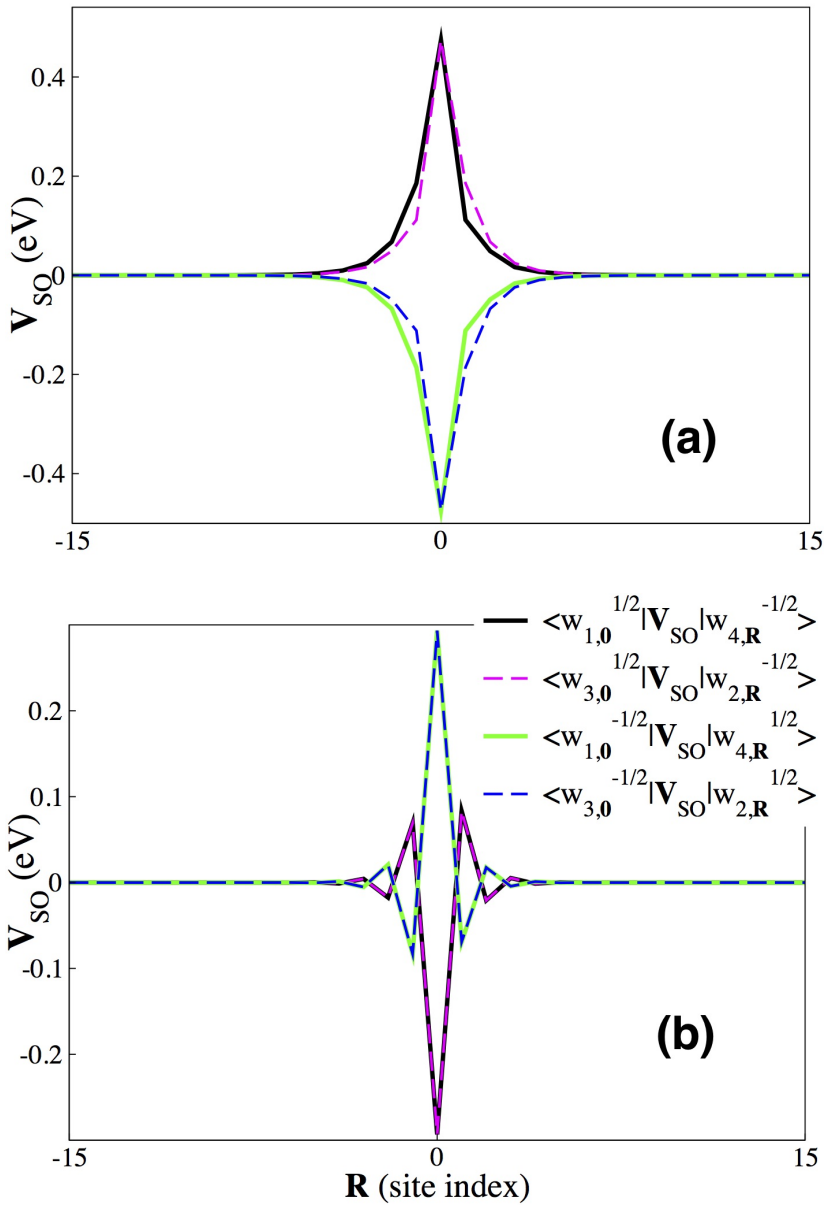

Figure 7.3: The SO matrix elements of a chain of lead atoms calculated with respect to some representative Wannier functions and plotted as a function of the site index, i.e. of the distance between the Wannier function. Panels (a) and (b) show the real and imaginary components respectively.

structure can be obtained even when the MLWFs are constructed only for a limited number of bands and not for the entire band manifold as in the case of Pb. This time the DFT band structure is calculated at the LDA level over a double-zeta polarized (DZP) SIESTA basis set, comprising 13 atomic orbitals per unit cell. In contrast, the MLWFs are constructed only from the first four bands, which are well isolated in energy from the rest and again describe the *sp* bands with σ and π symmetry. Since the SO interaction in carbon is small (the band split is of the order of a few meV) it is impossible to visualize the effects of the SO interaction in a standard band plot as that in Fig. 7.2. Hence, in Fig. 7.4 we plot the difference between the band structure calculated in the presence and in the absence of SO coupling. In particular we compare the bands calculated with SO-DFT by SIESTA (left-hand side panels in Fig. 7.4), with those obtained with the MLWFs scheme described here (right-hand side panels in Fig. 7.4). In the figure we have labelled the bands in order of increasing energy and neglecting the spin degeneracy. Thus, for instance, the ψ_1 and ψ_2 bands correspond to the two lowest σ spin sub-bands (note that the band structure of the linear carbon chain is qualitatively identical to that of the Pb one and we can use Fig. 7.2 to identify the various bands).

We note that the lowest σ bands, defined as ψ_1 and ψ_2, do not split at all due to the SO interaction, exactly as in the case of Pb. This contrasts the behaviour of both the π (ψ_3 through ψ_6) and σ^* (ψ_7 and ψ_8) bands, which instead are modified by the SO interaction. Notably the changes in energy of the eigenvalues is never larger then 8 meV and it is perfectly reproduced by our MLWFs representation. This demonstrates that truncating the bands selected for constructing the MLWFs is a possible procedure for materials where SO coupling is weak. However, we should note that the truncation still needs to be carefully chosen. Here for instance we have considered all the $2s$ and $2p$ bands and neglected those with either higher principal quantum number (e.g. $3s$ and $3p$) or higher angular momentum (e.g. bands with d symmetry originating from the p-polarized SIESTA basis), which appear at much higher energies. Truncations, where one considers only a particular orbital of a given shell (say the p_z orbital in an np shell), need to be carefully assessed since it is unlikely that a clear energy separation between the bands takes place.

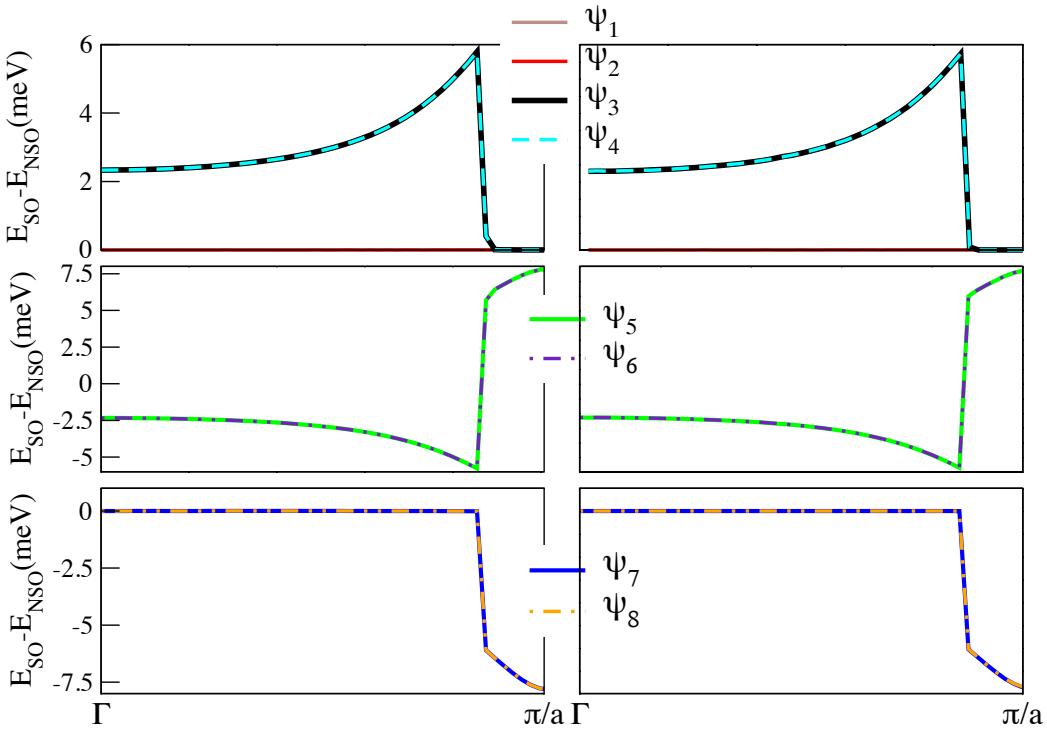

Figure 7.4: Difference, $E_{\mathrm{SO}} - E_{\mathrm{NSO}}$, between the band structure of chain of carbon atoms calculated with, E_{SO}, and without, E_{NSO}, considering SO interaction. The bands are labelled in increasing energy order without taking into account spin degeneracy. For instance the bands ψ_1 and ψ_2 are the two spin sub-bands corresponding to the σ band (see Fig. 7.2 for notation). The left-hand side panels show results for the SO-DFT calculations performed with SIESTA, while the right-hand side one, those obtained from the MLWFs.

7.3.4 Methane Chain

As a first basic prototype of 1D organic molecular crystal we perform calculations for a periodic chain of methane molecules. We use a double-zeta polarized basis set and a LDA-relaxed unit cell length of 3.45 Å (the cell contains only one molecule). Similarly to the previous case, the MLWFs are constructed over only the lowest 4 bands (8 when considering the spin degeneracy). When compared to the bands of the carbon chain, those of methane are much narrower. This is expected, since the bonding between the different molecules is small. In Fig. 7.5 we plot the difference between the eigenvalues (1D band structure) calculated with, E_{SO}, and without, E_{NSO}, including SO interaction.

When SO interaction is included the spin-degeneracy is broken and one has now eight bands. These are labeled as ψ_m in Fig. 7.5 in increasing energy order. Again we find no SO split for the lowermost band and then a split, which is significantly smaller than that found in the case of the C chain. This is likely to originate from the crystal field of the C atoms in CH_4, which is different from that in the C chain (the C-C distance is different and there are additional C-H bonds). Again, as in the previous case, we find that our MLWFs procedure perfectly reproduces the SO-DFT band structure, indicating that in this case of weak SO interaction band truncation does not introduce any significant error.

7.3.5 Triarylamine Chain

Finally we perform calculations for a real system, namely for triarylamine-based molecular nanowires. These can be experimentally grown through a photo-self-assembly process from the liquid phase [218], and have been subject of numerous experimental and theoretical studies [219, 220]. In general, triarylamines can be used as materials for organic light emitting diodes, while their nanowire form appears to possess good transport and spin properties, making it a good platform for organic spintronics [221]. Triarylamine-based molecular nanowires self-assemble only when particular radicals are attached to the main triarylamine backbone and here we consider the case of C_8H_{17}, H and Cl rad-

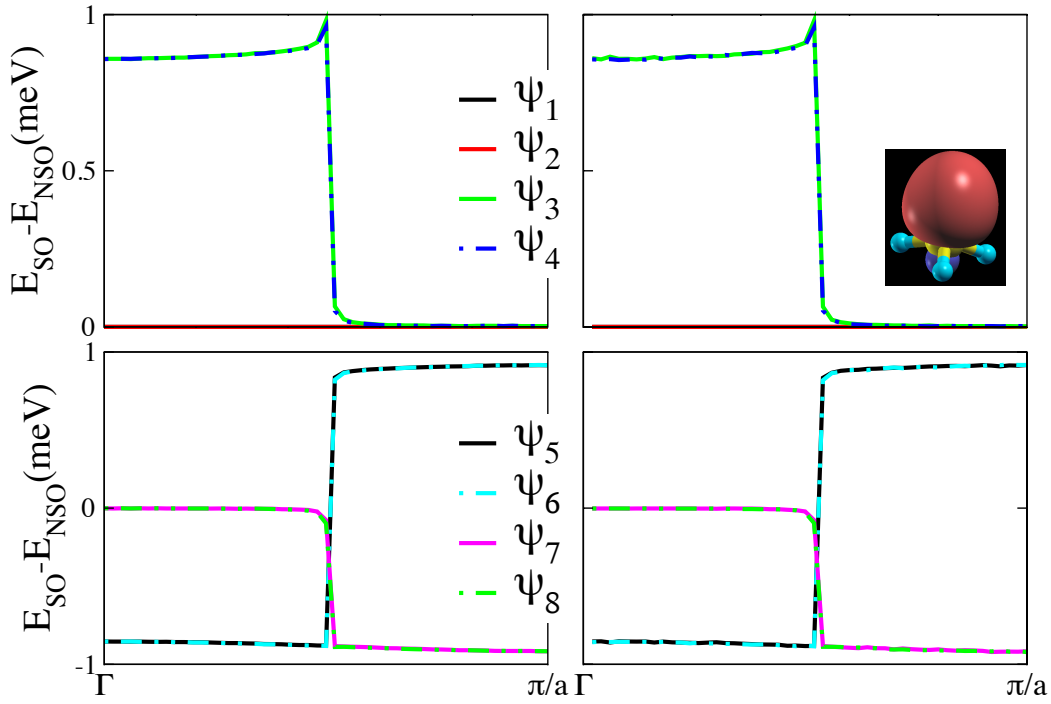

Figure 7.5: Difference, $E_{\mathrm{SO}} - E_{\mathrm{NSO}}$, between the band structure of chain of methane molecules calculated with, E_{SO}, and without, E_{NSO}, considering SO interaction. The bands are labelled in increasing energy order without taking into account spin degeneracy. The left-hand side panels show results for the SO-DFT calculations performed with SIESTA, while the right-hand side one, those obtained from the MLWFs. The inset shows an isovalue plot of one of the four MLWFs with the red and blue surfaces denoting positive and negative isovalues, respectively. All the MLWFs have similar structure and they resemble those of the isolated methane molecule because of the small intermolecular chemical bonding owing to the large separation.

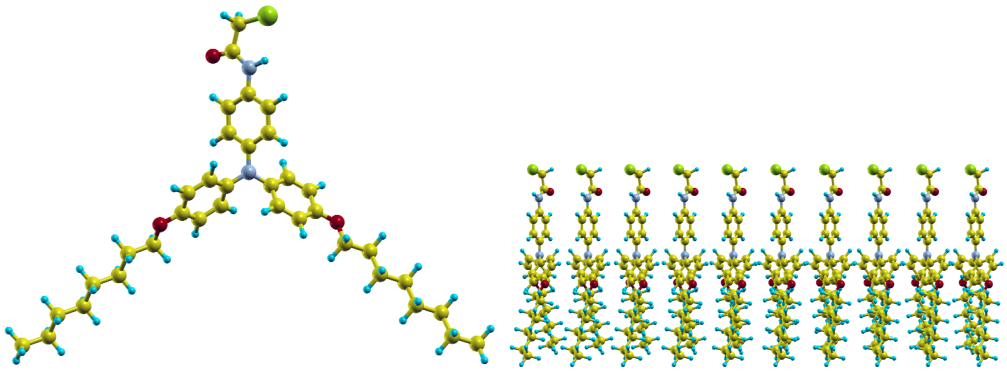

Figure 7.6: Structure of the triarylamine molecule (upper picture) and of the triarylamine-based nanowire investigated here. The radicals associated to the triarylamine derivative are C_8H_{17}, H and Cl, respectively. Colour code: C=yellow, H=light blue, O=red, N=grey, Cl=green.

icals, corresponding to the precursor **1** of Ref. [218] (see upper panel in Fig. 7.6). The nanowire then arranges in such a way to have the central N atoms aligned along the wire axis (see Fig. 7.6).

In general self-assembled triarylamine-based molecular nanowires appear slightly p-doped so that charge transport takes place in the HOMO-derived band. This is well isolated from the rest of the valence manifold and has a bandwidth of about 100 meV (see figure Fig. 7.7 for the band structure). Such band is almost entirely localized on the p_z orbital of the central N atoms (p_z is along the wire axis), a feature that has allowed us to construct a p_z-sp^2 model with the spin-orbit strength extracted from that of an equivalent mono-atomic N chain. The model was then used to calculate the temperature-dependent spin-diffusion length of such nanowires [222]. Here we wish to use our MLWFs method to extract the SO matrix elements of triarylamine-based molecular nanowires in their own chemical environment, i.e. without approximating the backbone with a N atomic chain.

For this system we use a 1D lattice with LDA-optimized lattice spacing of 4.8 Å and run the DFT calculations with double-zeta polarized basis and the LDA functional. The MLWFs are constructed by using only the HOMO-derived valence band, i.e. we have a single spin-degenerate Wannier orbital. We can then drop the band index and

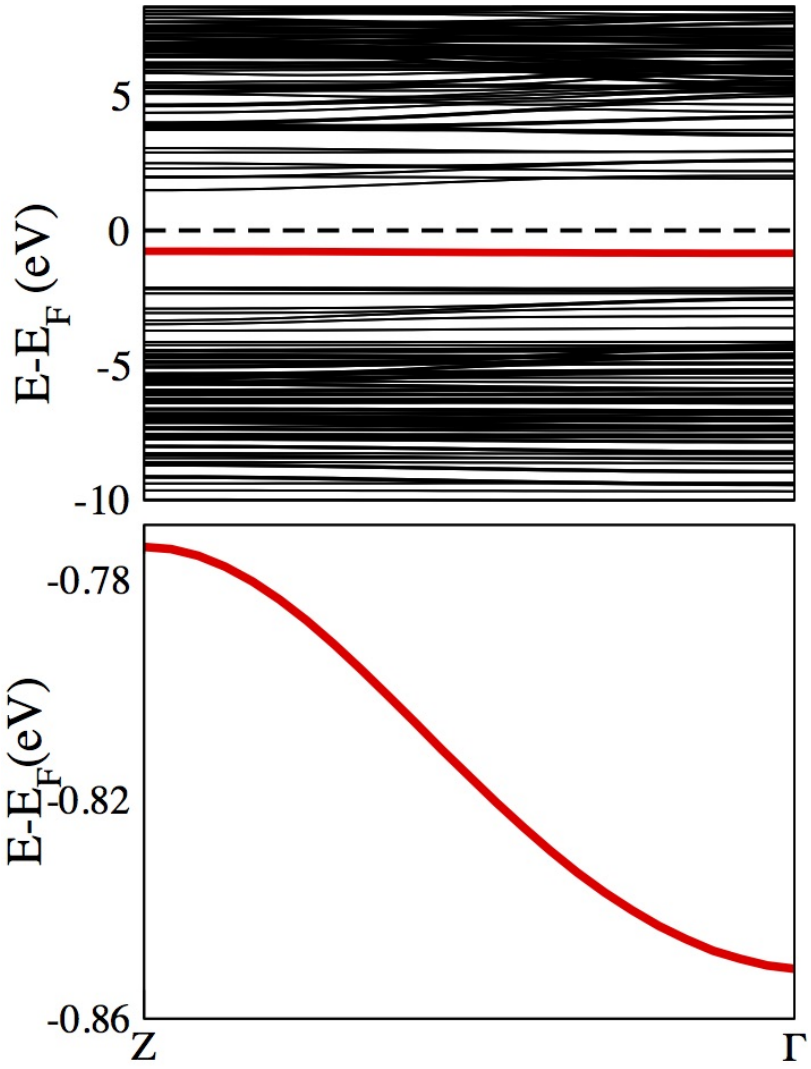

Figure 7.7: Band structure of the 1D triarylamine-based nanowire constructed with the precursor **1** of Ref. [218]. This is plotted over the 1D Brillouin zone (Z=π/a with a the lattice parameter). The Fermi level is marked with a dashed black line and it is placed just above the HOMO-derived valence band (in red). The lower panel is a magnification of the valence band. Note the bandwidth of about 100 meV and the fact that the band has a cosine shape, fingerprint of a single-orbital nearest-neighbour tight-binding-like interaction. Only the HOMO band is considered when constructing the MLWFs.

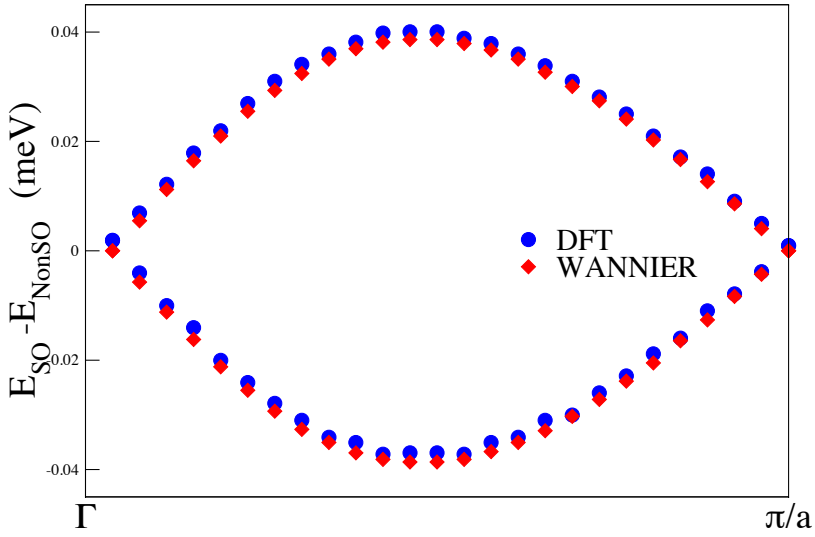

Figure 7.8: Plot of ($E_{\text{with SO}} - E_{\text{without SO}}$) as a function of $\mathbf{k}$ in arbitrary unit over a Brillouin zone for the highest occupied band of a 1-d chain of triarylamine derivatives. The blue and the red points correspond to calculations with SIESTA and WANNIER90 respectively.

write the SO matrix elements as

$$\begin{aligned}\langle w_{\mathbf{0}}^{s_1}|\,\mathbf{V}_{\text{SO}}\,|w_{\mathbf{R}}^{s_2}\rangle &= \frac{V}{(2\pi)^3}\int d\mathbf{k}U^*(\mathbf{k})U(\mathbf{k})e^{-i\mathbf{k}.\mathbf{R}}\,\langle\psi_{\mathbf{k}}^{s_1}|\,\mathbf{V}_{SO}\,|\psi_{\mathbf{k}}^{s_2}\rangle \\ &= \frac{V}{(2\pi)^3}\int d\mathbf{k}e^{-i\mathbf{k}.\mathbf{R}}\,\langle\psi_{\mathbf{k}}^{s_1}|\,\mathbf{V}_{\text{SO}}\,|\psi_{\mathbf{k}}^{s_2}\rangle\ ,\end{aligned} \tag{7.27}$$

or in a discrete representation of the reciprocal space

$$\begin{aligned}\langle w_{\mathbf{0}}^{s_1}|\,\mathbf{V}_{\text{SO}}\,|w_{\mathbf{R}}^{s_2}\rangle &= \frac{1}{N}\sum_{\mathbf{k}}U^*(\mathbf{k})U(\mathbf{k})e^{-i\mathbf{k}.\mathbf{R}}\,\langle\psi_{\mathbf{k}}^{s_1}|\,\mathbf{V}_{\text{SO}}\,|\psi_{\mathbf{k}}^{s_2}\rangle \\ &= \frac{1}{N}\sum_{\mathbf{k}}e^{-i\mathbf{k}.\mathbf{R}}\,\langle\psi_{\mathbf{k}}^{s_1}|\,\mathbf{V}_{\text{SO}}\,|\psi_{\mathbf{k}}^{s_2}\rangle\ ,\end{aligned} \tag{7.28}$$

where the second equality comes from the unitarity of the gauge transformation, $U(\mathbf{k})$.

In Fig. 7.8 we plot the difference between the band structure computed by including SO interaction and those calculated without. Notably our MLWFs band structure is almost identical to that computed directly with SO-DFT, again demonstrating both the accuracy of our method and the appropriateness of the drastic band truncation used here. In this particular case the SO band split is maximized half-way between the Γ point and the edge of the 1D Brillouin zone, where it takes a value of

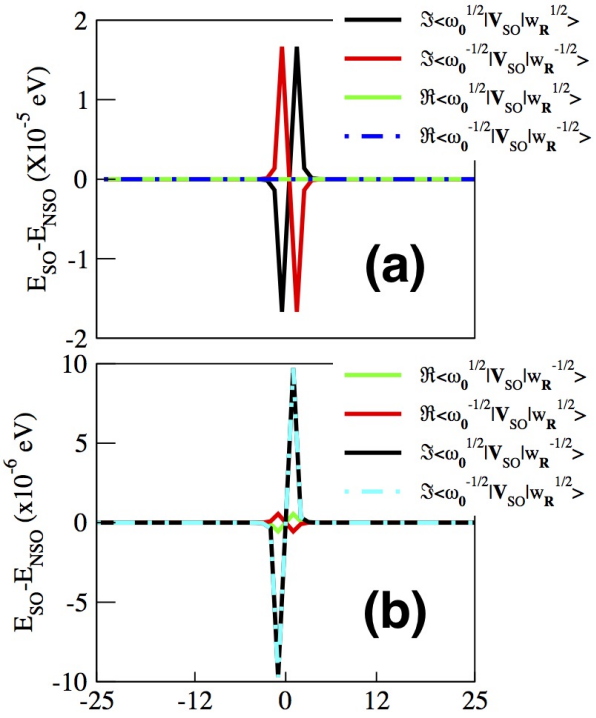

Figure 7.9: SO matrix elements of a triarylamine-based nanowire calculated with respect to the Wannier functions obtained from the HOMO band. Panels (a) and (b) correspond to matrix elements calculated between for same and different spins, respectively.

approximately 80 μeV. Clearly such split is orders of magnitude smaller than the value that one can possibly calculate by a direct construction of the MLWFs from the SO-splitted band structure. Note also that the SO split of the valence band is calculated here approximately a factor ten smaller than that estimated previously for a N atomic chain [222], indicating the importance of the details of the chemical environment in these calculations.

Finally we take a closer look at the calculated SO matrix elements. As mentioned earlier, in the SIESTA on-site approximation [215] only the matrix elements calculated over orbitals centred on the same atom do not vanish. As a consequence the components $\langle w_{\mathbf{R}}^{s_1} | \mathbf{V}_{\mathrm{SO}} | w_{\mathbf{R}'}^{s_2} \rangle$ drop to zero as $|\mathbf{R} - \mathbf{R}'|$ gets large. This can be clearly appreciated in Fig. 7.9(a) and Fig. 7.9(b), where we plot the SO matrix elements for same and different spins, respectively.

From Fig. 7.9(a) we can observe that $\mathbb{R} \langle w_{\mathbf{0}}^{s_1} | \mathbf{V}_{\mathrm{SO}} | w_{\mathbf{R}}^{s_1} \rangle$ vanishes for all $\mathbf{R}$. This

can be understood in the following way. In general any expectation value of $\mathbf{V}_{\mathrm{SO}}$, $\langle\psi^s_{\mathbf{k}}|\,\mathbf{V}_{\mathrm{SO}}\,|\psi^s_{\mathbf{k}}\rangle$, has to be real. This is in fact anti-symmetric with respect to $\mathbf{k}$, i.e we have $\langle\psi^s_{\mathbf{0}+\mathbf{k}}|\,\mathbf{V}_{\mathrm{SO}}\,|\psi^s_{\mathbf{0}+\mathbf{k}}\rangle = -\langle\psi^s_{\mathbf{0}-\mathbf{k}}|\,\mathbf{V}_{\mathrm{SO}}\,|\psi^s_{\mathbf{0}-\mathbf{k}}\rangle$, where $\mathbf{k}=\mathbf{0}$ denotes the Γ point of the Brillouin zone. Additionally, $e^{i\mathbf{k}\cdot\mathbf{R}}$ satisfies the relation $e^{i(\mathbf{0}+\mathbf{k})\cdot\mathbf{R}} = \left[e^{i(\mathbf{0}-\mathbf{k})\cdot\mathbf{R}}\right]^*$. Hence, by performing the $\mathbf{k}$-sum over first Brillouin zone we can write

$$\mathbb{R}\,\langle w^{s_1}_{\mathbf{0}}|\,\mathbf{V}_{\mathrm{SO}}\,|w^{s_1}_{\mathbf{R}}\rangle = \mathbb{R}\sum_{\mathbf{k}} e^{-i\mathbf{k}.\mathbf{R}}\,\langle\psi^{s_1}_{\mathbf{k}}|\,\mathbf{V}_{\mathrm{SO}}\,|\psi^{s_1}_{\mathbf{k}}\rangle = 0\,, \quad (7.29)$$

where $\langle w^{s_1}_{\mathbf{0}}|\,\mathbf{V}_{\mathrm{SO}}\,|w^{s_1}_{\mathbf{0}}\rangle$ is the expectation value of $\mathbf{V}_{\mathrm{SO}}$ and must be real. This implies

$$\langle w^{s_1}_{\mathbf{0}}|\,\mathbf{V}_{\mathrm{SO}}\,|w^{s_1}_{\mathbf{0}}\rangle = 0\,. \quad (7.30)$$

We can also see from Fig. 7.9(b) that for triarylamine the matrix elements $\langle w^{s_1}_{\mathbf{R}}|\,\mathbf{V}_{\mathrm{SO}}\,|w^{s_2}_{\mathbf{R}}\rangle$ are almost zero for $s_1 \neq s_2$. This follows directly from Eq. (7.22). In fact in the particular case of triarylamine nanowires the Wannier functions are constructed from one band only. As such, in order to have a non-zero matrix element, $\langle w^{s_1}_{\mathbf{R}}|\,\mathbf{V}_{\mathrm{SO}}\,|w^{s_2}_{\mathbf{R}}\rangle$, we must have non-zero values for $\langle w_{\mathbf{R}}|\,\hat{L}_{\pm}\,|w_{\mathbf{R}}\rangle$. Therefore, the band under consideration must contain an appreciable mix of components of both the $|l,p\rangle$ and $|l,p+1\rangle$ complex spherical harmonics for some l and p. As mentioned earlier, the triarylamine HOMO band is composed mostly of p_z N orbitals. Hence, it has to be expected that the $\langle w^{s_1}_{\mathbf{R}}|\,\mathbf{V}_{\mathrm{SO}}\,|w^{s_2}_{\mathbf{R}}\rangle$ matrix elements are small.

7.3.6 3D structures: FCC lead and $PhBr_2C_6Br_2$

So far we have discussed only 1-dimensional nanowire-like objects. Now we move to the more general case of bulk 3-D crystals. A crucial point to be noted for treating bulk crystals is that in WANNIER90, the direct lattice points, where the MLWFs are calculated, are the lattice points of the Wigner-Seitz cell about the cell $\mathbf{R}=\mathbf{0}$. Typically, one should expect the number of such lattice points to be the same as the number of k-points in the reciprocal space. However, in a 3-D crystal, it is possible to have lattice points, which are equidistant from the $\mathbf{R}=\mathbf{0}$ cell and (say) n number of other cells. This means that such lattice point is shared by Wigner-Seitz cells of $n+1$ cells. In this case,

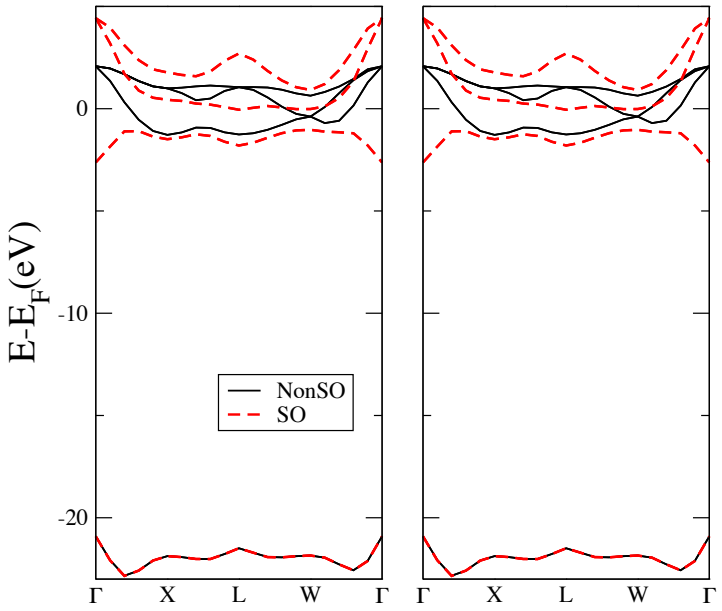

Figure 7.10: Band structure of FCC lead. Left and right columns show eigenvalues obtained with SIESTA and with our method respectively. Red and black lines are for the bands obtained with and without SO coupling, respectively.

this degenerate lattice point is taken into consideration by WANNIER90 but a degeneracy weight of $1/(n+1)$ is attached with it and consequently in further calculations (such as band structure interpolation), its contribution carries a factor of $1/(n+1)$.

First, as a quick test case, we treat a bulk system with appreciable SO split, a FCC crystal of Pb atoms. The left hand side and the right hand side panels of Fig. 7.10 show the bandstructure of this crystal calculated with SIESTA and with respect to MLWFs, respectively. The black and the red lines denote bands in absence and in presence of SO coupling, respectively. The match between the SIESTA and the MLWF plots confirm the applicability of our method for 3D bulk systems.

We note that for the procedure of construction of MLWFs, we typically work with a subset of Bloch states of interest (the highest occupied/lowest unoccupied bands and those in their vicinity). We are mostly interested in the matrix elements and eigenvalues corresponding to these bands only. Now, we know that for a diagonal matrix, the non-zero diagonal matrix elements are its eigenvalues. Therefore, if we take an $m \times m$ submatrix of an $n \times n$ diagonal matrix ($m < n$), then each eigenvalue of the

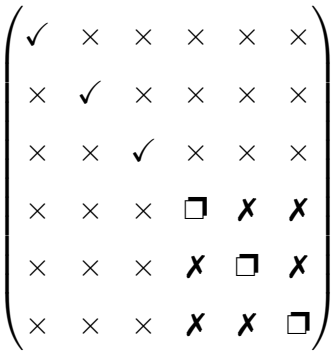

Figure 7.11: Figure shows a representative structure of the full $m \times m$ matrix and its $n \times n$ submatrix for $n = 3$ and $m = 6$. The ❒ and ✗ symbols stand for the diagonal and off-diagonal elements of submatrix, respectively, while the $\times$ and ✓ symbols are for diagonal and off-diagonal elements situated outside the submatrix, respectively. Roughly speaking, if $\times << ❒$, then one can expect the big matrix to have n (here $n = 3$) eigenvalues, which are close to the eigenvalues of the submatrix

submatrix will be present in the set of eigenvalues of the larger matrix. However, this is not the case if the $n \times n$ matrix is not diagonal. In this case, in general there is no reason to believe that the matrix and the submatrix will have even one common eigenvalue. Relating this observation with the physical problem at hand, we see that if we are interested only in a particular subset of the Bloch states, expressing the non SO Hamiltonian with respect to this subset does not change the relevant eigenvalues since the non SO Hamiltonian is diagonal with respect to the Bloch states. However, for the full SO Hamiltonian expressed in terms of the non-SO Bloch states, the presence of off-diagonal terms means that the eigenvalues of a submatrix will in general not be present in the set of those of the full matrix. Roughly speaking, *if the off-diagonal terms present outside the submatrix are small compared to the diagonal terms of the submatrix, the full matrix has 'm' eigenvalues which differ only slightly from eigenvalues of the submatrix* [See Fig. (7.11)]. Appendix A contains more details on this. For the matrix of $\hat{V}_{SO}$, represented in terms of the Bloch states of the non-SO Hamiltonian, in general the elements of the submatrix of interest are comparable to those outside it and therefore the above condition is not satisfied. Hence, eigenvalues of the submatrix are typically very different from all eigenvalues of the full matrix. In order to obtain the accurate

eigenvalues of $\hat{V}_{SO}$ from the MLWF representation, it is then necessary to construct MLWFs for the full set of bloch states. This is done for the organic crystal of $PhBr_2C_6Br_2$ (See Fig. 7.12 for structure), which is known to produce high phosphoresence due to relatively high intermolecular heavy-atom interaction [223]. Fig. 7.13(a) and (b) show the bandstructure of $\hat{V}_{SO}$ calculated with SIESTA and MLWFs respectively, where the MLWFs construction has been performed over the entire space.

For the full hamiltonian $\hat{H}_{\text{full}} = \hat{H}_{\text{non\_SO}} + \hat{H}_{\text{SO}}$, this is slightly different. Here, for the full matrix, the off-diagonal terms are much smaller than the diagonal terms and consequently, for most organic crystals, all the eigenvalues are only slightly different from the diagonal elements. Now, since the off-diagonal terms outside the submatrix are typically much smaller than the diagonal elements of the submatrix, the eigenvalues of the submatrix will have less inaccuracy compared to the relevant eigenvalues of the full matrix. In this case, it can be shown that (see Fig [A.3] of Appendix A), larger the difference in dimension between the submatrix and the full matrix, larger will be the deviation of the submatrix eigenvalues compared to the corresponding ones of the full matrix. So, for a small system (e.g. carbon or methane chain), a subset of eigenvalues of $\hat{H}_{\text{full}}$ can be found from the relevant submatrix with good level of accuracy. However, for a system with a large basis set (say, durene) the $\hat{H}_{\text{full}}$ eigenvalues obtained by diagonalizing only a submatrix is likely to be inaccurate.

7.4 Conclusion

We have presented an accurate method for obtaining the SO matrix elements between the MLWFs constructed in absence of SO coupling. Our procedure, implemented within the atomic-orbital-based DFT code SIESTA, allows one to avoid the construction of the Wannier functions over the SO-split band structure. In some cases, in particular for organic crystals, such splits are tiny and a direct construction is numerically impossible. The method is then put to the test for a number of materials systems, going from isolated molecules, to atomic nanowires, to 1D molecular crystals and finally to 3D crys-

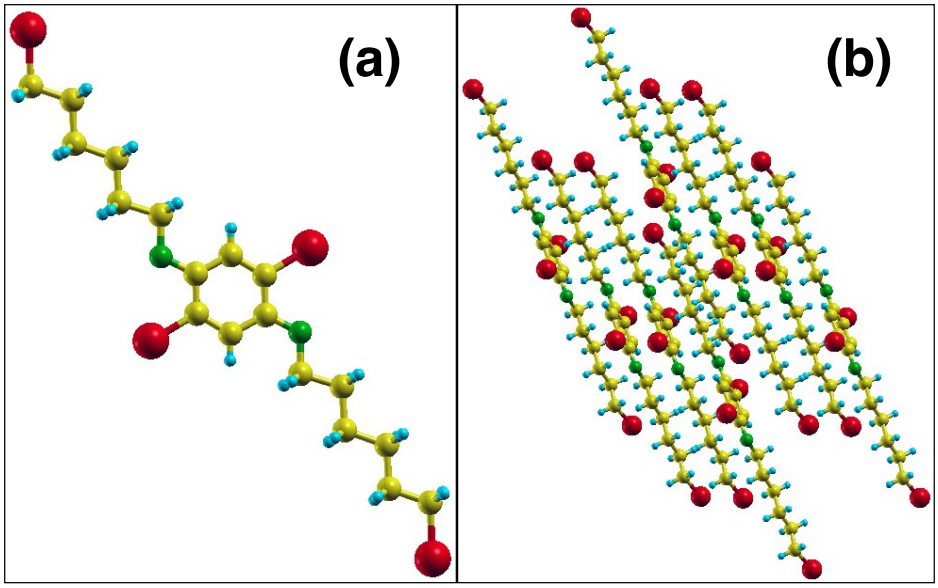

Figure 7.12: Structure of $PhBr_2C_6Br_2$. Panel (a) and (b) shows structure of the individual molecular unit and of the crystal respectively. Color code: Yellow- Carbon, Blue-Hydrogen, Green-Oxygen, Red- Bromine.

tals. When the entire band manifold is used for constructing the MLWFs the mapping between Bloch and Wannier orbitals is exact and the method can be used for both light and heavy elements. In contrast for weak spin-orbit interaction one can construct the MLWFs on a subset of the states in the band structures without much loss of accuracy in the resulting split, provided that the full basis set is small. As such our scheme appears as an important tool for constructing effective spin Hamiltonians for organic materials to be used as input in a multiscale approach to the their thermodynamic properties.

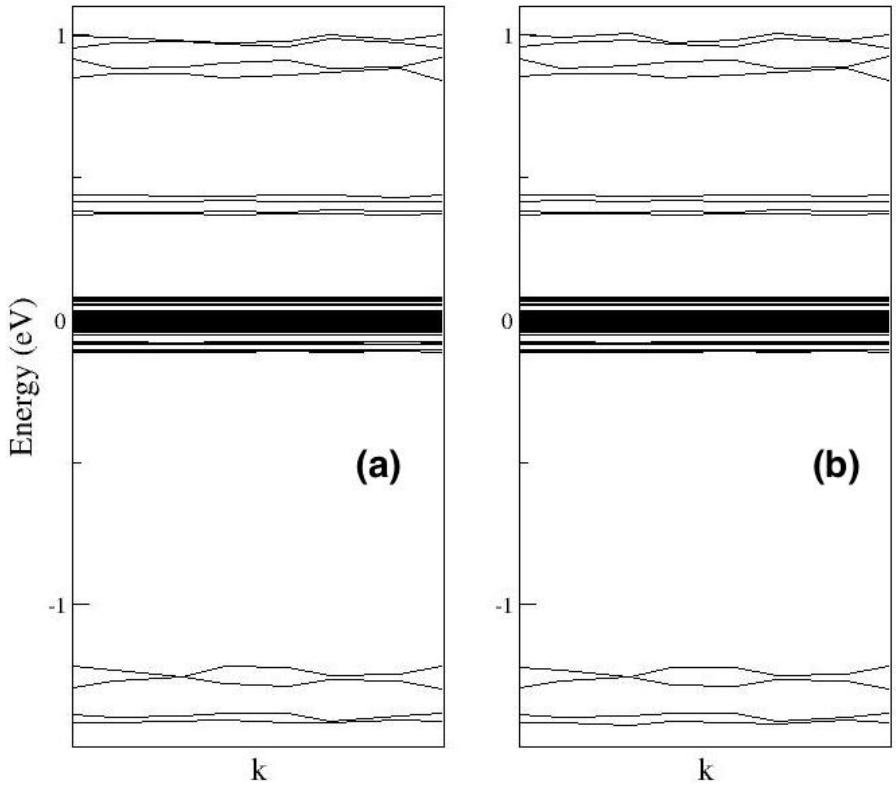

Figure 7.13: Band structure of $\hat{V}_{SO}$ for the organic crystal of $PhBr_2C_6Br_2$. The left and the right column show results calculated with SIESTA and from MLWFs respectively. The MLWFs have been constructed over Bloch states from the entire space containing 442 bands. Thus, for our case of non-collinear spin, the SO matrix has a dimension of 884x884. For such a large basis set, in order to keep the computation simple, only a (2x2x2) k-point grid has been considered. The match between the two plots show that with the proposed method the matrix elements of $\hat{V}_{SO}$ can be calculated accurately with respect to MLWFs for a 3 dimensional organic crystal.

Chapter 8

Calculation of Spin Phonon Coupling with respect to Wannier Functions

As mentioned earlier, in an actual organic crystal the atoms vibrate about their equilibrium positions and the strength of such vibrations increases with increasing temperature. As expected, such vibrations, which are Bosonic particles named *phonons*, change the potential felt by the electrons at any instant. Therefore, in order to describe the motion of electrons accurately, one needs to incorporate the coupling between electrons and phonons into the Hamiltonian.

Since the TB Hamiltonian operator $\hat{H}$ is a function of the ionic positions, vibrational motions give rise to a change in $\hat{H}$. Additionally, since the MLWFs, which are the basis functions with respect to which we want to express the Hamiltonian, are constructed from the Bloch states, which themselves depend on ionic coordinates, lattice vibrations result in a change of the MLWFs as well. Therefore, the change in the Hamiltonian matrix elements, i.e. in the onsite and hopping energies, is a combined effect of

1. change in $\hat{H}$ due to ionic motions, and

2. change in the MLWF basis functions due to ionic motions.

Hence, in the TB picture, the change in the onsite/hopping energy of a lattice site for some atomic displacement will be given by

$$\Delta\varepsilon_{nm} = \langle w_n^f|\hat{H}^f|w_m^f\rangle - \langle w_n^i|\hat{H}^i|w_m^i\rangle\,, \tag{8.1}$$

where w_m^i (w_m^f) and $\hat{H}^i$ ($\hat{H}^f$) are the initial (final) MLWF and Hamiltonian operator, respectively. Eq. (8.1) corresponds to change in onsite or hopping energy depending on whether the MLWFs are located on the same site or on different sites. Since any general lattice vibration can be expanded as a linear combination of normal mode vibrations, one is typically interested in calculating changes in such energies due to vibrations along normal mode coordinates. To quantify the rate of such change, one can define an electron-phonon coupling parameter g_{mn}^λ for some phonon mode λ as the rate of change ($\Delta\varepsilon_{mn}$) of the corresponding energy term of the Hamiltonian with respect to displacement ΔQ_λ pertaining to that phonon mode, namely

$$g_{mn}^\lambda = \left.\frac{\partial\varepsilon_{mn}}{\partial Q}\right|_{Q\to Q+\Delta Q_\lambda}, \tag{8.2}$$

where Q is an index denoting the geometry of the system. Here $Q \to Q+\Delta Q_\lambda$ indicates that the partial derivative is to be taken with respect to the atomic displacement along the phonon eigenvector corresponding to the mode λ.

We note that this coupling constant is fundamentally different from the conventionally used electron-phonon coupling constant, which, for, say the onsite energy corresponding to the m-th basis vector is written as

$$\alpha_{mm}^\lambda = \left.\frac{\partial\left(\langle\phi_m^i|\hat{H}^f - \hat{H}^i|\phi_m^i\rangle\right)}{\partial Q}\right|_{Q\to Q+\Delta Q_\lambda}. \tag{8.3}$$

Here, only the Hamiltonian operator is changed and this change is evaluated with respect to the fixed basis set corresponding to the equilibrium structure. Hence, unlike the coupling term defined in Eq. (8.2), these coupling elements do not correspond to the change in on-site or hopping energies of the crystal due to atomic movements. For the remaining of this paper, unless stated otherwise, electron-phonon coupling will

denote the first description, i.e. g^{λ}_{mn} of Eq. (8.2). The effect of such coupling on charge transport has been the subject of many previous investigations [224, 60, 225, 61] .

In a similar way, the SO matrix elements of a crystal with respect to ML-WFs also depend on the ionic coordinates. Once the spin-orbit coupling elements $\langle w^{s_1}_{m\mathbf{R}}|\hat{V}_{SO}|w^{s_2}_{n\mathbf{R}'}\rangle$ are known in terms of the MLWFs, it is possible to determine the spin-phonon coupling terms following a prescription similar to that for electron-phonon coupling presented in Eq. (8.2).

$$g^{s_1 s_2(\lambda)}_{m,n} = \left.\frac{\partial \varepsilon^{s_1 s_2}_{(SO)mn}}{\partial Q}\right|_{Q\to Q+\Delta Q_\lambda}, \tag{8.4}$$

where $\varepsilon^{s_1 s_2}_{(SO)mn}$ is the SO matrix element between the MLWFs $|w^{s_1}_m\rangle$ and $|w^{s_2}_n\rangle$, Q denotes the atomic positions and ΔQ refers to infinitesimal displacement of the coordinates along the λ-th phonon mode. As noted earlier, a change in atomic coordinates results in a change in the MLWFs and such change must be taken into account while calculating difference in SO elements $\Delta\varepsilon^{s_1 s_2}_{(SO)mn}$. We use the same symbol g to denote both the electron-phonon and the spin-phonon coupling. They can be distinguished by the presence or absence of the superscript for the spin indices. It must be noted that, in existing literature, the term 'spin-phonon' coupling has been used to denote different effects, most importantly, in the study of multiferroics to denote the modulation of phonon frequencies due to changes in magnetic ordering [226, 227, 228, 229, 230]

In a practical calculation, both for electron-phonon and spin-phonon coupling, each atom i of the unit cell is given a tiny displacement $\Delta Q_\lambda \mathbf{e}^{\mathbf{i}}_\lambda$ along the direction of the corresponding phonon eigenvector, $\mathbf{e}^{\mathbf{i}}_\lambda$, and the electron-phonon (spin-phonon) coupling is calculated as $\Delta\varepsilon_{mn}/\Delta Q_\lambda$ ($\Delta\varepsilon^{s_1 s_2}_{(SO)mn}/\Delta Q_\lambda$), i.e. from finite difference. If ΔQ_λ is too large then, the harmonic approximation, which is the basis of this approach, breaks down. In contrast, if ΔQ_λ is too low, then the quantity will have significant numerical error. Hence, for any system studied, one must evaluate the coupling term for a range of ΔQ_λ and from a plot of coupling terms vs ΔQ_λ, choose the most suitable value of ΔQ_λ. It is important to note that the coupling terms so defined have the dimension of Energy/Length. This is consistent with the definition of the coupling

term used in the Hamiltonian of Eq. (2.8) which is a prototype Hamiltonian for the proposed Monte-Carlo calculations of the transport properties. However, various other definitions and dimensions for the electron-phonon coupling can be found in existing literature [231, 232, 61, 64].

The spin-diffusion in an organic crystal at finite temperature will depend on the spin-phonon coupling and therefore the spin-phonon matrix elements are needed for any multiscale calculation of spin-relaxation length and time in OSCs. In this chapter we present our calculation of spin-phonon coupling in terms of MLWFs, with the help of the SIESTA software. We begin with the simplest non-trivial periodic system, namely a 1D chain of Pb atoms with 2 atoms per unit cell, before moving to a system of practical interest, namely a crystal of durene molecules.

8.1 One Dimensional Pb Chain

A linear chain of Pb atoms with a diatomic unit cell has 6 phonon modes for each wave-vector, $\mathbf{q}$. For simplicity, we restrict our calculations to the Γ-point i.e. $\mathbf{q} = \mathbf{0}$, so that equivalent atoms in all unit cells have the same displacements with respect to their equilibrium positions. This makes the 3 acoustic modes, for which the Γ-point frequency and the relative displacement between the atoms of unit cell is zero, redundant. We, therefore, are left with 3 modes of vibration as shown in the bottom panel of Fig. 8.1. The MLWFs are constructed by omitting the lowest two bands (made up mostly of s-orbitals) and retaining the remaining 6 valence bands[1]. This gives us 6 MLWFs per unit cell, 3 centred on each atom. For each of the three modes, we evaluate the coupling matrix elements between the MLWFs of the same unit cell for a range of ΔQ_λ. Analysing these results we find that $\Delta Q_\lambda = 0.03$ is an acceptable value for such fractional displacement.

The top panel of Fig. 8.1 shows the MLWFs corresponding to the first atom

[1]We have not presented the band strucutre of this system. However, since the present system has two atoms per unit cell, its bands can be obtained by a double band-folding of those shown in Fig. (7.2)

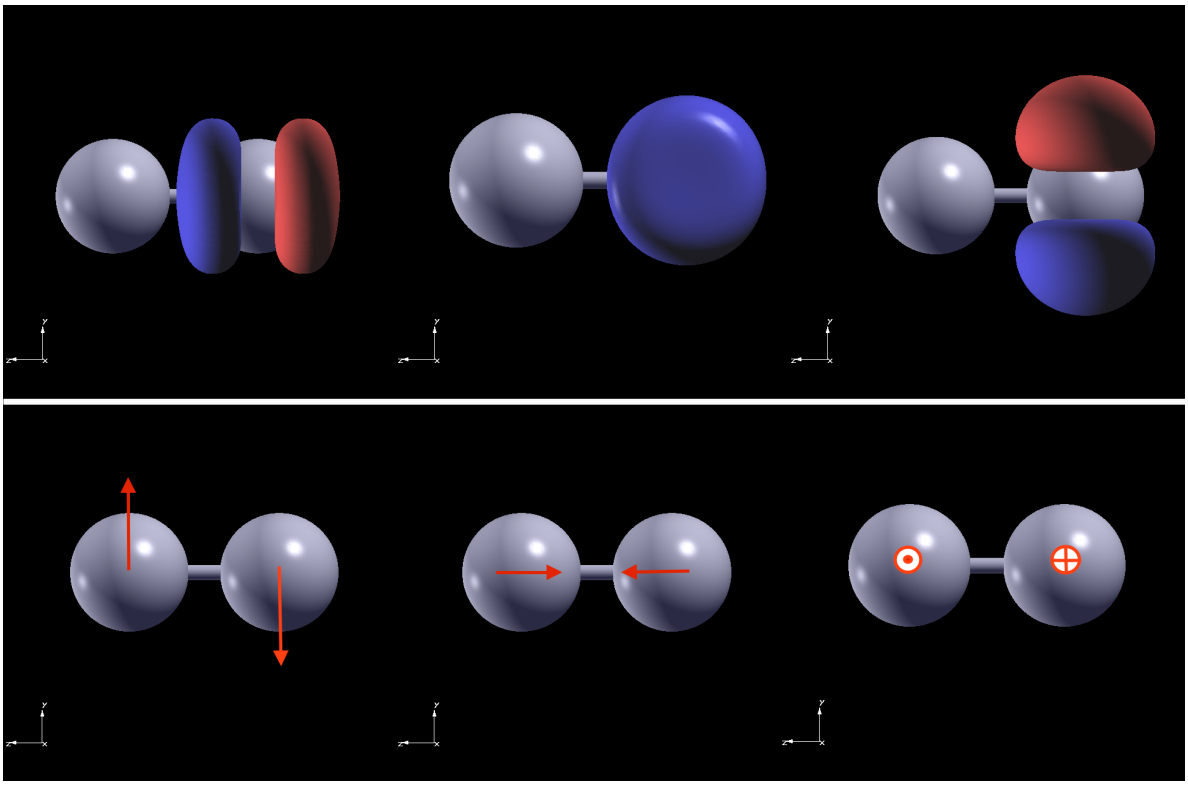

Figure 8.1: The unit cell of the Pb chain containing two atoms. The figures in the top panel show an isovalue plot of the three MLWFs (from left to right: $|w_{1,\mathbf{0}}\rangle$, $|w_{2,\mathbf{0}}\rangle$ and $|w_{3,\mathbf{0}}\rangle$) centred on the first atom. Figures in the bottom panel indicate the directions of the atomic motion corresponding to the three phonon modes (mode 1, mode 2 and mode 3 from left to right).

of the unit cell in the equilibrium geometry. From this figure one can see that $|w_{1,\mathbf{0}}\rangle$, $|w_{2,\mathbf{0}}\rangle$ and $|w_{3,\mathbf{0}}\rangle$ resemble the p_z, p_x and p_y orbitals of the first atom, respectively. By symmetry, $|w_{4,\mathbf{0}}\rangle$, $|w_{5,\mathbf{0}}\rangle$, $|w_{6,\mathbf{0}}\rangle$ can be associated with the p_z, p_x and p_y orbitals located on the second atom. However, it is important to note that *such similarity between the MLWFs and the orbital angular momentum eigenstates does not imply equality between them.* To appreciate this point, note that

- $\langle w_{i,\mathbf{0}}|w_{j,\mathbf{0}}\rangle = 0, \forall i \neq j$ but this is not necessarily true for $\langle p_{m,1}|p_{n,2}\rangle$ where $|p_{m,1}\rangle$ and $|p_{n,2}\rangle$ are orbital angular momentum eigenkets centred on the first and the second atom, respectively.

- When an atom is displaced from its equilibrium position, the p orbitals (e.g. the basis orbitals of SIESTA) experience a rigid shift only, but do not change in shape. In contrast, the MLWFs change in shape along with being displaced.

- Most importantly, in the on-site SO approximation used in SIESTA, the hopping term for SO coupling, i.e. the SO matrix element between two orbitals located on two different atoms, is always zero. As for the on-site term, the SO matrix element between two orbitals of the same atom is independent of the position of the other atom. Thus, in terms of the SIESTA basis set, with the on-site SO approximation, the spin-phonon coupling matrix is always zero. This is not the case with the MLWFs. Even when used in conjunction with the on-site SO approximation of SIESTA, the spin-phonon coupling is typically non-zero for an MLWF basis owing to the change in the basis functions themselves.

Before calculating the spin-phonon coupling, let us take a brief look at the electron-phonon coupling matrix elements for the 3 phonon modes. The non-zero matrix elements are presented in Tab. 8.1 for each normal mode. It is interesting to note that the change in overlap between the associated 'p' orbitals due to the atomic displacements corresponding to the normal modes can be intuitively expected to have the same trend as the electron-phonon coupling matrix elements with respect to the MLWFs. For example, for atomic motion along mode 3, $\langle p_{y,1}|p_{z,2}\rangle$ will be zero at any instant since $|p_{z,2}\rangle$ will

Mode	Element	value(meV/Å)
Mode 1	$[w_3\|w_4]$	-0.85
Mode 2	$[w_1\|w_4]$	4.03
	$[w_2\|w_5]$	-1.51
	$[w_3\|w_6]$	-1.51
Mode 3	$[w_2\|w_4]$	-0.85

Table 8.1: The non-zero electron-phonon coupling matrix elements for the Γ-point phonon modes of the lead chain with a diatomic unit cell. $[w_\mu|w_\nu]$ denotes the electron-phonon coupling matrix between the MLWFs $|w_\mu\rangle$ and $|w_\nu\rangle$. It must be kept in mind that the matrix elements are real and all other non-zero matrix elements can be found from the relation $[w_\mu|w_\nu] = [w_\nu|w_\mu]$. Please see Fig. 8.1 for diagram of the modes and the MLWFs.

always have equal overlap with the positive and negative lobe of $|p_{y,1}\rangle$. Keeping in mind that modes 1, 2 and 3 correspond to motions in the directions y, z and x respectively, we can convince ourselves that:

- $\Delta \langle p_{z,1}|p_{z,2}\rangle_{\text{mode:2}} > \Delta \langle p_{z,1}|p_{x,2}\rangle_{\text{mode:3}}$
- $\Delta \langle p_{z,1}|p_{x,2}\rangle_{\text{mode:3}} = \Delta \langle p_{x,1}|p_{z,2}\rangle_{\text{mode:3}} = \Delta \langle p_{y,1}|p_{z,2}\rangle_{\text{mode:1}}$
- $\Delta \langle p_{x,1}|p_{y,2}\rangle_{\text{mode:1}} = \Delta \langle p_{x,1}|p_{z,2}\rangle_{\text{mode:2}} = \Delta \langle p_{y,1}|p_{z,2}\rangle_{\text{mode:3}} = 0$

where Δ denotes change of the overlap.

Now we proceed to present our results for the spin-phonon coupling. Unlike electron-phonon coupling matrix elements, the spin-phonon counterparts are not necessarily real valued. For each mode, the non-zero spin-phonon coupling matrix elements are tabulated in Tab. 8.2. By denoting the spin-phonon matrix element between $|w_\mu^{s_1}\rangle$ and $|w_\nu^{s_2}\rangle$ as $[w_\mu^{s_1}|w_\nu^{s_2}]$, all other non-zero spin-phonon matrix elements can be found from the relations

Mode	Element	Value(meV/Å)
Mode 1	$[w_1^{\uparrow}\|w_5^{\uparrow}]$	(0.0,-0.07)
	$[w_2^{\uparrow}\|w_4^{\uparrow}]$	(0.0,0.07)
	$[w_2^{\uparrow}\|w_6^{\downarrow}]$	(-0.19,0.0)
	$[w_3^{\uparrow}\|w_5^{\downarrow}]$	(0.19,0.0)
Mode 2	$[w_1^{\uparrow}\|w_5^{\downarrow}]$	(0.05,0.0)
	$[w_2^{\uparrow}\|w_4^{\downarrow}]$	(-0.05,0.0)
	$[w_1^{\uparrow}\|w_6^{\downarrow}]$	(0.0,-0.05)
	$[w_3^{\uparrow}\|w_4^{\downarrow}]$	(0.0,0.05)
Mode 3	$[w_1^{\uparrow}\|w_6^{\uparrow}]$	(0.0,0.07)
	$[w_3^{\uparrow}\|w_4^{\uparrow}]$	(0.0,-0.07)
	$[w_2^{\uparrow}\|w_6^{\downarrow}]$	(0.0,-0.19)
	$[w_3^{\uparrow}\|w_5^{\downarrow}]$	(0.00,0.19)

Table 8.2: Spin-phonon coupling matrix elements for the Γ-point phonon modes of lead chain with diatomic unit cell. $[w_\mu^{s_1}|w_\nu^{s_2}]$ denotes the complex spin-phonon coupling matrix element between the MLWFs $|w_\mu^{s_1}\rangle$ and $|w_\nu^{s_2}\rangle$. The other non-zero matrix elements can be found from the relations in Eq. (8.5). The phonon modes and MLWFs are shown in Fig. 8.1

.

$$
\begin{aligned}
[w_\mu^\uparrow | w_\nu^\downarrow] &= -[w_\mu^\downarrow | w_\nu^\uparrow]^*, \\
[w_\mu^\uparrow | w_\nu^\downarrow] &= [w_\nu^\downarrow | w_\mu^\uparrow]^*, \\
\Im[w_\mu^\uparrow | w_\nu^\uparrow] &= -\Im[w_\mu^\downarrow | w_\nu^\downarrow].
\end{aligned} \tag{8.5}
$$

Also, from the symmetry of the MLWFs, it is easy to show that

$$[w_1^\uparrow | w_5^\uparrow]_{\text{Mode1}} = -[w_2^\uparrow | w_4^\uparrow]_{\text{Mode1}}, \tag{8.6}$$

$$[w_1^\uparrow | w_6^\uparrow]_{\text{Mode3}} = -[w_3^\uparrow | w_4^\uparrow]_{\text{Mode3}}. \tag{8.7}$$

We have noted that in the on-site approximation, the spin-phonon coupling (according to our definition) of the Pb chain should be zero in the SIESTA basis. However, not limiting oneself to such approximation, one can determine some analytical expression for these coupling elements in terms of the change in orbital overlaps. Such calculations have been presented in Appendix B. It is interesting to note that the analytical expressions calculated in this way share many qualitative similarities with those presented in Tab. 8.2. We summarize the findings of this section by noting that the spin-phonon couplings matrix elements corresponding to the two equivalent normal modes show the expected symmetry. We have also seen that the non-zero spin-phonon coupling for the inequivalent mode is in general smaller than those of the equivalent modes.

8.2 Durene Crystal

Finally we are in the position to discuss the spin-phonon coupling in a real organic crystal, namely durene. For the electron-phonon or spin-phonon coupling calculations, one needs to make sure that the construction of MLWFs converges to a global minimum (otherwise the various displaced geometries may correspond to different local minima resulting in the description of different energy landscapes). Typically, a MLWF calculation with dense k-mesh is likely to converge to a local minimum and a calculation

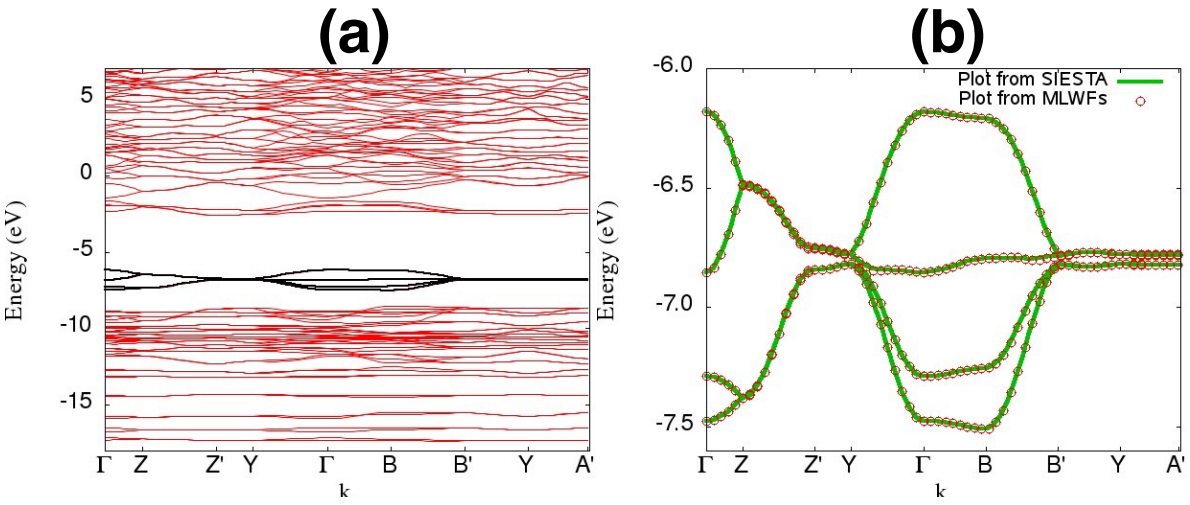

Figure 8.2: Band structure of the durene crystal. Panel (a) shows all the occupied and many unoccupied bands. MLWFs are constructed from the 4 highest occupied bands, which are plotted in black. Panel (b) shows the magnified structure of these 4 bands plotted with SIESTA (green line) and obtained from the MLWFs computed with WANNIER90 (red circle).

with sparse k-mesh has higher probability of giving the global minimum (Γ-point calculation always converges to the global minimum). However, a sparse k-mesh means small period for the BVK boundary condition, i.e. a poorer description of the crystal. In our calculation, we use a $4 \times 4 \times 4$ k-grid and construct MLWFs from the the top 4 valence bands. This enables the calculation to converge to a global minimum (indicated by zero or negligible imaginary elements in the Hamiltonian matrix). In Fig. 8.2(a) we show a plot of the bandstructure of durene (within a large energy window) and in Fig. 8.2(b), the bandstructure corresponding to the 4 bands from which we construct MLWFs. These are plotted with SIESTA and with respect to the MLWFs.

Since the durene unit cell contains 2 molecules, the 4 valence bands give us 4 MLWFs per unit cell such that each molecule has 2 MLWFs centred on it. In Fig. 8.3 we show an isovalue plot of the 4 MLWFs corresponding to $\mathbf{R} = \mathbf{0}$. We see that unlike $|w_{3,\mathbf{0}}\rangle$ and $|w_{4,\mathbf{0}}\rangle$, which are situated on the same molecule, $|w_{1,\mathbf{0}}\rangle$ and $|w_{2,\mathbf{0}}\rangle$ are on different but equivalent molecules displaced by a primitive lattice vector $\mathbf{a_2}$. Thus, $|w_{1,\mathbf{0}}\rangle$ and $|w_{2,\mathbf{R}'}\rangle$ will be on the same molecule for $\mathbf{R}' = -\mathbf{a_2}$, where $\{\mathbf{a_1}, \mathbf{a_2}, \mathbf{a_3}\}$ is the set of primitive

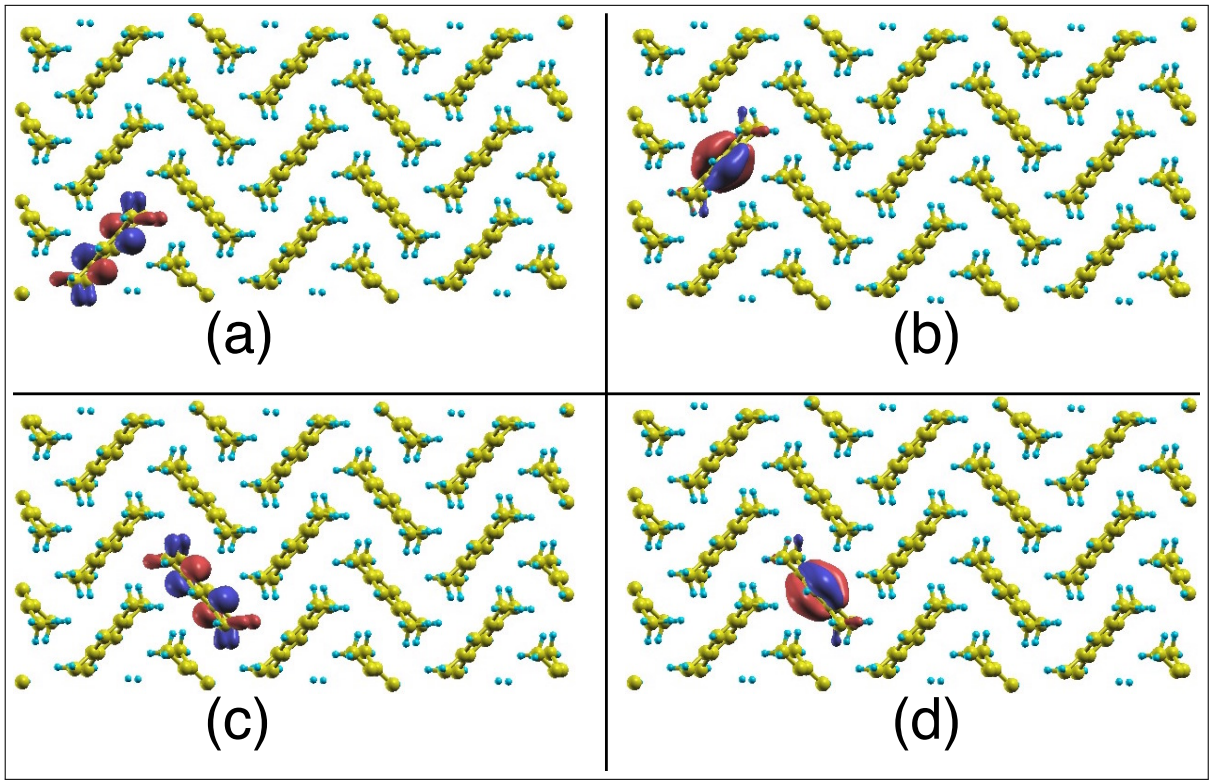

Figure 8.3: Isovalue plots for MLWFs of the four topmost valence bands of a durene crystal. Panels (a),(b),(c) and (d) correspond to $|w_{1,\mathbf{0}}\rangle$, $|w_{2,\mathbf{0}}\rangle$, $|w_{3,\mathbf{0}}\rangle$ and $|w_{4,\mathbf{0}}\rangle$ respectively.

vectors. This means that for our tight-binding picture $\langle w_{1,\mathbf{0}}|\hat{H}|w_{2,\mathbf{0}}\rangle$ corresponds to a non-local (hopping) matrix element, whereas $\langle w_{1,\mathbf{0}}|\hat{H}|w_{2,\mathbf{R}'}\rangle$ is a local (on-site) energy term. In the following, we shall calculate the electron-phonon and spin-phonon coupling corresponding to various modes of the durene crystal and compare

1. The relative contribution of the different modes,

2. For each mode, the relative contribution of the local and non-local terms.

Since the unit cell contains two molecules, each with 24 atoms (48 atoms in the unit cell), a Γ-point phonon calculation will give us 144 modes, 141 of which will be non-trivial. Among these, 12 will be predominantly intermolecular modes (3 translational and 9 rotational) and the remaining ones will be of predominantly intramolecular nature. Here we shall consider only the phonon modes with an energy less than 75 meV, as the modes with higher energy are accessible only at high temperature. Thus, we take into account 25 modes, of which the first 12 are intermolecular (these are lower in energy) and the rest are symmetry inequivalent intramolecular[2].

In order to compare the contributions of the different phonon modes and of the local and non-local coupling terms, we calculate the following effective electron-phonon coupling terms,

$$G_\lambda^{\mathrm{L}} = \sum_{m,n} |g_{mn}^\lambda|^2 \text{ (where } m \text{ and } n \text{ are on same molecule)},$$

and

$$G_\lambda^{\mathrm{N}} = \sum_{m \neq n} |g_{mn}^\lambda|^2 \text{ (where } m \text{ and } n \text{ are on different molecules)}, \tag{8.8}$$

where the superscripts L and N stand for Local and Non-local, respectively. Note that in this calculation, the contributions from the MLWFs of degenerate direct lattice points have been multiplied by their corresponding weight factors. Fig. 8.4 shows

[2]The phonon spectrum is calculated with FHI-AIMS. Calculation courtesy: Dr. Carlo Motta

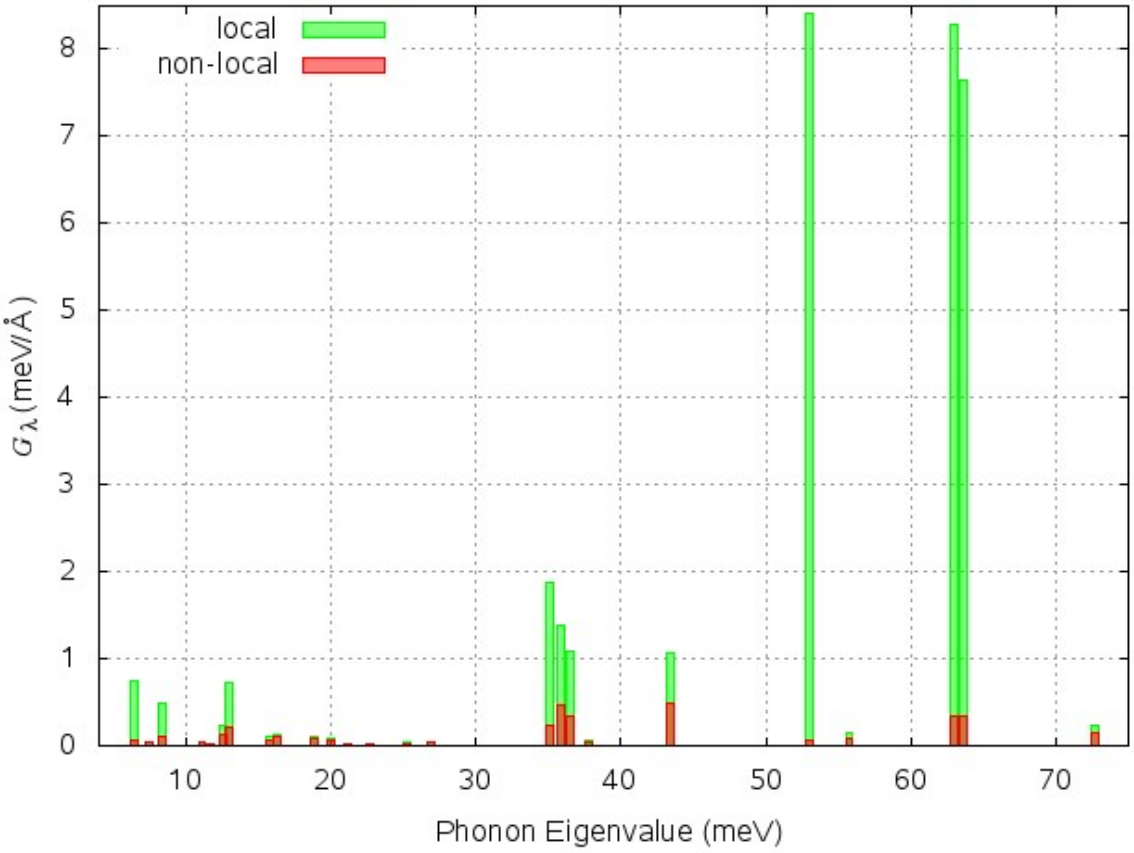

Figure 8.4: Histogram plot of the effective electron-phonon coupling as a function of phonon eigenvalue. The local and the non-local contributions are denoted by green and red bars, respectively.

a histogram plot of the G_λ terms as function of the phonon energy eigenvalues. It must be kept in mind that the coupling matrix elements are strongly dependent on the MLWFs. Therefore, constructing Wannier functions from a different set of Bloch states can in principle result in completely different values for G_λ. We see that in our case, most of the modes with high $G_\lambda (= G_\lambda^{\rm L} + G_\lambda^{\rm N})$ are located at high phonon energies. Also, the electron-phonon couplings for modes with lower G_λ are dominated by the non-local contributions, while those with higher G_λ are dominated by local contributions.

For the spin-phonon coupling, we can define the spin-dependent G_λ terms, i.e. the effective spin-phonon couplings as,

$$G_\lambda^{\rm L(s_1 s_2)} = \sum_{m,n} |g_{mn}^{s_1 s_2(\lambda)}|^2 \text{ (where } m \text{ and } n \text{ are on same molecule),}$$

and

$$G_\lambda^{\rm N(s_1 s_2)} = \sum_{m \neq n} |g_{mn}^{s_1 s_2(\lambda)}|^2 \text{ (where } m \text{ and } n \text{ are on different molecules).} \qquad (8.9)$$

In Fig. 8.5, we plot these effective spin-phonon coupling terms, separately denoting the local and non-local contributions. The top and the bottom panels correspond to $(s_1 = \uparrow, s_2 = \uparrow)$ and $(s_1 = \uparrow, s_2 = \downarrow)$ respectively. As expected, the spin-phonon terms are extremely small, owing to the small atomic masses in the crystal. As in the case of electron-phonon interaction, the effective spin-phonon coupling terms are dominated by non-local contributions for low $G_\lambda^{(s_1 s_2)} = G_\lambda^{\rm L(s_1 s_2)} + G_\lambda^{\rm N(s_1 s_2)}$ and by local contributions for high G_λ. We also see that the spin-phonon coupling (for same spin, as well as for different spins) is very small for the first few modes, which represent intermolecular motions. This is fully consistent with the short-ranged nature of SO coupling. An important message emerging from these results is that phonon modes having high effective electron-phonon coupling do not necessarily have high effective spin-phonon coupling, and vice-versa.

In conclusion, we have seen that in general both the electron-phonon and the spin-phonon coupling constants are dominated by the local coupling terms, though,

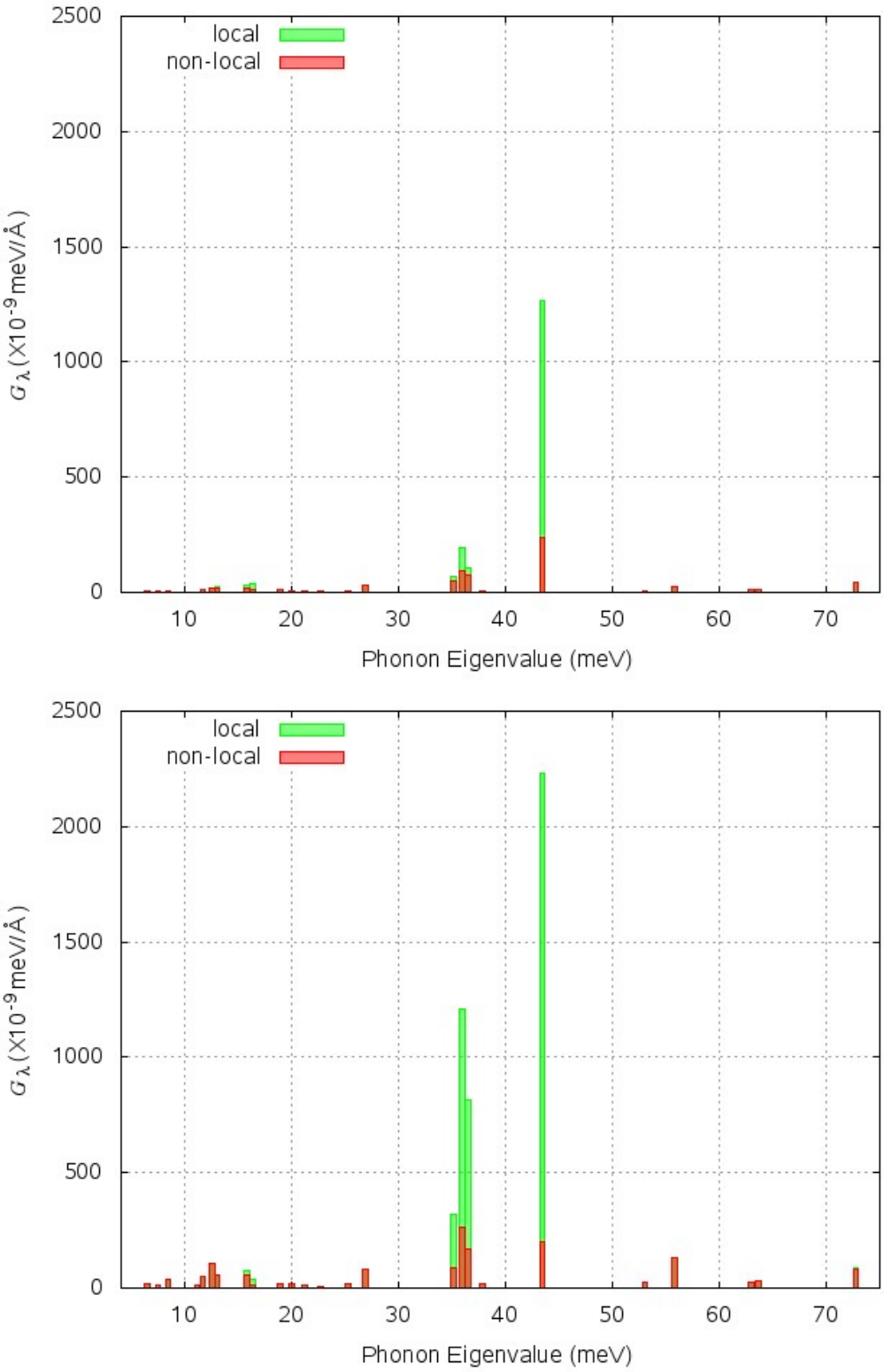

Figure 8.5: Histogram plot of the effective spin-phonon coupling as a function of phonon eigenvalue. The top panel corresponds to the case of same spins, while the bottom one corresponds to that of different spins. The local and the non-local contributions are denoted by green and red bars respectively.

modes with very small effective coupling tend to have larger relative contribution from non-local modes. However, no apparent correlation can be seen between the effective coupling constants pertaining to various phonon modes for the electron-phonon coupling with those for the spin-phonon coupling.

8.3 Approximated Wannier Basis Set

Before concluding this chapter we would like to discuss a problem, and a proposed solution thereof, pertaining to the construction of a Hamiltonian for the proposed calculation of thermodynamic quantities. Working with the MLWF basis, we have seen that (see section 7.3.6) the calculation of the SO matrix elements obtained only from a set of bands of interest can result in loss of information, since there is no guarantee that the SO matrix terms between such band and those ignored will be negligible. For example, the SO matrix calculated with respect to a subset of MLWFs is not guaranteed to yield the exact SO split of energy eigenvalues. The accurate remedy for this problem is to construct Wannier functions from all bands as we have shown in the previous chapter for the crystal of $PhBr_2C_6Br_2$ (see section 7.3.6). However, this poses two major problems,

1. One of the main motivations behind using MLWF basis over the localized atomic orbitals (e.g. basis orbitals of SIESTA) is that of being able to downsize the problem. If one ends up using the same number of MLWFs as atomic basis functions, then that purpose is totally lost.

2. A more serious problem arises for calculation of spin-phonon coupling. Obtaining MLWFS from the full band structure typically converges to a local minimum for the MLWFs. This makes comparison of SO matrix elements for two different geometries (one grounds state geometry and one obtained by displacing atoms along phonon eigenvectors) unjustified, since it is possible that the two geometries have converged to two different local minima.

In order to resolve these issues we settle for a middle ground compromising

between inaccuracy and computation. We use different BVK boundary conditions for the bands of interest (primary bands) and the other bands (secondary bands).

- For primary bands we use the regular BVK condition of

$$\psi_P(\mathbf{r}) = \psi_P(\mathbf{r} + N_i\mathbf{R}_i), \tag{8.10}$$

  where $i = 1, 2, 3$; $\mathbf{R}_i$ is the lattice vector in 'i' direction. Thus each band allows $N_1N_2N_3 = N$ values for $\mathbf{k}$.

- For each secondary band we use essentially a Γ point boundary condition

$$\psi^\Gamma_m(\mathbf{r}) = \psi^\Gamma_m(\mathbf{r} + \mathbf{R}_i). \tag{8.11}$$

Thus, in this new vector space each primary band contributes N states but each secondary band contributes one state only. The set of Bloch states for this new space is obtained from that of the full space by considering $\mathbf{k} = \mathbf{0}$ to be the only states of the secondary bands.

Dividing the infinite crystal into an infinite sum of supercells each composed of N units, the two types of states look like[3] (also see Eq. (3.13)):

$$\begin{aligned} |\psi_{P,\mathbf{k}}\rangle &= \sum_{l=-\infty}^{+\infty} \sum_{j=0}^{N-1} e^{i\mathbf{k}.(j\mathbf{R}+lN\mathbf{R})} \sum_{\mu} C_{\mu,P}(\mathbf{k}) \left|\phi_{\mu,(j\mathbf{R}+lN\mathbf{R}}\right\rangle, \\ &= \sum_{l=-\infty}^{+\infty} \sum_{j=0}^{N-1} e^{ij\mathbf{k}.\mathbf{R}} \sum_{\mu} C_{\mu,P}(\mathbf{k}) \left|\phi_{\mu,(j\mathbf{R}+lN\mathbf{R}}\right\rangle, \end{aligned} \tag{8.12}$$

$$|\psi^\Gamma_m\rangle = \sum_{l=-\infty}^{+\infty} \sum_{j=0}^{N-1} \sum_{\nu} C_{\nu,m}(\mathbf{0}) \left|\phi_{\nu,(j\mathbf{R}+lN\mathbf{R}}\right\rangle, \tag{8.13}$$

(This is written in 1D form to avoid notational complexity.)

The relevant matrix elements take the form:

[3]Note that l is index of the supercell, j is the index of the lattice point within the supercell and $i = \sqrt{-1}$

$$\langle \psi_m^{\Gamma(s_1)} | \hat{V}_{SO} | \psi_{P,\mathbf{k}}^{s_2} \rangle = \sum_{l=-\infty}^{+\infty} N \delta_{\mathbf{k},\mathbf{0}} \left[\sum_{\mu,\nu} C_{\nu,m}^{(s_1)*}(\mathbf{0}) C_{\mu,P}^{(s_2)}(\mathbf{k}) \langle \phi_\nu^{s_1} | \hat{V}_{SO} | \phi_\mu^{s_2} \rangle \right], \tag{8.14}$$

$$\langle \psi_m^{\Gamma(s_1)} | \hat{V}_{SO} | \psi_n^{\Gamma(s_2)} \rangle = \sum_{l=-\infty}^{+\infty} N \left[\sum_{\mu,\nu} C_{\nu,m}^{(s_1)*}(\mathbf{0}) C_{\mu,n}^{(s_2)}(\mathbf{0}) \langle \phi_\nu^{s_1} | \hat{V}_{SO} | \phi_\mu^{s_2} \rangle \right], \tag{8.15}$$

$$\langle \psi_{P,\mathbf{k_1}}^{s_1} | \hat{V}_{SO} | \psi_{Q,\mathbf{k_2}}^{s_2} \rangle = \sum_{l=-\infty}^{+\infty} N \delta_{\mathbf{k_1},\mathbf{k_2}} \left[\sum_{\mu,\nu} C_{\nu,P}^{(s_1)*}(\mathbf{k_1}) C_{\mu,Q}^{(s_2)}(\mathbf{k_2}) \langle \phi_\nu^{s_1} | \hat{V}_{SO} | \phi_\mu^{s_2} \rangle \right]. \tag{8.16}$$

This is essentially a block diagonal matrix with one non-zero block containing the $\mathbf{k} = \mathbf{0}$ parts of all the bands (primary as well as secondary ones) and the other non-zero block containing the $\mathbf{k} \neq \mathbf{0}$ parts of the primary bands. On diagonalization, the first block gives the exact Γ point eigenvalues of $\hat{V}_{SO}$. The second block gives the $\mathbf{k} \neq \mathbf{0}$ eigenvalues that one would obtain if one restricts oneself within the primary bands only.

For a set of bands defined only at $\mathbf{k} = \mathbf{0}$, construction of MLWFs amounts to a mere unitary rotation of the states and does not have any additional advantage. So, for the secondary bands, we skip this procedure and leave the bands intact. However, from the primary bands, we construct the Wannier functions so that the space spanned by $\{|\psi_{P,\mathbf{k}}\rangle\}\ \forall P, \mathbf{k}$ is now spanned by the set of corresponding MLWFs $\{|w_{m,\mathbf{R}}\rangle\}\ \forall m, \mathbf{R}$. The SO terms between the secondary band states and the MLWFs are now

$$\begin{aligned}
\langle \psi_m^{\Gamma(s_1)} | \hat{V}_{SO} | w_{m,\mathbf{R_i}} \rangle &= \frac{1}{N} \sum_{\mathbf{k}} \sum_{P} e^{-i\mathbf{k}.\mathbf{R}_i} U_{Pm}^{(s_2)}(\mathbf{k}) \langle \psi_m^{\Gamma(s_1)} | \hat{V}_{SO} | \psi_{P,\mathbf{k}}^{s_2} \rangle , \\
&= \frac{1}{N} \sum_{P} U_{Pm}^{(s_2)}(\mathbf{0}) \langle \psi_m^{\Gamma(s_1)} | \hat{V}_{SO} | \psi_{P,\mathbf{0}}^{s_2} \rangle , \\
&= \langle \psi_m^{\Gamma(s_1)} | \hat{V}_{SO} | w_{m,\mathbf{R_j}} \rangle \, [\forall i, j].
\end{aligned}$$

The final matrix is then written with respect to a basis set consisting of the Γ-point eigenstates of the secondary bands and all MLWFs calculated from the primary bands. Clearly, this matrix will have the same eigenvalues as those of the matrix obtained with respect to Bloch states [see Eq. (8.14)-Eq. (8.16)].

8.4 Conclusion

In this chapter, starting from our method of obtaining SO matrix elements developed in the previous chapter, we have presented calculations of spin-phonon coupling in periodic systems, corresponding to various normal modes. For a linear Pb chain, the spin-phonon matrix elements expressed with respect to MLWFs share many qualitative similarities with those obtained analytically with respect to atomic basis sets. For the durene crystal, we have obtained both the electron-phonon and spin-phonon coupling elements with respect to MLWFs obtained from the top four valence bands. We have shown that in general, both couplings are dominated by local contributions although the modes with very small net effective coupling tend to have larger non-local contribution. In terms of net effective coupling, the relative contribution of the different modes for electron-phonon coupling generally do not show much correlation with those of spin-phonon coupling. As a final point for this section, we have proposed a competent basis set for expressing the Hamiltonian for further calculations. This basis set contains the MLWFs obtained from the bands of interest, over the full range of allowed k-points in accordance with BVK boundary conditions, and the Γ-point eigenstates for all other bands.

Chapter 9

Conclusion

Owing to the high degree of mechanical flexibility, light weight and ease of synthesis and patterning, organic semiconductors have emerged as promising candidates with several interesting prospects for application in electronic and spintronic devices. A plethora of experimental and theoretical studies have been devoted to the study of their properties and potential applications. Therefore, it is imperative that a complete theoretical framework will be of great value for the study of charge and spin transport in such material. Such a theoretical treatment should ideally follow the first-principles approach, i.e., it should not rely on experimental data. Not only will it solidify our understanding of their transport properties, it will also help us in selecting and discovering organic semiconducting materials customized for specific applications. This thesis takes a step toward such goal.

With the vision of constructing and solving an effective Hamiltonian to compute transport-related observables, we calculate, starting with first principles techniques based on density functional theory (DFT), several parameters that are of interest for such an approach. Besides being important for the construction of the final Hamiltonian, many of these quantities are significant in their own rights as they represent important properties of these materials.

Since a typical organic electronic device will have conducting electrodes in

contact with an organic crystal, which is composed of several weakly bound molecular units, it is crucial to investigate the charge transfer between a conducting surface and a molecule adsorbed on it. With the help of constrained density functional theory, we calculate the energy cost of such charge transfer. Taking a step toward the simulation of a real device, we investigate the effect on the charge transfer energies of defects present in the conducting surface and also of other molecules present in the vicinity of the one under consideration. We also show that the results obtained in this way match, with a high level of accuracy, those obtained analytically with a classical electrostatic model.

Charge transfer between a molecule and a substrate results in relaxation of the ionic coordinates of the molecule and therefore, has an energy cost known as reorganization energy associated with it. The calculation of such energy terms requires a formalism for the accurate evaluation of the forces within the framework of constrained DFT. For efficient computation such formalism must be able to take into account the forces arising from the change in orbital overlaps as a result of the ionic motion, without having to resort to matrix diagonalization. In this thesis, we develop a novel method for such calculation and apply it to a problem requiring extremely high accuracy in the convergence namely for obtaining the re-organization energy of a pentacene molecule adsorbed on a flake of graphene.

Optoelectronic devices operate on the basis of creation and annihilation of a bound electron-hole pair, known as exciton. Therefore, the first-principles calculation of the optical gap of a material, which is the energy associated with creation of an excitonic state, is fundamentally important. We develop a technique, called *excitonic DFT*, rooted in the constraind DFT method, for calculating the optical gap of molecules. This method is computationally much more efficient than the existing standard schemes like TDDFT or methods based on a many-body approach. Excitonic DFT is then used for calculating the optical gap of several organic molecules. We also extend our approach to the evaluation of the optical gap of periodic solids. Finally, we show that this can be used to access double excitations.

Shifting the attention from charge to spin transport, we treat the spin-orbit

interaction, which is thought to be responsible for spin-relaxation in organic crystals. Since the basis functions typically used in first principles calculation are highly inefficient from our proposed effective Hamiltonian approach, we develop a method for calculating the spin-orbit matrix elements with respect to a different set of basis functions, known as the Maximally Localized Wannier Functions (MLWFs). We then apply this technique to several systems, starting from simple molecules, to 1-dimensional model systems to real organic crystals. We test the accuracy of the spin-orbit matrix elements obtained in this way by comparing the associated energy eigenvalues to those obtained directly with calculations based on DFT.

Finally, keeping in mind that real organic devices are expected to work at finite temperature, where the crystal vibrations affect the electronic properties, we extend the aforementioned formalism to include interaction between electronic spin with ionic oscillations. There parameters, known as spin-phonon coupling, are calculated for the model system of a 1-dimensional chain of lead atoms and then for an important organic crystal, namely durene. Such studies include the dependence of the spin-phonon coupling on the different normal modes and also a comparison of such terms with the electron-phonon coupling. In the case of durene we see that the for both the electron-phonon and spin-phonon interactions, the local coupling terms dominate over the non-local ones.

The work presented in this thesis can point to several possible future works.

- The obvious future direction indicated by this work is that of constructing the model Hamiltonian and calculating transport properties of real devices. Since we have obtained the *ab-initio* description of several electronic structural properties, for interfaces and bulk material both, it would be interesting to take this one step ahead by extracting quantities like mobility, spin-relaxation time, $I - V$ characteristics etc. from the resulting Hamiltonian.

- We have found the SO coupling matrix elements with respect to MLWFs. Another possible contributor to spin-relaxation in organic crystals is hyperfine interaction. It would be worth trying to find the coupling matrix elements of this form some DFT based software that takes core electrons directly into account.

- In this thesis, we have proposed a way of calculating optical gaps of solids. We are in the process of probing this further by applying the technique to various solids. We have seen that the excitonic DFT method, which assumes a certain level of equivalence between the KS system and the interacting system, is fundamentally different from the TDDFT method, which makes a linear-response approximation for calculating optical gaps. It would be interesting to further probe the ramifications of such difference in assumption.

- We have shown that the charge transfer energy of a molecule adsorbed on a surface depends on the dielectric constant of the surface. The plot of CT energies as a function of distance between the molecule and the substrate shows good agreement with the plot calculated from classical electrostatic considerations with the knowledge of the dielectric constant. It might be interesting to see if such a plot can be used as a tool for estimating dielectric constants of materials.

- In the spin-phonon coupling calculation, we have obtained the coupling matrix elements with respect to changing MLWF basis functions. It would be worth comparing these results with spin-phonon coupling matrix elements calculated with respect to a fixed basis set.

In closing, we would like to say that this thesis contains several interesting advances, both in terms of development of methods and of calculation of material properties. We hope that the research presented here will prove to be helpful in future endeavours in the direction of theoretical treatments of transport in organic semiconductors.

Appendix A

Dependence of the Eigenvalue on Matrix Size and the Off-Diagonal Elements

In this appendix we discuss some general trends related to eigenvalues of a matrix and those of its submatrices. For a diagonal matrix, the eigenvalues of any submatrix are contained in the set of eigenvalues of the original matrix. However, this is not the case for a non-diagonal matrix where, due to the presence of the off-diagonal elements, typically all eigenvalues of any submatrix differ from all the eigenvalues of the full matrix. Here we shall show how such difference correlates with

- The off-diagonal elements outside the submatrix.
- The dimension of the full matrix.

In a (50×50) matrix, we define the (1,1) element as 10.0, all other diagonal elements to 8.0 and all off-diagonal elements of a (4×4) submatrix of the top left corner (i.e. a submatrix containing the element (1,1)) to 0.05[1]. Keeping these elements fixed, we vary all other elements of the matrix- i.e. the off-diagonal elements outside the submatrix from $x = 0.0$ to $x = 1.0$ and note the difference in the highest eigenvalue

[1]Note that for the complete hamiltonian $\hat{H}_{\text{full}} = \hat{H}_{\text{non SO}} + \hat{H}_{\text{SO}}$ expressed with respect to the bloch states of $\hat{H}_{\text{non\_SO}}$, the diagonal elements are typically much larger than the off diagonal ones

$$\begin{pmatrix} 10.0 & 0.05 & x & x & x & ... & x \\ 0.05 & 8.0 & x & x & x & ... & x \\ x & x & 8.0 & x & x & ... & x \\ x & x & x & 8.0 & x & ... & x \\ x & x & x & x & 8.0 & ... & x \\ \vdots & \vdots & \vdots & \vdots & \vdots & \ddots & \vdots \\ x & x & x & x & x & ... & 8.0 \end{pmatrix}$$

Figure A.1: Figure shows a representative structure of the matrix mentioned in the text. The red block in the top left corner is the submatrix

of the submatrix (the submatrix remains the same[2]) and the full matrix. The matrix is shown is Fig. (A.1). We see that this difference, which is zero for $x = 0.0$ increases rapidly with increasing x. Thus, **diagonalizing only a selected submatrix will result in large error in the eigenvalues (compared to the corresponding ones of the full matrix), if the off-diagonal elements outside the submatrix are large**. Fig A.2, which shows a log-log plot of the eigenvalue difference with variation of x, confirms the above statement.

Next, keeping the dimension and the elements of the submatrix unchanged, we increase the dimension of the full matrix from 4 to 2000. All diagonal and the off-diagonal matrix elements outside the submatrix are kept fixed at 8.0 and 0.001 respectively. Fig A.3 shows a semi-log graph of the difference in the highest eigenvalue between the submatrix and the full matrix as a function of the dimension of the full matrix. The figure shows that, **if the submatrix has the same dimension, larger the dimension of the full matrix, larger will be the eigenvalue difference**.

[2]The results of this test, i.e. the trend of the plot A.2, remains the same even if 'x' equals all off-diagonal matrix elements of the full matrix, instead of equalling all off-diagonal matrix elements outside the submatrix.

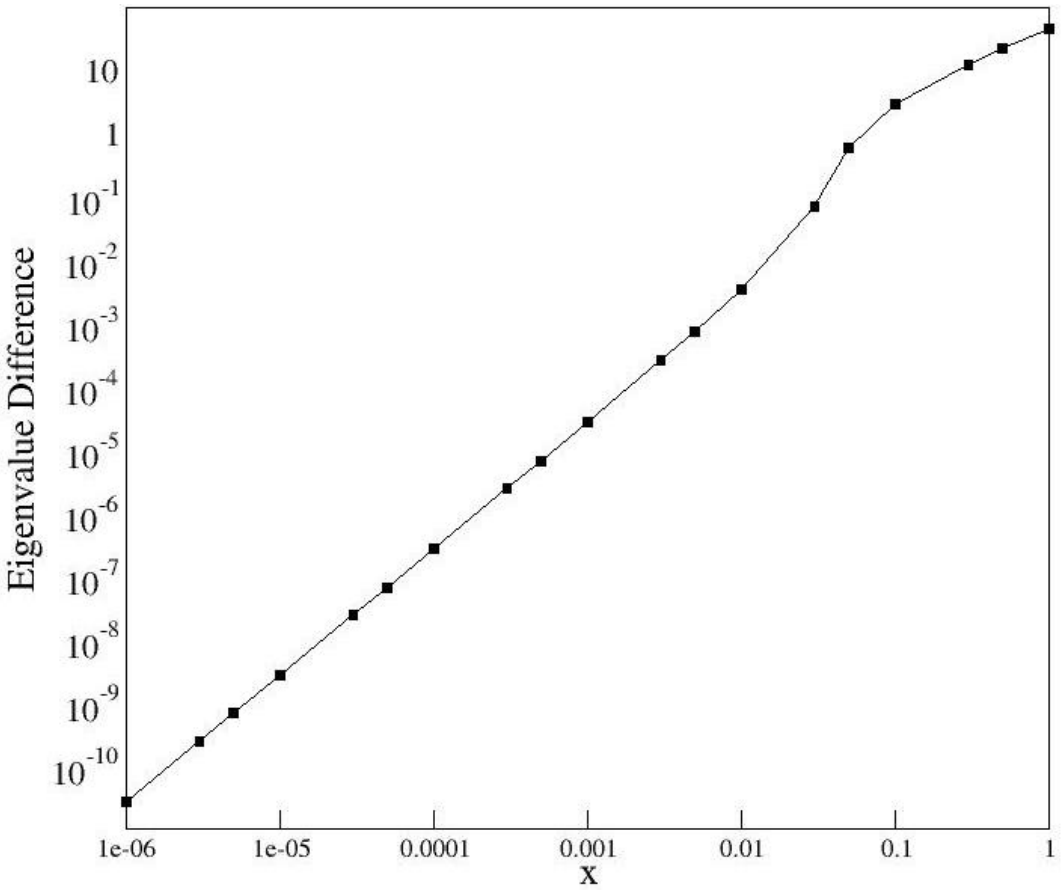

Figure A.2: Variation in the difference of the highest eigenvalue of a 50×50 matrix and its 4×4 submatrix with the change in off-diagonal elements outside the submatrix. The submatrix, which is kept fixed, contains the largest diagonal element of the full matrix.

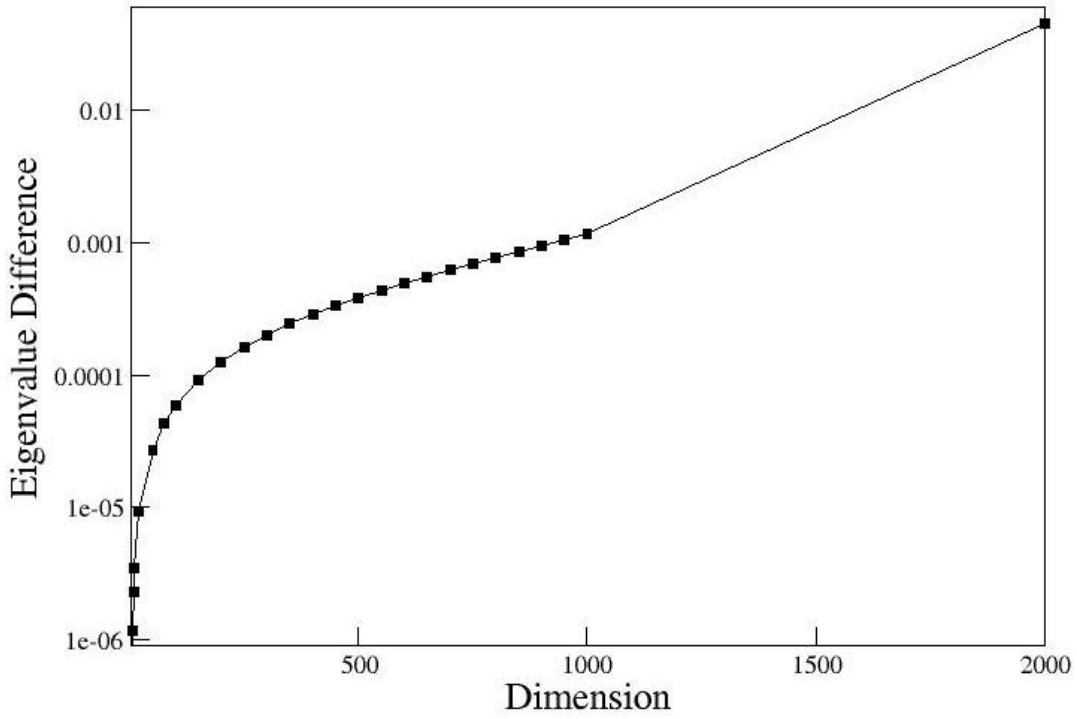

Figure A.3: Variation in the difference of the highest eigenvalue of a 50×50 matrix and its 4×4 fixed submatrix with the change in dimension of the full matrix. All the off-diagonal elements outside the submatrix are of the same value. The submatrix contains the largest diagonal element of the full matrix.

Appendix B

Spin-phonon coupling matrix elements of a Pb chain calculated with respect to 'p' orbitals

As mentioned earlier, in the on-site interaction for the spin-orbit approximation used in SIESTA, the spin-phonon matrix, as defined in Eq. (8.4), vanishes. However, without ignoring the hopping SO terms, one can obtain an analytic expressions for the SO coupling with respect to the atomic orbital basis and from these a qualitative comparison of the different spin-phonon terms can be made.

We are interested in SO terms for which the two p-orbitals are situated on neighbouring atoms of the same cell and both nuclei contribute to the coupling. Note that this means that the SO operator acting on an orbital is the result of two effects: the relative rotation (about the electron) of the nucleus of the same atom and that of the nucleus of the neighbouring atom. Denoting the $|p_m\rangle$ orbital of atom 'i' with spin s_1 as $|p_m^{s_1}(i)\rangle$ and the orbital angular momentum operator for atom i as $\hat{\mathbf{L}}(i)$ we can write:

$$\langle p_m^{s_1}(1)|\hat{V_{SO}}|p_n^{s_2}(2)\rangle = \tag{B.1}$$

$$= \left(\bar{V}_l^{SO}\,\langle p_m^{s_1}(1)|\,\hat{\mathbf{L}}(1)\cdot\hat{\mathbf{S}}\right)|p_n^{s_2}(2)\rangle + \langle p_m^{s_1}(1)|\left(\hat{\mathbf{L}}(2)\cdot\hat{\mathbf{S}}\,|p_n^{s_2}(2)\rangle\,\bar{V}_l^{SO}\right) \tag{B.2}$$

The operator $\hat{\mathbf{L}}(i)\cdot\hat{\mathbf{S}}$, in the 2×2 spin basis reads

$$\frac{1}{2}\begin{pmatrix} \hat{L_z}(i) & \hat{L_-}(i) \\ \hat{L_+}(i) & -\hat{L_z}(i) \end{pmatrix}.$$

Keeping in mind that

- $p_z = p_{1,0}$
- $p_x = \frac{1}{\sqrt{2}}\left[p_{1,1} - p_{1,-1}\right]$
- $p_y = -\frac{i}{\sqrt{2}}\left[p_{1,1} + p_{1,-1}\right]$
- $\hat{L}_\pm\,|p_{l,m}\rangle = \sqrt{l(l+1) - m(m\pm 1)}\,|p_{l,m\pm 1}\rangle$
- $\langle p_{l,m}|\,\hat{L}_\pm = \sqrt{l(l+1) - m(m\mp 1)}\,\langle p_{l,m\mp 1}|$[1]
- $\hat{L}_z\,|p_{l,m}\rangle = m\,|p_{l,m}\rangle$

with $\hbar = 1$, we can see that

1.

$$\begin{aligned}\langle p_x^{\uparrow}(1)|\hat{V}_{SO}|p_z^{\uparrow}(2)\rangle &= \bar{V}_l^{SO}\left[\langle p_x(1)|\hat{L}_z(1)|p_z(2)\rangle + \langle p_x(1)|\hat{L}_z(2)|p_z(2)\rangle\right] \\ &= -i\bar{V}_l^{SO}\,\langle p_y(1)|p_z(2)\rangle \\ &= \langle p_z^{\uparrow}(1)|\hat{V}_{SO}|p_x^{\uparrow}(2)\rangle\end{aligned}$$

Note that for an oscillation along the x or z-direction (i.e. mode 3 or mode 2 of Fig. 8.1), this should not change. Hence, the corresponding spin-phonon coupling

[1] $\hat{L_-}$ and $\hat{L_+}$ are the hermitian conjugate of each other.

should be zero. However, this is not necessarily true for motion along the y-axis. Hence, for motion along mode 3, this spin-phonon coupling term should be imaginary.

2.

$$\begin{aligned}\langle p_x^{\uparrow}(1)|\hat{V}_{SO}|p_y^{\downarrow}(2)\rangle &= \bar{V}_l^{SO}\left[\langle p_x(1)|\hat{L}_-(1)|p_y(2)\rangle + \langle p_x(1)|\hat{L}_-(2)|p_y(2)\rangle\right] = \\ &= -\bar{V}_l^{SO}\left[\langle p_z(1)|p_y(2)\rangle + i\,\langle p_x(1)|p_z(2)\rangle\right] = \\ &= \langle p_y^{\uparrow}(1)|\hat{V}_{SO}|p_x^{\downarrow}(2)\rangle\end{aligned}$$

Both terms should remain unchanged for motion along the z-direction. However, for motion along x (y)-direction, the first (second) term should remain unchanged. Hence, this spin-phonon coupling term should be real (imaginary) for oscillation along y (x) direction.

3.

$$\begin{aligned}\langle p_z^{\uparrow}(1)|\hat{V}_{SO}|p_z^{\downarrow}(2)\rangle &= \bar{V}_l^{SO}\left[\langle p_z(1)|\hat{L}_-(1)|p_z(2)\rangle + \langle p_z(1)|\hat{L}_-(2)|p_z(2)\rangle\right] = \\ &= \bar{V}_l^{SO}\left[\sqrt{2}\,\langle p_{1,1}(1)|P_z(2)\rangle + \langle P_z(1)|p_{1,-1}(2)\rangle\,\sqrt{2}\right] = \\ &= \bar{V}_l^{SO}\left[\langle p_x(1)|p_z(2)\rangle - i\,\langle p_y(1)|p_z(2)\rangle\right. \\ &\left.+i\,\langle p_z(1)|p_y(2)\rangle - \langle p_z(1)|p_x(2)\rangle\right] = \\ &= 0\end{aligned}$$

4.

$$\begin{aligned}\langle p_x^{\uparrow}(1)|\hat{V}_{SO}|p_z^{\downarrow}(2)\rangle &= \bar{V}_l^{SO}\left[\langle p_x(1)|\hat{L}_-(1)|p_z(2)\rangle + \langle p_x(1)|\hat{L}_-(2)|p_z(2)\rangle\right] = \\ &= \bar{V}_l^{SO}\left[-\langle p_z(1)|p_z(2)\rangle - \langle p_x(1)|p_x(2)\rangle + i\,\langle p_x(1)|p_y(2)\rangle\right]\end{aligned}$$

From symmetry, the imaginary part should be zero at the equilibrium position or for movement purely along the x, y or z axis. So, this spin-phonon coupling matrix element should be reaal.

5.

$$\begin{aligned}\langle p_x^{\uparrow}(1)|\hat{V}_{SO}|p_y^{\uparrow}(2)\rangle &= \bar{V}_l^{SO}\left[\langle p_x(1)|\hat{L}_z(1)|p_y(2)\rangle + \langle p_x(1)|\hat{L}_z(2)|p_y(2)\rangle\right] = \\ &= -i\bar{V}_l^{SO}\left[\langle p_y(1)|p_y(2)\rangle - \langle p_x(1)|p_x(2)\rangle\right]\end{aligned}$$

For motion along the z-direction, the change in the first term of the right-hand side should cancel that in the second term. So, for such motion, the change of this quantity should be zero.

6.

$$\begin{aligned}\langle p_z^{\uparrow}(1)|\hat{V}_{SO}|p_z^{\uparrow}(2)\rangle &= \bar{V}_l^{SO}\left[\langle p_z(1)|\hat{L}_z(1)|p_z(2)\rangle + \langle p_z(1)|\hat{L}_z(2)|p_z(2)\rangle\right] = \\ &= 0\end{aligned}$$

7.

$$\begin{aligned}\langle p_x^{\uparrow}(1)|\hat{V}_{SO}|p_x^{\uparrow}(2)\rangle &= \bar{V}_l^{SO}\left[\langle p_x(1)|\hat{L}_z(1)|p_x(2)\rangle + \langle p_x(1)|\hat{L}_z(2)|p_x(2)\rangle\right] = \\ &= i\left[\langle p_x(1)|p_y(2)\rangle - \langle p_y(1)|p_x(2)\rangle\right]\end{aligned}$$

This should always be zero from symmetry requirement.

8.

$$\langle p_x^{\uparrow}(1)|\hat{V}_{SO}|p_x^{\downarrow}(2)\rangle = \bar{V}_l^{SO}\left[-\langle p_z(1)|p_x(2)\rangle + \langle p_x(1)|p_z(2)\rangle\right] = 0$$

Appendix C

The Response Function and the Exciton

We have previously introduced the concept of greater (lesser) Green's function $G^{>}_{ij}(t,t')$ $\left(G^{<}_{ij}(t,t')\right)$, which can be interpreted as a propagator for the electron (hole) from (j,t') to (i,t). In a similar way, it is possible to define a two particle greater Green's function $G^{>}(\mathbf{r_1}t_1,\mathbf{r_2}t_2,\mathbf{r_3}t_3,\mathbf{r_4}t_4)$, which propagates two indistinguishable particles from $(\mathbf{r_1}t_1,\mathbf{r_2}t_2)$ to $(\mathbf{r_3}t_3,\mathbf{r_4}t_4)$. Such propagation can be expressed as combination of three kinds of propagations

1. Propagation of one particle from $(\mathbf{r_1}t_1)$ to $(\mathbf{r_3}t_3)$ and another particle from $(\mathbf{r_2}t_2)$ to $(\mathbf{r_4}t_4)$ without interacting with each other.

2. Propagation of one particle from $(\mathbf{r_1}t_1)$ to $(\mathbf{r_4}t_4)$ and another particle from $(\mathbf{r_2}t_2)$ to $(\mathbf{r_3}t_3)$ without interacting with each other.

3. All propagations which take into account the interactions between the particles under consideration.

In the Keldysh space, the two particle Green's function can be expressed as

$$\begin{aligned} G_2(1,2;3,4) &= G(1;3)G(2;4) - G(1;4)G(2;3) \\ &\quad + \int G(1;1')G(3';3)K_r(1',2';3',4')G(4';4)G(2;2'), \end{aligned} \tag{C.1}$$

where the number i denotes the point $(\mathbf{r}_i, z_i)$ in the Keldysh space, z_i being the complex time argument. The integral on the right-hand side is to be carried out over all the primed indices. In Eq. (C.1) K_r is a term accounting for all interactions among the two particles. The negative of the last two terms is collectively called the two particle XC-function and is denoted by $L(1,2;3,4)$.

$$L(1,2;3,4) = -[G_2(1,2;3,4) - G(1;3)G(2;4)]. \tag{C.2}$$

$L(1,2;3,4)$ follows a Dyson-like equation, known as the Bethe-Salpeter equation

$$L(1,2;3,4) = G(1;4)G(2;3) + \int G(1;1')G(3';3)K(1'2';3'4')L(4'2;2'4), \tag{C.3}$$

where $K(1,2;3,4)$ can be defined from the self-energy Σ as

$$K(1,2;3,4) = -\frac{\delta\Sigma(1;3)}{\delta G(4;2)}. \tag{C.4}$$

The diagramatic expansion for $L(1,2;1,2)$ looks as follows

$L(1,2;1,2)$

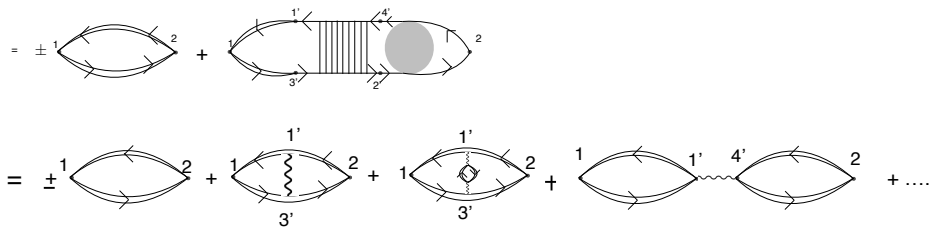

(C.5)

where the striped square and the grey circle denote $K(1'2';3'4')$ and $L(4'2;2'4)$ respectively. The first term in Eq. (C.5) is $G(1;2)G(2;1)$. Since either $z_1 > z_2$ or $z_2 > z_1$, in real time, one of the two Green's functions corresponds to the lesser Green's function, while the other corresponds to the greater one (from the Langreth's rules [233]). Therefore, the first term essentially denotes a non-interacting particle-hole propagator. All the other terms in the infinite series can be interpreted as particle-hole propagators corresponding to various levels of interaction.

It can be shown that the above series (sum of polarization diagrams joined by Coulomb interaction) represents the density response function $\chi(1;2)$ as well (see Section (11.7) of Ref. [102]). Thus we have

$$L(1,2;1,2) = \chi(1,2). \tag{C.6}$$

The discussions here shows that $L(1,2;1,2)$ and therefore, $\chi(1,2)$ acts as an interacting particle-hole propagator in the same way as $G^{>}(G^{<})$ acts as the particle (hole) propagator. This is the physical justification behind the exciton being an interacting-particle hole pair.

Bibliography

[1] W. Shockley, "The theory of p-n junctions in semiconductors and p-n junction transistors," *The Bell System Technical Journal*, vol. 28, pp. 435–489, July 1949.

[2] B. G. Yacobi, *Semiconductor Materials: An Introduction to Basic Principles (Microdevices)*. Springer Publishing Company, Incorporated, 1st ed., 2013.

[3] N. F. Mott, "The electrical conductivity of transition metals," *Proceedings of the Royal Society of London A: Mathematical, Physical and Engineering Sciences*, vol. 153, no. 880, pp. 699–717, 1936.

[4] B. Dieny, V. S. Speriosu, S. S. P. Parkin, B. A. Gurney, D. R. Wilhoit, and D. Mauri, "Giant magnetoresistive in soft ferromagnetic multilayers," *Phys. Rev. B*, vol. 43, pp. 1297–1300, Jan 1991.

[5] S. A. Wolf, D. D. Awschalom, R. A. Buhrman, J. M. Daughton, S. von Molnár, M. L. Roukes, A. Y. Chtchelkanova, and D. M. Treger, "Spintronics: A spin-based electronics vision for the future," *Science*, vol. 294, no. 5546, pp. 1488–1495, 2001.

[6] S. Sanvito, "Organic spintronics: Filtering spins with molecules," *Nat Mater*, vol. 10, pp. 484–485, Jul 2011.

[7] M. N. Baibich, J. M. Broto, A. Fert, F. N. Van Dau, F. Petroff, P. Etienne, G. Creuzet, A. Friederich, and J. Chazelas, "Giant magnetoresistance of

(001)fe/(001)cr magnetic superlattices," *Phys. Rev. Lett.*, vol. 61, pp. 2472–2475, Nov 1988.

[8] G. Binasch, P. Grünberg, F. Saurenbach, and W. Zinn, "Enhanced magnetoresistance in layered magnetic structures with antiferromagnetic interlayer exchange," *Phys. Rev. B*, vol. 39, pp. 4828–4830, Mar 1989.

[9] J. S. Moodera, L. R. Kinder, T. M. Wong, and R. Meservey, "Large magnetoresistance at room temperature in ferromagnetic thin film tunnel junctions," *Phys. Rev. Lett.*, vol. 74, pp. 3273–3276, Apr 1995.

[10] J. Fabian, A. Matos-Abiague, C. Ertler, P. Stano, and I. Zutic, "Semiconductor spintronics," *Acta Phys. Slovaca*, vol. 57, no. 4, pp. 565–907, 2007.

[11] D. D. Awschalom and M. E. Flatte, "Challenges for semiconductor spintronics," *Nat Phys*, vol. 3, pp. 153–159, Mar 2007.

[12] E. I. Rashba, "Theory of electrical spin injection: Tunnel contacts as a solution of the conductivity mismatch problem," *Phys. Rev. B*, vol. 62, pp. R16267–R16270, Dec 2000.

[13] G. Malliaras and R. Friend, "An organic electronics primer," *Physics Today*, vol. 58, no. 5, pp. 53–58, 2005.

[14] M. Muccini, "A bright future for organic field-effect transistors," *Nat Mater*, vol. 5, pp. 605–613, Aug 2006.

[15] C. W. Tang and S. A. VanSlyke, "Organic electroluminescent diodes," *Applied Physics Letters*, vol. 51, no. 12, pp. 913–915, 1987.

[16] A. Dodabalapur, H. E. Katz, L. Torsi, and R. C. Haddon, "Organic heterostructure field-èffect transistors," *Science*, vol. 269, no. 5230, pp. 1560–1562, 1995.

[17] "Embracing the organics world," *Nat Mater*, vol. 12, pp. 591–591, Jul 2013. Editorial.

[18] C. Wang, H. Dong, L. Jiang, and W. Hu, "Organic semiconductor crystals," *Chem. Soc. Rev.*, pp. –, 2018.

[19] S. Sanvito, "Molecular spintronics," *Chem. Soc. Rev.*, vol. 40, pp. 3336–3355, 2011.

[20] S. R. Forrest, "The path to ubiquitous and low-cost organic electronic appliances on plastic," *Nature*, vol. 428, pp. 911–918, Apr 2004.

[21] A. Facchetti, "Organic semiconductors: Made to order," *Nat Mater*, vol. 12, pp. 598–600, Jul 2013. News and Views.

[22] S. R. Forrest, "Ultrathin organic films grown by organic molecular beam deposition and related techniques," *Chemical Reviews*, vol. 97, no. 6, pp. 1793–1896, 1997.

[23] G. Gu, P. E. Burrows, S. Venkatesh, S. R. Forrest, and M. E. Thompson, "Vacuum-deposited, nonpolymeric flexible organic light-emitting devices," *Opt. Lett.*, vol. 22, pp. 172–174, Feb 1997.

[24] P. Burrows, S. Forrest, L. Sapochak, J. Schwartz, P. Fenter, T. Buma, V. Ban, and J. Forrest, "Organic vapor phase deposition: a new method for the growth of organic thin films with large optical non-linearities," *Journal of Crystal Growth*, vol. 156, no. 1, pp. 91 – 98, 1995.

[25] M. Shtein, H. F. Gossenberger, J. B. Benziger, and S. R. Forrest, "Material transport regimes and mechanisms for growth of molecular organic thin films using low-pressure organic vapor phase deposition," *Journal of Applied Physics*, vol. 89, no. 2, pp. 1470–1476, 2001.

[26] M. Shtein, P. Peumans, J. B. Benziger, and S. R. Forrest, "Micropatterning of small molecular weight organic semiconductor thin films using organic vapor phase deposition," *Journal of Applied Physics*, vol. 93, no. 7, pp. 4005–4016, 2003.

[27] J. Wang, X. Sun, L. Chen, and S. Y. Chou, "Direct nanoimprint of submicron organic light-emitting structures," *Applied Physics Letters*, vol. 75, no. 18, pp. 2767–2769, 1999.

[28] J. Zaumseil, T. Someya, Z. Bao, Y.-L. Loo, R. Cirelli, and J. A. Rogers, "Nanoscale organic transistors that use source/drain electrodes supported by high resolution rubber stamps," *Applied Physics Letters*, vol. 82, no. 5, pp. 793–795, 2003.

[29] H. Sirringhaus, T. Kawase, R. H. Friend, T. Shimoda, M. Inbasekaran, W. Wu, and E. P. Woo, "High-resolution inkjet printing of all-polymer transistor circuits," *Science*, vol. 290, no. 5499, pp. 2123–2126, 2000.

[30] T. R. Hebner and J. C. Sturm, "Local tuning of organic light-emitting diode color by dye droplet application," *Applied Physics Letters*, vol. 73, no. 13, pp. 1775–1777, 1998.

[31] P. C. Duineveld, M. M. de Kok, M. Buechel, A. Sempel, K. A. H. Mutsaers, P. van de Weijer, I. G. J. Camps, T. van de Biggelaar, J.-E. J. M. Rubingh, and E. I. Haskal, "Ink-jet printing of polymer light-emitting devices," *Proc. SPIE*, vol. 4464, pp. 59–67, 2002.

[32] N. D. Treat, J. A. Nekuda Malik, O. Reid, L. Yu, C. G. Shuttle, G. Rumbles, C. J. Hawker, M. L. Chabinyc, P. Smith, and N. Stingelin, "Microstructure formation in molecular and polymer semiconductors assisted by nucleation agents," *Nat Mater*, vol. 12, pp. 628–633, Jul 2013. Letter.

[33] Y. Diao, B. C.-K. Tee, G. Giri, J. Xu, D. H. Kim, H. A. Becerril, R. M. Stoltenberg, T. H. Lee, G. Xue, S. C. B. Mannsfeld, and Z. Bao, "Solution coating of large-area organic semiconductor thin films with aligned single-crystalline domains," *Nat Mater*, vol. 12, pp. 665–671, Jul 2013. Article.

[34] B.-G. Kim, E. J. Jeong, J. W. Chung, S. Seo, B. Koo, and J. Kim, "A molecular design principle of lyotropic liquid-crystalline conjugated polymers with directed alignment capability for plastic electronics," *Nat Mater*, vol. 12, pp. 659–664, Jul 2013. Article.

[35] C. Groves, "Organic light-emitting diodes: Bright design," *Nat Mater*, vol. 12, pp. 597–598, Jul 2013. News and Views.

[36] W. Tress, *Organic Solar Cells*, pp. 67–214. Cham: Springer International Publishing, 2014.

[37] J. Nelson, "Organic photovoltaic films," *Materials Today*, vol. 5, no. 5, pp. 20 – 27, 2002.

[38] H. Koezuka, A. Tsumura, and T. Ando, "Field-effect transistor with polythiophene thin film," *Synthetic Metals*, vol. 18, no. 1, pp. 699 – 704, 1987. Proceedings of the International Conference of Science and Technology of Synthetic Metals.

[39] H. Yan, Z. Chen, Y. Zheng, C. Newman, J. R. Quinn, F. Dotz, M. Kastler, and A. Facchetti, "A high-mobility electron-transporting polymer for printed transistors," *Nature*, vol. 457, pp. 679–686, Feb 2009.

[40] Y. Yamashita, "Organic semiconductors for organic field-effect transistors," *Science and Technology of Advanced Materials*, vol. 10, no. 2, p. 024313, 2009.

[41] G. Szulczewski, S. Sanvito, and M. Coey, "A spin of their own," *Nat Mater*, vol. 8, pp. 693–695, Sep 2009.

[42] M. Cinchetti, K. Heimer, J.-P. Wustenberg, O. Andreyev, M. Bauer, S. Lach, C. Ziegler, Y. Gao, and M. Aeschlimann, "Determination of spin injection and transport in a ferromagnet/organic semiconductor heterojunction by two-photon photoemission," *Nat Mater*, vol. 8, pp. 115–119, Feb 2009.

[43] L. Schulz, L. Nuccio, M. Willis, P. Desai, P. Shakya, T. Kreouzis, V. K. Malik, C. Bernhard, F. L. Pratt, N. A. Morley, A. Suter, G. J. Nieuwenhuys, T. Prokscha, E. Morenzoni, W. P. Gillin, and A. J. Drew, "Engineering spin propagation across a hybrid organic/inorganic interface using a polar layer," *Nat Mater*, vol. 10, pp. 39–44, Jan 2011.

[44] Z. H. Xiong, D. Wu, Z. Valy Vardeny, and J. Shi, "Giant magnetoresistance in organic spin-valves," *Nature*, vol. 427, pp. 821–824, Feb 2004.

[45] S. Sanvito, "Molecular spintronics: The rise of spinterface science," *Nat Phys*, vol. 6, pp. 562–564, Aug 2010.

[46] P. A. Bobbert, T. D. Nguyen, F. W. A. van Oost, B. Koopmans, and M. Wohlgenannt, "Bipolaron mechanism for organic magnetoresistance," *Phys. Rev. Lett.*, vol. 99, p. 216801, Nov 2007.

[47] F. Kuemmeth, S. Ilani, D. C. Ralph, and P. L. McEuen, "Coupling of spin and orbital motion of electrons in carbon nanotubes," *Nature*, vol. 452, pp. 448–452, Mar 2008.

[48] M. D. McGehee, "Nanostructured organicinorganic hybrid solar cells," *MRS Bulletin*, vol. 34, no. 2, p. 95100, 2009.

[49] A. Troisi, "Charge transport in high mobility molecular semiconductors: classical models and new theories," *Chem. Soc. Rev.*, vol. 40, pp. 2347–2358, 2011.

[50] S. Datta, *Electronic Transport in Mesoscopic Systems*. Cambridge Studies in Semiconductor Physi, Cambridge University Press, 1997.

[51] A. R. Rocha, V. M. García-Suárez, S. Bailey, C. Lambert, J. Ferrer, and S. Sanvito, "Spin and molecular electronics in atomically generated orbital landscapes," *Phys. Rev. B*, vol. 73, p. 085414, Feb 2006.

[52] S. R. Forrest, "The path to ubiquitous and low-cost organic electronic appliances on plastic," *Nature*, vol. 428, p. 911, 2004.

[53] C. Dimitrakopoulos and P. Malenfant, "Organic thin film transistors for large area electronics," *Advanced Materials*, vol. 14, no. 2, pp. 99–117, 2002.

[54] O. D. Jurchescu, J. Baas, and T. T. M. Palstra, "Effect of impurities on the mobility of single crystal pentacene," *Applied Physics Letters*, vol. 84, no. 16, pp. 3061–3063, 2004.

[55] O. Ostroverkhova, D. G. Cooke, F. A. Hegmann, J. E. Anthony, V. Podzorov, M. E. Gershenson, O. D. Jurchescu, and T. T. M. Palstra, "Ultrafast carrier dynamics in pentacene, functionalized pentacene, tetracene, and rubrene single crystals," *Applied Physics Letters*, vol. 88, no. 16, p. 162101, 2006.

[56] K. Marumoto, S.-i. Kuroda, T. Takenobu, and Y. Iwasa, "Spatial extent of wave functions of gate-induced hole carriers in pentacene field-effect devices as investigated by electron spin resonance," *Phys. Rev. Lett.*, vol. 97, p. 256603, Dec 2006.

[57] T. Sakanoue and H. Sirringhaus, "Band-like temperature dependence of mobility in a solution-processed organic semiconductor," *Nat. Mater*, vol. 9, p. 736, 2010.

[58] K. Hannewald, V. M. Stojanović, J. M. T. Schellekens, P. A. Bobbert, G. Kresse, and J. Hafner, "Theory of polaron bandwidth narrowing in organic molecular crystals," *Phys. Rev. B*, vol. 69, p. 075211, Feb 2004.

[59] K. Hannewald and P. A. Bobbert, "Anisotropy effects in phonon-assisted charge-carrier transport in organic molecular crystals," *Phys. Rev. B*, vol. 69, p. 075212, Feb 2004.

[60] F. Ortmann, K. Hannewald, and F. Bechstedt, "Ab initio description and visualization of charge transport in durene crystals," *Applied Physics Letters*, vol. 93, no. 22, p. 222105, 2008.

[61] C. Motta and S. Sanvito, "Charge transport properties of durene crystals from first-principles," *Journal of Chemical Theory and Computation*, vol. 10, no. 10, pp. 4624–4632, 2014.

[62] A. Troisi and G. Orlandi, "Dynamics of the intermolecular transfer integral in crystalline organic semiconductors," *The Journal of Physical Chemistry A*, vol. 110, no. 11, pp. 4065–4070, 2006.

[63] V. Coropceanu, R. S. Snchez-Carrera, P. Paramonov, G. M. Day, and J.-L. Brdas, "Interaction of charge carriers with lattice vibrations in organic molecular semiconductors: Naphthalene as a case study," *J. Phys. Chem. C*, vol. 113, no. 11, pp. 4679–4686, 2009.

[64] V. Coropceanu, J. Cornil, D. A. da Silva Filho, Y. Olivier, R. Silbey, and J.-L. Brdas, "Charge transport in organic semiconductors," *Chem. Rev.*, vol. 107, no. 4, pp. 926–952, 2007.

[65] R. A. Marcus, "Electron transfer reactions in chemistry theory and experiment," *J. Electroanal. Chem.*, vol. 438, no. 1, pp. 251 – 259, 1997.

[66] A. Troisi and G. Orlandi, "Charge-transport regime of crystalline organic semiconductors: Diffusion limited by thermal off-diagonal electronic disorder," *Phys. Rev. Lett.*, vol. 96, p. 086601, Mar 2006.

[67] A. Troisi, D. L. Cheung, and D. Andrienko, "Charge transport in semiconductors with multiscale conformational dynamics," *Phys. Rev. Lett.*, vol. 102, p. 116602, Mar 2009.

[68] A. M. Souza, I. Rungger, U. Schwingenschlogl, and S. Sanvito, "The image charge effect and vibron-assisted processes in coulomb blockade transport: a first principles approach," *Nanoscale*, vol. 7, pp. 19231–19240, 2015.

[69] C. D. Pemmaraju, I. Rungger, and S. Sanvito, "Ab initio calculation of the bias-dependent transport properties of mn12 molecules," *Phys. Rev. B*, vol. 80, p. 104422, Sep 2009.

[70] N. Marzari, A. A. Mostofi, J. R. Yates, I. Souza, and D. Vanderbilt, "Maximally localized wannier functions: Theory and applications," *Rev. Mod. Phys.*, vol. 84, pp. 1419–1475, Oct 2012.

[71] P. A. Bobbert, W. Wagemans, F. W. A. van Oost, B. Koopmans, and M. Wohlgenannt, "Theory for spin diffusion in disordered organic semiconductors," *Phys. Rev. Lett.*, vol. 102, p. 156604, Apr 2009.

[72] G. H. Wannier, "The structure of electronic excitation levels in insulating crystals," *Phys. Rev.*, vol. 52, pp. 191–197, Aug 1937.

[73] G. H. Wannier, "Dynamics of band electrons in electric and magnetic fields," *Rev. Mod. Phys.*, vol. 34, pp. 645–655, Oct 1962.

[74] J. Hafner, C. Wolverton, and G. Ceder, "Toward computational materials design: The impact of density functional theory on materials research," *MRS Bulletin*, vol. 31, no. 9, p. 659668, 2006.

[75] P. J. Hasnip, K. Refson, M. I. J. Probert, J. R. Yates, S. J. Clark, and C. J. Pickard, "Density functional theory in the solid state," *Philosophical Transactions of the Royal Society of London A: Mathematical, Physical and Engineering Sciences*, vol. 372, no. 2011, 2014.

[76] N. Ashcroft and N. Mermin, *Solid State Physics*. Philadelphia: Saunders College, 1976.

[77] M. Levy, "Universal variational functionals of electron densities, first-order density matrices, and natural spin-orbitals and solution of the v-representability problem," *Proceedings of the National Academy of Sciences*, vol. 76, no. 12, pp. 6062–6065, 1979.

[78] M. Levy, "Electron densities in search of hamiltonians," *Phys. Rev. A*, vol. 26, pp. 1200–1208, Sep 1982.

[79] P. Hohenberg and W. Kohn, "Inhomogeneous electron gas," *Phys. Rev.*, vol. 136, pp. B864–B871, Nov 1964.

[80] W. Kohn and L. J. Sham, "Self-consistent equations including exchange and correlation effects," *Phys. Rev.*, vol. 140, pp. A1133–A1138, Nov 1965.

[81] P. Mori-Sánchez, A. J. Cohen, and W. Yang, "Localization and delocalization errors in density functional theory and implications for band-gap prediction," *Phys. Rev. Lett.*, vol. 100, p. 146401, Apr 2008.

[82] A. J. Cohen, P. Mori-Sánchez, and W. Yang, "Insights into current limitations of density functional theory," *Science*, vol. 321, no. 5890, pp. 792–794, 2008.

[83] E. Engel and R. Dreizler, *Density Functional Theory: An Advanced Course*. Theoretical and Mathematical Physics, Springer Berlin Heidelberg, 2011.

[84] J. P. Perdew and M. Levy, "Physical content of the exact kohn-sham orbital energies: Band gaps and derivative discontinuities," *Phys. Rev. Lett.*, vol. 51, pp. 1884–1887, Nov 1983.

[85] W. Yang, A. J. Cohen, and P. Mori-Snchez, "Derivative discontinuity, bandgap and lowest unoccupied molecular orbital in density functional theory," *The Journal of Chemical Physics*, vol. 136, no. 20, p. 204111, 2012.

[86] D. D. O'Regan and G. Teobaldi, "Optimization of constrained density functional theory," *Phys. Rev. B*, vol. 94, p. 035159, Jul 2016.

[87] Q. Wu and T. Van Voorhis, "Direct optimization method to study constrained systems within density-functional theory," *Phys. Rev. A*, vol. 72, p. 024502, Aug 2005.

[88] B. Kaduk, T. Kowalczyk, and T. Van Voorhis, "Constrained density functional theory," *Chem. Rev.*, vol. 112, no. 1, pp. 321–370, 2012.

[89] T. L. Gilbert, "Hohenberg-kohn theorem for nonlocal external potentials," *Phys. Rev. B*, vol. 12, pp. 2111–2120, Sep 1975.

[90] M. C. Payne, M. P. Teter, D. C. Allan, T. A. Arias, and J. D. Joannopoulos, "Iterative minimization techniques for ab initio total-energy calculations: molecular dynamics and conjugate gradients," *Rev. Mod. Phys.*, vol. 64, pp. 1045–1097, Oct 1992.

[91] D. R. Hamann, M. Schlüter, and C. Chiang, "Norm-conserving pseudopotentials," *Phys. Rev. Lett.*, vol. 43, pp. 1494–1497, Nov 1979.

[92] R. Martin, *Electronic Structure: Basic Theory and Practical Methods*. Cambridge University Press, 2004.

[93] O. V. Gritsenko, P. R. T. Schipper, and E. J. Baerends, "Exchange and correlation energy in density functional theory: Comparison of accurate density functional theory quantities with traditional hartreefock based ones and generalized gradient approximations for the molecules li2, n2, f2," *The Journal of Chemical Physics*, vol. 107, no. 13, pp. 5007–5015, 1997.

[94] J. P. Perdew, K. Burke, and M. Ernzerhof, "Generalized gradient approximation made simple," *Phys. Rev. Lett.*, vol. 77, pp. 3865–3868, Oct 1996.

[95] J. M. Soler, E. Artacho, J. D. Gale, A. Garca, J. Junquera, P. Ordejn, and D. Snchez-Portal, "The siesta method for ab initio order- n materials simulation," *Journal of Physics: Condensed Matter*, vol. 14, no. 11, p. 2745, 2002.

[96] C.-K. Skylaris, P. D. Haynes, A. A. Mostofi, and M. C. Payne, "Introducing onetep: Linear-scaling density functional simulations on parallel computers," *J. Chem. Phys.*, vol. 122, no. 8, p. 084119, 2005.

[97] P. D. Haynes, C.-K. Skylaris, A. A. Mostofi, and M. C. Payne, "Density kernel optimization in the onetep code," *J. Phys. Condens. Matter*, vol. 20, no. 29, p. 294207, 2008.

[98] P. D. Haynes, C.-K. Skylaris, A. A. Mostofi, and M. C. Payne, "Density kernel optimization in the onetep code," *Journal of Physics: Condensed Matter*, vol. 20, no. 29, p. 294207, 2008.

[99] P. Lwdin, "On the nonorthogonality problem connected with the use of atomic wave functions in the theory of molecules and crystals," *J. Chem. Phys.*, vol. 18, no. 3, pp. 365–375, 1950.

[100] H. Bruus and K. Flensberg, *Many-Body Quantum Theory in Condensed Matter Physics: An Introduction*. Oxford Graduate Texts, OUP Oxford, 2004.

[101] A. Fetter and J. Walecka, *Quantum Theory of Many-particle Systems*. Dover Books on Physics, Dover Publications, 2003.

[102] G. Stefanucci and R. van Leeuwen, *Nonequilibrium Many-Body Theory of Quantum Systems*. Cambridge: Cambridge University Press, 2013.

[103] A. R. Holt, "On the simplified second born approximation," *Journal of Physics B: Atomic and Molecular Physics*, vol. 5, no. 1, p. L6, 1972.

[104] K. Held, C. Taranto, G. Rohringer, and A. Toschi, "Hedin equations, gw, gw+dmft, and all that," *arXiv:1109.3972 [cond-mat.mtrl-sci]*, 2011.

[105] K. S. Thygesen and A. Rubio, "Renormalization of molecular quasiparticle levels at metal-molecule interfaces: Trends across binding regimes," *Phys. Rev. Lett.*, vol. 102, p. 046802, 2009.

[106] J. F. Janak, "Proof that eni= in density-functional theory," *Phys. Rev. B*, vol. 18, p. 7165, 1978.

[107] D. A. Egger, Z.-F. Liu, J. B. Neaton, and L. Kronik, "Reliable energy level alignment at physisorbed moleculemetal interfaces from density functional theory," *Nano Letters*, vol. 15, no. 4, pp. 2448–2455, 2015.

[108] Z.-F. Liu, D. A. Egger, S. Refaely-Abramson, L. Kronik, and J. B. Neaton, "Energy level alignment at molecule-metal interfaces from an optimally tuned range-separated hybrid functional," *The Journal of Chemical Physics*, vol. 146, no. 9, p. 092326, 2017.

[109] A. M. Souza, I. Rungger, C. D. Pemmaraju, U. Schwingenschloegl, and S. Sanvito, "Constrained-dft method for accurate energy-level alignment of metal/molecule interfaces," *Phys. Rev. B*, vol. 88, p. 165112, Oct 2013.

[110] R. Dovesi, B. Civalleri, C. Roetti, V. R. Saunders, and R. Orlando, "Ab initio quantum simulation in solid state chemistry," *Reviews in Computational Chemistry*, vol. 21, pp. 1–125, 2005.

[111] Y.-H. Zhang, Kai-GeZhou, Ke-FengXie, JingZeng, H.-L. Zhang, and Y. Peng, "Tuning the electronic structure and transport properties of graphene by non-covalent functionalization: effects of organic donor, acceptor and metal atoms," *Nanotechnology*, vol. 21, p. 065201, 2010.

[112] K. Kimura, S. Katsumata, Y. Achiba, T. Yamazaki, and S. Iwata, *Hand- book of HeI Photoelectron Spectra of Fundamental Organic Molecules*. Japan Scientific Societies Press, 1981.

[113] J. C. Rienstra-Kiracofe, G. S. Tschumper, H. F. S. III, S. Nandi, and G. B. Ellison, "Atomic and molecular electron affinities: Photoelectron experiments and theoretical computations," *Chem. Rev.*, vol. 102, p. 231282, 2002.

[114] V. Despoja, I. L. , D. J. Mowbray, and L. M. , "Quasiparticle spectra and excitons of organic molecules deposited on substrates: G0w0-bse approach applied to benzene on graphene and metallic substrates," *Phys. Rev. B*, vol. 88, p. 235437, 2013.

[115] F. Banhart, J. Kotakoski, and A. V. Krasheninnikov *ACS Nano*, vol. 5, p. 26, 2001.

[116] N. D. Lang and W. Kohn, "Theory of metal surfaces: Work function," *Phys. Rev. B*, vol. 3, no. 4, p. 1215, 1971.

[117] B. Wunsch, T. Stauber, F. Sols, and F. Guinea, "Dynamical polarization of graphene at finite doping," *New Journal of Physics*, vol. 8, no. 12, p. 318, 2006.

[118] V. I. Anisimov, J. Zaanen, and O. K. Andersen, "Band theory and mott insulators: Hubbard u instead of stoner i," *Phys. Rev. B*, vol. 44, pp. 943–954, Jul 1991.

[119] B. Himmetoglu, A. Floris, S. de Gironcoli, and M. Cococcioni, "Hubbard-corrected dft energy functionals: The lda+u description of correlated systems," *Int. J. Quantum Chem.*, vol. 114, no. 1, pp. 14–49, 2014.

[120] V. I. Anisimov, A. I. Poteryaev, M. A. Korotin, A. O. Anokhin, and G. Kotliar, "First-principles calculations of the electronic structure and spectra of strongly correlated systems: dynamical mean-field theory," *J. Phys. Condens. Matter*, vol. 9, no. 35, p. 7359, 1997.

[121] G. Kotliar, S. Y. Savrasov, K. Haule, V. S. Oudovenko, O. Parcollet, and C. A. Marianetti, "Electronic structure calculations with dynamical mean-field theory," *Rev. Mod. Phys.*, vol. 78, pp. 865–951, Aug 2006.

[122] S. J. Bennie, M. Stella, T. F. M. III, and F. R. Manby, "Accelerating wavefunction in density-functional-theory embedding by truncating the active basis set," *J. Chem. Phys.*, vol. 143, no. 2, p. 024105, 2015.

[123] P. Sherwood, A. H. de Vries, S. J. Collins, S. P. Greatbanks, N. A. Burton, M. A. Vincent, and I. H. Hillier, "Computer simulation of zeolite structure and

reactivity using embedded cluster methods," *Farad. Discuss.*, vol. 106, pp. 79–92, 1997.

[124] F. WEINHOLD and C. R. LANDIS, "Natural bond orbitals and extensions of localized bonding concepts," *Chem. Educ. Res. Pract.*, vol. 2, pp. 91–104, 2001.

[125] N. Marzari and D. Vanderbilt, "Maximally localized generalized wannier functions for composite energy bands," *Phys. Rev. B*, vol. 56, pp. 12847–12865, Nov 1997.

[126] L. Peng, F. L. Gu, and W. Yang, "Effective preconditioning for ab initio ground state energy minimization with non-orthogonal localized molecular orbitals," *Phys. Chem. Chem. Phys.*, vol. 15, pp. 15518–15527, 2013.

[127] O. K. Andersen, T. Saha-Dasgupta, R. W. Tank, C. Arcangeli, O. Jepsen, and G. Krier, "Developing the MTO Formalism," in *Electronic Structure and Physical Properties of Solids. The Use of the LMTO Method* (H. Dreyssé, ed.), vol. 535 of *Lecture Notes in Physics, Berlin Springer Verlag*, p. 3, 2000.

[128] M. Soriano and J. J. Palacios, "Theory of projections with nonorthogonal basis sets: Partitioning techniques and effective hamiltonians," *Phys. Rev. B*, vol. 90, p. 075128, Aug 2014.

[129] D. Jacob, "Towards a full ab initio theory of strong electronic correlations in nanoscale devices," *J. Phys. Condens. Matter*, vol. 27, no. 24, p. 245606, 2015.

[130] D. D. O'Regan, M. C. Payne, and A. A. Mostofi, "Subspace representations in ab initio methods for strongly correlated systems," *Phys. Rev. B*, vol. 83, p. 245124, Jun 2011.

[131] Y.-C. Wang, Z.-H. Chen, and H. Jiang, "The local projection in the density functional theory plus u approach: A critical assessment," *J. Chem. Phys.*, vol. 144, no. 14, p. 144106, 2016.

[132] K. Haule, C.-H. Yee, and K. Kim, "Dynamical mean-field theory within the full-potential methods: Electronic structure of ceirin$_5$, cecoin$_5$, and cerhin$_5$," *Phys. Rev. B*, vol. 81, p. 195107, May 2010.

[133] D. Novoselov, D. M. Korotin, and V. I. Anisimov, "Hellmannfeynman forces within the dft + u in wannier functions basis," *Journal of Physics: Condensed Matter*, vol. 27, no. 32, p. 325602, 2015.

[134] P. F. Barbara, T. J. Meyer, and M. A. Ratner, "Contemporary issues in electron transfer research," *J. Phys. Chem.*, vol. 100, no. 31, pp. 13148–13168, 1996.

[135] V. Rhle, A. Lukyanov, F. May, M. Schrader, T. Vehoff, J. Kirkpatrick, B. Baumeier, and D. Andrienko, "Microscopic simulations of charge transport in disordered organic semiconductors," *J. Chem. Theory Comput.*, vol. 7, no. 10, pp. 3335–3345, 2011.

[136] Y. Yamashita, "Organic semiconductors for organic field-effect transistors," *Sci. Tech. Adv. Mater.*, vol. 10, no. 2, p. 024313, 2009.

[137] T. Hasegawa and J. Takeya, "Organic field-effect transistors using single crystals," *Sci. Tech. Adv. Mater.*, vol. 10, no. 2, p. 024314, 2009.

[138] N. E. Gruhn, D. A. da Silva Filho, T. G. Bill, M. Malagoli, V. Coropceanu, A. Kahn, and J.-L. Brdas, "The vibrational reorganization energy in pentacene: molecular influences on charge transport," *Journal of the American Chemical Society*, vol. 124, no. 27, pp. 7918–7919, 2002.

[139] V. Coropceanu, M. Malagoli, D. A. da Silva Filho, N. E. Gruhn, T. G. Bill, and J. L. Brédas, "Hole- and electron-vibrational couplings in oligoacene crystals: Intramolecular contributions," *Phys. Rev. Lett.*, vol. 89, p. 275503, Dec 2002.

[140] R. S. Snchez-Carrera, V. Coropceanu, D. A. da Silva Filho, R. Friedlein, W. Osikowicz, R. Murdey, C. Suess, W. R. Salaneck, and J.-L. Brdas, "Vibronic coupling in the ground and excited states of oligoacene cations," *J. Phys. Chem. B*, vol. 110, no. 38, pp. 18904–18911, 2006.

[141] S. Kera, H. Yamane, and N. Ueno, "First-principles measurements of charge mobility in organic semiconductors: Valence holevibration coupling in organic ultrathin films," *Progress in Surface Science*, vol. 84, no. 5, pp. 135 – 154, 2009.

[142] X. Yang, L. Wang, C. Wang, W. Long, and Z. Shuai, "Influences of crystal structures and molecular sizes on the charge mobility of organic semiconductors: Oligothiophenes," *Chem. Mater.*, vol. 20, no. 9, pp. 3205–3211, 2008.

[143] H. Nakano and H. Sato, "Introducing the mean field approximation to cdft/mmpol method: Statistically converged equilibrium and nonequilibrium free energy calculation for electron transfer reactions in condensed phases," *J. Chem. Phys.*, vol. 146, no. 15, p. 154101, 2017.

[144] L. E. Ratcliff, L. Grisanti, L. Genovese, T. Deutsch, T. Neumann, D. Danilov, W. Wenzel, D. Beljonne, and J. Cornil, "Toward fast and accurate evaluation of charge on-site energies and transfer integrals in supramolecular architectures using linear constrained density functional theory (cdft)-based methods," *J. Chem. Theory Comput.*, vol. 11, no. 5, pp. 2077–2086, 2015.

[145] K. M. Pelzer, A. Vazquez-Mayagoitia, L. E. Ratcliff, S. Tretiak, R. A. Bair, S. K. Gray, T. Van Voorhis, R. E. Larsen, and S. B. Darling, "Molecular dynamics and charge transport in organic semiconductors: a classical approach to modeling electron transfer," *Chem. Sci.*, vol. 8, pp. 2597–2609, 2017.

[146] A. Droghetti, I. Rungger, C. Das Pemmaraju, and S. Sanvito, "Fundamental gap of molecular crystals via constrained density functional theory," *Phys. Rev. B*, vol. 93, p. 195208, May 2016.

[147] S. Roychoudhury, C. Motta, and S. Sanvito, "Charge transfer energies of benzene physisorbed on a graphene sheet from constrained density functional theory," *Phys. Rev. B*, vol. 93, p. 045130, Jan 2016.

[148] H. Yamane, S. Nagamatsu, H. Fukagawa, S. Kera, R. Friedlein, K. K. Okudaira, and N. Ueno, "Hole-vibration coupling of the highest occupied state in pentacene thin films," *Phys. Rev. B*, vol. 72, p. 153412, Oct 2005.

[149] P. B. Paramonov, V. Coropceanu, and J.-L. Brédas, "Electronic and vibronic interactions at weakly bound organic interfaces: The case of pentacene on graphite," *Phys. Rev. B*, vol. 78, p. 041403, Jul 2008.

[150] lvaro Ruiz-Serrano, N. D. M. Hine, and C.-K. Skylaris, "Pulay forces from localized orbitals optimized in situ using a psinc basis set," *J. Chem. Phys.*, vol. 136, no. 23, p. 234101, 2012.

[151] Q. Wu and T. Van Voorhis, "Direct calculation of electron transfer parameters through constrained density functional theory," *J. Phys. Chem. A*, vol. 110, no. 29, pp. 9212–9218, 2006.

[152] E. Artacho and L. Miláns del Bosch, "Nonorthogonal basis sets in quantum mechanics: Representations and second quantization," *Phys. Rev. A*, vol. 43, pp. 5770–5777, Jun 1991.

[153] D. H. P. Turban, G. Teobaldi, D. D. O'Regan, and N. D. M. Hine, "Supercell convergence of charge-transfer energies in pentacene molecular crystals from constrained dft," *Phys. Rev. B*, vol. 93, p. 165102, Apr 2016.

[154] B. G. Pfrommer, M. Ct, S. G. Louie, and M. L. Cohen, "Relaxation of crystals with the quasi-newton method," *Journal of Computational Physics*, vol. 131, no. 1, pp. 233 – 240, 1997.

[155] N. D. M. Hine, M. Robinson, P. D. Haynes, C.-K. Skylaris, M. C. Payne, and A. A. Mostofi, "Accurate ionic forces and geometry optimization in linear-scaling density-functional theory with local orbitals," *Phys. Rev. B*, vol. 83, p. 195102, May 2011.

[156] N. Marzari, D. Vanderbilt, and M. C. Payne, "Ensemble density-functional theory for ab initio molecular dynamics of metals and finite-temperature insulators," *Phys. Rev. Lett.*, vol. 79, pp. 1337–1340, Aug 1997.

[157] lvaro Ruiz-Serrano and C.-K. Skylaris, "A variational method for density functional theory calculations on metallic systems with thousands of atoms," *J. Chem. Phys.*, vol. 139, no. 5, p. 054107, 2013.

[158] G. J. Martyna and M. E. Tuckerman, "A reciprocal space based method for treating long range interactions in ab initio and force-field-based calculations in clusters," *J. Chem. Phys.*, vol. 110, no. 6, pp. 2810–2821, 1999.

[159] N. D. M. Hine, J. Dziedzic, P. D. Haynes, and C.-K. Skylaris, "Electrostatic interactions in finite systems treated with periodic boundary conditions: Application to linear-scaling density functional theory," *J. Chem. Phys.*, vol. 135, no. 20, p. 204103, 2011.

[160] M. Elstner, P. Hobza, T. Frauenheim, S. Suhai, and E. Kaxiras, "Hydrogen bonding and stacking interactions of nucleic acid base pairs: A density-functional-theory based treatment," *J. Chem. Phys.*, vol. 114, no. 12, pp. 5149–5155, 2001.

[161] Q. Hill and C.-K. Skylaris, "Including dispersion interactions in the onetep program for linear-scaling density functional theory calculations," *Proc. R. Soc. A*, vol. 465, no. 2103, pp. 669–683, 2009.

[162] S. J. A. van Gisbergen, C. Fonseca Guerra, and E. J. Baerends, "Towards excitation energies and (hyper)polarizability calculations of large molecules. application of parallelization and linear scaling techniques to time-dependent density functional response theory," *Journal of Computational Chemistry*, vol. 21, no. 16, pp. 1511–1523, 2000.

[163] N. T. Maitra, F. Zhang, R. J. Cave, and K. Burke, "Double excitations within time-dependent density functional theory linear response," *The Journal of Chemical Physics*, vol. 120, no. 13, pp. 5932–5937, 2004.

[164] P. Elliott, S. Goldson, C. Canahui, and N. T. Maitra, "Perspectives on double-excitations in tddft," *Chemical Physics*, vol. 391, no. 1, pp. 110 – 119, 2011. Open problems and new solutions in time dependent density functional theory.

[165] N. T. Maitra, "Perspective: Fundamental aspects of time-dependent density functional theory," *J. Chem. Phys.*, vol. 144, no. 22, p. 220901, 2016.

[166] M. Rohlfing and S. G. Louie, "Electron-hole excitations and optical spectra from first principles," *Phys. Rev. B*, vol. 62, pp. 4927–4944, Aug 2000.

[167] G. Onida, L. Reining, and A. Rubio, "Electronic excitations: density-functional versus many-body green's-function approaches," *Rev. Mod. Phys.*, vol. 74, pp. 601–659, Jun 2002.

[168] M. P. Ljungberg, P. Koval, F. Ferrari, D. Foerster, and D. Sánchez-Portal, "Cubic-scaling iterative solution of the bethe-salpeter equation for finite systems," *Phys. Rev. B*, vol. 92, p. 075422, Aug 2015.

[169] D. Sangalli, P. Romaniello, G. Onida, and A. Marini, "Double excitations in correlated systems: A manybody approach," *The Journal of Chemical Physics*, vol. 134, no. 3, p. 034115, 2011.

[170] E. Pavarini, E. Koch, J. van den Brink, and G. Sawatzky, *Quantum Materials: Experiments and Theory*, vol. 6 of *Modeling and Simulation*. Jlich: Forschungszentrum Jlich, Sep 2016.

[171] M. Levy and A. Nagy, "Variational density-functional theory for an individual excited state," *Phys. Rev. Lett.*, vol. 83, pp. 4361–4364, Nov 1999.

[172] J. P. Perdew and M. Levy, "Extrema of the density functional for the energy: Excited states from the ground-state theory," *Phys. Rev. B*, vol. 31, pp. 6264–6272, May 1985.

[173] P. W. Ayers and M. Levy, "Time-independent (static) density-functional theories for pure excited states: Extensions and unification," *Phys. Rev. A*, vol. 80, p. 012508, Jul 2009.

[174] C.-L. Cheng, Q. Wu, and T. V. Voorhis, "Rydberg energies using excited state density functional theory," *The Journal of Chemical Physics*, vol. 129, no. 12, p. 124112, 2008.

[175] T. Kowalczyk, S. R. Yost, and T. V. Voorhis, "Assessment of the scf density functional theory approach for electronic excitations in organic dyes," *The Journal of Chemical Physics*, vol. 134, no. 5, p. 054128, 2011.

[176] L. N. Oliveira, E. K. U. Gross, and W. Kohn, "Ensemble-density functional theory for excited states," *International Journal of Quantum Chemistry*, vol. 38, no. S24, pp. 707–716, 1990.

[177] Z.-h. Yang, A. Pribram-Jones, K. Burke, and C. A. Ullrich, "Direct extraction of excitation energies from ensemble density-functional theory," *Phys. Rev. Lett.*, vol. 119, p. 033003, Jul 2017.

[178] K. Deur, L. Mazouin, and E. Fromager, "Exact ensemble density functional theory for excited states in a model system: Investigating the weight dependence of the correlation energy," *Phys. Rev. B*, vol. 95, p. 035120, Jan 2017.

[179] T. Ziegler, M. Seth, M. Krykunov, J. Autschbach, and F. Wang, "On the relation between time-dependent and variational density functional theory approaches for the determination of excitation energies and transition moments.," *The Journal of Chemical Physics*, vol. 130, no. 15, p. 154102, 2009.

[180] M. Krykunov, S. Grimme, and T. Ziegler, "Accurate theoretical description of the 1la and 1lb excited states in acenes using the all order constricted variational density functional theory method and the local density approximation," *Journal of Chemical Theory and Computation*, vol. 8, no. 11, pp. 4434–4440, 2012.

[181] A. T. B. Gilbert, N. A. Besley, and P. M. W. Gill, "Self-consistent field calculations of excited states using the maximum overlap method (mom)," *The Journal of Physical Chemistry A*, vol. 112, no. 50, pp. 13164–13171, 2008.

[182] M. W. D. Hanson-Heine, M. W. George, and N. A. Besley, "Calculating excited state properties using kohn-sham density functional theory," *The Journal of Chemical Physics*, vol. 138, no. 6, p. 064101, 2013.

[183] K. Sneskov and O. Christiansen, "Excited state coupled cluster methods," *Wiley Interdiscip. Rev. Comput. Mol. Sci.*, vol. 2, no. 4, pp. 566–584, 2012.

[184] Q. Wu and T. Van Voorhis, "Constrained density functional theory and its application in long-range electron transfer," *Journal of Chemical Theory and Computation*, vol. 2, no. 3, pp. 765–774, 2006.

[185] M. Casida and M. Huix-Rotllant, "Progress in time-dependent density-functional theory," *Annual Review of Physical Chemistry*, vol. 63, no. 1, pp. 287–323, 2012.

[186] M. E. CASIDA, *Time-Dependent Density Functional Response Theory for Molecules*, pp. 155–192.

[187] M. R. Silva-Junior, M. Schreiber, S. P. A. Sauer, and W. Thiel, "Benchmarks for electronically excited states: Time-dependent density functional theory and density functional theory based multireference configuration interaction," *The Journal of Chemical Physics*, vol. 129, no. 10, p. 104103, 2008.

[188] D. Jacquemin, V. Wathelet, E. A. Perpte, and C. Adamo, "Extensive td-dft benchmark: Singlet-excited states of organic molecules," *Journal of Chemical Theory and Computation*, vol. 5, no. 9, pp. 2420–2435, 2009.

[189] D. Jacquemin, E. A. Perpte, I. Ciofini, and C. Adamo, "Assessment of functionals for td-dft calculations of singlettriplet transitions," *Journal of Chemical Theory and Computation*, vol. 6, no. 5, pp. 1532–1537, 2010.

[190] M. Schreiber, M. R. Silva-Junior, S. P. A. Sauer, and W. Thiel, "Benchmarks for electronically excited states: Caspt2, cc2, ccsd, and cc3," *The Journal of Chemical Physics*, vol. 128, no. 13, p. 134110, 2008.

[191] C. R. Jacob and M. Reiher, "Spin in density-functional theory," *International Journal of Quantum Chemistry*, vol. 112, no. 23, pp. 3661–3684, 2012.

[192] J. P. Perdew, A. Ruzsinszky, L. A. Constantin, J. Sun, and G. I. Csonka, "Some fundamental issues in ground-state density functional theory: A guide for the perplexed," *Journal of Chemical Theory and Computation*, vol. 5, no. 4, pp. 902–908, 2009.

[193] J. Wang, A. D. Becke, and V. H. S. Jr., "Evaluation of s2 in restricted, unrestricted hartreefock, and density functional based theories," *The Journal of Chemical Physics*, vol. 102, no. 8, pp. 3477–3480, 1995.

[194] A. J. Cohen, D. J. Tozer, and N. C. Handy, "Evaluation of s2 in density functional theory," *The Journal of Chemical Physics*, vol. 126, no. 21, p. 214104, 2007.

[195] J. M. Wittbrodt and H. B. Schlegel, "Some reasons not to use spin projected density functional theory," *The Journal of Chemical Physics*, vol. 105, no. 15, pp. 6574–6577, 1996.

[196] J. GRFENSTEIN and D. CREMER, "On the diagnostic value of (2) in kohn-sham density functional theory," *Molecular Physics*, vol. 99, no. 11, pp. 981–989, 2001.

[197] M. K. Y. Chan and G. Ceder, "Efficient band gap prediction for solids," *Phys. Rev. Lett.*, vol. 105, p. 196403, Nov 2010.

[198] O. Brafman and I. T. Steinberger, "Optical band gap and birefringence of zns polytypes," *Phys. Rev.*, vol. 143, pp. 501–505, Mar 1966.

[199] W. M. Yim, E. J. Stofko, P. J. Zanzucchi, J. I. Pankove, M. Ettenberg, and S. L. Gilbert, "Epitaxially grown aln and its optical band gap," *Journal of Applied Physics*, vol. 44, no. 1, pp. 292–296, 1973.

[200] T. Harris, *Optical Properties of Si, Ge, GaAs, GaSb, InAs, and InP at Elevated Temperatures*. 2010.

[201] B. Hammer, L. B. Hansen, and J. K. Nørskov, "Improved adsorption energetics within density-functional theory using revised perdew-burke-ernzerhof functionals," *Phys. Rev. B*, vol. 59, pp. 7413–7421, Mar 1999.

[202] C. Adamo and V. Barone, "Toward reliable density functional methods without adjustable parameters: The pbe0 model," *Journal of Chemical Physics*, vol. 110, no. 13, pp. 6158–6170, 1999. cited By 6371.

[203] A. D. Becke, "A new mixing of hartreefock and local densityfunctional theories," *The Journal of Chemical Physics*, vol. 98, no. 2, pp. 1372–1377, 1993.

[204] C. Adamo and V. Barone, "Toward reliable adiabatic connection models free from adjustable parameters," *Chemical Physics Letters*, vol. 274, no. 1, pp. 242 – 250, 1997.

[205] S. Hirata and M. Head-Gordon, "Time-dependent density functional theory within the tammdancoff approximation," *Chemical Physics Letters*, vol. 314, no. 3, pp. 291 – 299, 1999.

[206] A. Kramida and W. C. Martin, "A compilation of energy levels and wavelengths for the spectrum of neutral beryllium (be i)," *Journal of Physical and Chemical Reference Data*, vol. 26, no. 5, pp. 1185–1194, 1997.

[207] D. J. Tozer and N. C. Handy, "On the determination of excitation energies using density functional theory," *Phys. Chem. Chem. Phys.*, vol. 2, pp. 2117–2121, 2000.

[208] V. I. Krinichnyi *Synth. Met.*, vol. 108, no. 108, pp. 173–222, 2000.

[209] S. Bandyopadhyay, "Dominant spin relaxation mechanism in compound organic semiconductors," *Phys. Rev. B*, vol. 81, p. 153202, Apr 2010.

[210] A. J. Drew *et al.*, "Direct measurement of the electronic spin diffusion length in a fully functional organic spin valve by low-energy muon spin rotation," *Nature Materials*, vol. 8, no. 2, pp. 109–114, 2009.

[211] F. J. Wang, C. G. Yang, Z. V. Vardeny, and X. G. Li, "Spin response in organic spin valves based on $la_{23}sr_{13}Mno_3$ electrodes," *Phys. Rev. B*, vol. 75, p. 245324, Jun 2007.

[212] V. Dediu, L. E. Hueso, I. Bergenti, A. Riminucci, F. Borgatti, P. Graziosi, C. Newby, F. Casoli, M. P. De Jong, C. Taliani, and Y. Zhan, "Room-temperature spintronic effects in alq_3-based hybrid devices," *Phys. Rev. B*, vol. 78, p. 115203, Sep 2008.

[213] C. Cohen-Tannoudji, B. Diu, and F. Laloė, *Quantum mechanics. 2.* Textbook physics, John Wiley & Sons, 1977.

[214] B. A. He, C. M. Marian, U. Wahlgren, and O. Gropen, "A mean-field spin-orbit method applicable to correlated wavefunctions," *Chemical Physics Letters*, vol. 251, no. 5, pp. 365 – 371, 1996.

[215] L. Fernández-Seivane, M. A. Oliveira, S. Sanvito, and J. Ferrer, "On-site approximation for spin–orbit coupling in linear combination of atomic orbitals density functional methods," *J. Phys. Condens. Matter*, vol. 18, no. 34, p. 7999, 2006.

[216] A. A. Mostofi, J. R. Yates, Y.-S. Lee, I. Souza, D. Vanderbilt, and N. Marzari, "wannier90: A tool for obtaining maximally-localised wannier functions," *Comput. Phys. Commun.*, vol. 178, no. 9, pp. 685 – 699, 2008.

[217] S. Romanov, "Electronic structure of the minimum-diameter tl, pb and bi quantum wire superlattices," *Journal of Physics: Condensed Matter*, vol. 5, no. 8, p. 1081, 1993.

[218] E. Moulin, F. Niess, M. Maaloum, E. Buhler, I. Nyrkova, and N. Giuseppone, "The hierarchical self-assembly of charge nanocarriers: A highly cooperative process promoted by visible light," *Angew. Chem. Int. Ed.*, vol. 49, no. 39, pp. 6974–6978, 2010.

[219] Z. Ning and H. Tian, "Triarylamine: a promising core unit for efficient photovoltaic materials," *Chem. Commun.*, vol. 37, pp. 5483–5495, 2009.

[220] V. Faramarzi, F. Niess, E. Moulin, M. Maaloum, J.-F. Dayen, J.-B. Beaufrand, S. Zanettini, B. Doudin, and N. Giuseppone, "Light-triggered self-construction of supramolecular organic nanowires as metallic interconnects," *Nature Chemistry*, vol. 4, pp. 485–490, 06 2012.

[221] A. Akande, S. Bhattacharya, T. Cathcart, and S. Sanvito, "First principles study of the structural, electronic, and transport properties of triarylamine-based nanowires," *J. Chem. Phys*, vol. 140, no. 7, 2014.

[222] S. Bhattacharya, A. Akande, and S. Sanvito, "Spin transport properties of triarylamine-based nanowires," *Chem. Commun.*, vol. 50, pp. 6626–6629, 2014.

[223] H. Shi, Z. An, P.-Z. Li, J. Yin, G. Xing, T. He, H. Chen, J. Wang, H. Sun, W. Huang, and Y. Zhao, "Enhancing organic phosphorescence by manipulating heavy-atom interaction," *Crystal Growth & Design*, vol. 16, no. 2, pp. 808–813, 2016.

[224] F. Ortmann, K. Hannewald, and F. Bechstedt, "Electronic properties of durene crystals: Implications for charge transport," *physica status solidi (b)*, vol. 245, no. 5, pp. 825–829, 2008.

[225] H. Ishii, N. Kobayashi, and K. Hirose, "Charge transport calculations by a wave-packet dynamical approach using maximally localized wannier functions based on density functional theory: Application to high-mobility organic semiconductors," *Phys. Rev. B*, vol. 95, p. 035433, Jan 2017.

[226] T. Birol and C. J. Fennie, "Origin of giant spin-lattice coupling and the suppression of ferroelectricity in eutio$_3$ from first principles," *Phys. Rev. B*, vol. 88, p. 094103, Sep 2013.

[227] J. H. Lee and K. M. Rabe, "Large spin-phonon coupling and magnetically induced phonon anisotropy in sr$m$o$_3$ perovskites (m = V,cr,mn,fe,co)," *Phys. Rev. B*, vol. 84, p. 104440, Sep 2011.

[228] J. Hong, A. Stroppa, J. Íñiguez, S. Picozzi, and D. Vanderbilt, "Spin-phonon coupling effects in transition-metal perovskites: A dft + u and hybrid-functional study," *Phys. Rev. B*, vol. 85, p. 054417, Feb 2012.

[229] T. Birol, N. A. Benedek, H. Das, A. L. Wysocki, A. T. Mulder, B. M. Abbett, E. H. Smith, S. Ghosh, and C. J. Fennie, "The magnetoelectric effect in transition metal oxides: Insights and the rational design of new materials from first principles," *Current Opinion in Solid State and Materials Science*, vol. 16, no. 5, pp. 227 – 242, 2012. Multiferroics.

[230] M. Mochizuki, N. Furukawa, and N. Nagaosa, "Theory of spin-phonon coupling in multiferroic manganese perovskites $r$mno$_3$," *Phys. Rev. B*, vol. 84, p. 144409, Oct 2011.

[231] K. Kaasbjerg, K. S. Thygesen, and K. W. Jacobsen, "Phonon-limited mobility in n-type single-layer mos$_2$ from first principles," *Phys. Rev. B*, vol. 85, p. 115317, Mar 2012.

[232] A. Girlando, L. Grisanti, M. Masino, I. Bilotti, A. Brillante, R. G. Della Valle, and E. Venuti, "Peierls and holstein carrier-phonon coupling in crystalline rubrene," *Phys. Rev. B*, vol. 82, p. 035208, Jul 2010.

[233] D. C. Langreth, *Linear and Nonlinear Response Theory with Applications*, pp. 3–32. Boston, MA: Springer US, 1976.